EXCLUSIVELY AVAILABLE VIA IEEE Xplore® DIGITAL LIBRARY

ISSN 2475-742X (Print)
ISSN 3066-2427 (Online)

CPSS Transactions on Power Electronics and Applications

VOLUME 10 NUMBER 4 DECEMBER 2025

REGULAR PAPERS

A PUBLICATION OF THE CHINA POWER SUPPLY SOCIETY

CPSS Transactions on Power Electronics and Applications

CPSS Transactions on Power Electronics and Applications (CPSS TPEA) is sponsored and published by China Power Supply Society and technically co-sponsored by IEEE Power Electronics Society. It publishes original and high quality peer reviewed papers in the field of power electronics and its applications. With the goal of promoting the technology of power electronics including concepts, theory, modeling and control, analysis and simulation, emerging technology and applications, CPSS TPEA is expected to be a favorable platform to strengthen information exchange in this area. Interested authors are welcome to submit your papers via the Manuscript Central (https://mc03.manuscriptcentral.com/tpea-cpss) online submission system. You can find more information on our website: http://tpea.cpss.org.cn.

Improved Transformer-Less Grid-Connected PV Inverter with CCMV for Enhanced Efficiency

Aditi Atul DESAI and Suresh MIKKILI

***Abstract*—This paper introduces a new inverter design known as "Novel H6 inverter" with six switches to address the challenges related to common mode voltage fluctuations, leakage current, conduction losses and efficiency in a grid connected inverter that does not use transformer. Its working and performance is further compared with prevailing inverters without transformer, namely H5, H6-I, H6-II, and HERIC. The focus is on evaluating the common mode voltage and common mode current produced by these inverters. All five inverters are modelled on MATLAB/Simulink platform and a comparative study based on simulation outcome is carried out. Subsequently, the simulation results are confirmed through practical implementation on hardware prototype. The hardware validation provides concrete evidence of the proposed inverter's performance and serves to enhance the credibility of the study's conclusions.**

***Index Terms*—Common mode current, common mode voltage, parasitic capacitance, six switch inverter, transformer-less inverters.**

I. Introduction

THE increasing popularity of inverters without transformer in photovoltaic (PV) systems connected to the grid can be attributed to their advantages, such as lower cost, reduced weight and improved efficiency. This has led to their widespread adoption in distributed PV power generation systems [1]. Nevertheless, the leakage current is also referred as common mode current (CMC) present in transformer-less inverters (TLI) can give rise to electromagnetic interference, and issues related to reliability and security.

The block diagram shown in Fig. 1 depicts a direct link of the solar system to the grid, removing the requirement for a transformer.

In this system, stray capacitance is created due to voltage variation amid PV and ground. C_{pv1} indicates the incidental capacitance between the PV positive terminal and ground; C_{pv2} represents the incidental capacitance between the PV negative terminal and ground; C_{pv} indicates effective stray capacitance. Common mode voltage (CMV) refers to the voltage difference between PV system and ground. The elements that affect parasitic capacitance include the PV cell and module surfaces, the distance between them, dust, and humidity.

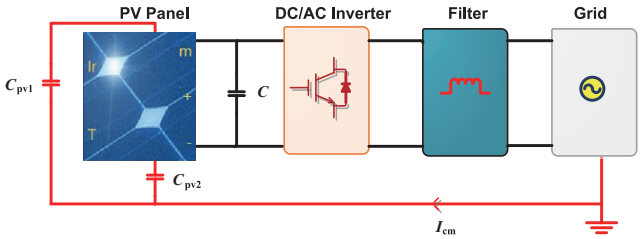

Fig. 1. Representation of PV and Grid integration.

CMV charges and discharges C_{pv} which generates CMC and is indicated as I_{cm}. This CMC affects the safety of the person [2] and also increases electromagnetic interference, grid current variations, and overall system losses.

To ensure the safe functioning of grid connected PV system using TLI, adherence to established safety standards is essential [3]. One crucial safety requirement outlined by VDE 0126-1-1 is that if the CMC exceeds 30 mA, the protective mechanism must initiate the disconnection within 0.3 seconds [4]. This specification aims to swiftly mitigate any potential hazards associated with excessive CMC. Many researchers have compared the existing TLI to eliminate the CMC [5]–[10]. Accordingly, some researchers have suggested methods such as AC isolation, DC isolation, and topologies with the common ground or CMV clamping [11]–[20].

A common-ground inverter based on the Cuk converter with high voltage gain is proposed in [21] to suppress the leakage current. A coupled inductor and a capacitor are connected in series to enhance the Boost capability in the circuit. [22] has proposed a general topology derivation method of the double-grounded single-phase inverters based on graph theory. In [23], a new Buck-Boost DC-AC inverter is developed for PV system with broad input voltage range coverage. [24] proposed to eliminate CMC by a method based on modulation. The suggested carrier-assist modulation stabilized the flying capacitor voltage by altering the pulse sequence and could eliminate CMV. [25] recommended a TLI with five level switched capacitor and boosting capability. [26] proposed a quasi-one-stage four switches inverter with an ability to eliminate CMC. A common mode equivalent circuit is developed in [27], considering the filter and grounding system. In order to

Manuscript received August 2, 2024; revised May 1, 2025 and August 7, 2025; accepted September 7, 2025. Date of publication December 30, 2025; date of current version December 2, 2025. This work was supported in part by Anusandhan National Research Foundation (ANRF) under the grant ANRF/PAIR/2025/000017/EPAIR. (*Corresponding author: Suresh Mikkili.*)

A. A. Desai is with the Electrical and Electronics Engineering, Goa College of Engineering, Goa 403401, India (e-mail: aditi@gec.ac.in).

Suresh Mikkili is with the Electrical and Electronics Engineering, National Institute of Technology, Goa 403703, India (e-mail: mikkili.suresh@nitgoa.ac.in).

Digital Object Identifier 10.24295/CPSSTPEA.2025.00034

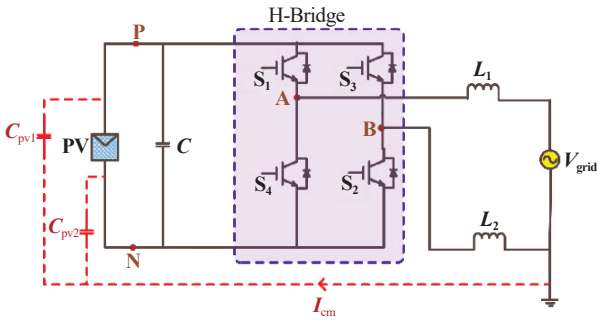

Fig. 2. Path of leakage current between grid and PV in the absence of transformer.

overcome the low-frequency leakage currents, a CMV control method is proposed. A high-dimensional space vector PWM is introduced to synthesize both differential mode voltage and CMV references for the single/three-phase PWM converter. A nine-level inverter with four times the input voltage gain is proposed in [28]. The configuration is designed based on a switched capacitor (SC) along with common ground structure. The common ground helps in avoiding parasitic capacitance. CCMV switched capacitor PV inverter configuration is proposed in [29] that maintains a low-frequency terminal voltage while considering the effect of switch device junction capacitance. In a two stage topology, [30] has proposed a gain unit circuit in the front-stage to improve the Boost capability. In addition, the rear-stage converter has double Buck inverter, which is able to prevent the short circuit of the bridge arms and improves the reliability of the system. Also, it ensures that there is no high-frequency component in the parasitic capacitor voltage, and suppresses the leakage current. A novel reconfigurable LCL filter in PV transformer less inverters is proposed in [31], which eliminates the need for a DC link connection. It also clamps the common-mode voltage to neutral at high frequencies, resulting in the reduction of leakage current. [32] has designed single-phase onboard charger to achieve low leakage current with an MPC based zero sequence control method. A hybrid topology using both decoupling and midpoint clamping technique is adopted in [33] to reduce the root mean square and peak value of leakage current.

In this paper an effort is made to reinforce the current research by recommending a new six switch TLI called Novel six switch inverter to eradicate the CMC, minimize the conduction loss and improve the efficiency. Therefore, this paper first analyzes the working of H5, H6-I, H6-II, and HERIC TLI and then recommends a Novel six switch TLI to improve the limitations of the above inverters. MATLAB/Simulink software is utilized, to simulate these inverters and are further confirmed experimentally in a laboratory setup.

II. Concept of Leakage Current

The PV panel supplies DC input to the 4 switch inverter as shown in Fig. 2. P and N represent the terminals of solar panel; A and B represent the TLI output terminals. The output of the inverter is filtered by symmetrical inductors and fed to a single-phase grid. It is seen that parasitic capacitance C_{pv1} and C_{pv2} exist between PV and ground.

V_{AN} and V_{BN} are averaged to form CMV (V_{cm}), where V_{AN} represents the voltage across node A and N; V_{BN} represents the voltage across node B and N. The expression for V_{cm} is as follows [34], [35]:

$$V_{cm} = \frac{V_{AN+}V_{BN}}{2} \tag{1}$$

The difference between V_{AN} and V_{BN} is called differential mode voltage (V_{dm}). It is given by (2).

$$V_{dm} = V_{AN} - V_{BN} \tag{2}$$

V_{dm} generates a surplus V_{cm} called V_{cm_dm}. It is given by (3).

$$V_{cm\_dm} = \frac{V_{AN} - V_{BN}}{2} \cdot \frac{L_2 - L_1}{2(L_2 + L_1)} \tag{3}$$

Therefore, the total V_{cm} (V_{cm_total}) is given by (4).

$$\begin{cases} V_{cm\_total} = V_{cm} + V_{cm\_dm} \\ V_{cm\_total} = \dfrac{V_{AN} + V_{BN}}{2} + \dfrac{V_{AN} - V_{BN}}{2} \cdot \dfrac{L_2 - L_1}{2(L_2 + L_1)} \end{cases} \tag{4}$$

If identical inductors are used as a filter, such that $L_1 = L_2$, then (4) is reduced to $V_{cm\_total} = V_{cm}$.

CMC (I_{cm}) depends on V_{cm} and equivalent parasitic capacitance C_{pv}. The equation for I_{cm} is given by (5).

$$I_{cm} = C_{pv} \frac{dV_{cm}}{dt} \tag{5}$$

If CMV is maintained constant, then the CMC can be made zero. V_{AN} and V_{BN} values are defined by inverter topologies and modulation schemes. Hence, constant CMV (CCMV) can be obtained by implementing various inverter topologies and modulation methods.

The most commonly used modulation techniques are Unipolar (UPWM) and Bipolar (BPWM). The advantage of UPWM is that it generates three-level voltage, produces low losses, and generates high efficiency. The main disadvantage is that it generates significant CMC due to varying CMV.

Bipolar modulation on the other side results in a two-level voltage and effectively manages the challenges of high core and switching losses. Hence it generates low efficiency in comparison with UPWM. Yet, it produces stable CMV and a low magnitude of CMC.

To exploit the numerous advantages of UPWM technique, this paper employs the same to generate the triggering pulses across all the considered inverters.

III. Existing Transformer-Less Topologies

The TLI topologies which already exist in literature are H5, H6, and HERIC. H5 and H6 topologies are DC-decoupled whereas, HERIC topology is AC-decoupled. H5, HERIC, and two versions of H6 TLI are discussed in this paper in terms of their working, nature of CMV, amount of CMC, conduction losses produced, and efficiency generated.

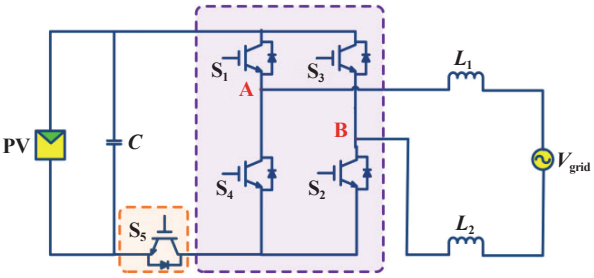

Fig. 3. Illustration of H5 topology.

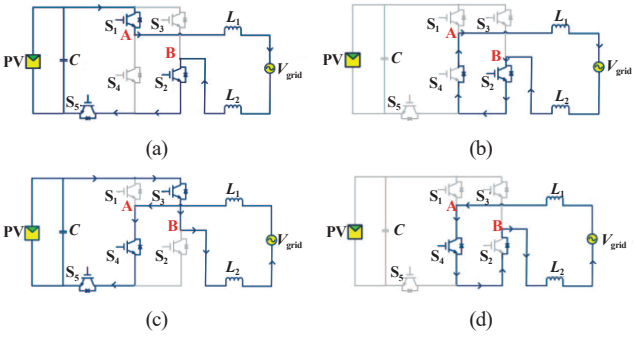

Fig. 4. Demonstration of H5 topology working. (a) Conduction mode for V_g>0, (b) Freewheeling mode for V_g>0, (c) Conduction mode for V_g<0, (d) Freewheeling mode for V_g<0.

A. H5 Inverter Topology:

This topology is an extension of full bridge (FB) inverter with an intermediate switch S_5 between PV system and the FB inverter. Including the fifth switch assures separation of the PV and grid while switching to zero voltage. Fig. 3 represents the H5 topology. In this topology, S_2 operates at 50 Hz during V_g>0; S_4 operates at 50 Hz during V_g<0 whereas, switches S_1 and S_3 function at 10 kHz during the alternate phases of V_g, respectively. S_5 maintains a constant switching frequency for the full cycle.

The H5 topology has four modes of working.

When S_1, S_2, and S_5 are triggered in mode 1, as shown in Fig. 4(a), they establish a conductive pathway between PV and grid. In mode 2, as per Fig. 4(b), the current finds a path through S_2 and built-in diode of switch S_4. In mode 3, as per Fig. 4(c), the grid current has reversed its direction and flows through S_3, S_4, and S_5 and connects the PV to the grid. In mode 4, as per Fig. 4(d), the current finds a path through S_4 and built-in diode of switch S_2.

CMV shuffles between $V_{pv}/2$ and 0 in 4 modes, where V_{pv} is the voltage across the solar panel. Hence, in the H5 topology, CMC flows between PV and grid. Fig. 13(a) and Fig. 13(b) depicts the waveforms for V_{AN}, V_{BN}, and V_{AB}, V_{cm}, and I_{cm} of H5 inverter.

B. H6-I Inverter Topology:

In this topology, there are two symmetrical switches connected with the FB topology. Fig. 5 represents the H6-I topology proposed in [36].

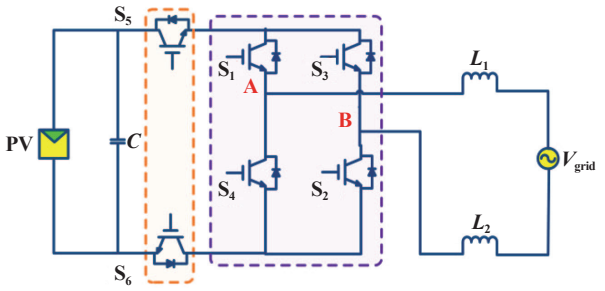

Fig. 5. Demonstration of H6-I inverter.

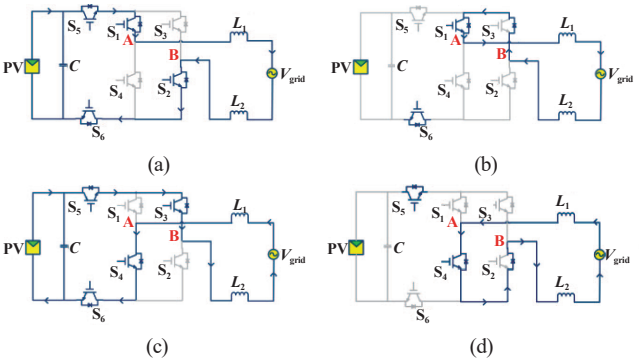

Fig. 6. Demonstration of H6-I topology working. (a) Conduction mode for V_g>0, (b) Freewheeling mode for V_g>0, (c) Conduction mode for V_g<0, (d) Freewheeling mode for V_g<0.

In H6-I inverter, switch S_1 and S_4 function at line frequency, whereas S_2 and S_3 are triggered at switching speed of 10 kHz. To achieve the DC-decoupling, two symmetrical switches, S_5 and S_6, are triggered in a sequential manner at both line frequency and switching speed. The four modes of working are depicted in Fig. 6(a) to 6(d) respectively. In mode 1, S_5, S_1, S_2, and S_6 switches are triggered, leading to positive grid current.

In mode 2, since S_2 and S_5 are off, the voltage V_{AN} gradually decreases whereas V_{BN} increases until the voltages are equal and the inductor current flows between built in diode of S_3 and switch S_1. In mode 3, current through the inductor increases in the reverse direction and flows through S_5, S_3, S_4, and S_6 switches. In mode 4, since S_3 and S_6 switches are off, the voltage V_{AN} gradually increases whereas V_{BN} decreases until the voltages are equal and the current through inductor circulates between S_4 switch and S_2 body diode.

It is seen that CMV does not change in any of the modes. Fig. 13(c) and Fig. 13(d) indicates the waveforms of H6-I inverter topology.

C. H6-II Inverter Topology:

This inverter was proposed in [37]. It has six switches and two diodes. Fig. 7 represents the H6-II topology. The top two and bottom two switches operate at 10 kHz during positive and reverse half cycles, respectively. The middle two switches operate at line frequency.

In mode 1, as depicted in Fig. 8(a), S_1, S_2, and S_3 carry the

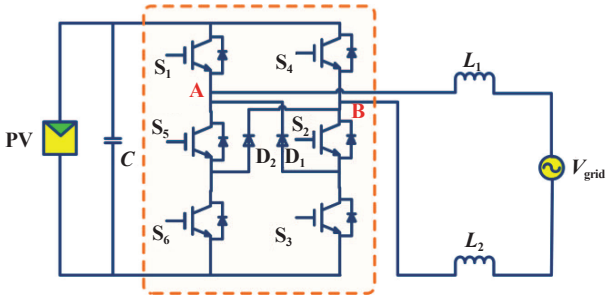

Fig. 7. Demonstration of H6-II inverter.

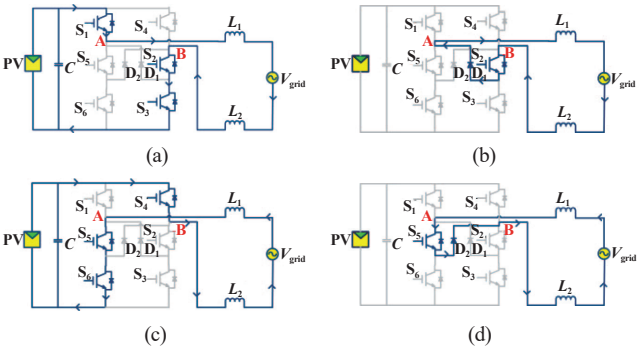

Fig. 8. Demonstration of H6-II topology functioning. (a) Working mode for V_g>0, (b) Idling mode for positive V_g, (c) Working mode for negative V_g, (d) Idling mode for negative V_g.

current. In mode 2, as seen in Fig. 8(b), switch S_2 and diode D_1 carry the current flow. Hence it isolates the PV and the grid. However, CMV remains unchanged and is $V_{PV}/2$. In the third mode, as depicted in Fig. 8(c), the current reverses itself since switches S_4, S_5, and S_6 are operated. In mode 4, as seen in Fig. 8(d), switch S_5 and diode D_2 allow the current to circulate. Thus it disconnects the PV from the grid. From the above, it can be seen that CMV remains constant in all four modes.

Fig. 13(e) and Fig. 13(f) depicts the waveforms of H6-II inverter.

D. HERIC Inverter Topology:

The highly efficient and reliable inverter concept (HERIC) topology is AC-decoupled since two additional switches are added at the output of the inverter terminals. Fig. 9 represents HERIC topology. S_5 and S_6 operate at 50 Hz, while S_1, S_2, S_3, and S_4 switches function at 10 kHz.

The system works in four distinct modes. In mode 1, as depicted in Fig. 10(a), S_1, S_2, and S_5 are turned on. Mode 2, as per Fig. 10(b), is the circulating mode. The current flows through S_6 built in diode and switch S_5. Thus there is no link between PV and grid. In mode 3, as per Fig. 10(c), the current reverses its direction and conducts through S_3 and S_4. Mode 4 is like mode 2, as depicted in Fig. 10(d), where the current through inductor circulates between the body diode of S_5 and switch S_6. Thus there is no connection between PV and grid.

From the above, it can be seen that HERIC inverter maintains constant CMV (CCMV) in all four modes.

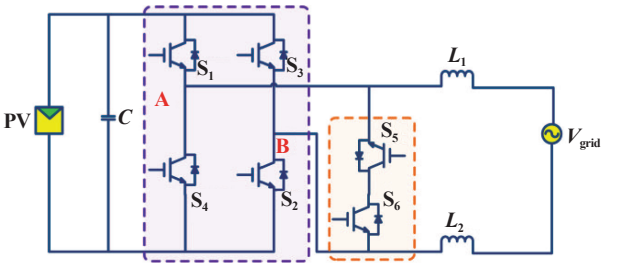

Fig. 9. Illustration of HERIC inverter.

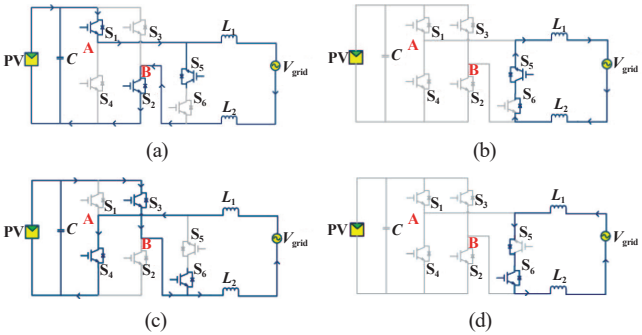

Fig. 10. Demonstration of HERIC topology working. (a) Conduction mode for V_g>0, (b) Freewheeling mode for V_g>0, (c) Conduction mode for V_g<0, (d) Freewheeling mode for V_g<0.

The simulated waveforms of V_{AN}, V_{BN}, and V_{AB}, V_{cm}, I_{cm} of HERIC topology are depicted in Fig. 13(g) and Fig. 13(h) respectively.

IV. Novel H6 Inverter Topology

This Novel H6 inverter is derived from H5 topology. The limitation of the H5 inverter of not maintaining CMV constant throughout 4 modes is overcome in this proposed inverter. Secondly, the conduction losses are reduced in Novel six switch inverter in comparison with H5 inverter. A supplementary switch S_6 is connected in the circuit amid point A and N of PV panel. This extra switch acts as a bypass path and helps in minimizing the conduction loss. Fig. 11(a) denotes the circuit of the Novel H6 inverter. Fig. 11(b) demonstrates the switching technique for the proposed inverter. Fig. 11(c) illustrates the control strategy for the proposed six switch Inverter topology. Second order generalized integrator-phase locked loop (SOGI-PLL) and PR controller is utilized to generate PWM pulses.

A. Working of Novel H6 Inverter Topology:

Novel H6 TLI has four modes of working as follows:

Mode 1:

S_1, S_2, and S_5 are triggered so that PV and grid is connected. This is evident from Fig. 12(a). S_1 and S_5 switches function at 10 kHz, while S_2 works at 50 Hz. Following are the voltage equations:

$$V_{AN} = V_{PV} \tag{6}$$

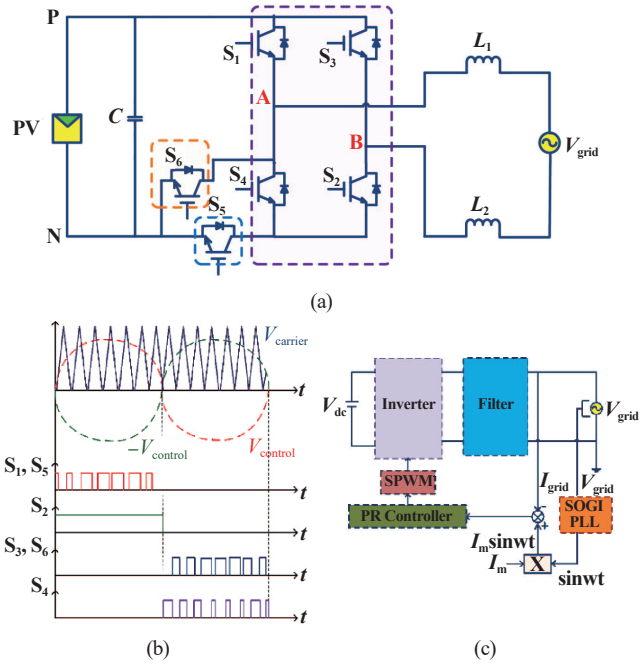

Fig. 11. (a) Novel H6 inverter, (b) PWM pulses, (c) Control strategy.

$$V_{BN} = 0 \tag{7}$$

$$V_{cm} = \frac{V_{AN} + V_{BN}}{2} = \frac{V_{PV} + 0}{2} = \frac{V_{PV}}{2} \tag{8}$$

Mode 2:

It denotes the circulating mode. The current freely circulates from S_2 and diode of S_4. Therefore, there is disconnection between the PV and grid. This can be observed in Fig. 12(b). Following are the voltage equations in this mode:

$$V_{AN} = \frac{V_{PV}}{2} \tag{9}$$

$$V_{BN} = \frac{V_{PV}}{2} \tag{10}$$

$$V_{cm} = \frac{\frac{V_{PV}}{2} + \frac{V_{PV}}{2}}{2} = \frac{V_{PV}}{2} \tag{11}$$

Mode 3:

PV and grid are linked in this conduction mode. There is flow of reverse current which is visible in Fig. 12(c). S_3 and S_6 operate at 10 kHz during grid voltage's reverse half cycle. Only two switches conduct in proposed inverter whereas one extra switch operates in H5 inverter. Hence, proposed inverter reduces conduction losses and enhances the efficiency. The expressions pertaining to voltage are as following:

$$V_{AN} = 0 \tag{12}$$

$$V_{BN} = V_{PV} \tag{13}$$

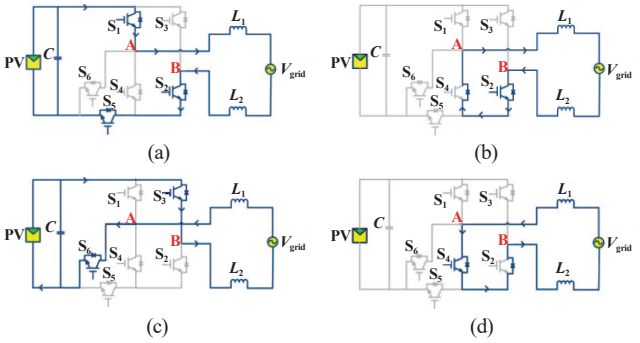

Fig. 12. Demonstration of Novel H6 topology working. (a) Conduction mode for V_g>0, (b) Idling mode for positive V_g, (c) Working mode for negative V_g, (d) Idling mode for negative V_g.

TABLE I
VALUES OF PARAMETER

Parameters	Values
Input D.C Voltage	400 V
Grid r.m.s voltage/Grid Frequency	230 V/50 Hz
Current through grid	7.07 A
DC link Capacitance (C)	500 µF
Switching frequency	10 kHz
Inductance (L_1, L_2)	4.06 mH
Stray capacitor (C_{pv1}, C_{pv2})	1 nF
Resistance of ground	5 Ω

$$V_{cm} = \frac{V_{AN} + V_{BN}}{2} = \frac{0 + V_{PV}}{2} = \frac{V_{PV}}{2} \tag{14}$$

Mode 4:

This is the circulating mode in which the current through inductor flows through S_4 and body diode of S_2 switch. Therefore, S_4 is complementary to switch S_6 during V_g<0. Therefore, by no chance switch S_4 and S_6 can turn on simultaneously. It is depicted in Fig. 12(d). The expressions pertaining to voltage are as following:

$$V_{AN} = \frac{V_{PV}}{2} \tag{15}$$

$$V_{BN} = \frac{V_{PV}}{2} \tag{16}$$

$$V_{cm} = \frac{\frac{V_{PV}}{2} + \frac{V_{PV}}{2}}{2} = \frac{V_{PV}}{2} \tag{17}$$

The simulated waveforms for V_{AN}, V_{BN}, and V_{AB}, V_{cm}, I_{cm} for Novel six switch inverter are seen in Fig. 13(i) and Fig. 13(j) respectively.

Table I shows the values of parameters for simulation in MATLAB.

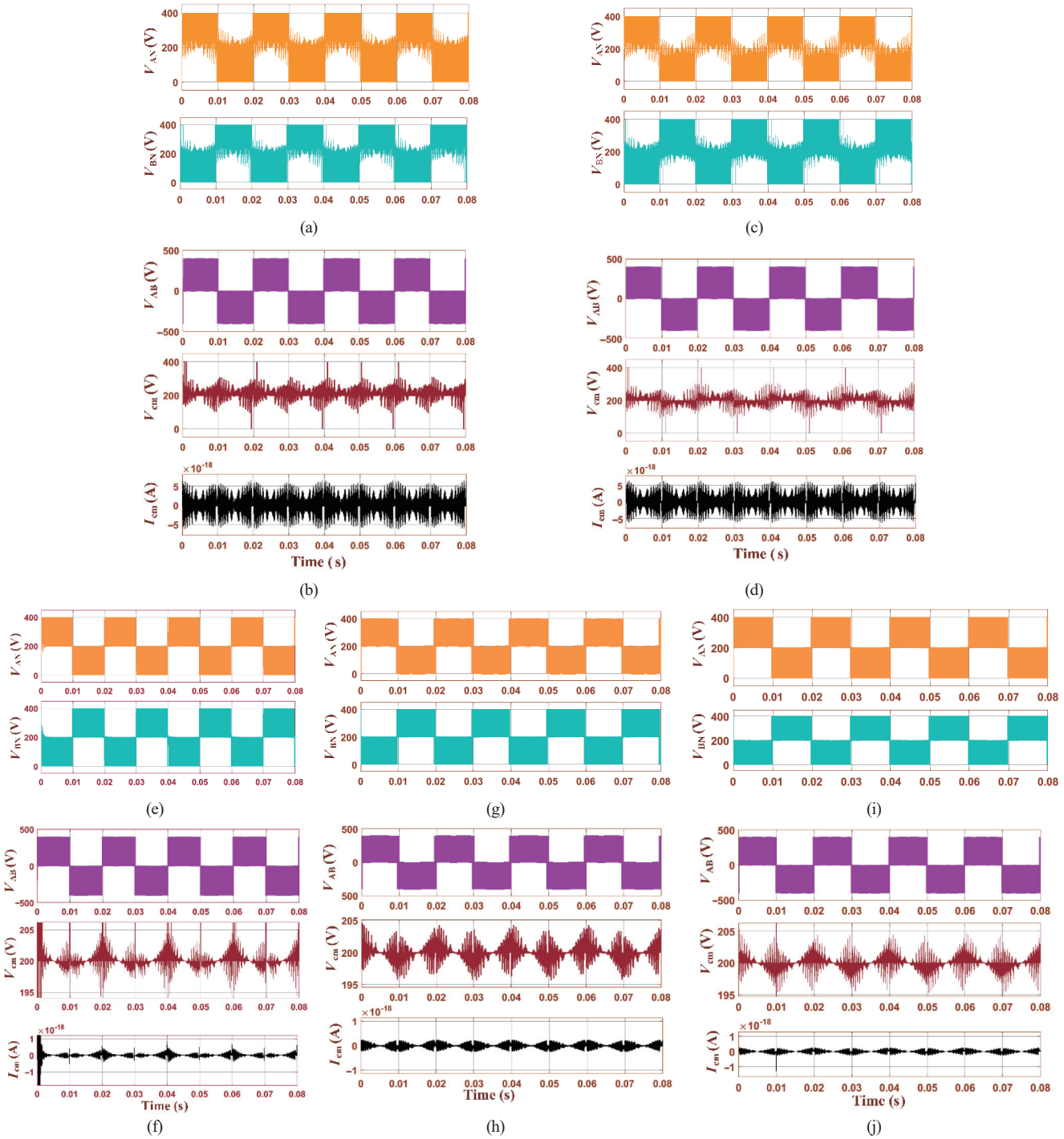

Fig. 13. Simulated waveforms of H5. (a) V_{AN}, V_{BN}, (b) V_{AB}, V_{cm}, and I_{cm}; waveforms of H6-I, (c) V_{AN}, V_{BN}, (d) V_{AB}, V_{cm}, and I_{cm} ; waveforms of H6-II, (e) V_{AN}, V_{BN}. (f) V_{AB}, V_{cm}, and I_{cm}; waveforms of HERIC, (g) V_{AN}, V_{BN}, (h) V_{AB}, V_{cm}, and I_{cm}; waveforms of Novel H6 inverter topology, (i) V_{AN}, V_{BN}, (j) V_{AB}, V_{cm}, and I_{cm}.

V. Hardware Implementation of H5, H6-I, HERIC, and Novel H6 Inverter

To further strengthen the simulation findings, H5, H6-I, HERIC, and novel H6 inverter are implemented in hardware. Hardware is carried out based on the equipment available in the laboratory. Three phase four leg IGBT inverter is used with SKM100GB125DN IGBTs having maximum voltage of 1200 V, maximum current of 100 A and maximum switching frequency of 100 kHz. OP 4500 OPAL-RT, PF515043S01, is used as a controller to produce PWM signals for the inverter. Input DC voltage of 35 V is fed to the inverter circuit by DC power supply. The circuit is realized by connecting a rheostat of 100 Ω, 2 A rating across the output of the inverter. The results are displayed on the Digital Storage Oscilloscope. The waveforms of V_{AN}, V_{BN}, V_{AB}, load current, and $V_{AN} + V_{BN}$ of the inverters are depicted in Fig. 14(a) – (h). The experimental hardware setup for implementation of these inverters is depicted in Fig. 15.

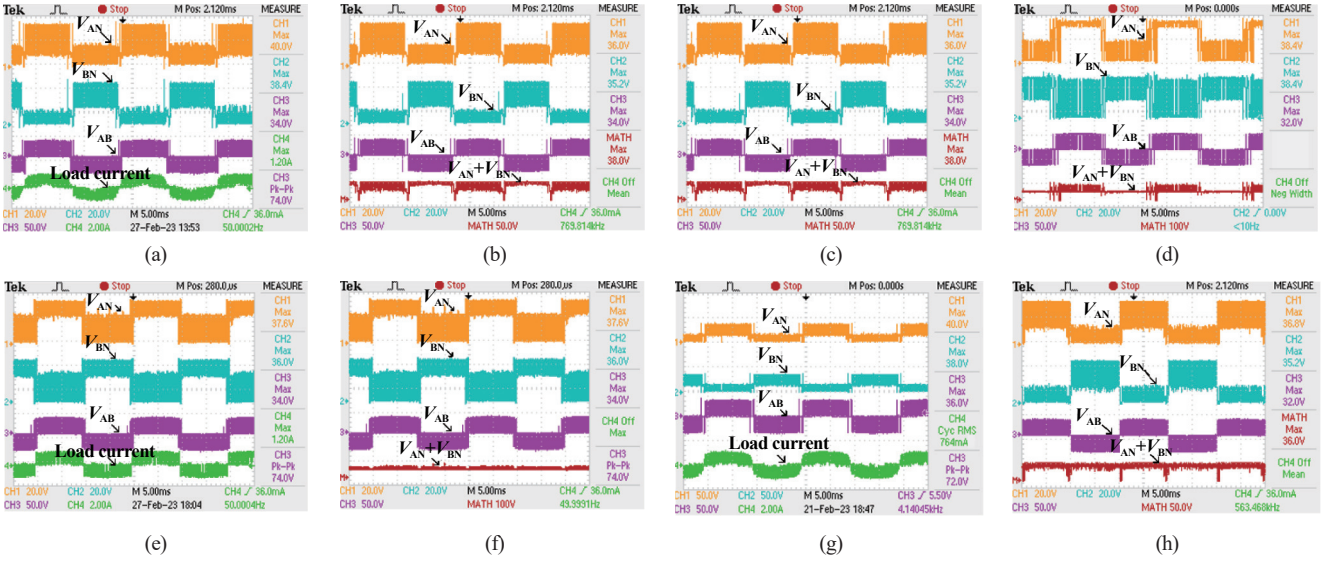

Fig. 14. Hardware results of H5. (a) V_{AN}, V_{BN}, V_{AB}, and load current, (b) V_{AN}+V_{BN}; hardware results of H6-I, (c) V_{AN}, V_{BN}, V_{AB}, and load current, (d) V_{AN}+V_{BN}; hardware results of HERIC, (e) V_{AN}, V_{BN}, V_{AB}, and load current, (f) V_{AN}+V_{BN}; hardware results of Novel H6, (g) V_{AN}, V_{BN}, V_{AB}, and load current, (h) V_{AN}+V_{BN}.

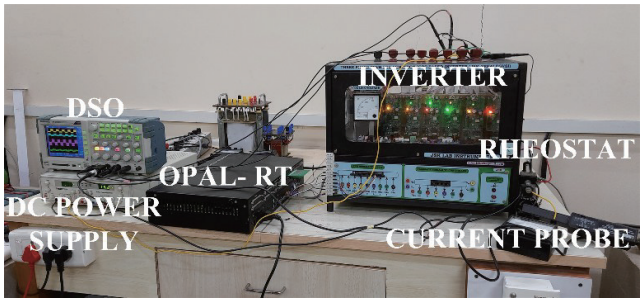

Fig. 15. Experimental Hardware Set up.

Figs. 14(a) and (b) shows the hardware results of the H5 inverter, Figs. 14(c) and (d) depicts the hardware results of the H6-I inverter, Figs. 14(e) – (f) displays the hardware results of HERIC inverter and Figs. 14(g) – (h) showcases the hardware results of Novel H6 inverter. From the above hardware findings, it can be concluded that the simulated results and hardware results are in sync. It is noticed that H5 inverter cannot maintain CMV constant and hence has some CMC flowing from the grid to the PV. H6-I inverter performs better as compared to H5 in maintaining CMV constant. However, H6-I has four switches conducting in both the active modes, whereas H5 inverter has three switches conducting in active modes. Therefore, conduction losses in H6-I inverter are more as compared to H5 inverter. As seen from simulation results and hardware results, it is proved that HERIC inverter maintains constant CMV in comparison with H5 and H6-I inverter.

The proposed Novel H6 inverter also tries to maintain CMV constant in comparison with H5 and H6-I inverter. Thus, the Novel H6 inverter can be regarded at par with HERIC in suppressing the CMC. In H6-II inverter, three switches operate during each conduction mode and it uses two additional diodes in the circuit. In HERIC inverter, in conduction mode, two switches are in operation. Whereas in Novel H6 inverter, three switches operate during positive conduction mode and two switches operate during negative conduction mode. Compared to the HERIC inverter, the Novel H6 inverter experiences higher conduction losses, which can impact its overall efficiency. However, when compared to the DC decoupled inverters, the Novel H6 inverter demonstrates lower conduction losses. As a result, the proposed Novel H6 inverter achieves a higher level of efficiency in comparison with other inverters.

TABLE II
COMPARATIVE ANALYSIS OF TLI

Inverter	H5	H6-I	H6-II	HERIC	Novel H6
Number of switches	5	6	6	6	6
Decoupling	DC	DC	DC	AC	DC
Leakage current (mA) [20]	26.5	31.4	25.4	16.4	19.7
Switching loss (watts)	5.801	5.79	6.235	5.78	5.73
Conduction loss (watts)	5.637	7.28	4.926	4.012	4.75
% efficiency	99.03	98.94	98.98	99.13	99.09

VI. COMPARATIVE ANALYSIS

Table II represents the comparison between various inverters and proposed inverter in terms of number of switches, coupling method used, leakage current, switching loss, conduction loss and efficiency.

The efficiency analysis is obtained by determining the inverter topology losses in MATLAB/Simulink [20]. This technique is suitable for calculation of losses for comparison purpose. Leakage current is obtained from the OPAL RT output [20]. Figs. 16(a) and 16(b) depicts the switching loss and conduction loss respectively in the various TLI with reference current of 10 A. Fig. 17 represents the efficiency of various TLI. It is observed that the conduction loss generated by HERIC inverter

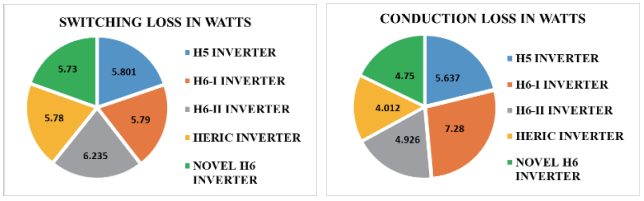

(a) (b)

Fig. 16. (a) Switching losses of TLI, (b) Conduction losses of TLI.

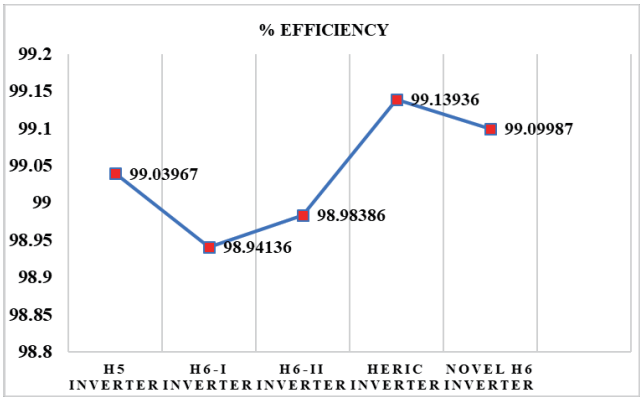

Fig. 17. % efficiency of various TLI.

is 4.01 watts and is least among all the inverters, followed by Novel H6 inverter with a conduction loss of 4.75 watts. Also HERIC inverter has highest efficiency of 99.139% followed by Novel H6 inverter with an efficiency of 99.099%. Figs. 18(a) and 18(b) represents the grid current and grid voltage of H5 and Novel H6 inverter respectively. The total harmonic distortion (THD) of grid voltage for H5 inverter is 5.04% whereas for Novel H6 inverter is found to be 1.99%.

VII. Conclusion

This paper proposes the utilization of a Novel H6 inverter as a recommended solution for mitigating the CMC in PV system connected to the grid without transformer.

The novel H6 inverter succeeds in retaining CMV equivalent to $V_{pv}/2$. The inclusion of S_6, gives an alternate way for the current during the second half cycle of conduction mode. Thus recommended Novel H6 inverter eradicates CMC and also reduces the conduction losses despite the circuit having six switches. The findings from model testing and physical implementation signify the superiority of the recommended Novel H6 inverter in comparison with the conventional inverters considered. Notably, the Novel H6 inverter effectively suppresses the CMC, minimizes conduction losses and enhances overall efficiency. Based on these findings, it can be concluded that the Novel H6 stands out as a highly promising option for PV system connected to the grid. Its performance is deemed second only to the well-established HERIC inverter. The superiority of Novel H6 inverter in terms of CMC suppression, reduced conduction losses, and improved efficiency reinforces its potential as a favorable choice for integrating PV system into the grid.

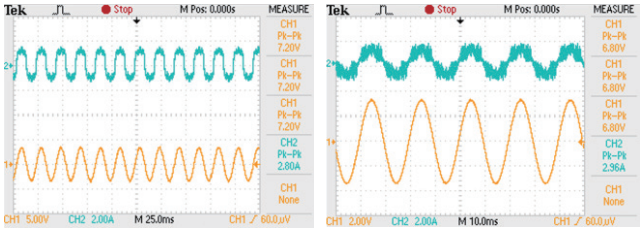

(a) (b)

Fig. 18. (a) Grid current and grid voltage of H5 inverter, (b) Grid current and grid voltage of Novel H6 inverter.

References

[1] H. Li, Y. Zeng, B. Zhang, T. Q. Zheng, R. Hao, and Z. Yang, "An improved H5 topology with low common-mode current for transformerless PV grid-connected inverter," in *IEEE Transactions on Power Electronics*, vol. 34, no. 2, pp. 1254–1265, Feb. 2019.

[2] M. N. H. Khan, M. Forouzesh, Y. P. Siwakoti, L. Li, T. Kerekes, and F. Blaabjerg, "Transformerless inverter topologies for single-phase photovoltaic systems: A comparative review," in *IEEE Journal of Emerging and Selected Topics in Power Electronics*, vol. 8, no. 1, pp. 805–835, Mar. 2020.

[3] W. Li, Y. Gu, H. Luo, W. Cui, X. He, and C. Xia, "Topology review and derivation methodology of single-phase transformerless photovoltaic inverters for leakage current suppression," in *IEEE Transactions on Industrial Electronics*, vol. 62, no. 7, pp. 4537–4551, Jul. 2015.

[4] T. Kerekes "Analysis and modeling of transformerless photovoltaic inverter systems". Ph.D. dissertation, Dept. Elect. Eng., Aalborg Vniv., Aalborg, Denmark, 2009.

[5] M. Shayestegan, "Overview of grid-connected two-stage transformer-less inverter design," in *Journal of Modern Power Systems and Clean Energy*, vol. 6, no. 4, pp. 642–655, Jul. 2018.

[6] D. Kolantla, S. Mikkili, S. R. Pendem, and A. A. Desai, "A critical review on various inverter topologies for PV system architectures," in *IET Renewable Power Generation*, vol. 14, no. 17, pp. 3418–3438, Dec. 2020.

[7] R. Barzegarkhoo, S. S. Lee, S. A. Khan, Y. P. Siwakoti, and D. D. -C. Lu, "A novel generalized common-ground switched-capacitor multilevel inverter suitable for transformerless grid-connected applications," in *IEEE Transactions on Power Electronics*, vol. 36, no. 9, pp. 10293–10306, Sept. 2021.

[8] A. A. Desai, S. Mikkili, and T. Senjyu, "Novel H6 transformer-less inverter for grid connected photovoltaic system to reduce the conduction loss and enhance efficiency," in *Energies 2022*, vol. 15, no. 10, 2022.

[9] H. K. Jahan, "A new transformerless inverter with leakage current limiting and voltage boosting capabilities for grid-connected PV applications," in *IEEE Transactions on Industrial Electronics*, vol. 67, no. 12, pp. 10542–10551, Dec. 2020.

[10] G. Rizzoli, M. Mengoni, L. Zarri, A. Tani, G. Serra, and D. Casadei, "Comparative performance evaluation of full bridge, H5 and H6 topologies for transformer-less solar converters," in *IET Power Electronics*, vol. 12, no. 1, pp. 22–29, Jan. 2019.

[11] N. Vosoughi, S. H. Hosseini, and M. Sabahi, "A new transformer-less five-level grid-tied inverter for photovoltaic applications," in *IEEE Transactions on Energy Conversion*, vol. 35, no. 1, pp. 106–118, Mar. 2020.

[12] Z. Tang, Y. Yang, J. Wan, and F. Blaabjerg, "Hybrid transformer-less PV converters with low leakage currents: Analysis and configuration," in *IET Renewable Power Generation*, vol. 15, no. 2, pp. 368–381, Feb. 2021.

[13] M. M. Rahman, M. Shafayet Hossain, M. S. Islam Talukder, and M. Nasir Uddin, "Transformerless six-switch (H6)-based single-phase inverter for grid-connected photovoltaic system with reducd leakage current," in *2020 IEEE Industry Applications Society Annual Meeting*, Detroit, MI, USA, 2020, pp. 1–8.

[14] H. Tian, M. Chen, G. Liang, and X. Xiao, "A single-phase transformerless

common-ground type PV inverter with active power decoupling," in *IEEE Transactions on Industrial Electronics*, vol. 70, no. 4, pp. 3762–3772, Apr. 2023.

[15] M. Shahabadini, N. Moeini, M. Bahrami-Fard, and H. Iman-Eini, "HERIC-based cascaded H-bridge inverter for leakage current suppression in PV systems," in *IEEE Transactions on Power Electronics*, vol. 38, no. 3, pp. 4005–4014, Mar. 2023.

[16] P. K. Chamarthi, M. S. E. Moursi, V. Khadkikar, K. H. A. Hosani, A. Al-Durra, and T. H. M. EL-Fouly, "A single stage doubly grounded transformerless inverter topology with Buck-Boost voltage capability for grid connected PV systems," in *IEEE Transactions on Power Delivery*, vol. 37, no. 6, pp. 5044–5058, Dec. 2022.

[17] S. Kumari, N. Sandeep, A. Verma, U. R. Yaragatti, and H. Pota, "Design and implementation of transformer-less common-ground Inverter with reduced components," in *IEEE Transactions on Industry Applications*, 2022.

[18] M. Bahrami-Fard, N. Moeini, M. Shahabadini, H. Iman-Eini, and M. Liserre, "A new topology and modulation strategy to suppress the leakage current in transformerless cascaded H-bridge inverters in PV application," in *IEEE Journal of Emerging and Selected Topics in Power Electronics*, vol. 11, no. 1, pp. 1219–1229, Feb. 2023.

[19] B. Guo, X. Zhang, M. Su, H. Ma, Y. Yang, and Y. P. Siwakoti, "A single-phase common-ground five-level transformerless inverter with low component count for PV applications," in *IEEE Transactions on Industrial Electronics*, vol. 70, no. 3, pp. 2662–2674, Mar. 2023.

[20] A. A. Desai, S. Mikkili, and K. Nanshikar. "Hardware implementation of improved transformer-less grid-connected PV inverter topologies with constant common mode voltage and enhanced efficiency." in *Electrical Engineering*, vol.107, pp. 301–311, Jun. 2024.

[21] L. Wang and X. Yang, "A single-stage common-ground inverter with high-voltage-gain ability," in *IEEE Transactions on Power Electronics*, vol. 40, no. 5, pp. 7058–7069, May 2025.

[22] Z. Yao and Q. Xu, "Topology derivation method of common-ground transformerless single-phase inverters based on graph theory," in *IEEE Transactions on Power Electronics*, vol. 40, no. 3, pp. 4510–4521, Mar. 2025.

[23] H. F. Ahmed and D. Siddiqui, "Single-phase non-isolated inverter with shared-ground and broad input voltage operation," in *IEEE Journal of Emerging and Selected Topics in Industrial Electronics*, vol. 6, no. 2, pp. 849–858, Apr. 2025.

[24] X. Zhao, D. Jiang, J. Chen, Z. Shen, and Q. Li, "Leakage current suppression with capacitor voltage control of three-level flying capacitor grid-connected inverters," in *IEEE Transactions on Industrial Electronics*, vol. 69, no. 3, pp. 2191–2201, Mar. 2022.

[25] S. Mondal, S. P. Biswas, M. R. Islam, and S. M. Muyeen, "A five-level switched-capacitor based transformerless inverter with boosting capability for grid-tied PV applications," in *IEEE Access*, vol. 11, pp. 12426–12443, 2023.

[26] F. Peng, G. Zhou, N. Xu, and S. Gao, "Zero leakage current single-phase quasi-single-stage transformerless PV inverter with unipolar SPWM," in *IEEE Transactions on Power Electronics*, vol. 37, no. 11, pp. 13755–13766, Nov. 2022.

[27] J. Lee, D. Lee, and J. -I. Ha, "Control and modulation methods of single-/three-phase PWM converter for suppressing leakage current," in *IEEE Transactions on Power Electronics*, vol. 40, no. 7, pp. 9137–9152, Jul. 2025.

[28] A. Srivastava and J. Seshadrinath, "Design and implementation of a new nine level Boost inverter for transformerless grid-tied PV application," in *IEEE Transactions on Energy Conversion*, vol. 38, no. 4, pp. 2298–2309, Dec. 2023.

[29] M. Vital, V. Sonti, Y. P. Siwakoti, S. S. Lee, and S. Jain, "A constant common mode voltage single-phase five-level transformerless PV inverter considering the effect of switch device junction capacitance," in *CPSS Transactions on Power Electronics and Applications*, vol. 9, no. 3, pp. 313–324, Sept. 2024.

[30] Y. Wei, X. Guo, Z. Zhang, L. Wang, and J. M. Guerrero, "A high-voltage gain transformerless grid-connected inverter," in *2022 4th International Conference on Smart Power & Internet Energy Systems (SPIES)*, Beijing, China, 2022, pp. 533–536.

[31] J. Dadkhah, C. N. M. Ho, and K. K. -M. Siu, "Three-phase transformerless PV inverter with reconfigurable LCL filter and reactive power capability," in *IEEE Transactions on Power Electronics*, vol. 39, no. 7, pp. 8229–8241, Jul. 2024.

[32] L. Zhou and M. Preindl, "Single-phase transformerless onboard charger with reduced DC capacitance and leakage current," in *IEEE Transactions on Vehicular Technology*, vol. 74, no. 5, pp. 7497–7507, May 2025.

[33] M. F. Kibria, S. Mekhilef, M. Mubin, K. S. Tey, A. Elsanabary, and M. Seyedmahmoudian, "A hybrid single-phase transformerless solar photovoltaic grid-connected inverter with reactive power capability and reduced leakage current," in *IEEE Access*, vol. 13, pp. 39235–39247, 2025.

[34] E. Gubía, P. Sanchis, A. Ursúa, J. López, and L. Marroyo, "Ground currents in single-phase transformerless photovoltaic systems", in Progress in *Photovoltaics: Research and Applications*, vol. 15, no. 7, pp. 629–650, May 2007.

[35] Y. Chen, D. Xu, and J. Xi, "Common-mode filter design for a transformerless ZVS full-bridge inverter," in *IEEE Journal of Emerging and Selected Topics in Power Electronics*, vol. 4, no. 2, pp. 405–413, Jun. 2016.

[36] B. Yang, W. Li, Y. Gu, W. Cui, and X. He, "Improved transformerless inverter with common-mode leakage current elimination for a photovoltaic grid-connected power system," in *IEEE Transactions on Power Electronics*, vol. 27, no. 2, pp. 752–762, Feb. 2012.

[37] W. Yu, J. -S. J. Lai, H. Qian, and C. Hutchens, "High-efficiency MOSFET inverter with H6-type configuration for photovoltaic nonisolated AC-module applications," in *IEEE Transactions on Power Electronics*, vol. 26, no. 4, pp. 1253–1260, Apr. 2011.

Aditi Atul Desai was born in Goa, India, in 1976. She completed B.E. and M.E. in Electrical Engineering from Goa College of Engineering, Goa, India in the year 1998 and 2014 respectively. She received Ph.D. degree in Electrical Engineering from National Institute of Technology, Goa in 2023. She is currently working as Assistant Professor at Goa College of Engineering since December 2010. Her research interest includes renewable energy sources and electrical machines.

Suresh Mikkili obtained his M.Tech. and Ph.D. degrees in Electrical Engineering from the National Institute of Technology, Rourkela in the years 2008 and 2013, correspondingly. He holds the position of Associate Professor in the Department of Electrical and Electronics Engineering at the National Institute of Technology Goa, India, starting from January 2013.

His research interest includes Smart Electric Grid, Electric vehicles, Grid connected/Stand-Alone PV systems, wireless power transfer, power quality issues, and applications of soft computing techniques. He has authored two books, one is published by CRC Press, Taylor & Francis Group, in August 2015 and the other is published by AICTE in 2024 respectively. He has published over 145 papers in prestigious international journals (SCI/SCI-E) and international conferences (Annual/Bi-Annual). He has executed three projects of worth 85 lakhs and executing one project (ANRF PAIR) of worth 100 crores (individual budget is 1.47 crores). He is among the top 2% of scientists worldwide, as reported by Stanford University and Elsevier, for the year 2025.

From Frontier Research Progress to Education: Using Series-End Winding Motor Drives as Example

Dong JIANG, Zicheng LIU, Min ZHOU, Lanhua ZHANG, Wei SUN, and Wenli XU

***Abstract*—Capable and highly motivated engineering students are constantly on the lookout for opportunities to engage in cutting-edge research. However, effectively translating the progress made in such research into educational content presents a formidable challenge for both researchers and educators alike. An example of Google Little Box Challenge by university team is introduced at first. Then, this article endeavors to showcase an attempt at integrating the latest research advancements in the domains of power electronics and motor drives into education, with the innovative series-end winding motor drives (SWMD) serving as a prime illustration. Recent breakthroughs in topology, control algorithms, and reliability have been swiftly adopted by students in the development of high-performance drives for applications such as drones, electric vehicles, and magnetic bearings. These efforts have culminated in remarkable achievements and significant milestones in various competitions. This study proposes a methodology for bridging the gap between recent research progress and education, particularly tailored to meet the needs of students possessing strong capabilities and intrinsic motivation. The case study centered around the novel SWMD not only elucidates the educational approach but also demonstrates its tangible outcomes as manifested through diverse student contest implementations.**

***Index Terms*—Contests, drone, education, electrical vehicle, magnetic bearing research, series-end winding motor drives.**

I. Introduction

In scientific research, advances at the frontier are often assumed to be distant from education. However, many recent research findings have been integrated into classrooms and educational laboratories in electrical engineering, becoming a powerful driving force for training graduate and undergraduate students to pursue further studies.

As early as 1925, the California Institute of Technology studied the relationship between research and engineering education, highlighting the importance of research in training undergraduate students for the future [1]. In recent years, studying how to deliver engineering research concepts and results to students has become increasingly important in various areas of electrical and computer engineering [2]−[4].

A notable example is the recent progress of artificial intelligence (AI). In 2022, formal AI curricula were implemented in secondary education, significantly enhancing students' understanding of AI [5]. Additionally, at the end of 2022, ChatGPT was released as an innovative chatbot. Soon after, similar technology was used to assist students in learning programming skills [6].

Unlike software or algorithm-based research, which is more aligned with students' course projects, advancements in hardware—especially high-power hardware—are typically more distant from undergraduate coursework. Even in graduate-level courses, while conveying the basic concepts of cutting-edge research in hardware is manageable, implementing and expanding these results in the classroom can be quite challenging.

The major barrier between frontier research in hardware and education is the significant effort required to develop novel prototypes for specific applications for students. However, for students with ambition and motivation to work in related fields, the opportunity to engage with frontier research can serve as strong encouragement and valuable training of future research.

The best opportunities for this purpose are scientific contests for graduate and undergraduate students. These contests should not have rigidly defined procedures but should offer relatively open approaches to the contest goals. Such contest allows frontier research results to be applied to specific problems, providing a platform for students to solve challenges independently. This process effectively achieves the overall training goals for students.

Just as many top athletes develop their skills through high-level competition from a young age, top talents in electrical engineering can similarly grow through education based on frontier research.

A good example is the Google Little Box Challenge, which took place during the 2014−2015 period. In July 2014, Google and IEEE launched this contest, offering $1 million to the winner for designing and developing a small kW-scale single-phase inverter with a power density greater than 50 W/in^3, while meeting specifications for efficiency, electromagnetic compatibility (EMC), and thermal performance. Over 2,000 teams from around the world registered for the contest, and 18 teams were selected to attend the final testing at the National

Manuscript received January 18, 2025; revised August 30, 2025; accepted October 12, 2025. Date of publication December 30, 2025; date of current version December 2, 2025. This work was supported in part by the National Natural Science Foundation of China (NSFC) under the grant 52477189. *(Corresponding author: Zicheng Liu.)*

D. Jiang, Z. Liu, M. Zhou, W. Sun, and W. Xu are with Huazhong University of Science and Technology, Wuhan 430074, China (e-mail: jiangd@hust.edu.cn; liuzc@hust.edu.cn; minzhou0729@hust.edu.cn; sunwei77@hust.edu.cn; wenli_xu@hust.edu.cn).

L. Zhang is with Apple Inc. Cupertino, CA, USA (email: Lanhua_zhang@apple.com).

Digital Object Identifier 10.24295/CPSSTPEA.2025.00038

TABLE I
MAJOR SCIENTIFIC CONTESTS IN CHINA

Title	Area	Major Targets
National Challenge Cup: Scientific Track	Nation-wide, organized by China Youth League, Chinese Scientific Association and Ministry of Education	Open topic, face to all university students, show scientific contribution, every two years (2021, 2023, 2025...).
National Challenge Cup: Business Track		Open topic, face to all university students, show scientific contribution for starting new business, every two years (2020, 2024, 204...).
China International College Student Innovation Competition	Nation-wide, organized by China Youth League and Ministry of Business	Open topic, face to all university, show business planning for novel technologies.
The China Graduate Electronics Design Contest	Nation-wide, organized by Ministry of Education and Chinese Institute of Electronics	Open topic, face to all graduate students, show electronics innovative results, held every year.
Huawei e-campaign	Industry Organized	With given area for topic, face to all university students, held every year.
Sungrow university innovation contest	Industry Organized	With given area for topic for power electronics and renewable energy, held every year.

Renewable Energy Laboratory (NREL). The final winner was CE+T Power's Red Electrical Devils from Belgium.

Many university-based teams performed exceptionally well in this contest. Many frontier research results in power electronics topologies, control, package, integration, and thermal management were implemented by students in pursuit of the specifications for this single-phase inverter [7]–[10]. To overcome the major barrier of power density due to 2nd order power pulsation in single-phase inverters, many university teams adopted the recent achievement of the active 2nd order power filter used in the Rolls-Royce project [11].

The Virginia Tech FEEC team achieved the highest ranking among university teams in the final contest (3rd place). The team's experience with novel GaN devices provided a solid foundation for high-density design [12]. The Texas A&M team learned from the active 2nd order power filter method and proposed the novel active power decoupling stage for compensating double line frequency ripple [13]. The University of Tennessee team introduced a novel 2nd order notch filter in the DC-link to mitigate 2nd order power pulsation [14]. The ETH Zurich team utilized Pareto optimization of the Power Pulsation Buffer (PPB) in their prototype to improve the power density [15]. The University of Illinois team implemented recent research results on switching capacitor converters to develop their prototype using a relative different approach [16].

These examples demonstrate that, under the goal of a contest, university students are motivated to actively learn about recent research results and incorporate them into design and development. During this process, students' R&D capabilities, teamwork spirit, and hands-on experience are developed more effectively than through regular classroom training. This approach helps eliminate the major barrier between hardware-based research and learners.

Based on the authors' research and education experience over the past 10 years, a notable example has emerged. Recent research on novel series-end winding motor drives (SWMD) has shown great promise for high-performance motion control across a wide speed range [17]. This research has inspired many motivated students to apply SWMD in various applications, addressing specific problems and generating new ideas.

Major national innovation contests in China have provided excellent opportunities for students to collaborate, gaining experience and re-inventing frontier research results. The tradition of student innovation contest serves as a crucial platform for working on novel technologies and showcasing results. Major contests related to electrical engineering in China with relatively open topics are listed in Table I, serving as the key platforms discussed in this paper.

Government-organized nationwide contests typically feature open topics for student competition. The National Challenge Cup, the most significant contest for university students, has a history of over 30 years. It features a scientific track in odd years and a business track in even years, encouraging innovation in product development. The China Graduate Electronics Design Contest, held annually, allows graduate students to compete on open topics in the field of electronics. Major industries in China also host their own contests with specific topics, such as the Google Little Box. Similar contests are likely held in other countries.

This paper summarizes and analyzes examples of student work from various contests, set against the backdrop of recent SWMD research, demonstrating the transfer of frontier research to education. Part II briefly introduces the research on SWMD as a foundation. Part III discusses the application of SWMD by students in heavy drone propulsion systems. Part IV presents another example of SWMD applied to electrical vehicle implementation by students. Additionally, SWMD has been applied to active magnetic bearing drives by students, as discussed in Part V. Part VI provides a summary of the entire paper.

II. RESEARCH TO CONTEST: INTERNATIONAL EXPERIENCE

Before presenting the examples of SWMD in student contests, an international example is used to see how the world leading research group of power electronics did for the contest. There are many technical contests for students in electrical engineering in the world. As mentioned in Part I, the Google

Little Box Challenge in 2014–2015 is a unique and influential example. Although it is not a contest just for students, the example of an university students team can share a good experience.

More than 2,000 teams from across the world registered for Google's $1 million Little Box Challenge, an open competition to design and build a small kilowatt-scale inverter with a power density greater than 50 watts per cubic inch. Virginia Tech ECE's Future Energy Electronics Center team was the only U.S. team to place in the top three—and the only student team. L. Zhang, X. Zhao, and R. Born, advised by ECE professor Jin-Sheng (Jason) Lai, competed in the January 2016 challenge to drastically decrease the size of a power inverter.

The Future Energy Electronics Center (FEEC), part of the Bradley Department of Electrical and Computer Engineering at Virginia Tech, promotes and develops energy-efficient electronic technologies for the transportation and industrial automation industries. The Center's capabilities include modeling, simulation, and design and test of power-electronics devices, components, circuits, and systems.

VT FEEC's overall approach was to create a two-stage inverter design: a DC/DC stage that stepped down the voltage and actively canceled the 120 Hz input ripple, followed by a DC/AC stage. Four-phase interleaved DC/DC stage reaches efficiency higher than 99% and DC/AC stage is HERIC topology with good EMI performance to reduce the stress on EMI filter design. Meanwhile, The enclosure we used was made entirely out of copper. The lid served as the heat sink for the DC/DC stage and the rest of the case served as the heat sink for the DC/AC stage PCB. Originally, we had hoped to reach such a high efficiency that the case-as-heatsink would be enough and we wouldn't require any forced-air cooling. In the end, however, we added a handful of 0.1W micro-fans for some forced air cooling. The thin, top-cooled GaN Systems transistors allowed us to place the devices on the bottom of the PCB and directly connect to the case-as-heatsink while the remaining components were populated on the top of the PCB and faced the inside of the box.

Several experiences have been summarized by the FEEC teams for their success in this contest:

(1) Hands-On Experience and Skill Development: The challenge provided students with practical experience in hardware design, problem-solving, and systems engineering, helping them develop valuable technical and project management skills.

(2) Networking and Career Opportunities: Students gained exposure to industry professionals and Google engineers, opening doors for mentorship, internships, and job opportunities while boosting their professional visibility.

(3) Portfolio and Recognition: Participation in the contest gave students a notable addition to their resumes, enhancing their credibility and showcasing their ability to innovate, making them more attractive to potential employers.

FEEC team is based on the strong background of high density power electronics converter of the research group for few decades. 99% efficiency milestone in research projects has been successfully delivered to the Google's targets. This experience has inspired us that the research achievements can be combined with certain targets or applications, to train students with the platform of technical contests. This process can give students an opportunity to learn organization, management, teamwork, and real-problem solving. The examples of SWMD for students contests are based on that.

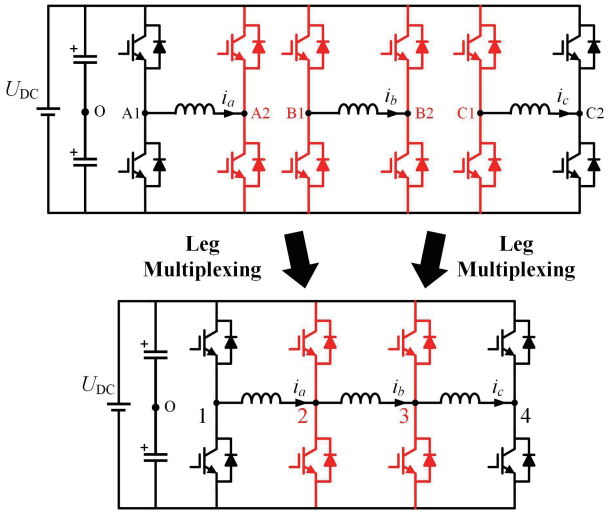

Fig. 1. From open-winding to SWMD.

III. The Frontier Research of SWMD

The scientific research on SWMD has been supported by the Natural Science Foundation of China (NSFC) under the grant 51877091 from 2019 to 2022. The initial purpose of this research was to develop novel motor drives with zero-sequence current control capability for reluctance motors. Progress has been made in advancing from open-winding motor drives to SWMD to reduce the number of power electronics devices, as shown in Fig. 1 [17]. However, the proposed novel topology of SWMD has proven to be more valuable than just for reluctance motor drives. It could serve as an alternative for open-winding motor drives for all types of AC motors, offering numerous advantages.

SWMD has been with systematical progress since its proposing in 2018. The space vector PWM of the four-leg SWMD has been developed together with the field-oriented control (FOC) considering zero-axis. It has been further extended to multi-phase SWMD. Beside HUST, City University of Hongkong is another major contributor for the progress of SWMD. This concept has been well recognized by academia now.

The most notable advantage of SWMD is its significantly wider speed range compared to regular voltage source inverter-based motor drives, achieved by adding just one extra phase-leg. With the same DC-link voltage, SWMD can produce 70% more output phase voltage in the motor windings. Fig. 2 illustrates the experimental results of the torque-speed curve for SWMD and Y-connected VSI.

Moreover, with the increase in maximum voltage output on

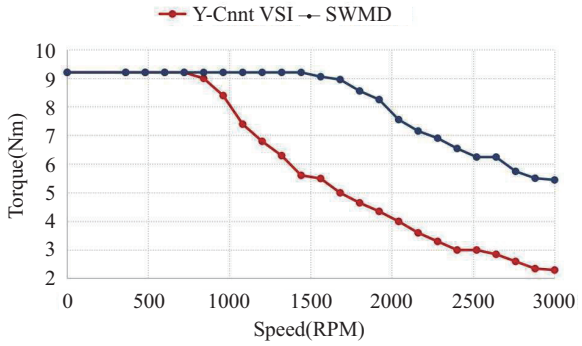

Fig. 2. Comparison of experimental results for torque-speed curve between regular VSI and SWMD [17].

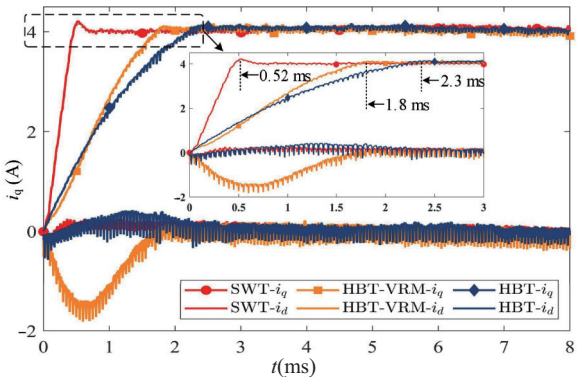

Fig. 3. Current step response comparison [17].

the motor windings, the dynamic performance of SWMD is also improved. Faster step responses can be achieved with the series winding topology (SWT) compared to the half-bridge topology (HBT), as shown in Fig. 3.

Additionally, due to the relatively independent winding connections in SWMD, enhanced fault-tolerant capabilities can be achieved. Automatic fault-tolerant control systems have been developed for SWMD [18].

Starting with the three-phase SWMD concept, the research has been extended to multi-phase SWMD, known as the "N+1 inverter". The N+1 inverter can achieve performance similar to a 2N-phase-leg open-winding motor drive using only N+1 phase-legs. Key technologies for the N+1 inverter include optimized phase sequence theory and carrier-based PWM methods [19]–[20].

Drawing on the similarity between rotational motors (tangential force) and magnetic levitation (radial force), the SWMD concept has also been applied to series-end winding magnetic bearing drives. Using this novel concept, N-axis magnetic bearing can be driven with nearly half the number of devices required for regular magnetic bearing drives [21].

The scientific research on SWMD has been ongoing for half a decade, resulting in over 20 IEEE journal publications and more than 30 granted patents in this field. The basic concept of SWMD has been awarded the "Gold Medal with Congratulations from the Jury" at the 47th Geneva Invention Expo. These pioneering research results have laid

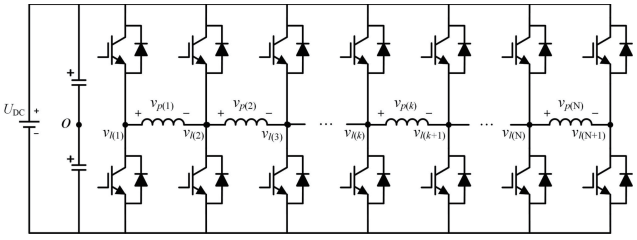

Fig. 4. Multi-phase SWMD —— N+1 inverter.

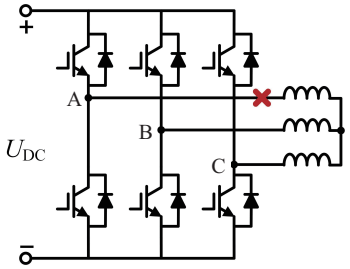

Fig. 5. Three-phase half-bridge topology.

the foundation for the next generation of SWMD applications, though specific challenges remain in different use cases.

Additionally, these fundamental research results offer a broad scope for talented and motivated students to explore. Leveraging student technical contests as a platform, this concept has been implemented in drones, electrical vehicles and magnetic bearings by students in these contests. The following three sections introduce three major examples.

IV. Case 1: Implementation in Drone

In recent years, drones have made significant strides in lightweight design and intelligent capabilities. With the rapid advancements in batteries, motors, and power electronic controllers focusing on high power density, drones have become highly promising solutions for agricultural crop protection, logistics delivery, and even manned flight. This suggests that drones are on track to become an indispensable part of daily life in the future.

Given their integral role in critical human activities, the reliability of drones has become a crucial metric for evaluating their performance. Reliability risks—primarily associated with switching devices and motor winding failures—directly impact drone performance. If a high-speed drone experiences a power interruption, it could damage valuable cargo or even pose a threat to human safety. Consequently, research aimed at improving the reliability of drone power systems is urgently needed.

The most common motor drive topology available is the three-phase half-bridge, which offers minimal switch numbers and high power density, as illustrated in Fig. 5. However, in the event of a switch or winding failure, the faulty phase may become uncontrollable. For instance, if an open-phase fault occurs on Phase-A, only currents flowing in opposite directions can pass through remaining Phase-B and C windings. In this scenario, the motor can only produce pulsating torque, which

Fig. 6. High-power drone platform.

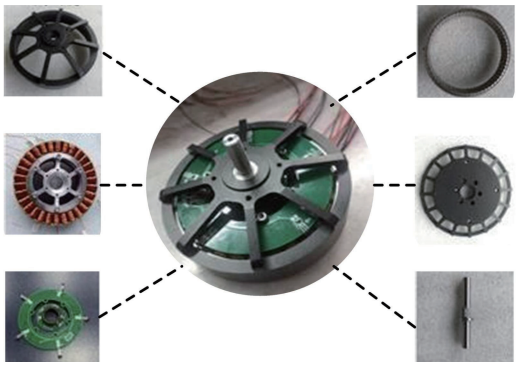

Fig. 7. Five-phase open-winding motor.

may not meet the power requirements for the drone. The SWMD discussed in this paper is expected to offer solutions to these problems.

It should be noted that the SWMD was only prototype-verified in the laboratory at the time, and its performance was tested using a generic platform with reconfigured windings. To enhance drone solutions, it is necessary to establish a dedicated drone testing platform where both the half-bridge and the SWMD can be compared.

Additionally, given the limited research on drone systems in our laboratory, we encourage students to use the contest timeline as key milestones for completing the prototype design. The contest will also serve as an opportunity to invite experts in various fields to provide feedback and suggestions on the research.

During prototype development, students are expected to face numerous challenges due to a lack of prior training on drones and the absence of a suitable platform. Therefore, a practical approach is to purchase a commercial drone platform, study its key components, and replace the circuit parts we aim to optimize based on this foundation. Consequently, we instructed the students to acquire a commercial drone platform, as shown in Fig. 6. This high-power drone, designed for agricultural crop protection, features four rotors, each driven by a three-phase motor and a corresponding inverter. Our task is to install the SWMD system we designed onto this drone platform and conduct testing.

A key component of the work involved designing a single-rotor test platform. As depicted in Figs. 7-8, we developed a five-phase permanent magnet synchronous motor, and a five-phase six-leg series-end winding motor controller. The five-

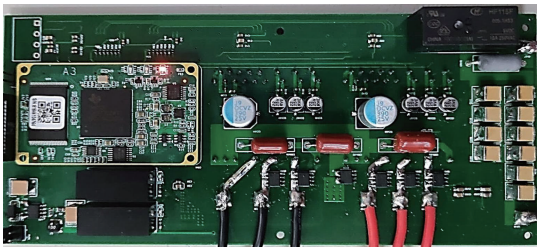

Fig. 8. Motor drive with five-phase SWMD.

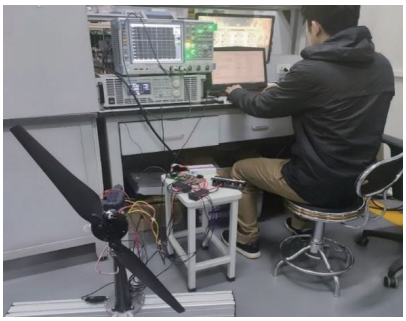

Fig. 9. The testing platform for single propeller power system.

phase motor is with 2 kW power rating and Halbach structure. The reliability of this setup was confirmed through experiments shown in Fig. 9.

During the contest, experts offered several suggestions, including optimizing transient responses, making the structure more compact, and reducing costs. These recommendations led to improvements in system performance. Throughout the process, students deepened their understanding of motor control topologies. More importantly, the contest provided comprehensive training, guiding students through problem identification, method proposal, method validation, and the precise and fluent presentation of their research findings.

V. Case 2: Implementation in Electrical Vehicle

Electrical vehicles (EVs) are a key focus in the field of transportation electrification. Currently, EVs often face challenges such as weak power output and high demagnetization losses during high-speed operation, which hinder development and affect long-distance user experience.

Recent research on the SWMD's inherent ability to efficiently utilize high DC voltage aligns well with the demands of high-speed operation in EVs. This capability can reduce demagnetization currents at high speeds, significantly improving operational efficiency. Fig. 10 illustrates the speed-efficiency test conducted on a SPMSM prototype by students in the laboratory at rated torque. At speeds over 1500 RPM, the efficiency of SWMD is more than 10% higher than that of half-bridge.

However, EV design cannot focus solely on high-speed performance for highways, and it must also optimize efficiency for urban driving. The SWMD introduces higher device losses due to the increased number of legs. Consequently, the half-bridge

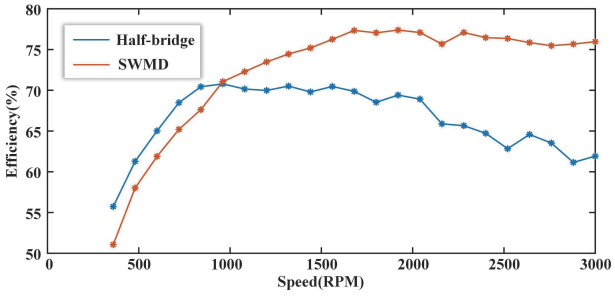

Fig. 10. Speed-efficiency comparison between half-bridge and SWMD [22].

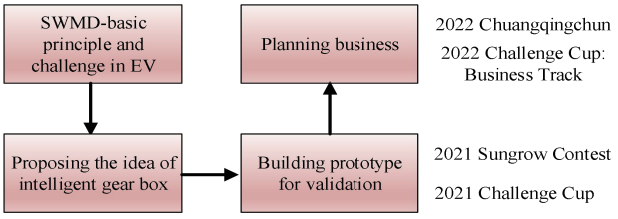

Fig. 11. Training progress of intelligent gear box and major milestones.

topology shows a greater efficiency advantage at low speed.

This issue has created an immediate barrier for the SWMD in EV applications but also presents an opportunity for students to overcome this challenge through research training. In 2020, We organized a team of students for EV applications. Over the next two years, this group has advanced significantly due to progress in technology and EV applications. The training process and major milestones are detailed in Fig. 11.

To leverage the advantages of both topologies while addressing their drawbacks, students proposed a topology transition method to achieve optimal performance at both low and high speeds. They designed a modular switching topology, named the "power electronics gearbox" to facilitate this transition. The "power electronics gearbox" is suitable for the current driving framework, and its framework and prototype are shown in Fig. 12. When K2 and K4 are on, the topology is equivalent to a half-bridge, and when K1 and K3 are on, the topology is equivalent to SWMD [22].

In 2021, this innovative hardware framework earned first prize in the Sungrow College Innovation Competition, with the judges highly praising it. However, the judges also raised a concern: frequent switching using relays could introduce potential instability issues to the system, such as overvoltage, switching safety risks, and motor torque fluctuations.

After the competition, the students explored whether they could achieve topology switching without affecting torque output and reducing stress on relays, as shown in Fig. 13. By fully utilizing the control freedom of the motor system, they discovered that the zero-axis current, which is generally not used, can indeed be utilized.

The students conducted research and found that injecting the appropriate zero-axis current, which has minimal impact on torque output, can reduce the current through the switches to zero. The operation speed range has been extended from

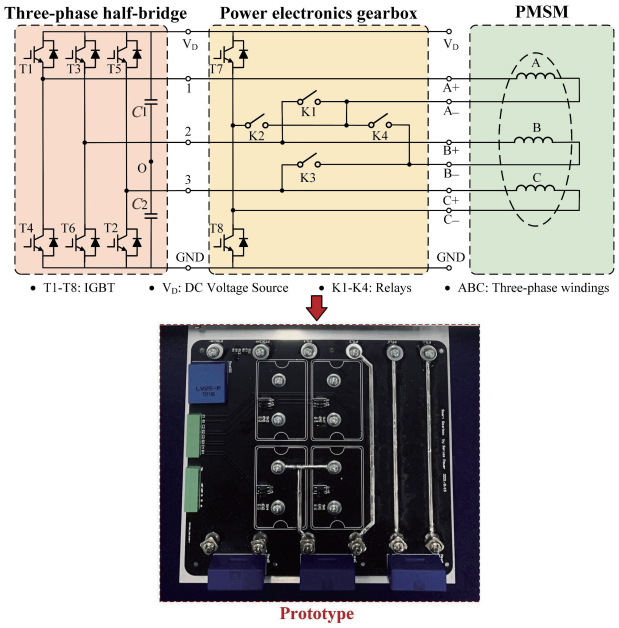

Fig. 12. Power electronics gearbox framework and prototype.

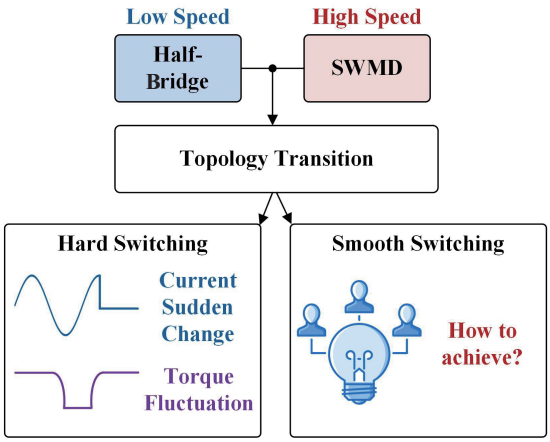

Fig. 13. Process of students' research.

1500 rpm to 3000 rpm in the test.

The student team designed a comprehensive control framework and renamed it the "power electronics intelligent gearbox". This innovative solution won the top prize in the 2021 Challenge Cup.

Additionally, the students collaborated with EV companies to conduct performance tests. In 2022, the team participated in the Business Track of the Challenge Cup and the Chuangqingchun Contest, winning national bronze awards. They received high praise and attention. As shown in Table II, SWMD served as the foundation for their work, bridging theory and practical application. The students' expertise spanned from platform hardware design to the development of flexible switching algorithms integrated with motor control. Ultimately, they collaborated with EV companies to conduct system research.

TABLE II
STUDENTS' PROGRESS IN EVS

Competition	Students' Progress
2021 Sungrow Contest	Proposed topology transition to adjust different speeds and designed prototype
2021 Challenge Cup	Proposed smooth switching method to optimize transient behavior
2022 Challenge Cup: Business Track	Collaborated with EVs companies for vehicle test

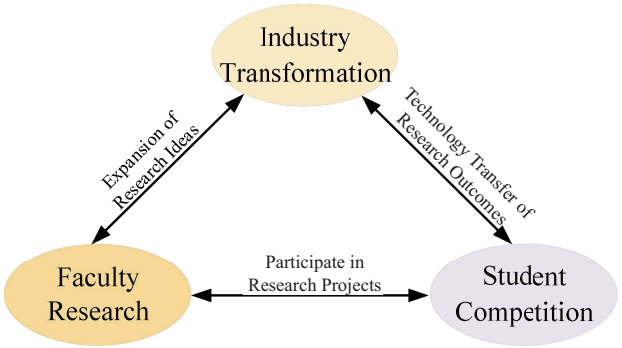

Fig. 14. Completely new interactive model.

VI. CASE 3: IMPLEMENTATION IN MAGNETIC BEARINGS

The final key case involved students using series-winding motor drive technology to overcome the limitations of traditional electric drives, achieving a novel application in the magnetic bearing drive system and realizing significant commercial value.

Unlike previous efforts, the team engaged in both technical and business-oriented competitions. Their goal was to explore a new interactive model of "Faculty Research, Student Competition, and Industry Transformation" as illustrated in Fig. 14. Early on, the project team proactively planned and integrated both horizontal and vertical research related to magnetic bearings, using these tasks to actively engage students in research projects. The team also simulated or engaged in real-world industrialization processes through business competitions, transitioning research outcomes into marketable products. This market-oriented approach enabled the team to evaluate the commercial potential of their research. Additionally, insights from market-driven activities informed and guided the faculty's scientific research, continuously opening new research fields and expanding ideas. This created a comprehensive loop from faculty research to student competition and industry transformation, forming a deeply integrated graduate education model that seamlessly connects academe, research, and industry.

This interactive model also established a new capability framework for engineering science graduate students in the modern era. It developed a multidimensional skill development system, as shown in Fig. 15, focusing on three aspects: research capability, innovation and entrepreneurship skills, and engineering application ability. This approach offers students practical motivation and platform support, fostering self-directed learning and practical skills. By breaking free from campus

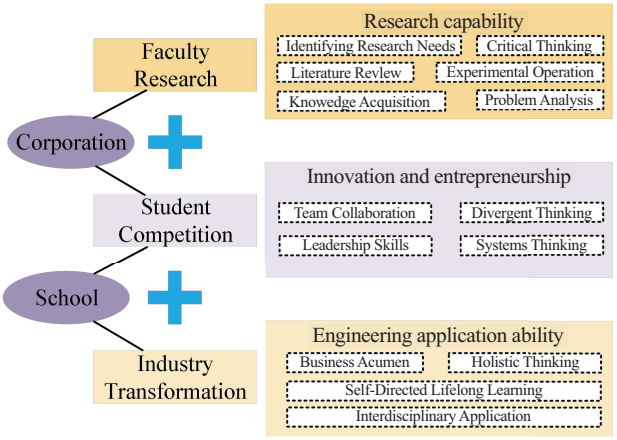

Fig. 15. Student comprehensive capability development system.

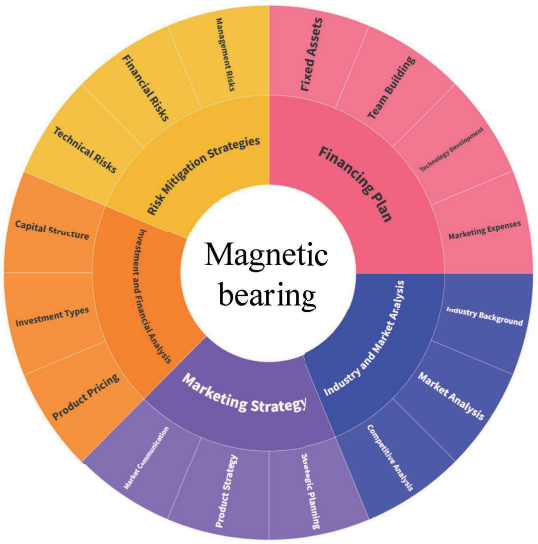

Fig. 16. Magnetic bearing industrialization analysis.

constraints and integrating resources both within and outside the university, the model allowed businesses and society to play roles in education. This encouraged students to continuously identify and solve problems, enhancing their research capabilities and practical innovation skills. The involvement of industry and society in the educational process proved beneficial for cultivating students' research quality and advancing their practical innovate abilities.

During the Graduate Electronic Design Contest—Business Plan Competition, the student team utilized university and college resources while leveraging the benefits of school-enterprise collaboration. They worked directly with SYiTech Co., Ltd., a startup specializing in magnetic bearings, to gain an in-depth understanding of transitioning magnetic bearing technology from research to industrialization. During the business competition, the student team conducted targeted research on every aspect of the entrepreneurial process, including industry and market analysis, marketing strategies, financing plans, investment and financial analysis, and risk mitigation strategies, as shown in Fig. 16. Through their participation, students in-

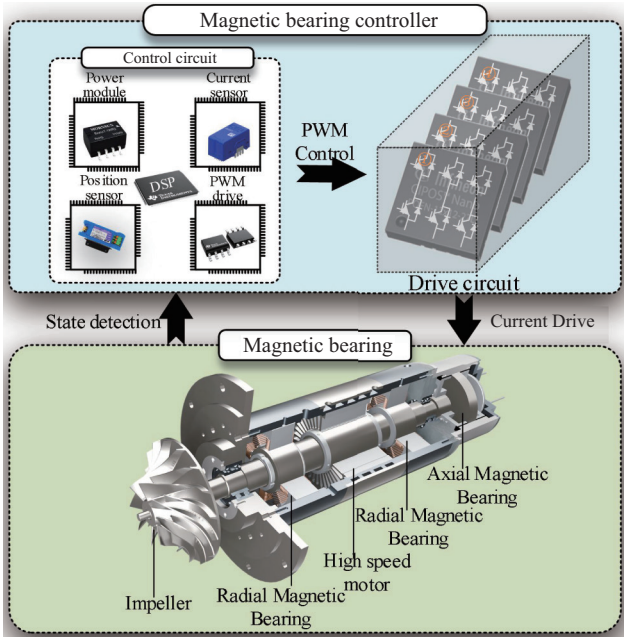

Fig. 17. Magnetic bearing system.

sights into the entire process, from developing magnetic bearing controller products to factory production and sales. This experience transcended the traditional, technology-focused constraints of conventional school-based education, broadening their perspectives and expanding their thinking.

By incorporating market factors into product development, the team established higher standards for the industrialization of the technology. Specifically, active magnetic bearings require electromagnetic force control in five degrees of freedom, including two radial magnetic bearings and one axial magnetic bearing, as shown in Fig. 17. This involves controlling 10 sets of winding currents, necessitating more switching devices compared to traditional motors. For a conventional half-bridge circuit, 4N switching transistors and 4N diodes are needed, where N represents the number of degrees of freedom for the magnetic bearings. This significantly increases the cost and risk of failure for the magnetic bearing controller.

Additionally, the magnetic bearing system depends on the magnetic bearing controller to manage the magnetic bearing motor. The magnetic bearing controller consists of power modules, current sampling, position sampling, PWM drive circuits, and power electronics topology. The entire system integrates mechanical and electrical components, resulting in a high level of complexity.

Through research conducted within the company and market, the student team identified stability and reliability as key factors limiting the large-scale application of magnetic bearings. Building on the university's scientific research, the team integrated a series-winding topology with a magnetic bearing driver to develop a high-performance magnetic bearing controller, as shown in Fig. 18. This controller offers several advantages:

1. Series-Winding Topology: By employing a series-winding topology, the number of power switching devices in the magnetic bearing is reduced by nearly half, significantly lowering the likelihood of failures. The current control bandwidth can be with the same level of H-bridge based controller.

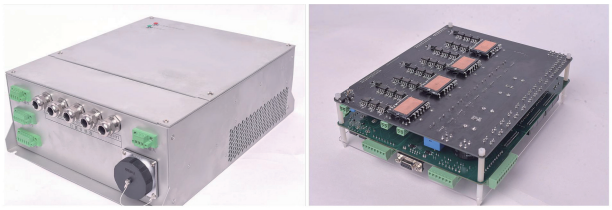

Fig. 18. High-reliability magnetic bearing controller.

2. Fault-Tolerant Design: The team developed a fault-tolerant scheme at the power electronics level for the series-winding topology, ensuring the stable suspension of the bearings even under fault conditions. The ride-through of device open circuit failure is within maximum position error of less than 100 μm.

3. Sensorless Vibration Suppression Strategy: The team developed a strategy to suppress vibrations without relying on speed sensors, thereby addressing sensor failure risks, further reducing system costs, and significantly enhancing the system's resistance to disturbances. The rotational trajectory is with less than 10% of the regular case without vibration suppression strategy.

Unlike technical competitions, business competitions greater emphasis on market adoption challenges. Students prioritize safety, reliability, and long-term operational stability as ultimate technical goals, integrating factors such as material costs, assembly costs, and testing expenses into their evaluation of technical merits, directly linking these factors to product benefits. This approach contrasts sharply with the isolated technical indicators typically found in academic research. In this competition, market needs were incorporated into the research process, integrating reliability and safety considerations into both faculty and student research activities. The research focus expanded to encompass the reliability of power electronics in magnetic bearing systems, including in-depth studies on active fault-tolerant control strategies for device short circuits and open circuits. This research was further extended to explore alternative topologies beyond the series-winding configuration [23]–[26].

The student team participated in both the China Graduate Electronics Design Contest and the Business Plan Competition, where they designed a high-performance magnetic bearing controller. This controller was used in various fields, including magnetic bearing blowers, compressors, and energy storage motors, and won first prize. Later, in 2024, the team competed in the China International College Student Innovation Competition, where they applied the magnetic bearing controller to Organic Rankine Cycle (ORC) generators and won a provincial gold medal. During the competition, they engaged extensively with the market and businesses, collaborating with multiple companies on various magnetic bearing application scenarios. This establishment led to the creation of a school-enterprise communication platform, facilitating the integrated development of industry, academia, and research.

VII. Conclusions

This paper presents a systematic study of transferring cutting-edge research to education, particularly focusing on hardware-based research for talented students in the power electronics field. The primary barrier between research and education in the field of power electronics is the development of hardware prototypes for high-performance testing. For talented young students with the right motivation and skills, training can be provided through suitable platforms, such as contest. The Google Little Box Challenge as an excellent example. The Virginia Tech FEEC team's example shows that the frontier research contribution can be a solid foundation for students to develop prototypes for certain target and to train students with many important capabilities.

The Chinese education system is characterized by a series of scientific competitions designed for university students, which afford copious opportunities to put cutting-edge research findings to use in a wide array of applications, spanning both technical and business arenas. This paper takes the recent advancements in series-end winding motor drives as an exemplar and delves into diverse instances of student applications within contests across three distinct domains..

Case 1 illustrates the initial attempt to train students on SWMD, focusing on drone applications. This example demonstrates students' ability to transfer complex technology to transportation elements.

Case 2 showcases the implementation of SWMD in the mass production of EV. This example highlights students' breakthroughs in overcoming application barriers and planning business strategies based on technical progress.

Case 3 demonstrates the application of SWMD in the specific area of magnetic bearing drives, illustrating how students are trained to innovate and develop business plans beyond traditional areas.

In these three examples, the frontier research achievement of SWMD is a solid source of innovation. Then, the students can organize the teams for different targets and develop prototypes for different applications. During this process, the students will be highly motivated for a purpose, much more than just doing a research project, but for leadership, teamwork, real problem solving and business model.

These three cases exemplify significant success in education, not only through nationwide contest medals but also in training a group of talent students. Contest participants have a winning rate for national scholarships in China that is five times higher than that of regular students. Two of the contest team members have won the highest award of the university, which is less than 0.1% of the whole group of graduate school. Graduates with this type of training have taken on leadership roles as faculty members and co-founders of start-up companies.

References

[1] R. W. Sorensen, "The relation between engineering education and research, with particular reference to the California Institute of technology plan," in *Journal of the A.I.E.E.*, vol. 44, no. 12, pp. 1288–1290, Dec. 1925.

[2] J. Sonnenberg-Klein and E. J. Coyle, "Leadership growth over multiple semesters in project-based student teams embedded in faculty research (vertically integrated projects)," in *IEEE Transactions on Education*, vol. 67, no. 3, pp. 443–452, Jun. 2024.

[3] R. Nelson, V. Marone, S. A. Garcia, T. T. Yuen, E. P. Bonner, and J. Browning, "Transformative practices in engineering education: The embedded expert model," in *IEEE Transactions on Education*, vol. 64, no. 2, pp. 187–194, May 2021.

[4] I. G. Guardiola, C. Dagli, and S. Corns, "Using university-funded research projects to teach system design processes and tools," in *IEEE Transactions on Education*, vol. 56, no. 4, pp. 377–384, Nov. 2013.

[5] T. K. F. Chiu, H. Meng, C. -S. Chai, I. King, S. Wong, and Y. Yam, "Creation and evaluation of a pretertiary artificial intelligence (AI) curriculum," in *IEEE Transactions on Education*, vol. 65, no. 1, pp. 30–39, Feb. 2022.

[6] D. Roldán-Álvarez and F. J. Mesa, "Intelligent deep-learning tutoring system to assist instructors in programming courses," in *IEEE Transactions on Education*, vol. 67, no. 1, pp. 153–161, Feb. 2024.

[7] C. W. Halsted and M. D. Manjrekar, "A critique of little box challenge inverter designs: Breaking from traditional design tradeoffs," in *IEEE Power Electronics Magazine*, vol. 5, no. 4, pp. 52–60, Dec. 2018.

[8] D. Neumayr, D. Bortis, and J. W. Kolar, "The essence of the little box challenge-part A: Key design challenges & solutions," in *CPSS Transactions on Power Electronics and Applications*, vol. 5, no. 2, pp. 158–179, Jun. 2020.

[9] D. Neumayr, D. Bortis, and J. W. Kolar, "The essence of the little box challenge-part B: Hardware demonstrators & comparative evaluations," in *CPSS Transactions on Power Electronics and Applications*, vol. 5, no. 3, pp. 251–272, Sept. 2020.

[10] K. A. Kim, Y. -C. Liu, M. -C. Chen, and H. -J. Chiu, "Opening the box: Survey of high power density inverter techniques from the little box challenge," in *CPSS Transactions on Power Electronics and Applications*, vol. 2, no. 2, pp. 131–139, 2017.

[11] R. Wang, F. Wang, D. Boroyevich, R. Borgos, R. Lai, P. Ning, and K. Rajashekara, "A high power density single-phase PWM rectifier with active ripple energy storage," in *IEEE Transactions on Power Electronics*, vol. 26, no. 5, pp. 1430–1443, May 2011.

[12] L. Zhang, R. Born, X. Zhao, and J. -S. Lai, "A high efficiency inverter design for Google little box challenge," in *2015 IEEE 3rd Workshop on Wide Bandgap Power Devices and Applications (WiPDA)*, Blacksburg, VA, USA, 2015, pp. 319–322.

[13] A. S. Morsy and P. N. Enjeti, "Comparison of active power decoupling methods for high-power-density single-phase inverters using wide-bandgap FETs for Google little box challenge," in *IEEE Journal of Emerging and Selected Topics in Power Electronics*, vol. 4, no. 3, pp. 790–798, Sept. 2016.

[14] C. Zhao, B. Trento, L. Jiang, E. A. Jones, B. Liu, Z. Zhang, D. Costinett, F. F. Wang, L. M. Tolbert, J. F. Jansen et al., "Design and implementation of a GaN-based, 100-kHz, 102-W/in3 single-phase inverter," in *IEEE Journal of Emerging and Selected Topics in Power Electronics*, vol. 4, no. 3, pp. 824–840, Sept. 2016.

[15] D. Neumayr, D. Bortis, and J. W. Kolar, "Ultra-compact power pulsation buffer for single-phase DC/AC converter systems," in *2016 IEEE 8th International Power Electronics and Motion Control Conference (IPEMC-ECCE Asia)*, Hefei, China, 2016, pp. 2732–2741.

[16] Y. Lei, C. Barth, S. Qin, W. -C. Liu, I. Moon, A. Stillwell, D. Chou, T. Foulkes, Z. Ye, Z. Liao et al., "A 2-kW single-phase seven-level flying capacitor multilevel inverter with an active energy buffer," in *IEEE Transactions on Power Electronics*, vol. 32, no. 11, pp. 8570–8581, Nov. 2017.

[17] D. Jiang, X. Sun, A. Li, Z. Liu, and R. Qu, "Series-end winding power electronics converter: principles and applications," in *IEEE Industrial Electronics Magazine*, vol. 18, no. 1, pp. 58–73, Mar. 2024.

[18] X. Sun, Z. Liu, A. Li, Z. Wang, D. Jiang, and R. Qu, "Self-adaptive fault-tolerant control of three-phase series-end winding motor drive," in *IEEE Transactions on Power Electronics*, vol. 37, no. 9, pp. 10939–10950, Sept. 2022.

[19] A. Li, D. Jiang, Z. Liu, X. Sun, and W. Kong, "Unified analysis of winding connection sequence in series-end winding topology," in *IEEE Transactions on Industry Applications*, vol. 57, no. 1, pp. 516–527, Jan.-Feb. 2021.

[20] A. Li, D. Jiang, Z. Liu, and X. Sun, "Generalized PWM method for series-end winding motor drive," in *IEEE Transactions on Power Electronics*, vol. 36, no. 4, pp. 4452–4462, Apr. 2021.
[21] J. Yang, D. Jiang, H. Sun, A. Li, and Z. Liu, "Series-winding topology converter for active magnetic bearing drive," in *IEEE Transactions on Industrial Electronics*, vol. 68, no. 12, pp. 11772–11782, Dec. 2021.
[22] A. Li, D. Jiang, X. Sun, and Z. Liu, "Online drive topology conversion technology for PMSM speed range extension," in *IEEE Transactions on Power Electronics*, vol. 37, no. 6, pp. 7113–7121, Jun. 2022.
[23] J. Yang, D. Jiang, H. Sun, J. Ding, A. Li, and Z. Liu, "A series-winding topology converter with capability of fault-tolerant operation for active magnetic bearing drive," in *IEEE Transactions on Industrial Electronics*, vol. 69, no. 7, pp. 6678–6687, Jul. 2022.
[24] J. Ding, H. Sun, D. Jiang, J. Yang, and Z. Liu, "Open-circuit fault-tolerant control and topology switching strategy of active magnetic bearing power electronics controller," in *IEEE Transactions on Power Electronics*, vol. 37, no. 9, pp. 10928–10938, Sept. 2022.
[25] Y. Shuai, D. Jiang, and Z. Liu, "An improved transient control strategy for active magnetic bearing open-circuit fault-tolerant," in *IEEE Journal of Emerging and Selected Topics in Power Electronics*, vol. 12, no. 1, pp. 827–837, Feb. 2024.
[26] Y. Shuai, D. Jiang, F. Hu, M. Zhou, and Z. Liu, "General switch short-circuit fault-tolerant strategy of active magnetic bearing power electronics drive," in *IEEE Transactions on Power Electronics*, vol. 38, no. 11, pp. 14504–14515, Nov. 2023.

Dong Jiang received the B.S. and M.S. degrees in Electrical Engineering from Tsinghua University, China, and Ph.D degree from University of Tennessee, Knoxville, USA. He has been with the Huazhong University of Science and Technology, Wuwan, China, as a Professor, since July 2015. His main research interests include power electronics and motor drives.

Zicheng Liu received the B.S. degree from Huazhong University of Science and Technology (HUST), Wuhan, China, in 2011, and the Ph.D. degree from Tsinghua University, Beijing, China, in 2016. He is currently a Professor at HUST. His research interests include multiphase motor control systems and transportation electrification.

Min Zhou is an associate Professor in the School of Electrical and Electronic Engineering, Huazhong University of Science and Technology (HUST). She received her PhD from Wuhan University in China in 2014. Her research is focused on the investigation of advanced energy storage materials and novel energy storage devices for large-scale energy storage applications.

Lanhua Zhang received his B.S. and M.S. degrees in Electrical Engineering from Shandong University, China, in 2009 and 2012, respectively. He earned his Ph.D. degree from Virginia Tech in 2016. He is currently a Senior Hardware Engineer at Apple Inc. Dr. Zhang has published more than 40 conference and journal papers. In 2015, he led the FEEC team to achieve a top-three ranking in Google's $1 Million Little Box Challenge.

Wei Sun received the B.S. degree from Beijing Jiaotong University, and the M.S. and Ph.D. from Harbin Institute of Technology, all in electrical engineering. He is now an associate Professor in Huazhong University of Science and Technology, Wuhan. His main field of interest is AC motor drive, control theory application in power electronics system.

Wenli Xu received her B.S. degree from Huazhong University of Science and Technology (HUST), China, and the M.S. degree from the University of Michigan–Dearborn, USA, both in Electrical Engineering. She is currently serving at the School of Electrical and Electronic Engineering, HUST, where she has successively held positions as Graduate Counselor, Student Affairs Officer, and Deputy Director of the Student Education and Management Center.

Data-Driven Control of Electrical Drives: A Deep Reinforcement Learning with Feature Embedding

Xing LIU, Dengyin JIANG, and Chenghao LIU

***Abstract*—Classical model-based control solutions dominated the research field of numerous electrical drives applications in the past forming a strong basis, since they usually result in control approaches with excellent performance. However, the design of these controllers strongly depends on the available knowledge of the controlled plant, which often leads to the lack of robustness owing to model-dependent nature. To take account of the defect, this work aims to provide a control framework that combines intelligent data-driven-based control protocol with the deep reinforcement learning technique for electrical drives. Specifically, the two key features of this developed control framework that, first, a data-driven control architecture along with deep reinforcement learning technique that embedding the features of the agents' inputs is developed to enhance the performance, second, the environment for the current agent is reformulated so as to avoid mutual interference between the two agents (controllers) in training for both speed and current in a dual-loop system. Finally, we demonstrate our solution and highlight its superiority on a case study, and the results presented are promising and motivate further research in this field.**

***Index Terms*—Feature embedding, intelligent control, motor drives, permanent magnet synchronous motor (PMSM), reinforcement learning (RL).**

I. Introduction

In recent decades, permanent magnet synchronous motor (PMSM) drives, due to their prominent merits, such as high energy efficiency, high power density, high reliability, and wide speed control range, have gained tremendous spread in various industrial and automotive applications. In particular, its applications are expanding rapidly, such as industrial robots, electric vehicles, industrial automation, and power transmission systems. Various control techniques for PMSM drives have been extensively explored in the literature [1]–[3]. Among them, the well-developed method used to control PMSM drive system is proportional-integral (PI) regulator together with pulse width modulation (PWM) modulator designed in continuous-time. To be specific, the PI controller regulates the system state variable to track its desired value by generating a reference voltage signal to the PWM stage. This approach has a simple structure and easy to implement which uses a feedback loop to adjust the control signal based on the difference between the desired and actual values of the motor speed and currents. Although this is a reasonable approach, the controller parameters have to be properly tuned to ensure fast transient response and less steady-state errors.

A. Literature Review and Motivation

Recently, model predictive control (MPC) is receiving considerable attention in electric drive systems [4], [5]. The popularity of this solution stems largely from the possibility to explicitly address multivariable nonlinear systems constraints. In electrical drives, MPC solutions can be loosely categorized in two categories based on whether a modulation stage is needed or not. Continuous control-set MPC (CCS-MPC) produces the continuous-time control inputs to the modulation stage in the controller formulation [6], while finite control-set MPC (FCS-MPC) replaces the cascaded control structure without the intervention of the intermediate stage [7]. The CCS-MPC method can be favored in applications where keeping a fixed switching frequency is crucial. The latter offers an improved dynamic performance which rely on a sophisticated mathematic model to predict future behavior of system state and optimize the control signal. Although extensive research works in the control of CCS-MPC and FCS-MPC have brought some improvements, pursuing excellent control performance while ensuring safety and reliability in the presence of uncertainties remains open for PMSM drive system [8], [9].

The rapid development of data-driven algorithm has provided new avenues to overcome the aforementioned inherent limitation for control system design [10]–[12]. Its main workflow is to obtain the parameters of a function approximator (is

Manuscript received April 2, 2025; revised May 14, 2025 and September 16, 2025; accepted October 12, 2025. Date of publication December 30, 2025; date of current version December 2, 2025. This work was supported by State Key Laboratory of Highspeed Maglev Transportation Technology under the grant SKLM-SFCF-2023-020, National Natural Science Foundation of China under the grant 52577218, Key Laboratory of Special Machine and High Voltage Apparatus (Shenyang University of Technology), Ministry of Education under the grant KFKT202403, Open Research Project of the State Key Laboratory of Industrial Control Technology under the grant ICT2025B53, Open Research Project of the State Key Laboratory of Power Transmission Equipment Technology under the grant SKLPET-kfkt202406, and the key Laboratory of Marine Power Engineering and Technology of Ministry of Transport under the grant KLMPET2025-04. (*Corresponding authors: Dengyin Jiang and Chenghao Liu.*)

X. Liu is with the College of Electrical Engineering, Shanghai Dianji University, Shanghai 201306, China, and State Key Laboratory of Power System, Department of Electrical Engineering, Tsinghua University, Beijing 100084, China, and College of Electrical Engineering, Zhejiang University, Hangzhou 310027, China (e-mail: xingldl@zju.edu.cn).

D. Jiang is with the College of Electrical Engineering, Shanghai Dianji University, Shanghai 201306, China (e-mail: jiangdy@sdju.edu.cn).

C. Liu is with the College of Electrical Engineering, Zhejiang University, Hangzhou 310027, China (e-mail: liuchenghao@zju.edu.cn).

Digital Object Identifier 10.24295/CPSSTPEA.2025.00037

usually a neutral network) by training it with a large amount of data based on observable variables of the controlled plant, and apply it in control process. The data-based supervised method can be utilized to tune controller parameters, calculate nonlinear magnetic flux, or identify motor parameters. It is even possible to train a neutral network to imitate the output of a PI or an MPC controller [13]. However, during the supervised training, both input and output data for an approximator are required in these applications, thus it is not possible to directly obtain a controller through this method.

Subsequently, with respect to another line of research, reinforcement learning (RL) has been predominantly studied in the electric drive field for many years and it has attracted much attention from researchers [14], [15]. Its workflow is to use the output of a random actor to interact with the environment, and train the actor through the rewards (the output of a critic) generated by the interaction. In this approach, the critic and actor are both neutral networks. The critic network approximates the reward through supervised learning, while the actor network maximizes the reward through exploration and feedback. For general problems in finite action space, deep-Q-network (DQN) can achieve excellent performance, which makes RL applicable for controlling inverter switch states [16]. However, for a complete motor control system, continuous control may be more suitable, especially for the speed-to-current conversion, which involves continuous input and output. It is worth remarking that deep deterministic policy gradient (DDPG) has solved the problems of implementing RL in continuous action space. It is an actor-critic, model-free algorithm based on the deterministic gradient which employs some methods such as experience reply, target network, and soft updates to improve training stability and solve physics tasks robustly. The emergence of DDPG enables the possibility of directly learning the controllers for electric drive systems solely through data-driven approaches.

Some research studies on using RL controllers in PMSM drive system have been devoted to the enhancement of the robustness against parameter mismatch and disturbances. An RL current controller is proposed in [17], where the concept of PMSM controller design by DDPG is first proved. The authors in [18] exploited an RL torque controller by deploying a complex reward rule so as to make the operating point adhere to maximum torque per current strategy. The results in [19] leverage an RL speed controller to reject active disturbance. Overall, for PMSM speed (or torque) control, it is possible to use a single RL controller to track the reference. However, in this sense, the control strategies for torque and current, such as maximum torque per ampere (MTPA) or maximum torque per voltage (MTPV), cannot be guaranteed, unless a complex multi-objective reward can be designed. On the other hand, it is still uncertain how to train two independent RL controllers for the dual-loop system and ensure their convergence while maintaining a strategy module for torque and currents. Motivated by these issues, it is expected to exploit a data-driven control architecture along with deep RL technique that embedding the features of the agents' inputs for electrical drives in a dual-loop system. This consideration encourages the main innovation of the current research.

B. Main Contribution

Pursuing the aforementioned observations, we will launch a crucial study on the deep RL control problem, and we hope that this work lays a theoretical foundation and also inspires new achievements in the intersection of artificial intelligence (AI) technique and deep learning control theory. In this work, we further focus on investigating a novel intelligent data-driven control architecture together with two RL controllers that embedding the features of the agents' inputs for a dual-loop control system. This implies that both the speed controller and current controller are entirely learned by intelligent agents, rather than being designed through model-based approaches. To avoid mutual interference between the two controllers, this paper adopts a sequential training method, where the current controller is trained first, followed by the training of the speed controller. In particular, the current agent interacts only with the inner loop during training. The convergence and performance of the controllers have been validated under different operating conditions. The performance evaluation shows that the RL dual-loop controllers can achieve desired performance to the model-based approaches [17], [18], while also demonstrating better dynamics. Furthermore, this paper leverages embedding techniques to the controller variables, significantly enhancing the accuracy of reference tracking compared to [20], and this method can be naturally extended toward various control systems. Finally, extensive investigations for the electrical drives confirm the interest and the viability of the proposed design methodology.

Compared to existing literature, our method has the following novel aspects.

- Building upon the RL control protocol, in contrast to previously known results, this work goes one step further and accomplishes both speed and current control in a dual-loop PMSM drive system relying solely on data. To be more precise, the sequential training method used in this article avoids mutual interference between the two controllers and effectively aids in the convergence.
- Unlike much prior studies, by transforming the variables into embeddings before inputting them into the controllers, significant improvements are achieved in both training and testing, which facilitate the alleviation of performance deterioration. This modification is quite general and easy to implement in engineering applications and can be conveniently extended to other RL controllers, without sacrificing the simplicity of the control structure.
- Last but not least, effectiveness and performance of the proposal are validated extensively and highlighted by benchmarking it against other state-of-the-art control approaches including RL-based controller and PI-based controller. The extensive testing results in this paper indicate that when designing intelligent controllers, using data from various operating conditions in training is crucial. This literature opens up even more possibilities of

connections with power converter and/or motor control fields.

C. Outline of the Article

The remaining parts are structured as follows. In section II, we briefly describe the PMSM dual-loop drive system. Section III presents the speed and current controllers designed formulation. Meanwhile, we provide a distinctive alternative and details of the proposed RL methodology. To be specific, we exploit an intelligent data-driven-based controller along with deep RL technique. In the following, to further enhance performance under different operation scenarios, our work further focuses on developing a method that embedding the features of the agents' inputs. Further, in order to avoid mutual interference between the two agents (controllers) in training, the environment for the current agent is reformulated for both speed and current in a dual-loop system. In section IV, we verify its merits with different benchmark examples from the literature. Finally, conclusions and future works on the suggested control protocol are summarized in Section V.

II. Physical System

The iteration of an RL intelligent agent is realized through interaction with its environment. The iteration of an RL intelligent agent is realized through interaction with its environment. To address a specific problem, it is crucial to determine the environment in which the agent operates. In this paper, the environment in which the two agents (current agent and speed agent) operate includes physical systems such as a PMSM, an inverter module and a module for selecting operating point. Note that the two agents belong to each other's external environment. This aspect will be discussed in the next session.

In a vector control system, a PMSM can be modeled by a set of differential equations, which is described in the d/q coordinate. It yields:

$$u_d = Ri_d + L_d\frac{\mathrm{d}i_d}{\mathrm{d}t} - \omega L_q i_q \tag{1}$$

$$u_q = Ri_q + L_q\frac{\mathrm{d}i_q}{\mathrm{d}t} + \omega(L_d i_d + \psi_\mathrm{f}) \tag{2}$$

$$T_\mathrm{e} = \frac{3}{2}p\left(\psi_\mathrm{p} i_q + (L_d - L_q)\, i_d i_q\right) \tag{3}$$

$$J\frac{\mathrm{d}\omega}{\mathrm{d}t} = T_\mathrm{e} - T_\mathrm{m} \tag{4}$$

where u_d, u_q, i_d, and i_q are the voltage and current of the motor, T_e and T_m represent the electromagnetic torque and load respectively, and ω represents the machine velocity. All variables in the equations are derived from observation and measurement of the PMSM, and the d/q components are obtained through coordinate transformation. In the completed trained control system, torques (T_e, T_m) are not required to be measured due to the fact that their effects are reflected in changes in velocity. However, during the training phase, they needed to be observed so as to calculate the rotational speed in the environment.

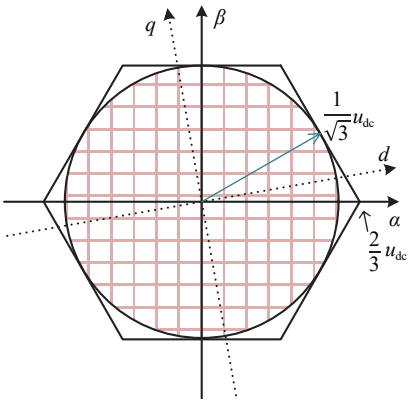

Fig. 1. Limitation of voltage vector.

A power electronic converter is usually deployed to drive the three-phase PMSM. The converter is powered by a constant DC bus and, hence, the voltage range at the stator of the PMSM is limited. When it observed in α/β coordinate in Fig. 1, the maximum voltage that the inverter can provide is limited in a hexagon. Accordingly, even though the output of the RL current controller is (–1,1), the modulation module still limits the actual voltage within a feasible range. This is a characteristic of the environment, which the RL agent needs to implicitly learn. Moreover, it is interesting to remark that the dead time of converter should be taken into account to ensure that RL actor can adapt to the real environment [14].

In order to make the PMSM operate at the optimal point, the desired control solution are necessary after decoupling control into d/q coordinates. The selection of the operating point must firstly satisfy the constraints on current and voltage. High current can lead to temperature rise and safety issues and, hence, the current should be limited:

$$\sqrt{i_d^2 + i_q^2} \leqslant i_{\max} \tag{5}$$

As for voltage constraint, the operating point voltage must satisfy the requirement that it can be achieved by the modulation module throughout the complete period. It should be noted that, unlike the limit in the inverter, the constraint here refers to the inscribed circle of the hexagon in Fig. 1, with a maximum value of $\frac{1}{\sqrt{3}}u_\mathrm{dc}$. According to (1) and (2), the voltage of PMSM is small at low speed, so the voltage limit can be ignored. At high speed, after neglecting the voltage drop across the resistance, this constraint can be expressed as:

$$\sqrt{(\omega(L_d i_d + \psi_\mathrm{f}))^2 + \omega(L_q i_q)^2} \leqslant \frac{1}{\sqrt{3}}u_\mathrm{dc} \tag{6}$$

After satisfying the current and voltage limits, the suggested strategy for the operating point is generally based on MTPA and MTPV. Based on (3) and the Lagrange Multiplier method, the reference values of d/q axis currents under MTPA strategy can be obtained:

$$i_d = -\frac{\psi_\mathrm{f}}{2(L_d - L_q)} + \sqrt{\frac{\psi_\mathrm{f}^2}{4(L_d - L_q)^2} + i_\mathrm{q}^2} \tag{7}$$

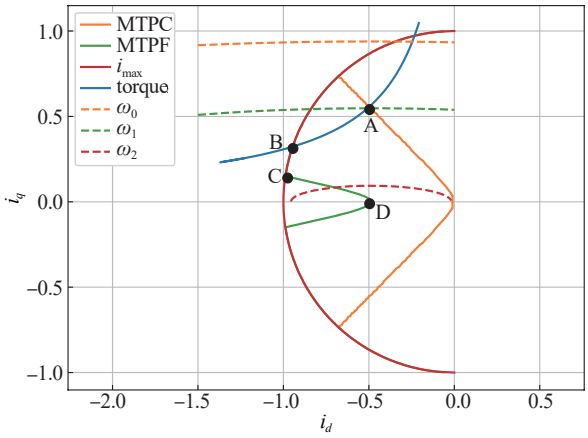

Fig. 2. Operating point selection strategy.

Similarly, the reference values under MTPV strategy are given as:

$$\begin{cases} i_d = \dfrac{3\psi_f L_q - 4\psi_f L_d + \sqrt{\psi_f^2 + \dfrac{8}{3}u_{dc}^2\left(\dfrac{L_d - L_q}{\omega L_q}\right)^2}}{4L_d(L_d - L_q)} \\ i_q = -\dfrac{i_q}{\omega L_q} \end{cases} \tag{8}$$

The operating point selection strategy is illustrated in Fig. 2, which aims to achieve the maximum torque while satisfying (5) and (6). For the reference torque shown in the figure (blue line), when the speed is low, the motor operates at point A determined by MTPA. Since the speed increases beyond the critical point of the voltage limit, the system will subsequently operate along the constant torque curve until point B. At this point, the current is saturated, and the PMSM is unable to maintain a constant torque. The motor will work along the current limit circle to provide maximum possible torque. Finally, the critical point of MTPV is reached. If the motor continues to accelerate, it will subsequently operate along the point C to D curve to fully utilize the voltage and obtain the maximum torque. The point D is a theoretical point at $(-\frac{\psi_f}{L_d}, 0)$. During training, the operating point is obtained through look-up-table (LUT) or analytical method. This strategy module, like the PMSM physical system, also belongs to the environment that the RL agent needs to adapt.

III. Design and Training

In this section, motivated by the aforementioned discussions, we aim at investigating on an intelligent data-driven-based controller design issues. To this aim, a data-driven control architecture along with deep RL technique that embedding the features of the agents' inputs is presented to enhance the performance. Meanwhile, the environment for the current agent is reformulated so as to avoid mutual interference between the two agents (controllers) in training for both speed and current in a dual-loop system for electrical drives. In what follows, the suggested control design procedure will be discussed in detail.

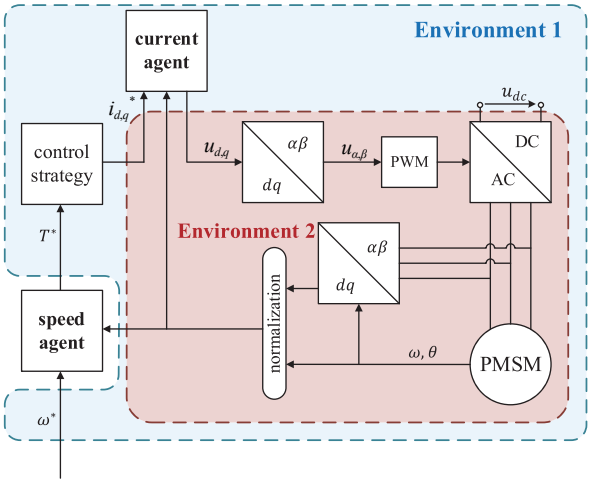

Fig. 3. The RL agents and their environments.

A. Design Training Algorithm

The overall system is shown in Fig. 3, where the blue box represents the environment of speed agent, and the burgundy box represents the environment of current agent. Ideally, the Environment 2 should include all components in the system except the current agent. However, in this sense, updating the parameters of the speed agent will lead to change in the environment of the current agent, which will require retraining. Similarly, variations in the parameters of the current agent will require retraining of the speed agent.

On the other hand, if training both agents synchronously, it may lead to instability due to their different objectives and the mutual influence of their convergence. To address the issues associated with the aforementioned methods, this paper leverages a solution where the current controller is first trained in Environment 2, followed by training the speed controller in Environment 1, and as shown in Fig. 3. Since the current loop is an inner loop, its dynamics should be faster than speed loop. Consequently, when the current controller is trained, the environment of the current agent can be simplified by neglecting the dynamic process of the outer loop, as long as the trained current controller can track the references under different speed conditions.

The RL controller is actually the actor of the agent, whose objective is to maximize the reward. For the both speed and current RL controllers, their rewards are the negative mean squared error (MSE) between the actual value and the reference value. Then, we can get

$$r_{speed} = -\left(\frac{\omega^* - \omega}{\omega_n}\right)^2 \tag{9}$$

$$r_{current} = -\left(\frac{i_d^* - i_d}{i_n}\right)^2 - \left(\frac{i_q^* - i_q}{i_n}\right)^2 \tag{10}$$

Next, the method for evaluating an actor's action is the action-value function, which can be described by the Bellman equation:

$$Q^{\mu}(s_t, a_t) = \mathrm{E}\left(r(s_t, a_t) + \gamma Q^{\mu}(s_{t+1}, \mu(s_{t+1}))\right) \tag{11}$$

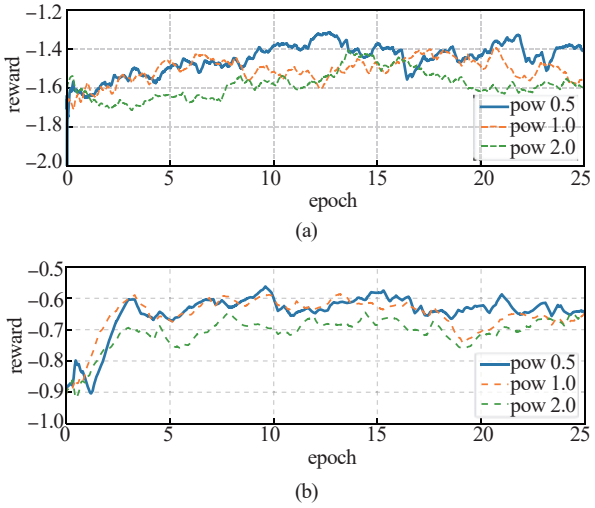

Fig. 4. The actual rewards during training using different power conditons. (a) The rewards of current agent, (b) The rewards of speed agent.

TABLE I
PARAMETERS AND VALUES

Parameters	Values
Stator resistance R	6.0e−2
d component of inductance L_d	1.3e−3
q component of inductance L_q	4.0e−3
Permanent flux ψ_f	125.1e−3
Pole of pairs J	1.324e−3
Moment of inertia R	6.0e−2
Nominal current i_n	195
DC bus voltage u_{dc}	450
Nominal velocity ω_n	2000 × π/30
Sampling time T_s	1e−4

This is a recursive function based on the temporal difference (TD) method, and it includes a discount factor for the future reward. The Q-function can be approximated by a neutral network which is the critic in the agent. During the training, its loss function is given as:

$$\text{Loss} = (r(s_t, a_t) + \gamma Q^{\mu}(s_{t+1}, \mu(s_{t+1})) - Q^{\mu}(s_t, a_t))^2 \quad (12)$$

The second term in the loss function depends on the actor and critic, which are constantly updated during training, and this can introduce instability into the training. Therefore, target functions for the actor (μ') and critic (Q′) are introduced to predict Q-value, and they are set to slowly approach the lasted actor and critic [21]. The calculation of the Q-value requires both state and action, making the actor and critic interdependent and requiring them to work in tandem. As a result of the cascading structure, the gradient can be propagated to the actor, enabling the implement of the gradient ascent algorithm to update the actor's parameters and achieve the maximum reward.

TABLE II
HYPERPARAMETERS USED IN TRAINING

Hyperparameters	Speed agent	Current agent
Number of layers	64/32/32	64/32/32
Activation function of actor	ReLu/ Tanh	ReLu/ Tanh
Activation function of critic	ReLu/ ReLu	ReLu/ ReLu
Learning rate of actor	5e−5	5e−5
Learning rate of critic	3e−5	3e−5
Batch size	128	128
Optimizer	Adam	Adam
Discount factor	0.99	0.99

Note that the environment and reward for the current and the speed controller should be differentiated, while the remaining process is mostly same. To avoid local optima, additional noise is added to actor's output:

$$a_t = \mu(s_t) + N_t \quad (13)$$

It is a crucial aspect of the exploration in RL, and in this paper the noise is used the Ornstein-Uhlenbeck process, which is suitable for physical systems with momentum [21].

B. Change of Reward and Feature Embedding

To ensure the convergence of the algorithm, as depicted in Fig. 3, all variables will be normalized to the range of [−1, 1]. However, normalization will cause the gradient of MSE to become very small as the error gradually converges, which limits the precision of the training. If the exponent of the error in reward is gradually reduced, the gradient of the reward will increase in cases where the error is small. This effect is particularly pronounced when the exponent is less than 1, because the reward becomes more sensitive to fine errors. Thus, this paper made adjustments to the exponent in the rewards. In Fig. 4, the training results of the currents (or speed) reward under three different conditions are demonstrated: when the exponent of error is equal to 2, equal to 1, and equal to 0.5. The system parameter values and the normalization values are given in TABLE I, and fixed hyperparameters used for training are given in TABLE II.

To facilitate comparison, the actual rewards during training in the figure have been uniformly normalized using pow (MAE, 0.1) in Python. It is evident from the figure that reducing the exponent leads to a stable improvement in the actual reward during training. The power is a hyperparameter that can be adjusted based on the specific circumstance. Due to the fact that the exponent becomes too small, it can also affect the gradient when the error is relatively large, and a value of 0.5 is used for the reward in this work.

Data and features are also important factors that influence the training results. In this literature, the features refer to the input vector of the network is expressed in the following form:

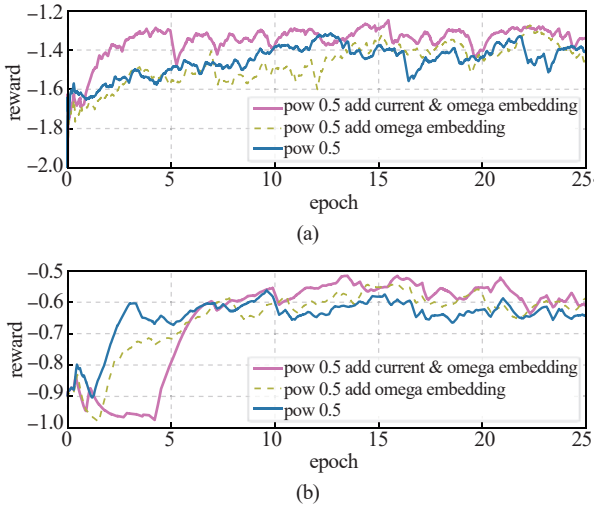

Fig. 5. The actual rewards during training using feature embedding. (a) The rewards of current agent, (b) The rewards of speed agent.

$$v = \left[\frac{i_d}{i_n} \quad \frac{i_q}{i_n} \quad \frac{u_d}{u_n} \quad \frac{u_q}{u_n} \quad \frac{\omega}{\omega_n} \quad \cos\theta \quad \sin\theta \quad \cdots \right. \\ \left. \left(\frac{\omega^* - \omega}{\omega_n} \right) \quad \left(\frac{i_q^* - i_q}{i_n} \right) \right] \tag{14}$$

Taking the example of the speed agent, the feature of speed error in the vector is inevitably important, since the value of the reward is directly determined by it. However, the speed error may only approach 1 during start-up, and for most part, it remains close to 0. This results in a highly imbalanced data distribution, where the feature is effective in distinguishing high and low levels of error, but lacks discriminability when error is low. To some extent, the error features of currents also suffer from a similar problem. Batch normalization can alleviate this limitation, but it relies on the statistical properties of the training data, which can introduce bias during prediction.

To circumvent this barrier, we leverage the feature embedding to better distinguish the magnitude of a certain feature. One approach is to bin the feature and use an LUT to store the embeddings corresponding to the different bins, and adaptively adjust these embeddings during training. The effectiveness of this method depends on the result of binning, and it requires an additional LUT. It is noticeable that, in this work, we use a practical solution by normalizing the same feature differently and concatenating the results into a vector to represent the embedding of this feature. Thus, the embedding of a feature can be express in the following equivalent form:

$$e_v = \left[\left(\frac{v^{(1/l)}}{v_n^{(1/l)}} \right) \quad \left(\frac{v^{(2/l)}}{v_n^{(2/l)}} \right) \quad \cdots \quad \left(\frac{v^{(1/l)}}{v_n^{(1/l)}} \right) \right] \tag{15}$$

where e_v denotes the embedding of feature v, and v can be any feature, such as speed or speed error. The l is a hyperparameter, which is related to the dimension of the embedding.

From (15), it can be seen that small errors will be amplified after normalization. Additionally, the dimension and normalization method can be adjusted based on the results obtained. Fig. 5 shows the actual rewards obtained by the current (or speed) controller during training with features embeddings when l = 4. The blue line in Fig. 5 represents the same results as the blue line in Fig. 4. It can be observed that after adding the current and current error embeddings, the current controller has significantly improved in terms of reward. Similarly, after adding the speed and speed error embeddings, the speed controller also shows prominent enhancement. To illustrate the practical implementation of our modification clearly, the pseudocode for training the controllers is provided in TABLE III.

TABLE III
PSEUDOCODE FOR THE CURRENT/SPEED CONTROLLER

Method: Implementation of the Suggested Controller

Initialize the Q and μ
Initialize the target functions Q', and μ',
for *episode* = 1, M do
  if training current controller, then
    Initialize the Environment 2.
    Neglect the (4) and select reward (10).
  else
    Initialize the Environment 1 and select reward (9).
  for t = 1, T do.
    Select action a_t through (13) and simulate.
    Observe the new state s_{t+1} and calculate the r_t.
    Store(a_t, s_t, r_t, s_{t+1}) in replay buffer.
    Sample a batch of data randomly from replay buffer.
    Update the parameters of Q by minimizing (12).
    Update the parameters of μ by maximizing (11).
    Softly update the target functions Q', and μ'.
    end for.
end for

IV. EVALUATION AND RESULTS

In this section, to verify our theoretical findings, a case study is carried out on a PMSM drive control system, and the functionality of the suggested algorithm will be demonstrated. For a fair comparison, same parameters are set.

The training data are generated by training the actor and critic networks with randomly selected speed setpoints until convergence. To ensure consistency between the training data and the real-world system behavior, a physics-based model of the inverter and PMSM is constructed within a Python environment, along with a discrete-time control system. Specifically, a simulation framework resembling Simulink is developed based on system equations and numerical solvers, allowing the agent to interact with the environment. Practical features such as dead-time effects and digital control delays are also preserved. As a result, the simulation environment produces outputs that match those of the actual physical system.

The speed control agent generates a reference torque based on the system states and the reference speed. Meanwhile, the current control agent outputs a reference voltage according to the system states and the reference torque. Further, the action

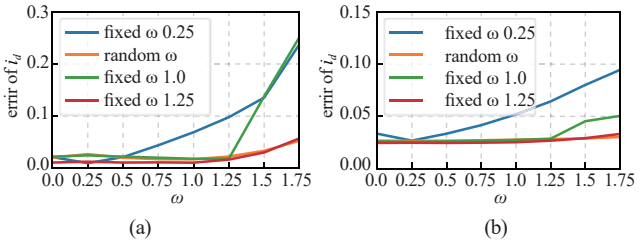

Fig. 6. Performance of the current controller at different speed conditions. (a) Performance of i_d traking, (b) Performance of i_q traking.

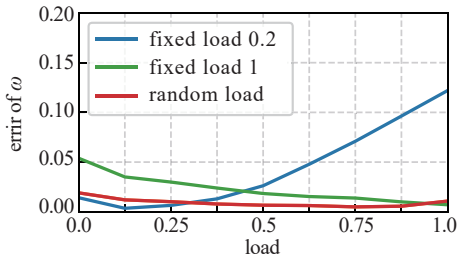

Fig. 7. Performance of the speed controller under different loads.

space of the current control agent is continuous and normalized to the range (–1, 1), based on the allowable voltage range at the inverter output. Similarly, the action space of the torque control agent is continuous and normalized to (–1, 1), according to the torque range at the motor output.

A. Training with Different Speeds and Loads

First, when the current controller is trained, it is important to vary the speed setting in Environment 2 to different values. Although the RL controller has some degree of robustness, in general, using a fixed speed during training can result in significant errors when tested at other speeds. Fig. 6 depicts the performance of the controllers at different speeds during test after being trained at either random range ([0, 1]) or fixed speeds. From Fig. 6, it can be observed that the tracking per formance of i_q (or i_d) is greatly affected when the fixed operating speed is 0.25 in training and the operating speed is 1 in test. This figure indicates that employing random speed during training or chose a larger fixed speed is necessary to maintain desired control performance across the full speed range.

Similarly, it is necessary to use different loads during training process of the speed controller. Fig. 7 also demonstrates that using random loads during training can result in a controller with better performance across different loads.

B. Effectiveness of Feature Embedding

The partially tested performance of the current controller trained using the scheme described above is shown in Fig. 8. As shown in the figure, the model trained using feature embedding outperforms the model without embedding in tracking. This is consistent with the result of reward during training.

Fig. 9 also demonstrates that for the RL speed controller,

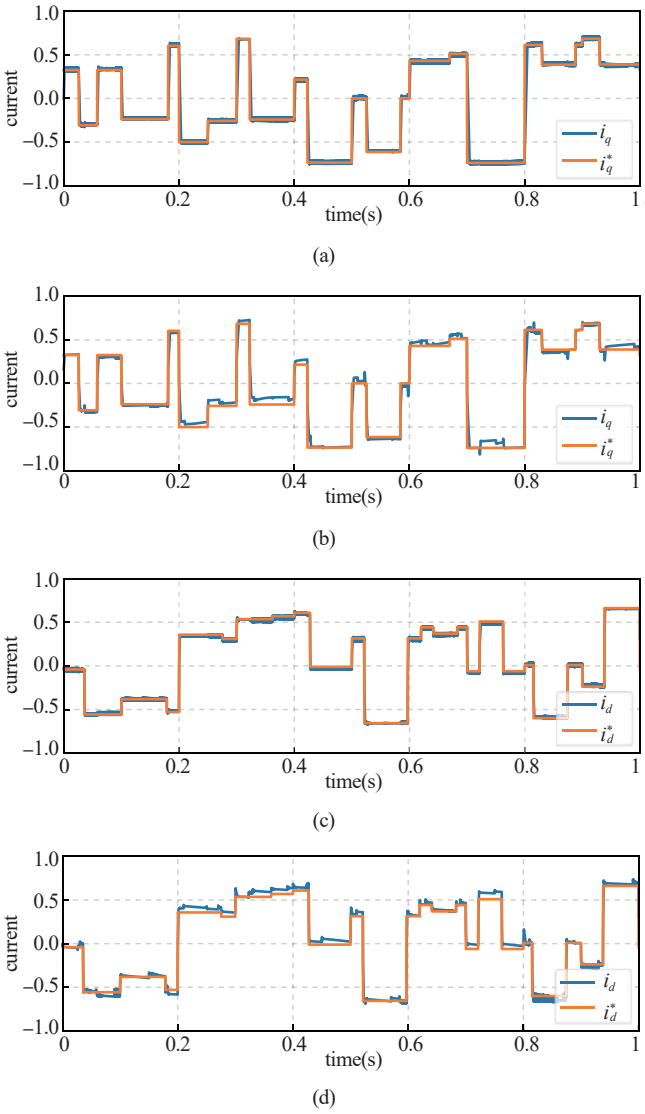

Fig. 8. Performance of the current controller at speed 1.0. (a) i_q traking of the RL controller with embedding, (b) i_q traking of the RL controller without embedding, (c) i_d traking of the RL controller with embedding, (d) i_d traking of the RL controller without embedding.

using embedding results in higher accuracy and less vibration. In Fig. 9, the speed trajectory using a PI controller is also shown. It can be observed that the dynamic performance of the RL controller is superior to that of the implemented traditional model-based controller, and with the help of feature embedding, it can approach the performance of the PI controller in steady-state.

Fig. 10 presents detailed test results, evaluating the performance of these two RL controllers under different operation conditions. This figure not only demonstrates the reliability of the benefits of using embedding, but also highlight two interesting points. In the current test results shown in the figure, it can be seen that the model without embedding experiences an immediate increase in error when the speed exceeds 1, even with random speed range ([0, 1]) during training. This suggests that the generalization ability of the model trained with random speeds still depends on the representation of the features. An-

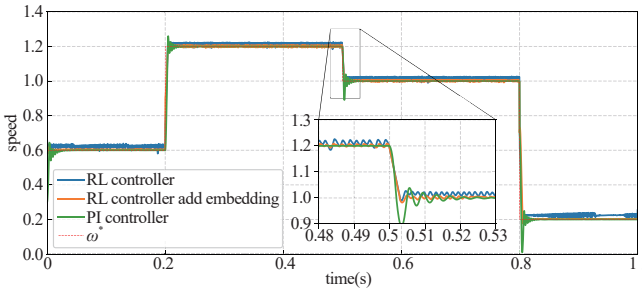

Fig. 9. Performance of the speed controller under load 0.75.

other point that can be observed by comparing D and E is that as long as the speed controller employs the embedding, the use of embedding in the current controller has little effect on speed control performance. This is because for the speed controller, the current controller is only a part of its external environment, which it needs to implicitly learn during training. However, in that sense, if the inner loop cannot accurately track the reference value, it will lead to a discrepancy between actual operating point and operating point from strategy selection module.

Finally, the comparison results also show that the controllers trained by the proposed approach can achieve desired performance to model-based controllers, and have better dynamics, while relying solely on data, and making it suitable for sensitive applications such as transportation. In conclusion, this test illustrates the capabilities of our method to obtain a high-performance under different operation conditions, and our solution works as expected.

V. Conclusions and Future Work

This article demonstrated how to train two cascaded RL controllers in a dual-loop system. By redefining the environments of the two agents and training them sequentially, the current and speed controllers can converge under different operating conditions successfully. Meanwhile, the proposal in this work, which utilized embedding to represent the speed, current and error, can significantly improve the accuracy of the RL controllers when compared to the previous RL controllers. This had been validated in both training and testing. Furthermore, the accuracy and robustness of the RL controller were enhanced by adjusting the reward function and using different operating conditions during training. Finally, the results demonstrated that our development can offer good tracking performance and regulation properties in contrast to two different control approaches, which enable the system to operate as their enhancement, facilitating its quick adoption by the industry.

Future investigations will focus on issues kept out of the scope of this work. First of all, it is expected that the results in this work can be extended to other electric drive systems under cyber attacks, where exploration would be beneficial by addressing an online safety-enhanced deep RL along this study line [22]–[24]. Alternatively, how to design a transferring learning-based long-horizon MPC solution subject to unknown uncertainties is another potential theme that needs further research [25], [26].

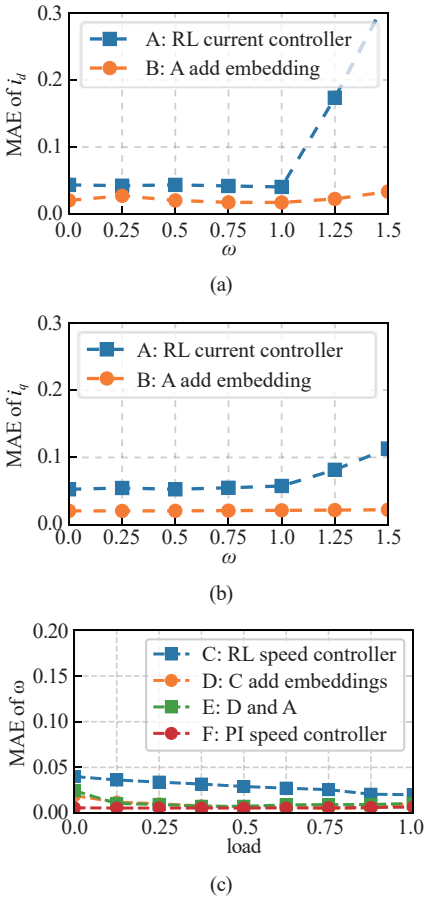

Fig. 10. Performance of the controllers under different conditions. (a) Performance of i_d traking, (b) Performance of i_q traking, (c) Performance of speed traking.

References

[1] J. Rodriguez, C. Gaecia, A. Mora, F. F.-Bahamonde, P. Acuna, M. Novak, Y. Zhang, L. Tarisciotti, S. A. Davari, Z. Zhang et al.,"Latest advances of model predictive control in electrical drives—Part I: Basic concepts and advanced strategies," in *IEEE Transactions on Power Electronics*, vol. 37, no. 4, pp. 3927–3942, Apr. 2022.

[2] J. Rodriguez, C. Garcia, A. Mora, S. A. Davari, J. Rodas, D. F. Valencia, M. Elmorshedy, F. Wang, K. Zuo, L. Tarisciotti et al., "Latest advances of model predictive control in electrical drives—Part II: Applications and benchmarking with classical control methods," in *IEEE Transactions on Power Electronics*, vol. 37, no. 5, pp. 5047–5061, May 2022.

[3] P. Catalán, Y. Wang, J. Arza, and Z. Chen, "Advanced fault ride-through operation strategy based on model predictive control for high power wind turbine," in *IEEE Transactions on Sustainable Energy*, vol. 15, no. 1, pp. 513–526, Jan. 2024.

[4] T. T. Nguyen, H. N. Tran, T. H. Nguyen, and J. W. Jeon, "Recurrent neural network-based robust adaptive model predictive speed control for PMSM with parameter mismatch," in *IEEE Transactions on Industrial Electronics*, vol. 70, no. 6, pp. 6219–6228, Jun. 2023.

[5] I. González-Prieto, M. J. Duran, A. Gonzalez-Prieto, and J. J. Aciego, "A simple multistep solution for model predictive control in multiphase electric drives," in *IEEE Transactions on Industrial Electronics*, vol. 71, no. 2, pp. 1158–1169, Feb. 2024.

[6] F. Wang, Y. Wei, H. Young, D. Ke, H. Xie, and J. Rodríguez, "Continuous-control-set model-free predictive fundamental current control for PMSM system," in *IEEE Transactions on Power Electronics*, vol. 38, no. 5, pp. 5928–5938, May 2023.

[7] S. Vazquez, J. Rodriguez, M. Rivera, L. G. Franquelo, and M.

Norambuena, "Model predictive control for power converters and drives: advances and trends," in *IEEE Transactions on Industrial Electronics*, vol. 64, no. 2, pp. 935–947, Feb. 2017.

[8] Y. Zhang, J. Jin, and L. Huang, "Model-free predictive current control of PMSM drives based on extended state observer using ultralocal model," in *IEEE Transactions on Industrial Electronics*, vol. 68, no. 2, pp. 993–1003, Feb. 2021.

[9] F. Wang and L. He, "FPGA-based predictive speed control for PMSM system using integral sliding-mode disturbance observer," in *IEEE Transactions on Industrial Electronics*, vol. 68, no. 2, pp. 972–981, Feb. 2021.

[10] X. Liu, L. Qiu, Y. Fang, K. Wang, Y. Li, and J. Rodríguez, "Combining data-driven and event-driven for online learning predictive control in power converters," in *IEEE Transactions on Power Electronics*, vol. 40, no. 1, pp. 563–573, Jan. 2025.

[11] X. Liu, L. Qiu, J. Rodríguez, K. Wang, Y. Li, and Y. Fang, "Learning-based resilient FCS-MPC for power converters under actuator FDI attacks," in *IEEE Transactions on Power Electronics*, vol. 39, no. 10, pp. 12716–12728, Oct. 2024.

[12] D. Jakobeit, M. Schenke, and O. Wallscheid, "Meta-reinforcement-learning-based current control of permanent magnet synchronous motor drives for a wide range of power classes," in *IEEE Transactions on Power Electronics*, vol. 38, no. 7, pp. 8062–8074, Jul. 2023.

[13] X. Liu, L. Qiu, Y. Fang, K. Wang, Y. Li, and J. Rodríguez, "Event-driven based reinforcement learning predictive controller design for three-phase NPC converters using online approximators," in *IEEE Transactions on Power Electronics*, vol. 40, no. 4, pp. 4914–4926, Apr. 2025.

[14] A. Traue, G. Book, W. Kirchgässner, and O. Wallscheid, "Toward a reinforcement learning environment toolbox for intelligent electric motor control," in *IEEE Transactions on Neural Networks and Learning Systems*, vol. 33, no. 3, pp. 919–928, Mar. 2022.

[15] X. Liu, L. Qiu, Y. Fang, K. Wang, Y. Li, and J. Rodríguez, "Predictive control of voltage source inverter: An online reinforcement learning solution," in *IEEE Transactions on Industrial Electronics*, vol. 71, no. 7, pp. 6591–6600, Jul. 2024.

[16] J. Ye, H. Guo, B. Wang, and X. Zhang, "Deep deterministic policy gradient algorithm based reinforcement learning controller for single-inductor multiple-output DC-DC converter," in *IEEE Transactions on Power Electronics*, vol. 39, no. 4, pp. 4078–4090, Apr. 2024.

[17] M. Schenke, W. Kirchgässner, and O. Wallscheid, "Controller design for electrical drives by deep reinforcement learning: A proof of concept," in *IEEE Transactions on Industrial Informatics*, vol. 16, no. 7, pp. 4650–4658, Jul. 2020.

[18] M. Schenke and O. Wallscheid, "A deep Q-learning direct torque controller for permanent magnet synchronous motors," in *IEEE Open Journal of the Industrial Electronics Society*, vol. 2, pp. 388–400, 2021.

[19] Y. Wang, S. Fang, and J. Hu, "Active disturbance rejection control based on deep reinforcement learning of PMSM for more electric aircraft," in *IEEE Transactions on Power Electronics*, vol. 38, no. 1, pp. 406–416, Jan. 2023.

[20] K. Liu, C. Hou, and W. Hua, "A novel inertia identification method and its application in PI controllers of PMSM drives," in *IEEE Access*, vol. 7, pp. 13445–13454, 2019.

[21] T. Lillicrap, J. J. Hunt, A. Pritzel, N. Heess, T. Erez, Y. Tassa, D. Silver, and D. Wierstra, "Continuous control with deep reinforcement learning," in *Computer Science*, pp. 1–14, Sept. 2015.

[22] Y. LeCun, Y. Bengio, and G. Hinton, "Deep learning," in *Nature*, vol. 521, no. 7553, pp. 436–444, May 2015.

[23] X. Liu, L. Qiu, Y. Fang, K. Wang, Y. Li, and J. Rodríguez, "Finite control-set learning predictive control for power converters," in *IEEE Transactions on Industrial Electronics*, vol. 71, no. 7, pp. 8190–8196, Jul. 2024.

[24] Y. Wan, Q. Xu, and T. Dragičević, "Safety-enhanced self-learning for optimal power converter control," in *IEEE Transactions on Industrial Electronics*, vol. 71, no. 11, pp. 15229–15234, Nov. 2024.

[25] M. Abu-Ali, F. Berkel, M. Manderla, S. Reimann, R. Kennel, and M. Abdelrahem, "Deep learning-based long-horizon MPC: robust, high performing, and computationally efficient control for PMSM dives," in *IEEE Transactions on Power Electronics*, vol. 37, no. 10, pp. 12486–12501, Oct. 2022.

[26] C. Cui, T. Yang, Y. Dai, C. Zhang, and Q. Xu, "Implementation of transferring reinforcement learning for DC-DC buck converter control via duty ratio mapping," in *IEEE Transactions on Industrial Electronics*, vol. 70, no. 6, pp. 6141–6150, Jun. 2023.

Xing Liu received the Ph.D. degree in Marine Electric Engineering from Dalian Maritime University, Dalian, China, in 2018. From Dec. 2018 to Jan. 2019, he joined the Key Laboratory of Marine Technology and Control Engineering of the Ministry of Communications at Shanghai Maritime University, Shanghai, China. He is currently a Research Fellow with the College of Electrical Engineering, Zhejiang University, Hangzhou, China. He is also currently a Research Fellow with the State Key Laboratory of Power Transmission Equipment Technology, Chongqing University, Chongqing, China. He is also currently a Research Fellow with the State Key Laboratory of High-Speed Maglev Transportation Technology, Qingdao, China. He is also currently a Visiting Scholar in the area of High-Power Converters and Renewable Energy Generation with the Department of Electrical Engineering, Tsinghua University, Beijing, China. He has authored more than 35 publications, all of which are the first authors, including papers in prestigious journal, such as *IEEE Transactions on Industrial Electronics, IEEE Transactions on Power Electronics, IEEE Transactions on Transportation Electrification, IEEE Transactions on Control Systems Technology, IEEE Transactions on Mechatronics, IEEE Journal of Emerging and Selected Topics in Power Electronics, ISA Transactions,* and *International Journal of Electrical Power & Energy Systems*, et al.

His main research interests include finite control-set model predictive control and data-driven predictive control of power converter control systems with applications in power grids, microgrids, and power electronics converters, cybersecurity of power-electronic-intensive electrical distributions systems and microgrids, and applications of artificial intelligence in industrial power electronics and systems.

Dengyin Jiang received the the Ph.D. degree in Control Theory and Control Engineering from Shanghai Jiao Tong University in 2016. He is currently a Lecturer with the School of Electrical Engineering, Shanghai Dianji University, Shanghai, China. His current research interests include intelligent control of electrical machines, transportation electrification, and secure operation of microgrids.

Chenghao Liu received the B.S. degree in Electrical Engineering from Nanjing Institute of Technology, Nanjing, China, in 2018. He is currently working toward the Ph.D. degree in electrical engineering with Zhejiang University, Hangzhou, China. His research interests include data-driven model predictive control and applications of artificial intelligence in industrial power electronics.

Calculation Method of Coupling Coefficient for Circular Coils with Bilateral Double-Layer Bounded Magnetic Shielding

Pengjie GUI, Zhiyuan LIN, and Zhongqi LI

***Abstract*—The calculation of coupling coefficient between coils is crucial for optimizing the efficiency of wireless power transfer (WPT) systems. For bilateral double-layer bounded magnetic shielding circular coils under horizontal displacement conditions, the accurate calculation of coupling coefficients currently relies mainly on time-consuming large-scale finite element simulations. To address this problem, the coupling model is divided into subregions using boundary conditions, the magnetic vector potential in each region is solved through Maxwell's equations, and a formula for the coupling coefficient of coaxial double-layer bounded magnetically shielded circular coils is derived. Additionally, a double-layer boundary vector-equivalence method is proposed, and the coupling coefficient formula for a circular coil with bilateral double-layer bounded magnetic shielding under horizontal offset is derived using spatial geometric relationships. The reliability of the proposed method is corroborated by the calculated, simulated, and laboratory-obtained values. The errors between calculated and simulated values are not more than 3.95%, and between calculated and laboratory-obtained values are not more than 4.51%, which confirms the accuracy of the proposed method. Furthermore, a significant computational speed advantage is demonstrated by the proposed method compared to simulation.**

***Index Terms*—Coupling coefficients, magnetic vector potential, vector boundary formulation, wireless power transfer.**

I. Introduction

WIRELESS power transfer (WPT) technology has emerged as a disruptive innovation in power electronics, enabling contactless energy transmission through electromagnetic coupling. This breakthrough addresses spatial constraints inherent in conventional wired systems while demonstrating superior performance in operational convenience, deployment flexibility, transmission reliability, and safety assurance. WPT systems have been widely implemented in transportation (electric vehicle charging), aerospace (satellite power systems), medical devices (implantable electronics), and underwater power applications (submarine equipment)[1]–[14]. The expanding applications of WPT technology, particularly in industrial and consumer electronics, have led to the development of diverse system architectures with varying power levels and transmission distances. Multilayer magnetic shielding, which provides superior eddy current suppression compared to single-layer designs, is typically employed to enhance electromagnetic shielding performance and improve coupling capability in WPT systems for different applications. In practical implementations, coil horizontal offset inevitably occurs due to installation tolerances or operational movements. Therefore, developing accurate calculation methods for coupling coefficients in bilateral multilayer shielded circular coils under horizontal offset is crucial for WPT systems, as it directly impacts system efficiency optimization and stability control. These calculation methods serve as fundamental tools for designing high-performance WPT systems with robust misalignment tolerance.

The current coupling coefficient calculation relies on precise mutual inductance estimation. Global research efforts have yielded diverse computational approaches for determining circular coil coupling parameters. When neither the receiver nor the transmitter has magnetic shielding, [15] and [16] apply the Biot-Savart law to compute the mutual inductance under arbitrary coil displacements. This is achieved by calculating the magnetic flux density and performing numerical integration. [17] and [18] propose an elliptic integration computational approach for determining inductive coupling between spatially misaligned circular coils, enhancing both computational speed and accuracy. [19] employs Euler angles to compute the magnetic coupling coefficient between two planar helical coils in arbitrary spatial configurations.

Incorporating magnetic shielding into the coil improves system coupling and reduces interference. For mutual inductance calculation with magnetic shielding, [20] proposed an analytical method using Fourier-Bessel expansion. It derives the mutual

Manuscript received April 21, 2025; revised July 22, 2025; accepted August 19, 2025. Date of publication December 30, 2025; date of current version September 9, 2025. This work was supported in part by Excellent Youth Project of Scientific Research of Hunan Provincial Department of Education under the grant 22B0577, Key Projects of Hunan Provincial Department of Education under the grant 23A0432, National Key R&D Program Project under the grant 2022YFB3403200, National Natural Science Foundation of China (NSFC) Youth Science Fund Project under the grant 62303178, Scientific Research Fund of Hunan Provincial Education Department under the grant 23C0182, and the Natural Science Foundation of Hunan Province under Grants under the grant 2022JJ30226. (*Corresponding author: Zhongqi Li.*)

P. Gui and Z. Lin are both with the School of Transportation and Electrical Engineering, Hunan University of Technology, Zhuzhou 412007, China (e-mail: 2284087484@qq.com; linzhiyuan 19@163.com).

Zhongqi Li is with the School of Transportation and Electrical Engineering, Hunan University of Technology, Zhuzhou 412007, China (e-mail: lizhongqi@hnu.edu.cn).

Digital Object Identifier 10.24295/CPSSTPEA.2025.00031

inductance expression for coaxial and horizontally offset circular coils, assuming the shielding material has infinite extent. [21] derived mutual inductance formulas for double-layer shielded circular coils in arbitrary positions using electric field strength and coordinate transformation. However, the assumption of infinite shielding extent in the horizontal plane limits practical applicability. For bounded magnetic shielding, [22]–[24] developed a truncated region eigenfunction expansion method to compute mutual inductance, expressing it in terms of magnetic vector potential. However, these studies only consider shielding on one side. [25] established a geometric-to-inductance mapping for bilateral bounded shielding coils using magnetic reluctance theory but was limited to coaxial configurations without addressing horizontal offsets. [26] and [27] simplify calculations using a core-less equivalent circuit, but only consider single-layer magnetic media. Similarly, although [28] derives the coupling coefficient under horizontal displacement, its theory is still limited to single-layer media and does not address the modeling of actual multi-layer shielding structures. In summary, for the bilateral multi-layer bounded magnetic shielding circular coil model, this paper proposes a more practical method for calculating the coupling coefficient of two layers.

A coupling model for bilateral double-layer bounded mag-netically shielded circular coils with horizontal offset is established in this paper. First, the model is partitioned into subregions using boundary conditions. The coaxial coupling coefficient is then derived by solving the magnetic vector potential of each subregion via Maxwell's equations. Second, a double-layer boundary vector equivalence method is proposed, and the horizontal-offset coupling coefficient is derived through spatial geometry analysis. Finally, the method is validated through numerical computation, finite-element simulation, and experimental measurement.

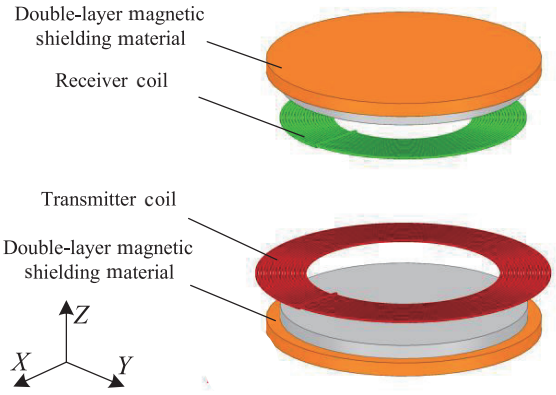

Fig. 1. 3D structure of a circular coil with double-layer magnetic shielding.

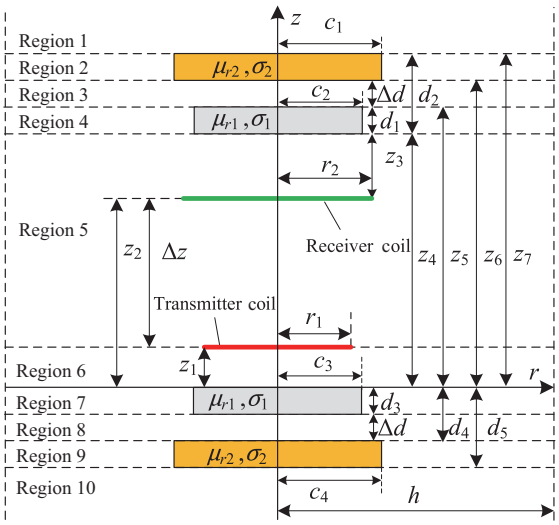

Fig. 2. Cross-section of a circular coil with double-layer magnetic shielding.

II. Calculation of the Coupling Coefficient Between Coaxial Circular Coils

A. Calculation of the Magnetic Vector Potential in Multi-Region Systems

To improve magnetic shielding performance and accommodate various application requirements, a circular coil with bilateral double-layer bounded magnetic shielding is proposed for the wireless energy transmission structure, as illustrated in Fig. 1.

Based on the cross-section of Fig. 1, Fig. 2 shows the modeled cross-section of a bilateral double-layer bounded magnetically shielded circular coil. The model divides into ten distinct regions bounded sequentially by planes at $z = -d_5$, $z = -d_4$, $z = -d_3$, $z = 0$, $z = z_1$, $z = z_4$, $z = z_5$, $z = z_6$, and $z = z_7$. Δz represents the axial offset between coil centers, with r_1 and r_2 denoting the transmitter and receiver radii respectively. The shielding materials have radii c_1, c_2, c_3 and c_4 with uniform thickness, separated by an air gap Δd. The relative permeabilities μ_{r1}, μ_{r2} and conductivities σ_1, σ_2 characterize each shielding layer. h is the hypothetical truncation distance of the magnetic vector potential. The transmitter carries current $Ie^{j\omega t}$, with amplitude I, angular frequency ω and time variation t.

Since both the magnetic shielding material and the coil in this transmission model are circular, this transmission structure has symmetry. Therefore, the magnetic vector potential $\boldsymbol{A}$ has only one component, and the direction of this component is uniformly distributed. Consequently, The electromagnetic field equations formulated in terms of the vector potential $\boldsymbol{A}$ can be simplified:

$$\nabla^2 \boldsymbol{A} = \frac{\partial^2 \boldsymbol{A}}{\partial r^2} + \frac{\partial \boldsymbol{A}}{\partial r}\frac{1}{r} + \frac{\partial^2 \boldsymbol{A}}{\partial z^2} - \frac{\boldsymbol{A}}{r^2} = -\mu J^2 \tag{1}$$

where ∇^2 is the Laplace operator, μ denotes the permeability, and J is the current density. Applying separation of variables to (1) yields the magnetic vector potential $A(r, z)$ satisfying:

$$\boldsymbol{A}(r,z) = \sum_{i=1}^{\infty} [A_o J_1(w_i r) + B_o Y_1(w_i r)](C_o e^{\lambda_i z} + C_o e^{\lambda_i z}) \tag{2}$$

In the above equation, A_o, B_o, C_o, and D_o denote the coefficients of each subregion, where subscript o serves as an index without physical meaning. The parameter w is the eigenvalue, satisfying $w^2 = \eta^2 - jw\mu_0\mu_r\sigma$, where μ_0 is the vacuum permea-

bility, and μ_r and σ are the relative permeability and conductivity of the shielding material. Here, J_1 ($w_i r$) and $Y_1(w_i r)$ represent the first-order Bessel functions J_1 and Y_1 (of the first and second kind, respectively), with i ranging from 1 to ∞ .

Since the magnetic vector potential must maintain finite values, while Y_1 ($w_i r$) diverges at the origin ($r \to 0$), to ensure convergence, the radial magnetic flux density B_s vanishes in regions 1, 3, 5, 6, 8, and 10, where the magnetic vector potential $\boldsymbol{A}(r, z)$ in these regions takes the form:

$$\boldsymbol{A}_1(r,z)=\sum_{i=1}^{\infty} J_1(w_i r) D_1 e^{-w_i z} \tag{3}$$

$$\boldsymbol{A}_3(r,z)=\sum_{i=1}^{\infty} J_1(w_i r)\left(C_3 e^{w_i z}+D_3 e^{-w_i z}\right) \tag{4}$$

$$\boldsymbol{A}_5(r,z)=\sum_{i=1}^{\infty} J_1(w_i r)\left(C_5 e^{w_i z}+D_5 e^{-w_i z}\right) \tag{5}$$

$$\boldsymbol{A}_6(r,z)=\sum_{i=1}^{\infty} J_1(w_i r)\left(C_6 e^{w_i z}+D_6 e^{-w_i z}\right) \tag{6}$$

$$\boldsymbol{A}_8(r,z)=\sum_{i=1}^{\infty} J_1(w_i r)\left(C_8 e^{w_i z}+D_8 e^{-w_i z}\right) \tag{7}$$

$$\boldsymbol{A}_{10}(r,z)=\sum_{i=1}^{\infty} J_1(w_i r) C_{10} e^{w_i z} \tag{8}$$

For eigenvalues w in (3)–(8), that can be determined by imposing the boundary condition that $\boldsymbol{A}$ is zero at the truncation boundary h. The eigenvalues are obtained when the non-exponential component vanishes at the boundary h. Consequently, the magnetic vector potential vanishes when J_1 ($w_i h$) is 0, where J_1 denotes the Bessel function of the first kind.

The inclusion of magnetic shielding materials in regions 2, 4, 7, and 9 introduces additional complexity to the boundary conditions. The domain partitions into air-filled regions and magnetic shielding material regions, where the solution in each subdomain can be expressed using boundary conditions and convergent Bessel function expansions:

$$\boldsymbol{A}_2^{\mathrm{al}}(r,z)=\sum_{i=1}^{\infty} J_1(x_i r)\left(C_2 e^{s_i z}+D_2 e^{-s_i z}\right) \tag{9}$$

$$\boldsymbol{A}_2^{\mathrm{air}}(r,z)=\sum_{i=1}^{\infty} R(s_i r)\left(C_2 e^{s_i z}+D_2 e^{-s_i z}\right) \tag{10}$$

$$\boldsymbol{A}_4^{\mathrm{fer}}(r,z)=\sum_{i=1}^{\infty} J_1(q_i r)\left(C_4 e^{p_i z}+D_4 e^{-p_i z}\right) \tag{11}$$

$$\boldsymbol{A}_4^{\mathrm{air}}(r,z)=\sum_{i=1}^{\infty} R(p_i r)\left(C_4 e^{p_i z}+D_4 e^{-p_i z}\right) \tag{12}$$

$$\boldsymbol{A}_7^{\mathrm{fer}}(r,z)=\sum_{i=1}^{\infty} J_1(q_i r)\left(C_7 e^{p_i z}+D_7 e^{-p_i z}\right) \tag{13}$$

$$\boldsymbol{A}_7^{\mathrm{air}}(r,z)=\sum_{i=1}^{\infty} R(p_i r)\left(C_7 e^{p_i z}+D_7 e^{-p_i z}\right) \tag{14}$$

$$\boldsymbol{A}_9^{\mathrm{al}}(r,z)=\sum_{i=1}^{\infty} J_1(x_i r)\left(C_9 e^{s_i z}+D_9 e^{-s_i z}\right) \tag{15}$$

$$\boldsymbol{A}_9^{\mathrm{air}}(r,z)=\sum_{i=1}^{\infty} R(s_i r)\left(C_9 e^{s_i z}+D_9 e^{-s_i z}\right) \tag{16}$$

where "al" denotes the aluminum plate material, "fer" denotes the ferrite material, and "air" denotes the air medium. q and x are the regional eigenvalues and satisfy $q^2 = p^2 - jw_i\mu_0\mu_{r1}\sigma_1$, $x^2 = s^2 - jw_i\mu_0\mu_{r2}\sigma_2$, $R(p_i r) = A_i J_1(p_i r) + B_i Y_1(p_i r)$, and $R(s_i r) = A_i J_1(s_i r) + B_i Y_1(s_i r)$, where the eigenvalues can be solved using $R(p_i h) = 0$ with $R(s_i h) = 0$.

B. Calculation of Mutual Inductance and Self-Inductance Between Circular Coils

The continuity conditions for normal and tangential components apply to the B-field and H-field of the system alike. Using this condition, the boundary conditions are satisfied as follows when the radius of the magnetic shielding material is r, taking region 2 as an example:

$$J_1(x_i c_1) = A_2 J_1(s_i c_1) + B_2 Y_1(s_i c_1) \tag{17}$$

$$\frac{1}{\mu_{r2}} x_i J_0(x_i c_1) = A_2 s_i J_0(s_i c_1) + B_2 s_i Y_0(s_i c_1) \tag{18}$$

The solution for A_2 and B_2 can be obtained by solving the simultaneous (17) and (18).

$$A_2 = \frac{s_i J_1(x_i c_1) Y_0(s_i c_1) - \frac{1}{\mu_{r2}} x_i J_0(x_i c_1) Y_1(s_i c_1)}{s_i J_1(s_i c_1) Y_0(s_i c_1) - s_i J_0(s_i c_1) Y_1(s_i c_1)} \tag{19}$$

$$B_2 = \frac{\frac{1}{\mu_{r2}} x_i J_0(x_i c_1) J_1(s_i c_1) - s_i J_0(s_i c_1) J_1(x_i c_1)}{s_i J_1(s_i c_1) Y_0(s_i c_1) - s_i J_0(s_i c_1) Y_1(s_i c_1)} \tag{20}$$

Similarly one can find the coefficients A_4, B_4, A_7, B_7, A_9, B_9 in regions 4, 7, 9. Using the boundary conditions between each neighboring region one can obtain the following:

$$\boldsymbol{A}_m(r, z_n) = \boldsymbol{A}_{m+1}(r, z_n) \tag{21}$$

$$\left.\frac{\partial \boldsymbol{A}_m(r,z)}{\partial z}\right|_{z=z_n} - \left.\frac{\partial \boldsymbol{A}_{m+1}(r,z)}{\partial z}\right|_{z=z_n} = -\mu J \tag{22}$$

Due to the presence of Bessel and Neumann functions in the proposed formula, which ensures rapid convergence, an approximation can be obtained by considering only a finite number of terms in the magnetic vector potential series. Taking (3) as an example, when i takes the first n terms, both sides of the equation are multiplied by $J_1(w_i r) \cdot r$, integrating over r from 0 to the truncated region h. Applying the orthogonality of Bessel functions yields the following simplified form:

$$\int_0^h \sum_{i=1}^{\infty} D_1 e^{-k_i z} J_1(w_i r) J_1(w_i r) r \,\mathrm{d}r = \sum_{i=1}^{\infty} \frac{h^2}{2} D_1 e^{-k_i z} J_2(w_i h) \tag{23}$$

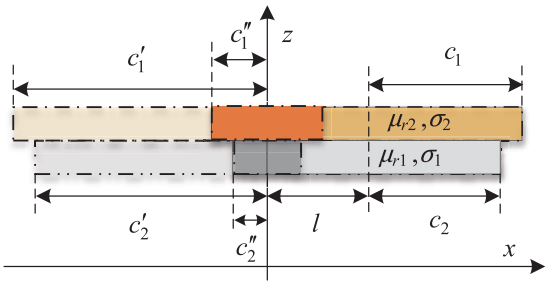

Fig. 3. Schematic cross-section of the two-layer boundary vector equivalence method after horizontal offsetting.

Similarly, the above method can be used to convert (21) and (22) into matrix form. Then, using Cramer's rule, the unknown coefficients $D_1 - D_9$ and $C_2 - C_{10}$ can be obtained. The solution process is shown in the appendix.

To determine the system's mutual inductance, only the magnetic flux through region 5 needs to be considered. The mutual inductance can then be expressed as:

$$M=\frac{2\pi r_2}{I}\sum_{i=1}^{\infty} J_1(wr_2)\left(C_5e^{uz_2}+D_5e^{-uz_2}\right) \tag{24}$$

The self-inductance parameter of the transmitting coil, L_1, and the self-inductance parameter of the receiver coil, L_2, can be calculated by considering identical coil geometries, while the mutual inductance at zero coaxial distance is derived by

$$L_1=\frac{2\pi r_1}{I}\sum_{i=1}^{\infty} J_1(wr_1)\left(C_5e^{uz_1}+D_5e^{-uz_1}\right) \tag{25}$$

$$L_2=\frac{2\pi r_2}{I}\sum_{i=1}^{\infty} J_1(wr_2)\left(C_5e^{uz_2}+D_5e^{-uz_2}\right) \tag{26}$$

The coupling coefficient k is given by (27)

$$k=\frac{M}{\sqrt{L_1\cdot L_2}} \tag{27}$$

III. Calculation of Inter-Coil Coupling Coefficient at Horizontal Offset

For horizontal offset analysis in double-layer magnetic shielding, a boundary vector equivalence method is proposed. Fig. 3 shows the cross-section after offset application, where l denotes the + x-axis offset. The initial radius of the original double-layer magnetic shielding is added and subtracted from the horizontal offset, respectively, and is equivalent to a large double-layer magnetic shielding material and a small double-layer magnetic shielding material. The radii after the equivalence are brought into the original parameters c_1 and c_2 to find the coefficients C_5 and D_5 of region 5.

In Fig. 3, the radius of the coaxial magnetic shielding material after the equivalent c_1' and c_1'', with respect to c_1, can be described by the matrix expression as follows:

$$\begin{bmatrix} c_1' \\ c_1'' \end{bmatrix}=\begin{bmatrix} 1 & -l \\ 1 & l \end{bmatrix}\begin{bmatrix} c_1 \\ 1 \end{bmatrix} \tag{28}$$

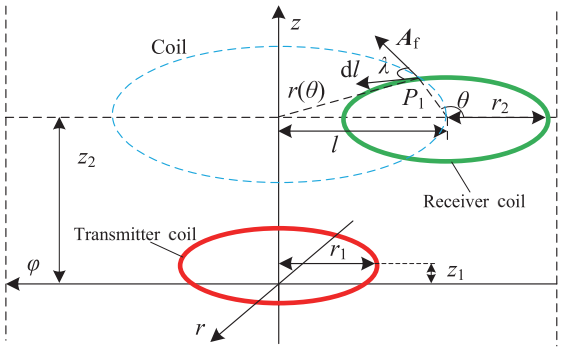

Fig. 4. Receiver coil horizontal offset 3D structural diagram.

To analyze the receiver coil's horizontal offset, Fig. 4 presents the corresponding 3D schematic. The parameter l represents the horizontal offset distance from the z-axis symmetry center. Considering point P_1 on the coil, its differential tangent vector element is denoted dl as its tangent component, and the tangent $\boldsymbol{A}_f$ of the Coil with $r(\theta)$ as the radius is the magnetic vector potential component, and the angle of both of them is λ.

The parametric equations of the receiver coil and coil are established separately as follows:

$$\begin{cases} x_c = r_2\cos\theta \\ y_c = r_2\sin\theta \\ z_c = z_2 \end{cases} \tag{29}$$

$$\begin{cases} x_o = r(\theta)\cos\varphi \\ y_o = r(\theta)\sin\varphi \\ z_o = z_2 \end{cases} \tag{30}$$

When offsetting the receiver coil alters its relative position, the following relationships hold

$$\begin{bmatrix} x_n \\ y_n \\ z_n \end{bmatrix}=\begin{bmatrix} x_c \\ y_c \\ z_c \end{bmatrix}+\begin{bmatrix} l \\ 0 \\ 0 \end{bmatrix} \tag{31}$$

Based on the geometric relationships

$$r(\theta)=\sqrt{x_2^2+y_2^2} \tag{32}$$

The corresponding tangent vectors are obtained by derivatives of θ and φ in (28) and (29), respectively.

$$\begin{cases} \alpha_1=[-r_2\sin\theta, r_2\cos\theta, 0]^{\mathrm{T}} \\ \beta_1=[-r(\theta)\sin\varphi, r(\theta)\cos\varphi, 0]^{\mathrm{T}} \end{cases} \tag{33}$$

Finally, the solution is obtained by substituting the cosine value between the two vectors into (24).

$$M=\frac{\Phi}{I}=\frac{r_2}{I}\int_0^{2\pi}\boldsymbol{A}_5[r(\theta),z_n]\frac{\alpha_1\cdot\beta_1}{|\alpha_1||\beta_1|}\mathrm{d}\theta \tag{34}$$

The horizontal offset coupling coefficient k is calculated by substituting (34), (25), and (26) into (27). Similarly, this meth-

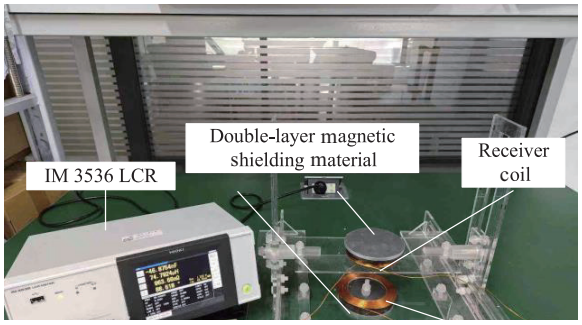

Fig. 5. Experimental setup diagram.

TABLE I
COIL AND MAGNETIC SHIELDING MATERIAL PARAMETERS

Symbol	Parameter	Value
T_1	Transmitter coil turns	17
T_2	Receiver coil turns	18
R_{t0}	Transmitter coil initial radius	35 mm
R_{r0}	Receiver coil initial radius	25 mm
ΔR	Radius change	1.1 mm
z_1	Transmitter coil height	12 mm
z_2	Receiver coil height	22–112 mm
z_3	Receiver side magnetic shielding	13 mm
c_2, c_3	Ferrite material radius	48.5 mm
c_1, c_4	Aluminum plate material radius	50 mm
d	Thickness of magnetic shielding material	5 mm
μ_{r1}	Ferrite relative permeability	2800
σ_1	Ferrite conductivity	0.01 S/m
μ_{r2}	Relative permeability of aluminum plate	1.000021
σ_2	Aluminum plate conductivity	3.8×10^7 S/m

od extends to multi-layer magnetic shielding structures of arbitrary sizes. The proposed calculation method calculates circular planar helical coils as concentric circles with different radii, so there are some minor errors.

IV. SIMULATION AND EXPERIMENTATION

To validate the proposed formula for horizontal-offset coupling coefficients in doubly-bounded magnetically shielded circular coils, simulations are performed using Ansys Maxwell, with results shown in Fig. 1. Experimental measurements use an IM3536 LCR meter at an 85 kHz operating frequency. Formula validity and computational efficiency are verified through comparative analysis of vertical/horizontal offsets and computation time. The experimental configuration appears in Fig. 5.

The mutual inductance measurement principle using an impedance analyzer is that the transmitter coil and receiver coil forward series results in L_1+L_2+2M; reverse series results in L_1+L_2-2M; and the mutual inductance M is determined by

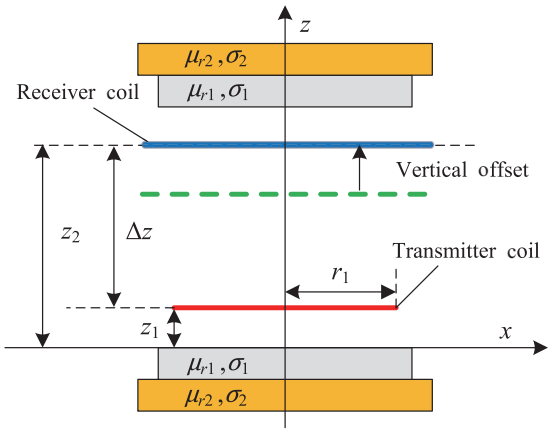

Fig. 6. Schematic of the vertical offset on the receiving side.

the following fundamental relation: $M = (L_1-L_2)/4$. Table I lists the coil and magnetic shielding parameters. For experimental consistency, all shielding materials share identical radius and thickness specifications. Given the negligible air-gap effect in practical operation, we set $\Delta d = 0$ for simulations.

For the purpose of analysis, it is necessary to define the simulation error coefficient ε_1 and the experimental error coefficient ε_2 for the coupling coefficients, as shown in (35) and (36):

$$\varepsilon_1 = \frac{|k_c - k_s|}{k_s} \times 100\% \tag{35}$$

$$\varepsilon_2 = \frac{|k_c - k_e|}{k_e} \times 100\% \tag{36}$$

where k_c, k_s, and k_e represent the calculated, simulated, and experimental coupling coefficients, respectively.

A. Vertical Offset

The receiver side magnetic shielding material and the receiver coil are collectively referred to as the receiver side in this paper, and for the receiver side vertical offset experiment, the receiver coil is set to be vertically offset from $z_2 = 22$ mm along the + z-axis to $z_2 = 112$ mm in steps of 10 mm in sequence, as shown in Fig. 6.

The vertical separation distance on the receiver side is Δz in the figure, and the dashed line is the starting position of the receiver side before the offset. The measured coupling coefficient data and error comparisons for the receiver side vertical offset are shown in Table II. The errors ε_1 of the coupling coefficients of the calculated and simulated values are not greater than 3.95%, and the errors ε_2 of the coupling coefficients of the calculated and experimental values are not greater than 4.51%. The results of the coupling coefficients of the computational results with the numerical simulations and the experimental measurements are in good agreement. Combined with Table II, the calculated, simulated, and experimental coupling coefficients with the vertical distance of the receiver side are established as shown in Fig. 7.

TABLE II
COUPLING COEFFICIENTS AND ERRORS FOR VERTICAL OFFSETS ON THE RECEIVER SIDE

Δz/mm	k_c	k_s	k_e	ε_1/%	ε_2/%
10	0.5823	0.5711	0.5782	1.97	0.71
20	0.3911	0.3796	0.3906	3.05	0.14
30	0.2615	0.2570	0.2585	1.75	1.14
40	0.1766	0.1780	0.1818	0.80	2.90
50	0.1234	0.1262	0.1266	2.26	2.56
60	0.0935	0.0915	0.0912	2.15	2.51
70	0.0651	0.0677	0.0672	3.95	3.16
80	0.0492	0.0511	0.0515	3.83	4.51
90	0.0381	0.0393	0.0388	3.08	1.91
100	0.0303	0.0307	0.0309	1.25	2.12

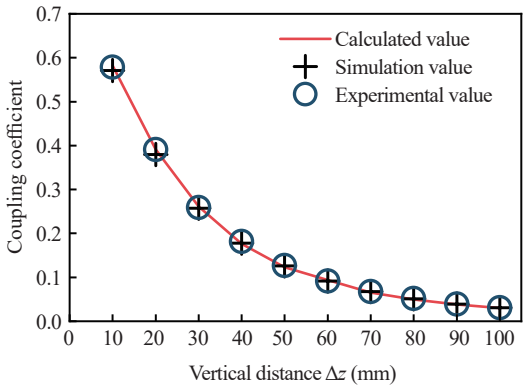

Fig. 7. Vertical offset coupling coefficient variation graph.

Analysis of Fig. 7 reveals that the coupling coefficient gradually decreases as the perpendicular distance between receiver and transmitter coils increases, because the enhanced coil separation progressively reduces their magnetic flux linkage, thereby diminishing the coupling degree.

B. Horizontal Offset

In the horizontal offset experiment on the receiver side, z_2 is set to 72 mm, and the vertical distance (Δz) between the receiver coil and the transmitting coil is 60 mm. The receiver side starts at a horizontal distance l = –50 mm and is offset along the positive x-axis in 10 mm increments up to l = 50 mm. The experimental setup is illustrated in Fig. 8. The measured coupling coefficients and their corresponding errors for horizontal offset are presented in Table III. l denotes the horizontal offset distance.

Analyzing Table III, it can be seen that the errors of both the calculated value coupling coefficients and the simulated value coupling coefficients are not greater than 3.69% at the lateral displacement of the receiver assembly. The error ε_2 between the calculated value coupling coefficient and the experimental value coupling coefficient is not more than 2.51%. The results of calculated values and simulated and experimental values

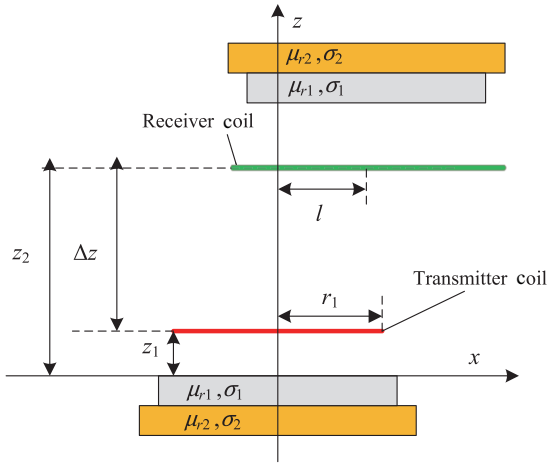

Fig. 8. Schematic diagram of horizontal offset on the receiver side.

TABLE III
COUPLING COEFFICIENTS AND ERRORS AT HORIZONTAL OFFSET ON THE RECEIVING SIDE

l/mm	k_c	k_t	k_s	ε_1/%	ε_2/%
–50	0.0411	0.0423	0.0421	2.86	2.35
–40	0.0565	0.0563	0.0563	0.32	0.25
–30	0.0724	0.0698	0.0738	3.69	1.87
–20	0.0834	0.0812	0.0837	2.69	0.31
–10	0.0916	0.0888	0.0896	3.09	2.26
0	0.0935	0.0915	0.0912	2.15	2.51
10	0.0916	0.0889	0.0903	3.05	1.46
20	0.0834	0.0813	0.0828	2.62	0.73
30	0.0724	0.0699	0.0713	3.57	1.57
40	0.0565	0.0564	0.0556	0.12	1.58
50	0.0411	0.0424	0.0410	3.07	0.25

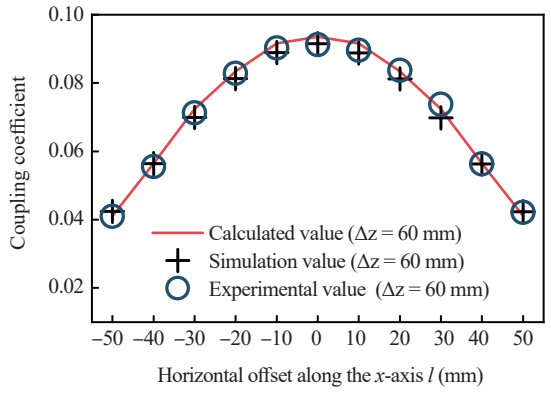

Fig. 9. Plot of variation of horizontal offset coupling coefficient at receiver side.

have good agreement at the lateral displacement of the receiver assembly. Combined with Table III, the variation curves of the coupling coefficients of the calculated, simulated, and experimental values with the horizontal offset of the receiver side are established as shown in Fig. 9.

TABLE IV
COUPLING COEFFICIENTS WHEN THE NUMBER OF TURNS OF THE RECEIVING COIL IS VARIED

N_2	k_c	k_s	k_e	ε_1/%	ε_2/%
14	0.0834	0.0828	0.0842	0.72	−0.95
15	0.0865	0.0851	0.0874	1.65	−1.03
16	0.0885	0.0872	0.0891	1.49	−0.67
17	0.0912	0.0894	0.0904	2.01	0.88
18	0.0935	0.0915	0.0938	2.19	−0.32
19	0.0955	0.0936	0.0942	2.03	1.38
20	0.0974	0.0957	0.0966	1.78	0.83
21	0.0998	0.0977	0.0969	2.15	2.99
22	0.1011	0.0997	0.0983	1.40	2.85
23	0.1045	0.1016	0.1025	2.85	1.95

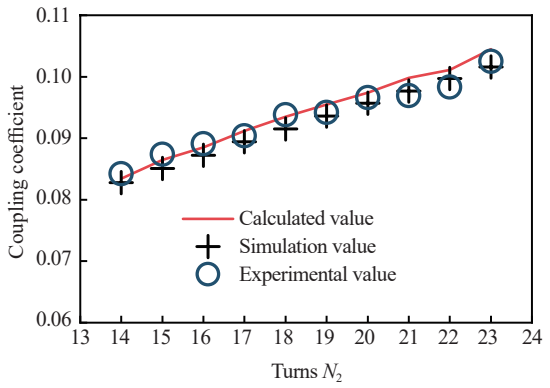

Fig. 10. Coupling coefficient curve when the number of turns of receiver coil changes.

Fig. 9 analysis reveals that at constant vertical height, as the receiver moves left or right along the *x*-axis (with *z* as central axis), the coupling coefficient decreases with increasing distance from the *z*-axis. This occurs because the structure's magnetic flux diminishes radially outward from the center, causing the coupling coefficient to decrease proportionally with horizontal offset distance.

C. Receiver Coil Turns Change

To verify the validity of the method for turn variations, only the receiver side coil turns were varied, keeping other parameters identical to Table I. The receiver side turns (N_2) increased from 14 to 23 in one-turn increments, with coupling coefficients recorded at 50 mm coaxial height, as shown in Table IV. Table IV shows that when the receiver coil turns vary from 14 to 23, the simulation error of the coupling coefficient remains no greater than 2.19% and experimental errors are not greater than 2.80%, validating the calculation method. Based on Table IV data, Fig. 10 plots the calculated, experimental, and simulated coupling coefficients versus turn count varia- tions.

TABLE V
COUPLING COEFFICIENTS WHEN THE NUMBER OF TURNS OF THE RECEIVER COIL IS VARIED

Δz/mm	t_a/s	t_b/s	l/mm	t_c/s	t_d/s	N_2	t_a/s	t_b/s
10	300	2.7777	−50	268	2.3827	14	209	2.2645
20	294	2.7737	−40	278	2.9921	15	230	2.2832
30	295	2.8111	−30	287	2.8100	16	254	2.3711
40	278	2.8956	−20	284	2.9646	17	278	2.4647
50	266	2.6279	−10	266	2.9646	18	304	2.5044
60	282	2.8171	0	304	2.7282	19	326	2.6362
70	304	2.8262	10	258	2.8922	20	361	2.6656
80	309	2.7725	20	286	2.6042	21	387	2.7422
90	286	2.7689	30	271	2.6494	22	401	2.8163
100	288	2.7952	40	282	2.5862	23	424	2.8940
110	281	2.7235	50	266	2.2565	24	440	2.9630

D. Comparison of Computation and Simulation Speed

This paper proposes an integrated computational model for systematically comparing the performance between Matlab programs and Ansys Maxwell simulations in electromagnetic system analysis. The study focuses on evaluating the coupling coefficients of bilateral double-layer magnetically shielded horizontally offset circular coil structures. Under identical hardware conditions (excluding Maxwell's initial modeling time), rigorous tests were conducted to ensure fair comparison. As shown in Table V, significant differences in computational efficiency were observed between the two approaches. The investigation examined three key variables. vertical offset distance, horizontal offset displacement, and receiver coil turns variation. Multiple trials were performed and average computation times were recorded to ensure statistical reliability.

Table V shows the Ansys Maxwell simulation averages 289.4 s for vertical offset, compared to 2.78 s for the Matlab program. Horizontal offset simulations average 278.4 s (Maxwell) versus 2.75 s (Matlab). Per additional coil turn, Maxwell requires 20.9 s versus 0.06 s of Matlab, demonstrating our method's substantial speed advantage.

E. Comparison of Domestic and International Calculation Methods

The proposed boundary vector equivalence method achieves superior performance in horizontal offset coupling coefficient calculation, demonstrating a maximum error of 4.51%. Table VI presents comparative results with existing methods from literature.

The abbreviations and acronyms presented in the table are explicitly defined and explained as follows: DTD stands for different transmission distances, HO represents horizontal offset, FMS denotes bounded magnetic medium, DS indicates that the magnetic medium demonstrates bilateral symmetry characteristics, and ERR signifies the maximum allowable computational error percentage.

TABLE VI
COUPLING COEFFICIENTS WHEN THE NUMBER OF TURNS OF THE RECEIVING COIL IS VARIED

Literatures	Methodologies	DTD	HO	FMS	DS	ERR
[20]	The Fourier-Bessel	√	√	×	√	/
[21]	Coordinate transformation	√	√	√	×	4.78%
[23]	Truncated zoning	√	√	√	×	4.76%
[24]	Space boundary vector	√	√	√	×	3.26%
[25]	Theory of magnetic circuit	×	×	√	√	8.13%
This work	Boundary vector equivalence	√	√	√	√	4.51%

V. CONCLUSION

This paper addresses the coupling coefficient calculation for horizontally offset circular coils with bilateral double-layer bounded magnetic shielding. The model divides the coupling region into subdomains by boundary characteristics and solves the magnetic vector potential of each region using Maxwell's equations and employs a double-layer boundary vector equivalence method to calculate magnetic shielding material offsets. Combined with spatial geometric relations, this enables coupling coefficient calculation for horizontally offset coils. The validity of the method is confirmed through calculated, simulated, and experimental results. Calculation errors remain below 3.95% versus simulations and 4.51% versus experiments. These results fully validate the proposed method for horizontal-offset bilateral double-layer shielded circular coils. Speed comparisons demonstrate the significant computational advantage of the method. The formulation provides crucial theoretical support for optimizing horizontal-offset bilateral double-layer shielded coil transmission structures. It also facilitates future research on coupling coefficients for multi-layer shielded coils at arbitrary positions.

APPENDIX

Cramer's Rule Implementation: By applying the boundary condition relations given in (21) and (22), we obtain the system of equations for the unknown variables:

$$\boldsymbol{S}=\boldsymbol{U}^{-1}\cdot\boldsymbol{I} \tag{37}$$

where $\boldsymbol{U}$ is an 18×18 boundary condition matrix, $\boldsymbol{S}$ is an 18×1 column vector of unknowns, and $\boldsymbol{I}$ is an 18×1 source term column vector. Take the boundary conditions of the first region as an example:

$$\boldsymbol{A}_1(r,z)\big|_{z=z_7}=\boldsymbol{A}_2(r,z)\big|_{z=z_7} \tag{38}$$

$$\frac{\partial \boldsymbol{A}_1}{\partial z}\bigg|_{z=z_7}=\frac{\partial \boldsymbol{A}_2}{\partial z}\frac{1}{\mu_{r2}}\bigg|_{z=z_7} \tag{39}$$

The boundary conditions for regions 2 to 10 are solved in the same way. The boundary condition matrix is as follows:

$$\begin{cases}\boldsymbol{U}_1=[-Ge^{s_i z_7}\ \cdots\ 0\ \ Ee^{-w_i z_7}\ -Ge^{-s_i z_7}\ \cdots\ 0\ \ 0]\\ \boldsymbol{U}_2=[-Nse^{s_i z_7}\ \cdots\ 0\ -Ewe^{-w_i z_7}\ \ Ne^{-s_i z_7}\ \cdots\ 0\ \ 0]\\ \boldsymbol{U}_3=[Ge^{s_i z_6}\ -Ee^{w_i z_6}\ \cdots\ 0\ \ Ge^{-s_i z_6}\ \ -Ee^{-w_i z_6}\ \cdots\ 0]\\ \vdots\\ \boldsymbol{U}_{15}=[0\ \cdots\ Ee^{w_i d_4}-Ge^{s_i d_4}\ \cdots\ 0\ \ Ee^{-w_i d_4}\ \ -Ge^{-s_i d_4}]\\ \boldsymbol{U}_{16}=[0\ \cdots\ Ewe^{w_i d_4}-Nse^{s_i d_4}\ \cdots\ 0\ -Ewe^{-w_i d_4}\ Nse^{-s_i d_4}]\\ \boldsymbol{U}_{17}=[0\ \ 0\ \cdots\ Ge^{s_i d_5}\ \ -Ee^{w_i d_5}\ \ \cdots\ \ 0\ \ Ge^{-s_i d_5}]\\ \boldsymbol{U}_{18}=[0\ \ 0\ \cdots\ Nse^{s_i d_5}\ \ -Ewe^{w_i d_5}\ \cdots\ 0\ -Nse^{-s_i d_5}]\end{cases} \tag{40}$$

$$\boldsymbol{S}=[C_2\ \ C_3\ \ \cdots\ \ C_9\ \ C_{10}\ \ D_1\ \ D_2\ \ \cdots\ \ D_8\ \ D_9]^{\mathrm{T}} \tag{41}$$

$$\boldsymbol{I}=\left[0\ \ 0\ \ \cdots\ \ \frac{-\mu_0 I\delta(r-r_0)J_1(w^{\mathrm{T}}r)}{E}\cdots\ 0\ \ 0\right]^{\mathrm{T}} \tag{42}$$

where E, G, N, U, and V represent nth-order diagonal matrices, with the explicit expressions for E, G, and N given below, and U and V following analogously to G and N.

$$E=\int_0^h J_1(w_i r)J_1(w_j r)r\mathrm{d}r=\delta\frac{[J_0(w_i h)]^2}{2} \tag{43}$$

$$G=\int_0^c J_1(s_i r)J_1(q_j r)r\mathrm{d}r+\int_c^h J_1(s_i r)R_1(p_j r)r\mathrm{d}r \tag{44}$$

$$N=\frac{1}{\mu_r}\int_0^c J_1(s_i r)J_1(q_j r)r\mathrm{d}r+\int_c^h J_1(s_i r)R_1(p_j r)r\mathrm{d}r \tag{45}$$

ACKNOWLEDGMENTS

This work was supported in part by the Natural Science Foundation of Hunan Province under Grants 2022JJ30226, National Key R&D Program Project (2022YFB3403200), Key Projects of Hunan Provincial Department of Education (23A0432), and in part by Excellent Youth Project of Scientific Research of Hunan Provincial Department of Education (22B0577), National Natural Science Foundation of China (NSFC) Youth Science Fund Project (62303178), and A Project Supported by Scientific Research Fund of Hunan Provincial Education Department (23C0182).

REFERENCES

[1] S. Y. R. Hui, "Past, present and future trends of non-radiative wireless power transfer," in *CPSS Transactions on Power Electronics and Applications*, vol. 1, no. 1, pp. 83–91, Dec. 2016.

[2] Y. Zhang, S. Chen, X. Li, and Y. Tang, "Design of high-power static wireless power transfer via magnetic induction: An overview," in *CPSS Transactions on Power Electronics and Applications*, vol. 6, no. 4, pp. 281–297, Dec. 2021.

[3] E. Abramov, I. Zeltser, and M. M. Peretz, "A network-based approach for modeling resonant capacitive wireless power transfer systems," in *CPSS Transactions on Power Electronics and Applications*, vol. 4, no. 1, pp. 19–29, Mar. 2019.

[4] Z. Li, Z. Chen, M. Yang, Y. Cheng, X. Xiong, and S. Huang, "Design of edge-enhanced coil structure to obtain constant mutual inductance with horizontal misalignment in wireless power transfer systems of electric vehicles," in *CPSS Transactions on Power Electronics and Applications*, vol. 9, no. 2, pp. 141–151, Jun. 2024.

[5] C. Liao, J. Li, and S. Li, "Design of lcc impedance matching circuit for wireless power transfer system under rectifier load," in *CPSS*

Transactions on Power Electronics and Applications, vol. 2, no. 3, pp. 237–245, Sept. 2017.

[6] Z. Li, W. Zhang, Z. Gan, and B. Li, "Study on composite structure of tian-font magnetic shielding and anti-series active coils for wireless power transfer system," in *CPSS Transactions on Power Electronics and Applications,* vol. 10, no. 1, pp. 97–109, Mar. 2025.

[7] A. Harhouz, D. Aissaoui, A. Chaabane, and M. Benaissa, "Highly efficient wireless power transfer systems for implantable medical devices," in *Proceedings of 2024 International Conference on Telecommunications and Intelligent Systems (ICTIS)*, Dec. 2024, pp. 1–4.

[8] C. Park, J. Park, Y. Shin, J. Kim, S. Huh, D. Kim, S. Park, and S. Ahn, "Separated circular capacitive coupler for reducing cross coupling capacitance in drone wireless power transfer system," in *IEEE Transactions on Microwave Theory and Techniques*, vol. 68, no. 9, pp. 3978–3985, Sept. 2020.

[9] X. Yi, W. Zheng, H. Cao, S. Wang, X. Feng, and Z. Yang, "Wireless power transmission for implantable medical devices using focused ultrasound and a miniaturized 1-3 piezoelectric composite receiving transducer," in *IEEE Transactions on Ultrasonics, Ferroelectrics, and Frequency Control*, vol. 68, no. 12, pp. 3592–3598, Dec. 2021.

[10] Z. Cheng, Y. Lei, K. Song, and C. Zhu, "Design and loss analysis of loosely coupled transformer for an underwater high-power inductive power transfer system," in *IEEE Transactions on Magnetics*, vol. 51, no. 7, pp. 1–10, Jul. 2015.

[11] Y. Yao and M. Nekovee, "Efficiency-enhanced holographic metasurface for wireless power transfer based in electric vehicles," in *IEEE Antennas and Wireless Propagation Letters*, vol. 24, no. 2, pp. 299–303, Feb. 2025.

[12] C. Da, F. Li, M. Nie, S. Li, C. Tao, and L. Wang, "Undersea capacitive coupled simultaneous wireless power and data transfer for multiload applications," in *IEEE Transactions on Power Electronics*, vol. 40, no. 1, pp. 2630–2642, Jan. 2025.

[13] D. Ferdous, S. Saha, and R. Ray, "A resonance based inductive wireless power transfer system for charging autonomous underwater vehicle (auv) batteries," in *Proceedings of 2024 International Conference on Electrical Electronics and Computing Technologies (ICEECT)*, vol. 1, Aug. 2024, pp. 1–6.

[14] V. Ramakrishnan, D. Savio A, M. Shorfuzzaman, and W. Mohammed Abdelfattah, "An enhanced vehicle-to-vehicle wireless power transfer system for electric vehicle applications using a reconfigurable coil approach," in *IEEE Access*, vol. 13, pp. 9931–9941, 2025.

[15] E. Yıldırız and S. B. Kemer, "Novel semi-analytical method for mutual inductance calculation of the thin spiral disk coils," in *IET Electric Power Applications*, vol. 13, pp. 1607–1612, 2019. [Online]. Available: https://digital-library.theiet.org/doi/abs/10.1049/iet-epa.2019.0206

[16] K.-H. Song, J. Feng, R. Zhao, and X.-L. Wu, "A general mutual inductance formula for parallel non-coaxial circular coils," in *The Applied Computational Electromagnetics Society Journal (ACES)*, pp. 1385–1390, 2019.

[17] Y.-L. Lyu, F.-Y. Meng, G.-H. Yang, B.-J. Che, Q. Wu, L. Sun, D. Erni, and J. L.-W. Li, "A method of using nonidentical resonant coils for frequency splitting elimination in wireless power transfer," in *IEEE Transactions on Power Electronics*, vol. 30, no. 11, pp. 6097–6107, Nov. 2015.

[18] S. Babic, F. Sirois, C. Akyel, G. Lemarquand, V. Lemarquand, and R. Ravaud, "New formulas for mutual inductance and axial magnetic force between a thin wall solenoid and a thick circular coil of rectangular cross-section," in *IEEE Transactions on Magnetics*, vol. 47, no. 8, pp. 2034–2044, Aug. 2011.

[19] H. Tavakkoli, E. Abbaspour-Sani, A. Khalilzadegan, A.-M. Abazari, and G. Rezazadeh, "Mutual inductance calculation between two coaxial planar spiral coils with an arbitrary number of sides," in *Microelectronics Journal*, vol. 85, pp. 98–108, 2019.

[20] Z. Luo and X. Wei, "Analysis of square and circular planar spiral coils in wireless power transfer system for electric vehicles," in *IEEE Transactions on Industrial Electronics*, vol. 65, no. 1, pp. 331–341, 2018.

[21] X. Zhang, C. Quan, and Z. Li, "Mutual inductance calculation of circular coils for an arbitrary position with electromagnetic shielding in wireless power transfer systems," in *IEEE Transactions on Transportation Electrification*, vol. 7, no. 3, pp. 1196–1204, Sept. 2021.

[22] Z. Dong, X. Li, S. Liu, Z. Xu, and L. Yang, "A novel all-direction antimisalignment wireless power transfer system designed by truncated region eigenfunction expansion method," in *IEEE Transactions on Power Electronics*, vol. 36, no. 11, pp. 12456–12467, Nov. 2021.

[23] J. Yi, P. Yang, Z. Li, P. Kong, and J. Li, "Mutual inductance calculation of circular coils for an arbitrary position with a finite magnetic core in wireless power transfer systems," in *IEEE Transactions on Transportation Electrification*, vol. 9, no. 1, pp. 1950–1959, Mar. 2023.

[24] Z. Lin, Z. Li, C. Hu, Z. Chen, and S. Huang, "Mutual inductance calculation method of arbitrarily positioned circular coils with convex ring type finite magnetic shielding in wireless power transfer," in *Transactions of China Electrotechnical Society*, vol. 39, no. 16, pp. 4918–4930, 2024.

[25] Y. Chen, K. Chen, S. Zheng, Y. Jiang, L. Yuan, and Z. Zhao, "Analytical modeling method for inductance of planar magnetic coupler in wireless power transfer," in *Proceedings of the CSEE*, vol. 43, no. 4, pp. 1504–1517, 2023.

[26] S. Dong, B. Wei, and B. Song, "An extensively applicable equivalent air gap method for mutual inductance calculation between coils with finite magnetic cores in wpt systems," in *IEEE Journal of Emerging and Selected Topics in Power Electronics*, vol. 13, no. 3, pp. 3966–3975, Jun. 2025.

[27] Y. Wu, Y. Jiang, Y. Li, H. Yuan, X. Wang, and Y. Tang, "Precise parameterized modeling of coil inductance in wireless power transfer systems," in *IEEE Transactions on Power Electronics*, vol. 39, no. 9, pp. 11746–11757, Sept. 2024.

[28] Z. Chen, Z. Li, M. Lyu, Z. Lin, and J. Li, "Coupling coefficient calculation method of circular coil with bilateral finite magnetic shields cat horizontal misalignment in wireless power transfer systems," in *International Journal of Circuit Theory and Applications*, vol. 53, no. 1, pp. 101–118, 2025.

Pengjie Gui was born in China in 2003. He received a bachelor's degree in electrical engineering and automation from Changsha University, Changsha, China, in 2017. He is currently working toward the master's degree in electronic information with Hunan University of Technology. His current research interests include wireless power transfer systems.

Zhiyuan Lin was born in China in 1996. He received the bachelor's degree in electronic information engineering from Hubei University of Technology Engineering and Technology College, Wuhan, China, in 2015, and the master's degree in electronic information from Hunan University of Technology in 2024. His current research interests include wireless power transfer systems.

Zhongqi Li was born in China in 1985. He received the M.Sc. degree from Hunan University of Technology, China, in 2012, and the Ph.D. degree from Hunan University in 2016. From 2016, he been working as an assistant professor at Hunan University of Technology, China. From 2020, he is now working as a postdoctoral fellow at Hunan University. His research interests include wireless power transfer systems and soft-switching power converters.

Minimizing Power Loss of Hybrid Quadra Tied Solar PV Arrays Using Cuckoo Search MPPT Algorithm During Shading Scenarios

Abhinav BHATTACHARJEE and Suresh MIKKILI

***Abstract*—This study assists in selecting the appropriate solar photovoltaic (SPV) array configuration and metaheuristic maximum power point tracking (MPPT) technique to minimise power loss in rooftop SPV systems resulting from partial shading conditions (PSCs) caused by tall adjacent buildings in urban environments. A hybrid SPV array configuration, termed alternate – quadra tied – cross tied (A-QT-CT), that integrates quadra tied (QT) and total cross tied (TCT) configurations is proposed. This configuration is designed to provide maximum power extraction comparable to the best performing TCT configuration, while incorporating a reduced number of cross-links. Simulations were conducted utilising MATLAB to evaluate the performance of these configurations in the context of typical PSCs found in urban environments. This evaluation includes a comparative analysis with the established TCT, series-parallel (SP), bridge linked – TCT (BL-TCT), and SP-TCT configurations. The proposed configurations are integrated with Perturb & Observe (P&O), Cuckoo Search (CS), and Particle Swarm Optimisation (PSO) MPPT techniques. These algorithms were evaluated under PSCs using MATLAB simulations, as well as a hardware model implemented with the Texas Instruments TMS320F28379D microcontroller. The time required to track the MPP and the steady-state MPPT efficiency are assessed. The combination of the CS MPPT method with A-QT-CT and TCT configurations has been identified as the optimal solution for minimising power loss in this application.**

***Index Terms*—Alternate – quadra tied – cross tied, Cuckoo Search, hybrid PV array configuration, maximum power point tracking, partial shading, Particle Swarm Optimization, quadra tied, total cross tied.**

I. Introduction

THE primary variable influencing the power output of a solar photovoltaic (SPV) system is solar insolation (G), measured in Watts per square meter (W/m^2). This research work aims to address the issue of changing solar insolation and its impact on the power output from SPV systems. The occurrence of partial shading on the SPV array impacts insolation levels and significantly reduces the power output generated by the array. In many instances, partial shading can be mitigated by carefully selecting the installation site of the SPV array. However, in densely populated urban environments, it is becoming progressively challenging to eliminate the shading effect caused by adjacent tall buildings. This research work focusses on minimising power loss in rooftop SPV arrays, which is attributed to partial shading from adjacent tall buildings.

The initial strategy investigated by researchers to alleviate the negative impacts of partial shading conditions (PSCs) involves the configuration design of the SPV array. The primary parameter to consider when developing SPV array configurations is the necessity for achieving the highest global maximum power point (GMPP) across the range of potential PSCs that may be encountered. The secondary and tertiary considerations include the necessity for a minimal number of interconnections or cross-links to optimise conductor material usage and reduce wiring complexity, as well as maintaining a minimal number of local maximum power points (LMPP) in the power-voltage (P-V) curve when addressing PSCs. Table I presents an overview of recent advancements in the development of SPV array configurations. It has been observed that a majority of papers have not addressed specific applications in the selection of PSCs. In certain instances, generalisations have been made based on the degree of shading on the array, while the shading pattern has been overlooked. This represents a research gap that we aim to address in our application.

The second approach to mitigate the adverse effects of partial shading in recent times involves the reconfiguration of SPV arrays. A comprehensive review of recent reconfiguration techniques available in the literature is presented in [1] and [2]. Static reconfiguration techniques demonstrate superior power extraction capabilities compared to conventional SPV array configurations. However, the additional wiring requirements and associated complexity render them impractical for large arrays. Conversely, dynamic reconfiguration, which theoretically maximises power extraction, is often not favoured in practical applications due to the necessity for a significant number of switches, along with the resulting switching and conduction losses, as well as the costs linked to additional components.

The final component in optimising power extraction from SPV arrays involves the implementation of maximum

Manuscript received April 23, 2025; revised June 28, 2025 and August 8, 2025; accepted August 24, 2025. Date of publication December 30, 2025; date of current version September 9, 2025. *(Corresponding author: Suresh Mikkili.)*

Both authors are with the Electrical & Electronics Engineering Department, National Institute of Technology, Goa 403703, India (e-mail: abhinavbhattacharjee@yahoo.com; mikkili.suresh@nitgoa.ac.in).

Digital Object Identifier 10.24295/CPSSTPEA.2025.00032

TABLE I
LITERATURE REVIEW OF SPV ARRAY CONFIGURATIONS

No.	Research contribution/Outcome	Highlights/Observations/Research gaps
[3] [4]	The TCT configuration offers the highest maximum power extraction on average over a wide range of PSCs.	TCT is used as a benchmark for comparing the performance of all other SPV array configurations.
[5]	6×6 Benzene configuration is proposed that has 20 cross-links compared to 25 cross-links of an equivalent sized TCT SPV array while extracting maximum power in the same range as the latter.	Testing is done under very light shading conditions which are different from those encountered in urban areas in the real world.
[6]	7×7 Triple Tied array is proposed which has 33% less cross links compared to an equivalent size TCT array. Maximum power extracted is also always lesser than TCT.	Shading conditions chosen are not suitable for urban areas.
[7]	A 9×9 triple tied-cross linked (TT-CL) SPV array is tested which offers maximum power extraction second only to TCT.	The connection pattern of the array is not applicable for arrays smaller than 9×9.
[8]	Comprehensive performance analysis of 6x6 basic SPV array configurations - Series (S), Parallel (P), SP, BL, HC, TCT and hybrid configurations formed out of these namely SP-CT, BL-CT, HC-CT, SP-TCT, BL-TCT, HC-TCT, BL-HC.	SP-TCT, BL-TCT, HC-TCT, BL-HC hybrid configurations described here don't have a symmetrical design. Therefore, their performance will vary for the same kind of shade shape depending on location of the shade on the array.
[9]	9×9 conventional and hybrid configurations based on SP, BL, and TCT are examined under different PSCs caused by neighbouring buildings and clouds. It is shown that in cases where the percentage of partial shading is less than 30%, the SP configuration extracts maximum power from the array while in case of partial shading above 30%, the TCT configuration extracts maximum power from the array.	The research work doesn't consider the critical significance of shadow pattern in determining maximum power extraction from the array. Generalizing the perform ance of the configuration based on percentage of shading doesn't always work.
[10]	Mounting panels in a landscape orientation in the array can improve power extraction compared to portrait orientation as losses due to accumulation of dirt on the modules is reduced.	Can be applied to all the SPV array configurations.

TABLE II
LITERATURE REVIEW OF MPPT TECHNIQUES

No.	Research contribution/Outcome	Highlights/Observations/Research gaps
[11]	MPSO-MPC method is developed where INC method is aided by PSO in searching for the global peak. It is shown to perform better than PSO and CS algorithms.	Experimental analysis is done with only 2 series connected SPV modules. Performance with PSCs having multiple LMPPs is not known.
[12]	A modified P&O algorithm is proposed which scans the current-voltage (I-V) curve of the SPV array to determine likely location of the global peak to begin search for the GMPP. It has been implemented using a buck-boost converter and is shown to track MPP faster than PSO, Jaya and Ajaya MPPT techniques.	Analysis done with 4×2 SPV array. Its performance with large arrays is unknown as the algorithm requires high computational capabilities.
[13]	MPSO-HALS method is developed, where the PSO method is modified to initialize an evenly distributed population along the P-V curve. The population is further partitioned to choose the best half for global and local search. Adaptive step sizes are also introduced to improve search speed while reducing oscillations in the steady state thus combining the benefits of the P&O and PSO methods on which it is based.	The P-V curves used for experimentation are created using only 2 SPV modules, thus performance with large arrays having multiple LMPPs is not known.
[14]	A deep study of the PSO technique is done using pole-zero analysis for varying value of tuning constants. Further, a technique to find the convex area of the P-V curve is developed which aids the GMPP search.	Testing is done with P-V curves having up to 2 distinct peaks. The performance of the algorithm with large arrays having multiple LMPPs in close proximity is unknown as it requires high computational capabilities.
[15]	A hermite interpolation based strategy is proposed and shown to perform better than PSO and INC methods.	The algorithm is tested under PSCs with only 3 series connected SPV modules. The performance of the MPPT algorithm with large arrays having multiple LMPPs is therefore unknown as the algorithm requires high computational capabilities.
[16]	An ant colony optimization (ACO) and FL combined approach to MPPT called AFO is presented, and its performance is compared with ACO, FL and PSO.	The P-V curves are chosen randomly to mimic PSCs. The performance of the MPPT algorithm with large arrays having multiple LMPPs in close proximity is unknown.
[17]	Salp swarm algorithm (SSA) based MPPT is proposed and compared with hill climbing, butterfly optimization algorithm (BOA), grasshopper optimization algorithm (GOA), grey wolf optimization (GWO) and PSO.	Testing is done with 4×3 SPV array in simulation and 4×1 SPV array experimentally. The performance of the MPPT algorithm with large arrays having multiple LMPPs in close proximity is unknown.
[18]	An algorithm that tracks MPP using mathematical equations instead of search-based approach is developed.	The method's performance with large arrays where determining mathematical equations to represent the PV array voltage and current is complex is not known.
[19]	A real time deterministic peak hopping MPPT algorithm is developed and tested with complex PSCs having 5 or more peaks. Performance has been compared with intelligent-GWO, improved team game optimization (ITGA), SSA, modified deterministic Jaya (DM-JAYA) and MPSO-HALS algorithms.	The paper provides useful insight into the performance of multiple recent MPPT algorithms under complex PSCs having multiple peaks.
[20]	Rat swarm optimization (RSO) technique incorporated with PSC detection technique is designed to trigger RSO only when PSC is detected and MPP is detected under uniform shading conditions (USC) analytically.	The method used for detecting MPP under USC is susceptible to change in system parameters due to temperature variation and would need re-calibration. The PSC detection technique can be incorporated with any MPPT algorithm.

power point tracking (MPPT) algorithms, which ensure that the operating point of the SPV array aligns with the GMPP. Conventional strategies, including Perturb & Observe (P&O), incremental conductance (INC), and hill climbing, are straight forward to implement and enable rapid tracking of the MPP. However, these methods often become trapped at LMPPs.

In contrast, metaheuristic algorithms, which draw inspiration from various natural phenomena, are capable of tracking the GMPP under PSCs, although they exhibit slower convergence rates compared to the aforementioned techniques. A literature review of recent MPPT techniques proposed by researchers to address the PSC problem is provided in Table II. Some strategies involve hybrid methods where a combination of metaheuristic and conventional strategies are used to leverage the strengths of each individual strategy. It is observed that in most of the recent research work, testing has been done by using only a few PV modules which provide a limited scope to test the algorithms on multiple P-V curves with a high number of LMPPs as encountered in our chosen application. This is another gap which we have tried to address in our testing where the simulations and experimental tests have been both performed using a moderately large sized 8×8 SPV array.

The MPPT algorithms chosen for analysis are the P&O, CS and Particle Swarm Optimisation (PSO). The P&O algorithm is the simplest and most used MPPT method. The CS algorithm has been shown in literature to give good results for continuous optimization problems such as MPPT under PSCs [21], [22]. The PSO is one of the oldest metaheuristic algorithms and can be extensively modified to be adapted to a wide range of problems. The P&O and PSO serve as a benchmark to compare the performance of the CS algorithm. Hybrid algorithms mentioned in literature review have been avoided as it is intended to be able to run the algorithms reliably on a basic microcontroller without needing large processing capability.

Thus, the work done in this paper is presented in the following subsections: Section II features the modelling of PSCs encountered in urban areas. The modeling of the SPV array configurations is provided in Section III. Section IV illustrates the P-V and I-V curves obtained when the SPV array configurations encounter PSCs. Section V explains the working of the metaheuristic MPPT algorithms analyzed. Section VI has experimental tests performed to assess the MPPT algorithms. Section VII provides concluding remarks on the findings of the research.

II. PSCs Encountered and Their Modelling

On observing the shadow patterns caused due to buildings which are largely rectangular, it is evident that most of the shadows are rectangular, triangular or in between the two in the form of a trapezium. The shadows interchange between these shapes as the time of the day and day of the year change. We also notice many instances of random shaped shading which may be caused due to some fixtures being installed on the buildings, accumulation of dirt or debris on the modules, and clouds. Therefore, we have modeled the PSCs based on these cases as illustrated in Fig. 1. Three different random shading cases are chosen, with 'Random 1' representing light shading, 'Random 2' representing moderately heavy shading and 'Random 3' illustrating very heavy shading with one side being more heavily shaded than the other. The three random shading cases are also used to simulate progressive increase in shading on the array due to the motion of clouds using dynamic MPPT tests discussed in Section VI. An 8×8 sized SPV array is chosen for analysis considering the area available on the rooftop of a moderately sized apartment or office complex.

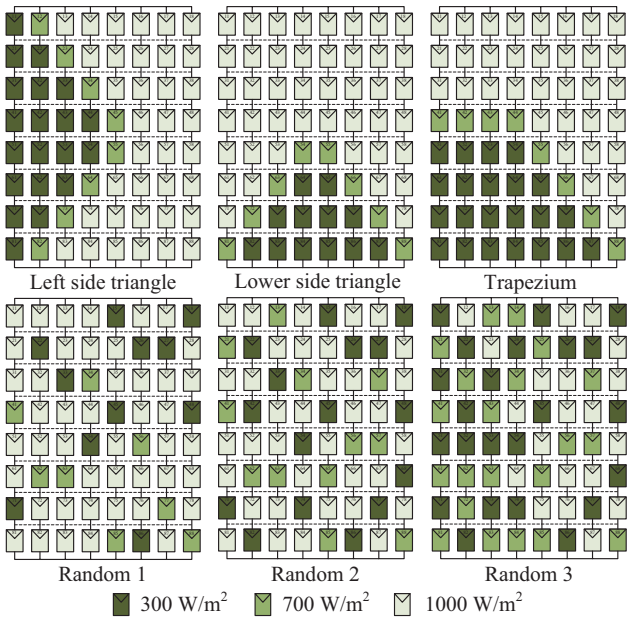

Fig. 1. Modelling of PSCs encountered in urban areas.

III. SPV Array Configurations Analyzed

This research work proposes a hybrid 8×8 SPV array configuration designated as alternate-quarda tied-cross tied (A-QT-CT). The configuration comprises alternating rows featuring Quadra tied connections, which are interspersed with rows that include a total cross link. The performance is evaluated in comparison to the quarda tied (QT) and total cross tied (TCT) configurations that serve as its foundation. The most commonly utilised series-parallel (SP) configuration has also been incorporated. SP configuration necessitates minimal conductor material due to the absence of cross-links, making it the simplest option for wiring and the most cost-effective. It experiences significant power loss under distributed shading conditions because there are insufficient parallel paths for current flow. The TCT configuration features cross-links between each module in the array, necessitating the highest amount of conductor material. The system delivers optimal performance across a diverse array of PSCs, demonstrating particular efficacy in scenarios involving random pattern PSCs. This effectiveness is attributed to the multiple current pathways it facilitates for current flow. Two other hybrid configurations, SP-TCT and bridge linked-TCT (BL-TCT) have also been analyzed to gauge the performance of the A-QT-CT configuration.

Fig. 2 depicts a general 8×8 SPV array configuration with

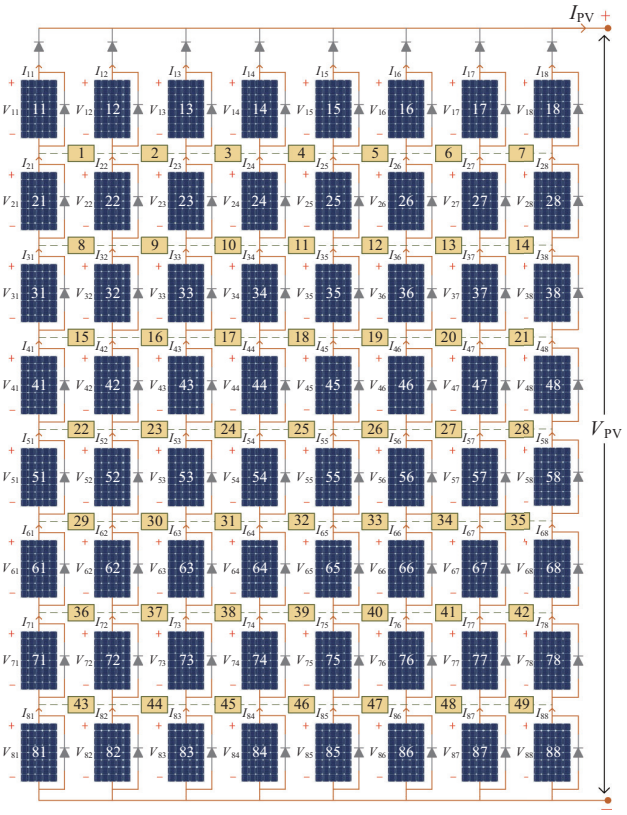

Fig. 2. Illustration of cross-link numbers in SPV arrays.

numbers allotted to every cross-link. The cross-link numbers which are present in each configuration along with the total number of cross-links are provided in Table III. The output voltage (V_{PV}) and current (I_{PV}) of the 8×8 SPV arrays are given in (1) where '*i*' and '*j*' stand for the row number and the column number of SPV array as per Fig. 2. The power output of the array (P_{PV}) is given by the product of V_{PV} and I_{PV}.

$$V_{PV} = \sum_{i=1}^{8} V_{i8}; \quad I_{PV} = \sum_{j=1}^{8} I_{1j} \tag{1}$$

IV. Testing of SPV Array Configurations Under PSCs

The theoretical approach to analysing the impact of PSCs on the P-V and I-V curves of a SPV array is notably complex for big arrays. The analysis of a 2×2 TCT layout under PSCs is presented in [23]. The number and positioning of LMPPs can be ascertained through the voltage and current equations derived. It has been noted that, even for a minimum-sized 2×2 array, the equations governing output voltage and current are large, resulting in increased complexity for a solution. Consequently, simulating the SPV arrays under PSCs represents a superior method that yields precise results. The PV module used in the array is Waaree Energies WSM-315 whose parameters are given as follows: max power (P_M) = 315 W, open circuit voltage (V_{OC}) = 43 V, short circuit current (I_{SC}) = 9.77 A, MPP voltage (V_M) = 35 V, MPP current (I_M) = 9 A. An 8×8 array made with this module produces 20.2 kW

TABLE III
Cross-Link Details of SPV Array Configurations

Configuration	Cross-link number present with reference to Fig. 2	Total number of cross-links
SP	–	0
TCT	1–49	49
SP-TCT	8–14, 22–28, 36–42	21
BL-TCT	2, 4, 6, 8–14, 16, 18, 20, 22–28, 30, 32, 34, 36–42, 44, 46, 48	33
QT	1–3, 5–7, 9–11, 13–14, 15, 17–19, 21, 22–23, 25–27, 29–31, 33–35, 37–39, 41–42, 43, 45–47, 49	37
A-QT-CT	1–3, 5–14, 16–18, 20–29, 31–33, 35–44, 46–48	42

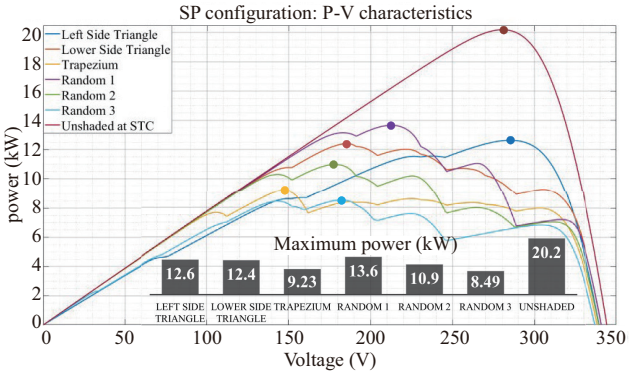

Fig. 3. P-V curves and P_M for SP array under PSCs.

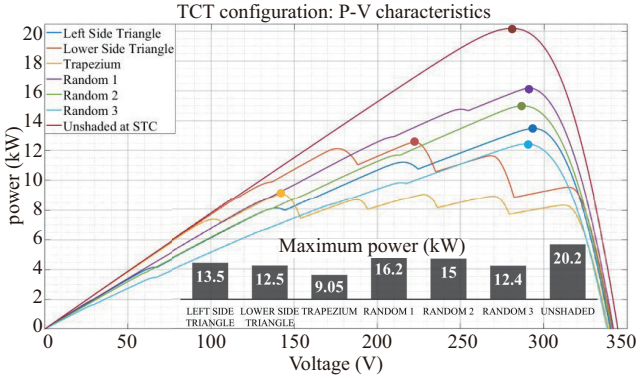

Fig. 4. P-V curves and P_M for TCT array under PSCs.

of maximum power under STC. The reason for choosing this module is that it is quite commonly used in rooftop installations and it is to be noted that the research results obtained in this paper are independent of the type of PV module being used. In this section, the P-V curves obtained by simulation using MATLAB for the SP, TCT, SP-TCT, BL-TCT, QT and A-QT-CT configurations under every PSC and unshaded condition are presented in Figs. 3–8 respectively. The maximum power extracted (P_M) under each case is also marked and mentioned in the above figures.

The analysis of P-V characteristics obtained under various PSCs confirms the enhanced performance of the TCT

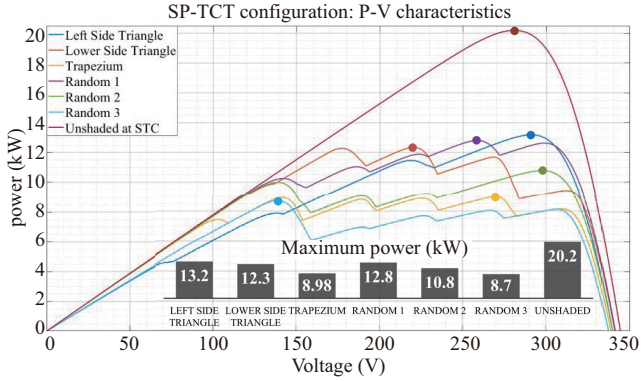

Fig. 5. P-V curves and P_M for SP-TCT array under PSCs.

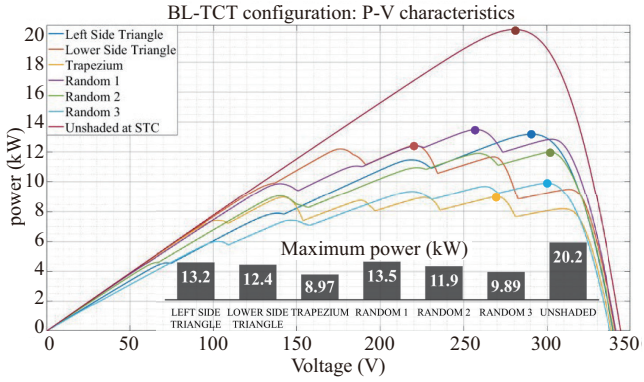

Fig. 6. P-V curves and P_M for BL-TCT array under PSCs.

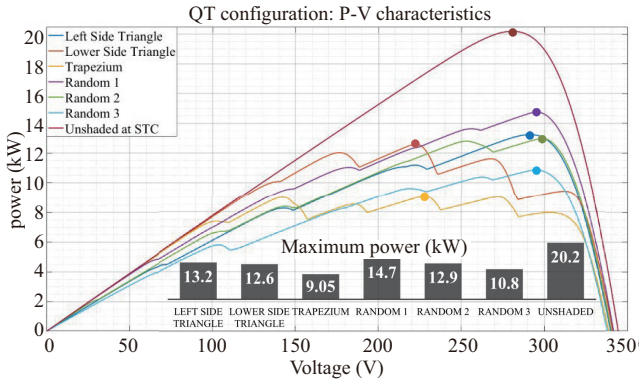

Fig. 7. P-V curves and P_M for QT array under PSCs.

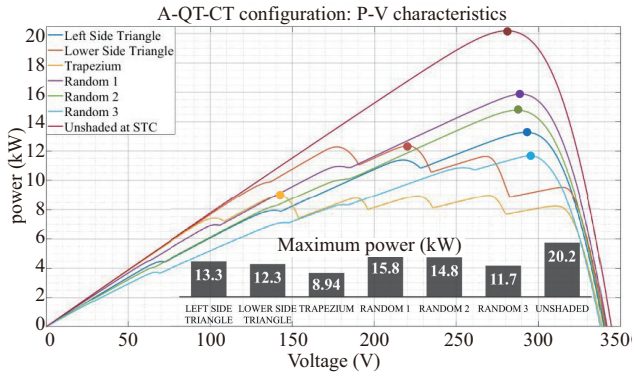

Fig. 8. P-V curves and P_M for A-QT-CT array under PSCs.

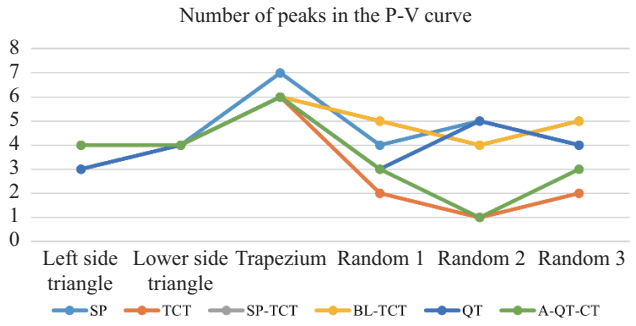

Fig. 9. Illustration of number of peaks in the P-V curves.

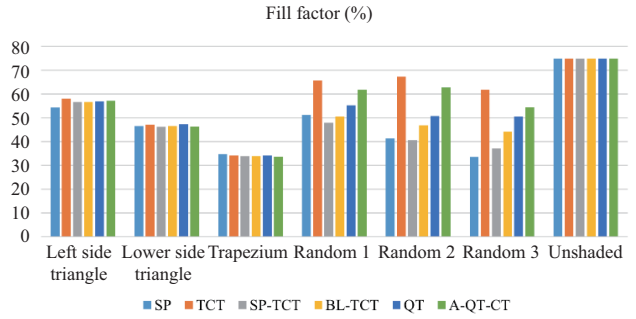

Fig. 10. Fill factor of the arrays under PSCs.

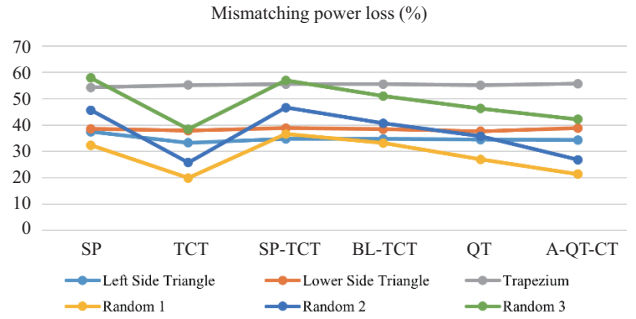

Fig. 11. Mismatching power loss of the arrays under PSCs.

configuration as it has an average P_M under PSCs of 13.12 kW while the A-QT-CT is second best with 12.82 kW. The remaining configurations in descending order of average P_M extraction are QT, BL-TCT, SP and SP-TCT with 12.25, 11.66, 11.23 and 11.13 kW, respectively. From Fig. 9 it can be observed that both TCT and A-QT-CT have the least number of peaks in the P-V curve under PSCs. These two configurations also have the highest fill factor and least mismatching power loss under PSCs as observed in Figs. 10 and 11. The A-QT-CT array also has 7 less cross-links than TCT for an 8×8 sized array which compensates for its slightly inferior performance compared to TCT. Therefore, these two configurations are chosen for analysis in Section VI to test the MPPT algorithms under the same PSCs and test the real-world power extraction capability of the combination.

V. Overview of the CS and PSO MPPT Techniques

We have considered two metaheuristics based MPPT algo-

rithms for comparison – CS and PSO, and P&O algorithm serves as a base to evaluate them.

The algorithms are also incorporated with an adjustable dwell time delay which can be used to adjust the speed of the duty cycle update process based on the limitations of system to get accurate tracking under all circumstances. This dwell time delay is not used in the software simulations but for the hardware tests, the duty cycle update process is made around 15 times slower than in the simulations by adjusting the dwell time to deal with the slow response of the system. The CS and PSO algorithms also check for change in irradiance in the array and restart the search for GMPP whenever PPV changes by 4% or above between successive measurements. This ensures the algorithms can track GMPP under dynamically changing PSCs, illustrated further in Section VI. The reason for choosing 4% as a threshold is that it provides an ideal balance between reacting to irradiance change and ensuring accurate tracking of GMPP without oscillation.

A. Cuckoo Search (CS) MPPT Technique

The CS optimisation method was developed based on the reproductive strategy of brood parasitism observed in cuckoo birds, which involves depositing their eggs in the nests of other host birds [24]. Cuckoos exhibit a strategic approach in selecting the timing for egg-laying, ensuring that their eggs hatch before those of the host bird. Upon hatching, cuckoos remove a portion of the host bird's eggs to increase the probability of their offspring obtaining sustenance. Host birds frequently identify and remove the eggs laid by cuckoos.

Identifying a suitable host bird's nest is critical for the reproductive strategy of the cuckoo. Fruit flies employ a sequence of linear flight trajectories, interspersed with abrupt 90° turns, to navigate their environment [25]. This flight pattern, referred to as Lévy flight is utilised by cuckoos for the purpose of identifying suitable nests for egg-laying. When used for MPPT, the mathematical representation of this process indicates that new solutions, denoted as 'd_{i+1}', are generated by cuckoos, as outlined in (2) [26].

$$d_{i+1}^{k} = d_{i}^{k} + \alpha \oplus Lévy(\lambda) \tag{2}$$

In this, 'd_i^k' represents the duty cycle sample, 'k' indicates the sample number, 'i' denotes the iteration number, 'α' signifies the positive step size selected by the designer, and '$\oplus$' indicates that 'α' is multiplied with each sample individually. A Lévy flight is mathematically characterised as a random walk where the step sizes are derived from the Lévy distribution, following a power law as described in (3), with 'l' representing the flight length and 'λ' denoting the variance, lying within the range $1 < \lambda < 3$. The process consists of numerous small steps and occasional significant leaps, attributable to the characteristics of the Lévy distribution. Extended jumps can significantly enhance the search efficiency of CS in particular contexts relative to other meta-heuristic algorithms.

$$Lévy(\lambda) \approx y = l^{-\lambda} \tag{3}$$

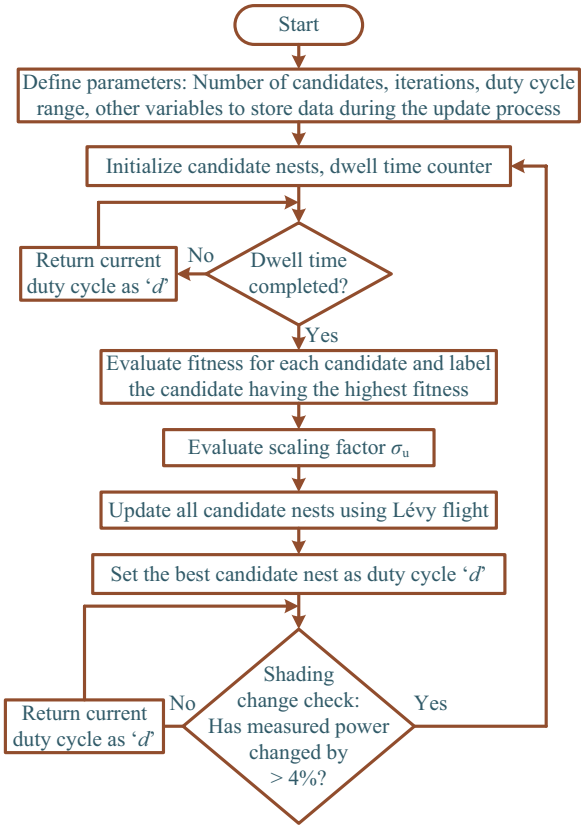

Fig. 12. Flow chart illustrating the CS MPPT algorithm.

The objective here is to optimise the fitness function, represented by the power output of the PV array calculated as the product of 'V_{pv}' and 'I_{pv}', through the selection of the optimal duty cycle 'd' for the DC-DC converter. (2) can be effectively applied as outlined in (4). The step size coefficient 'α' is set at 0.8, while 'β' is established at 1.5 after performing robustness analysis as discussed in Section VI.

$$d_{i+1}^{k} = d_{i}^{k} + \alpha \times \frac{|u|}{|v|^{1/\beta}} \times (d_{best} - d_{i}^{k}) \tag{4}$$

In the above equation, 'u' and 'v' are matrices having uniform distribution given by (5). 'σ_u' is defined by (6) and $\sigma_v = 1$. 'Γ' denotes the gamma operator.

$$\begin{cases} u \approx N(0, \sigma_u^2) \\ v \approx N(0, \sigma_v^2) \end{cases} \tag{5}$$

$$\sigma_u = \frac{\Gamma(1+\beta) \times \sin(\pi \times \frac{\beta}{2})}{\Gamma(\frac{1+\beta}{2}) \times \beta \times 2^{(\beta-1)/2}} \tag{6}$$

The execution of the CS algorithm for MPPT, as illustrated in Fig. 12, involves a procedure for selecting a nest that is comparable to identifying the optimal duty cycle for power maximisation. Four duty cycle values are initially selected from the search space. The fitness function value is utilised to eliminate the least effective duty cycles based on a specified

probability, determined by the condition that random number $r \in (0,1) > 0.25$ in this instance. This process is similar to the method of randomly destroying nests and eliminating eggs, while a new duty cycle is selected using the Lévy flight function. The procedure is performed in an iterative manner for a total of 20 iterations until the optimal duty cycle for maximising the SPV array power is determined.

B. PSO MPPT Technique

The PSO algorithm simulates the behaviour of a flock of birds in pursuit of an optimal food source [27], [28].

Each bird symbolises a solution, specifically the optimal duty cycle in this context. The location of an individual bird within a ock is influenced by the optimal bird in its immediate vicinity, referred to as 'P_{best}', as well as the most favourable solution identified by the entire flock, known as 'G_{best}'.When used for MPPT, the position of a bird is replaced by duty cycle and is updated by (7), where d_i^{t+1} is the updated duty cycle while d_i^t is the previous duty cycle. δ_i^{t+1} is the perturbation (δ) in current duty cycle. 'i' denotes the order number of the bird while 't' denotes the iteration number.

$$d_i^{t+1} = d_i^t + \delta_i^{t+1} \tag{7}$$

The updated perturbation in duty cycle is given by (8).

$$\delta_i^{t+1} = \omega\delta_i^t + c_1 r_1 (P_{best} - d_i^t) + c_2 r_2 (G_{best} - d_i^t) \tag{8}$$

where, 'ω' is inertia weight while 'c_1' and 'c_2' are the individual and social coefficients, taken as 1.0 and 1.2 respectively, after performing robustness analysis as discussed in Section VI. 'r_1' and 'r_2' are random numbers between 0 and 1. The inertia weight 'ω' is linearly decreased from 0.9 to 0.2 with every iteration 't' as given in (9). 'T' denotes the maximum iteration number.

$$\omega^t = \omega_{max} - \frac{t}{T}(\omega_{max} - \omega_{min}) \tag{9}$$

The flowchart of the PSO algorithm used to track MPP is illustrated in Fig. 13.

VI. Experimental Results

In this section, the two best performing SPV array configurations from Section IV – A-QT-CT and TCT are tested with P&O, CS and PSO MPPT methods under the six PSCs. Initially, simulations are performed using MATLAB where both SPV arrays are sequentially subjected to each PSC for 1 s before transitioning to the next. The parameters analyzed are MPPT efficiency, steady state oscillations and the time taken to achieve convergence. This is a better way to judge the performance of the MPPT algorithms' suitability for real world conditions than just measuring the time taken to converge under each PSC from a zero initial state as the results in the latter could vary if the values chosen for the initial variables are changed to suit every PSC. Fig. 14 provides the waveforms for the dynamic MPPT test for the A-QT-CT configuration.

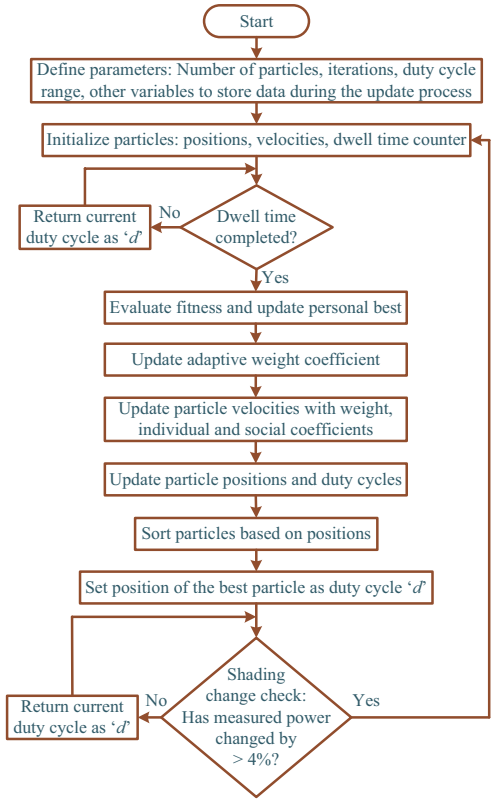

Fig. 13. Flowchart illustrating the PSO MPPT algorithm.

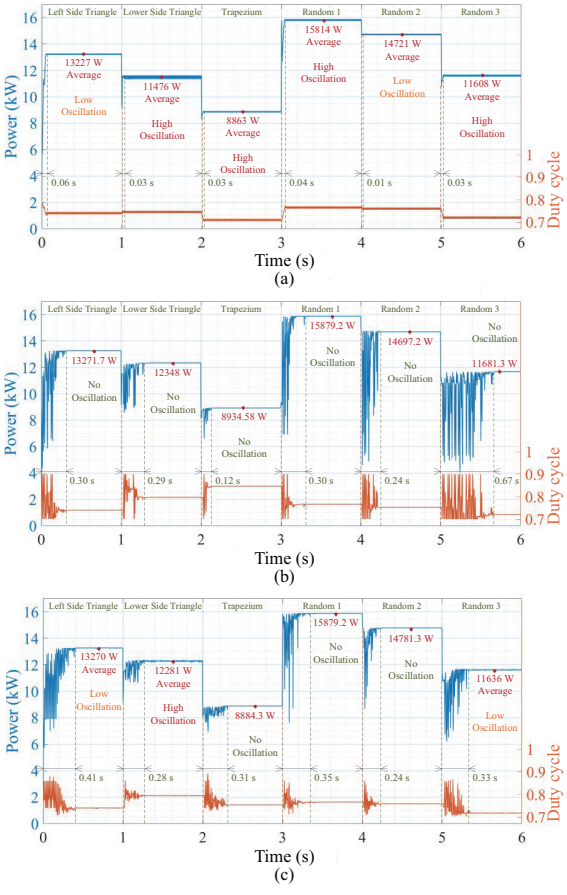

Fig. 14. Dynamic shading analysis of (a) P&O, (b) CS, and (c) PSO MPPT algorithms with A-QT-CT configuration.

TABLE IV
AVERAGE STEADY STATE MPPT EFFICIENCY (η) AND TIME TO TRACK MPP (T) – A-QT-CT CONFIGURATION (SIMULATION)

MPPT →	P&O		CS		PSO	
PSC ↓	η / %	T / s	η / %	T / s	η / %	T / s
Left side triangle	99.63	0.06	99.96	0.3	99.95	0.41
Lower side triangle	92.92	0.03	99.98	0.29	99.44	0.28
Trapezium	99.04	0.03	99.84	0.12	99.28	0.31
Random 1	99.55	0.04	99.96	0.3	99.96	0.35
Random 2	99.56	0.01	99.4	0.24	99.97	0.24
Random 3	99.34	0.03	99.97	0.67	99.58	0.33
Average	98.34	0.033	99.85	0.32	99.69	0.32

TABLE V
AVERAGE STEADY STATE MPPT EFFICIENCY AND TIME TO TRACK MPP – TCT CONFIGURATION (SIMULATION)

MPPT →	P&O		CS		PSO	
PSC ↓	η / %	T / s	η / %	T / s	η / %	T / s
Left side triangle	99.36	0.07	99.98	0.31	99.66	0.4
Lower side triangle	91.52	0.03	96.42	0.36	99.93	0.3
Trapezium	97.57	0.03	99.6	0.15	99.47	0.78
Random 1	99.18	0.06	99.98	0.29	99.79	0.4
Random 2	99.62	0.01	99.99	0.37	98.66	0.41
Random 3	99.62	0.02	99.95	0.16	99.93	0.85
Average	97.81	0.036	99.32	0.27	99.57	0.52

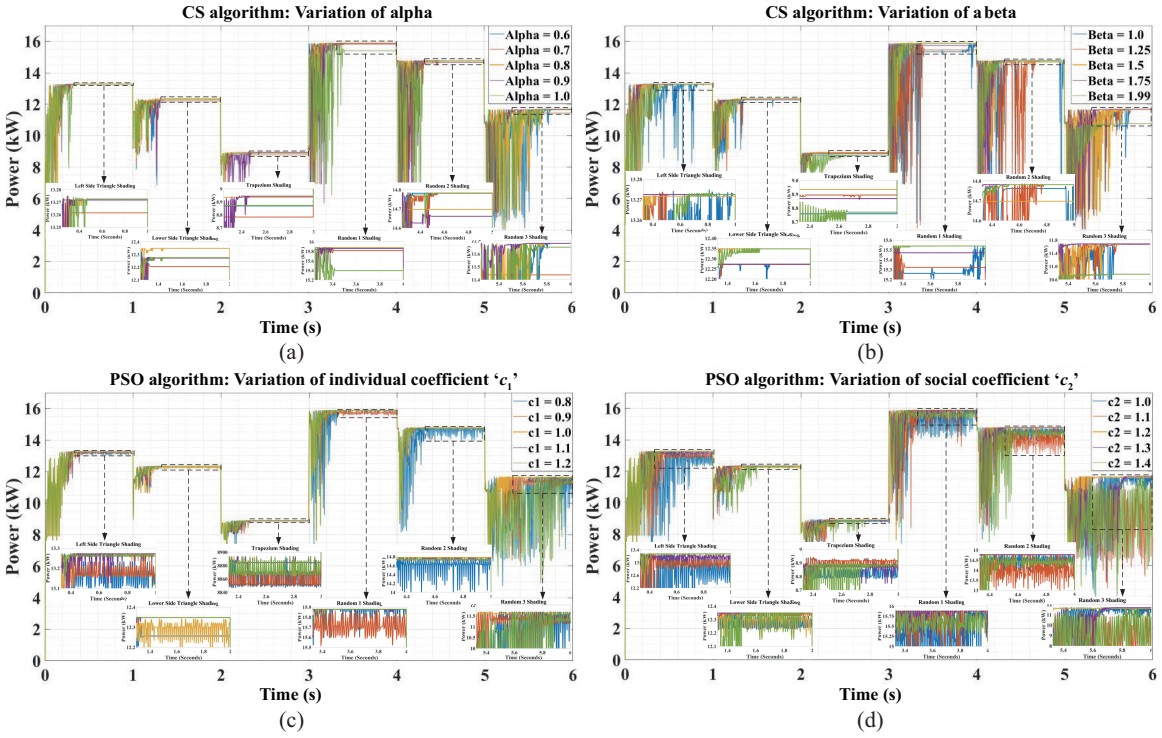

Fig. 15. Robustness analysis for the CS algorithm by varying (a) α, and (b) β, and the PSO algorithm by varying (c) c_1 and (d) c_2.

The maximum power tracked once convergence is achieved is labelled along with the quantum of oscillations present in the steady state. From this test, MPPT efficiency and time taken to converge for each new PSC case is determined and tabulated in Table IV. The same test is conducted for the TCT configuration and the results obtained are tabulated in Table V. It is observed that the CS algorithm performs the best in these tests as it shows no oscillation in the operating point once convergence is achieved while its tracking efficiency is the highest with the A-QT-CT configuration and slightly less than the PSO algorithm for the TCT configuration. The P&O algorithm is by far the fastest to converge, however it does get stuck at LMPP under one of the PSCs and shows continuous oscillation in the operating point even on convergence and as a result it has the least MPPT efficiency. The PSO method has a lower MPPT efficiency than the CS method for the A-QT-CT configuration while bettering the CS method's efficiency when tested with the TCT configuration. However, with the TCT configuration, the PSO algorithm shows heavy oscillation under Random 2 PSC. The PSO algorithm is also the slowest overall to converge to MPP.

Fig. 15 illustrates the robustness analysis of the tuning parameters chosen for the CS and PSO algorithms for the given system. Robustness analysis is performed by repeating the dynamic MPPT test with the A-QT-CT configuration while varying the tuning parameters of the CS algorithm - α and β, and PSO algorithm - c_1 and c_2. The results for the most optimum choice of parameters in all the cases are given in yellow and it is observed that these parameters offer a combination of high MPP, faster tracking and minimum steady state oscillations. For the CS algorithm, the optimum value of α is 0.8 and test results are provided in Fig. 15(a) for values

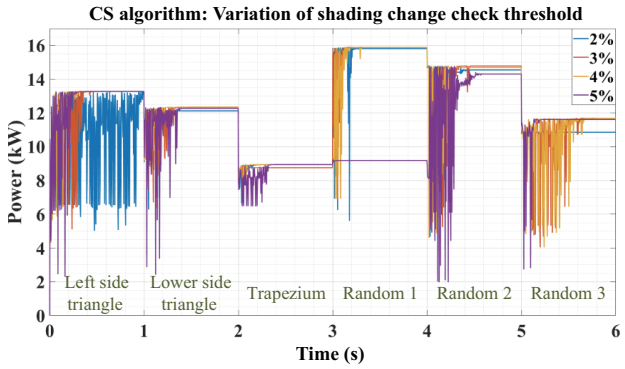

Fig. 16. Effect of varying the shading change check threshold.

of α ranging from 0.6 to 1 while keeping β constant at 1.5. Similarly, in Fig. 15(b), the test is repeated keeping α constant at 0.8 while β values are changed from 1.0 to 1.99. β = 1.5 gives the best results here and it is observed that performance significantly degrades for values of α and β outside these ranges. At β = 2.0, the algorithm fails to converge, hence the selection of β = 1.99 as the upper limit. Similarly, in Fig. 15(c) and (d), the dynamic MPPT test is carried out for different values of c_1 and c_2 respectively in the PSO algorithm. The parameters chosen here are kept the same while testing with the TCT configuration as well. This provides further validation of the robustness of the chosen parameters under different conditions. It is also noted that the performance of the PSO algorithm is more sensitive to parameter changes compared to the CS algorithm.

Another important factor is the setting of the shading change check threshold in CS and PSO algorithms. The effect of changing this threshold to restart the MPPT search which using the dynamic MPPT test for the CS algorithm is illustrated in Fig. 16, when significant shading change leading to change in PV array power is detected. Similar results are obtained with the PSO algorithm as well. It is observed that setting a low threshold of 2% leads to increased oscillation and non-convergence or slower convergence under some PSCs, as even minor oscillations in the PV power lead to restarting of the search process, while setting a high threshold of 5% leads to the algorithm not restarting the search process even under significant change in irradiation, as seen in the transition from trapezium to random 1 PSC. Therefore, in our application, a threshold value of 4% is chosen as it offers the best results while 3% can also be considered as the results are close.

The MPPT test is then performed using an experimental hardware model to evaluate real-world performance. The P-V curves generated by the SPV array configurations under PSCs are replicated utilising the Chroma Solar PV simulator model 62050H-600S. The MPPT algorithm is executed on the Texas Instruments TMS320F28379D microcontroller. Fig. 17 illustrates the experimental setup.

Two factors are evaluated to assess the performance of the MPPT algorithms. The initial metric is the MPPT efficiency over a duration of one minute, which serves as an indicator of the proximity of the operating point to the GMPP during

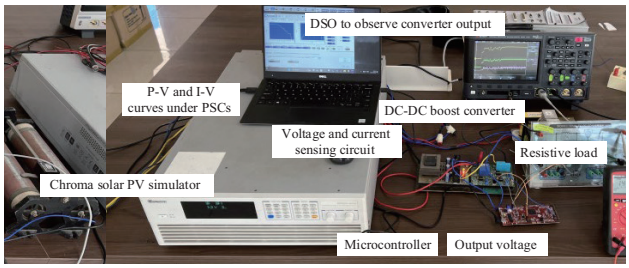

Fig. 17. Experimental setup for MPPT test.

steady-state operation. The steady state oscillation around the MPP is also taken into account in this metric. The second point of consideration is the duration required for the algorithm to reach the MPP. To ensure the MPPT test closely resembles real-world conditions, the dimensions of the SPV array and PSCs are maintained consistent with those utilised in the simulations conducted in Section IV. The power is reduced by a factor of 75 as a result of the hardware components' power limitations. The tests maintain the shape and number of peaks in the P-V curve while solely reducing the power level, thereby offering an accurate representation of the MPPT algorithm's performance in real-world conditions. These tests are performed five times for each configuration under each PSC to account for the randomness in the metaheuristic algorithms and the resulting change in results on every run. The average steady state MPPT efficiency and time taken to track MPP over 5 runs for the A-QT-CT configuration and TCT configuration are presented in Tables VI and VII respectively. It is observed that the MPPT efficiency of P&O algorithm is significantly lower in the hardware tests than in the dynamic MPPT tests in simulations. This is because the hardware tests have been conducted for each PSC separately. Therefore, the operating point often gets stuck at the first LMPP that it encounters as it starts scanning the P-V curve. In the simulations, the PSCs are sequentially applied one after the other and therefore the GMPP is tracked more often. In certain transitions, for example, from left side triangle to lower side triangle, where there is a greater difference in the duty cycle at which the MPP occurs for the PSCs, the P&O gets stuck at a LMPP after the PSC transition.

The MPPT test results for the A-QT-CT configuration under PSCs with P&O, CS and PSO MPPT algorithms for one of the runs are provided in Figs. 18–20 respectively. The MPPT efficiency during a 1 min test run is displayed on the Chroma SPV simulator interface, including the theoretical maximum power 'P_{mp}', V_{OC}, I_{SC}, maximum voltage (V_{mp}), maximum current (I_{mp}), and the measured average maximum power '$P_{average}$'. Additional parameters such as instantaneous voltage (V_{mea}), current (I_{mea}), and power (P_{mea}) are also visible. The time required for the algorithm to track the MPP is quantifiable by analysing the output voltage, current, and power waveforms of the DC-DC converter, as displayed on a digital storage oscilloscope (DSO).

The results obtained show the CS algorithm offers the best MPPT efficiency – around 0.6% higher than PSO while also being 0.8 s faster on an average to track MPP than the latter.

(a) Left side triangle shading

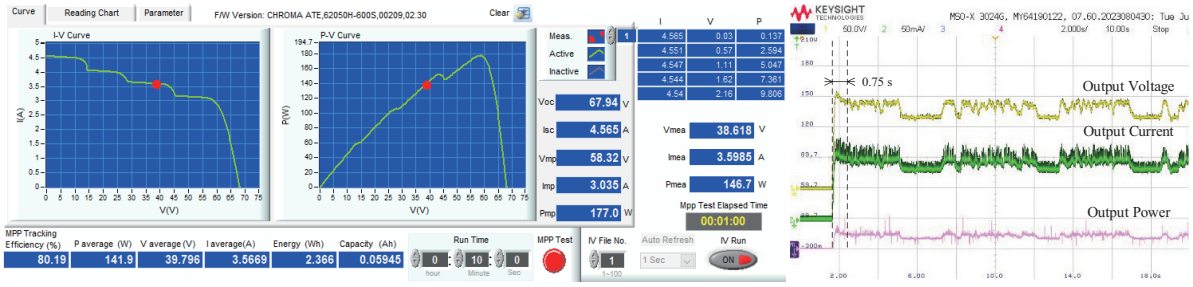

(b) Lower side triangle shading

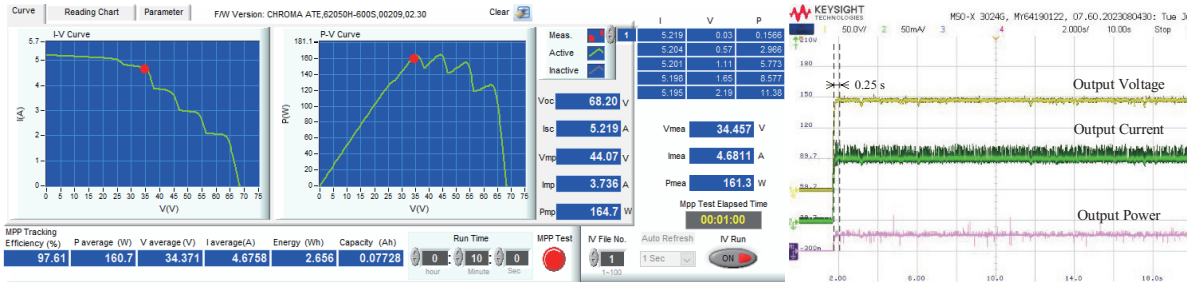

(c) Trapezium shading

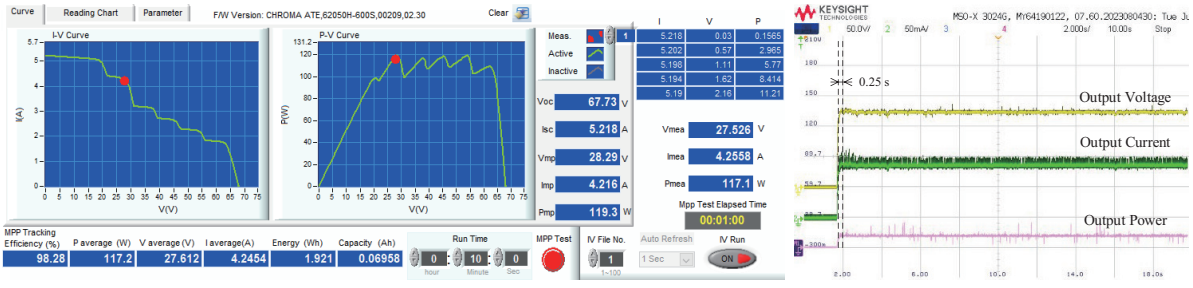

(d) Random 1 shading

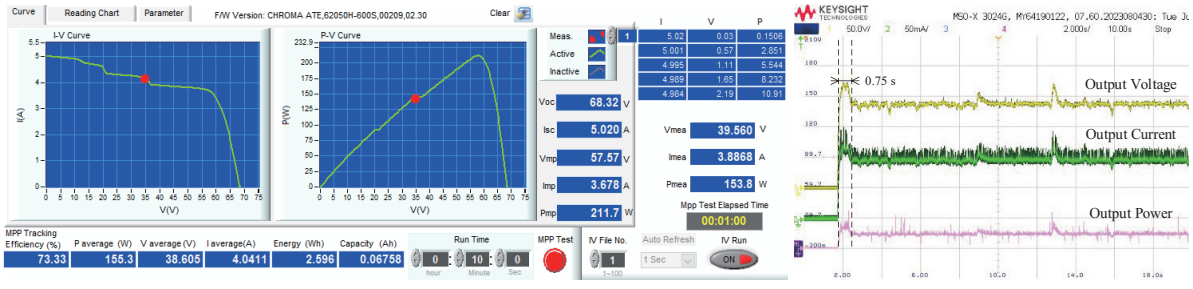

(e) Random 2 shading

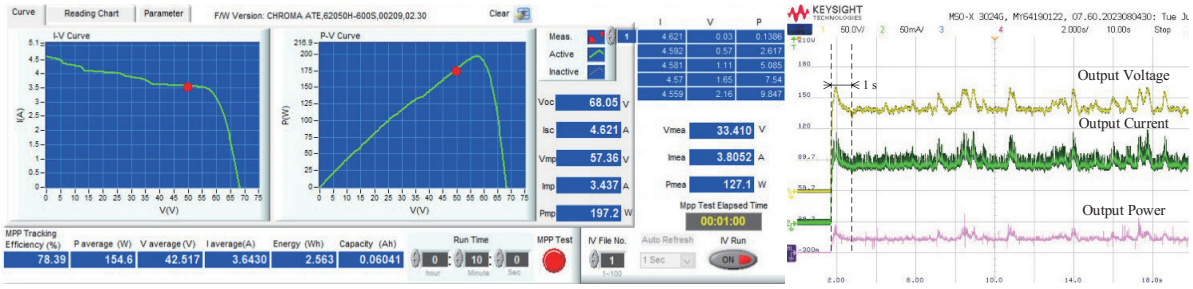

(f) Random 3 shading

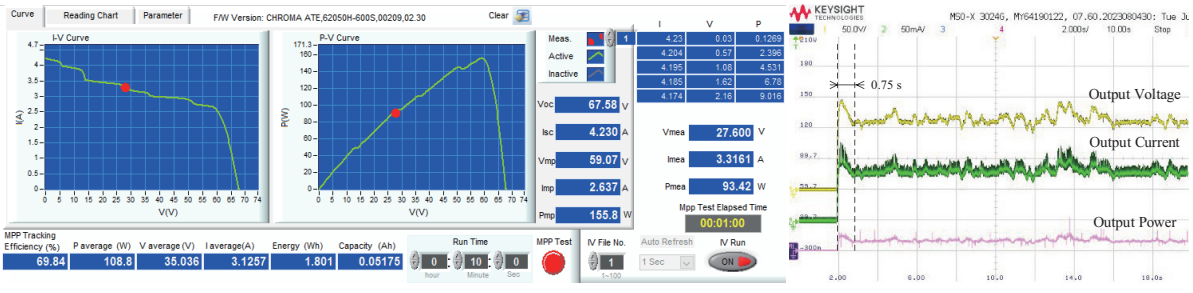

Fig. 18. Experimental hardware test results for A-QT-CT configuration with P&O MPPT algorithm.

(a) Left side triangle shading

(b) Lower side triangle shading

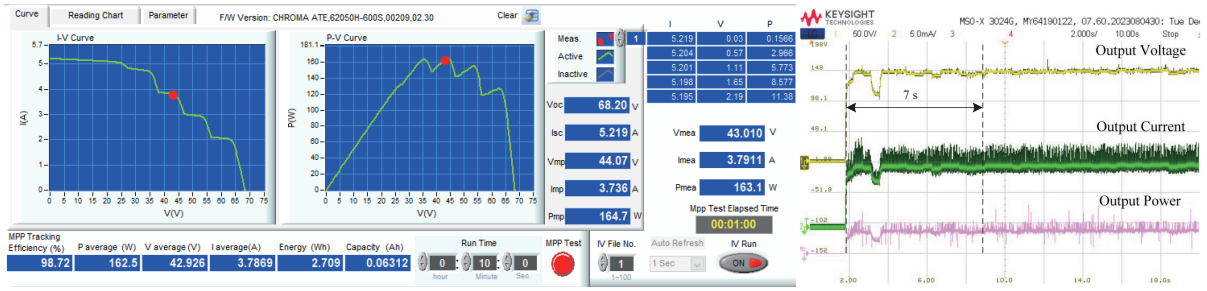

(c) Trapezium shading

(d) Random 1 shading

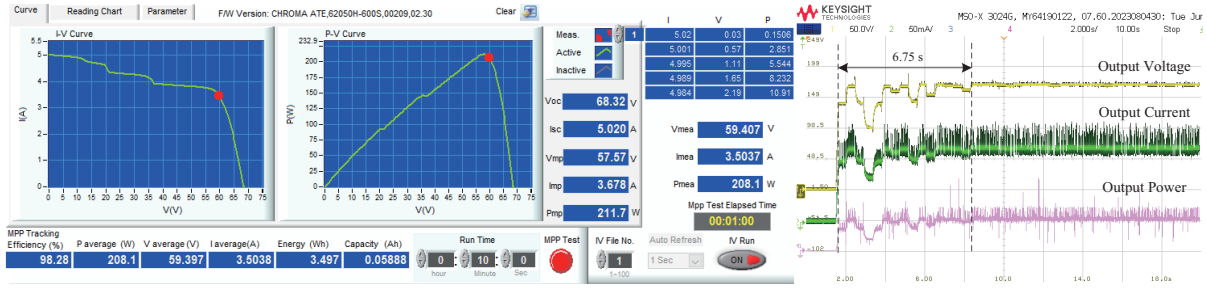

(e) Random 2 shading

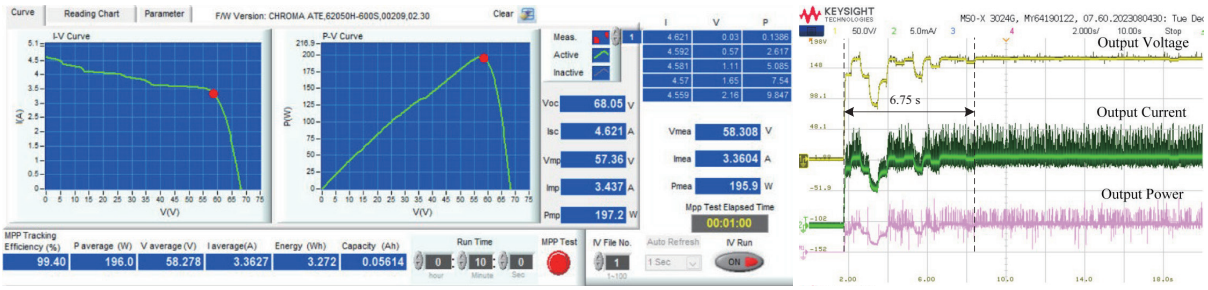

(f) Random 3 shading

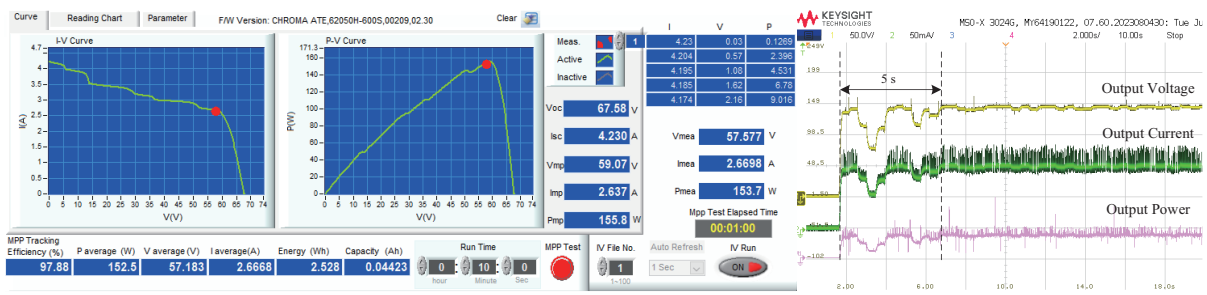

Fig. 19. Experimental hardware test results for A-QT-CT configuration with CS MPPT algorithm.

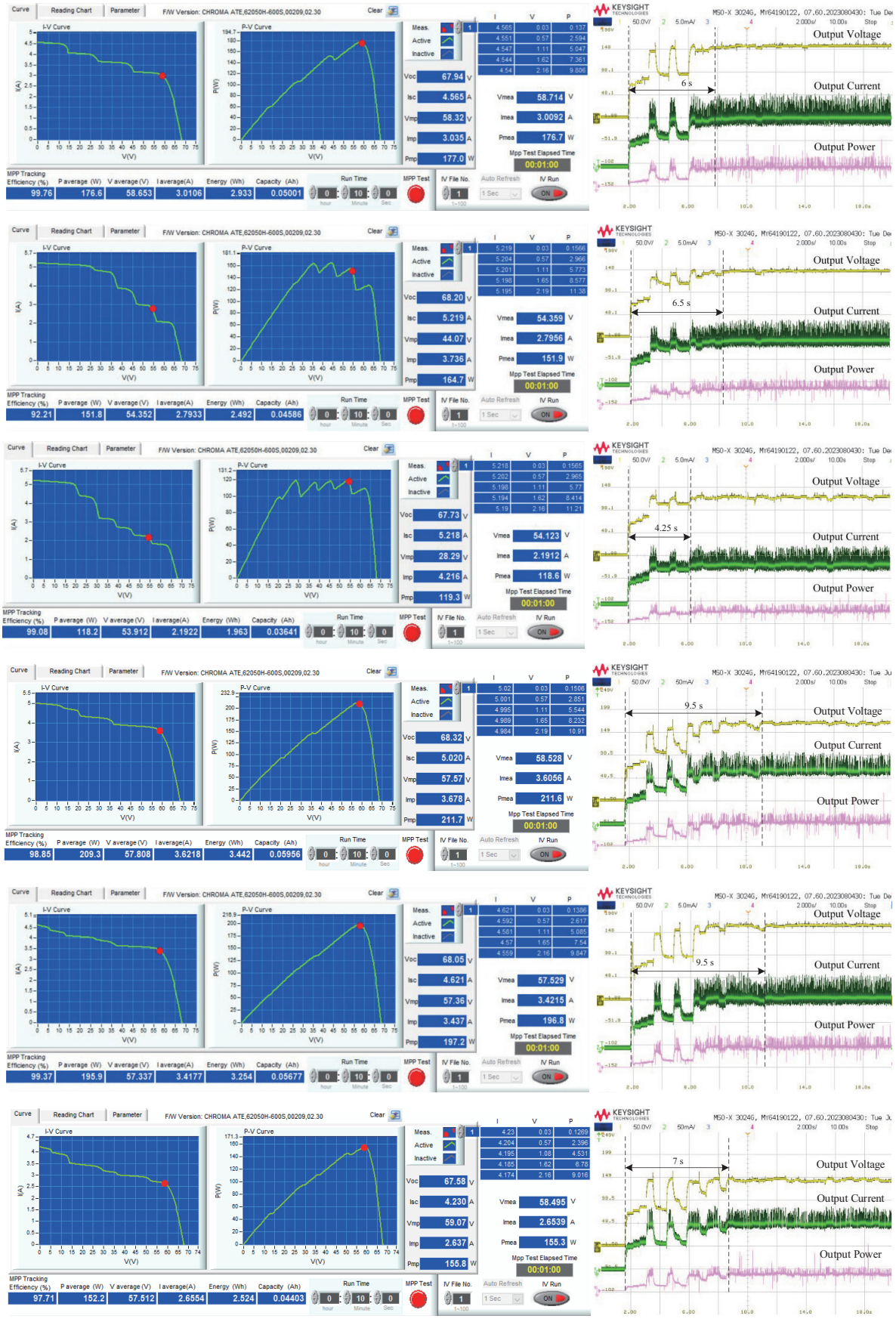

Fig. 20. Experimental hardware test results for A-QT-CT configuration with PSO MPPT algorithm.

TABLE VI
AVERAGE STEADY STATE MPPT EFFICIENCY AND TIME TO TRACK MPP – A-QT-CT CONFIGURATION (HARDWARE)

MPPT →	P&O		CS		PSO	
PSC ↓	η/%	T/s	η/%	T/s	η/%	T/s
Left side triangle	80.19	0.75	99.13	6.83	99.58	6.03
Lower side triangle	97.61	0.33	98.46	6.93	95.73	6.5
Trapezium	98.28	0.25	98.92	4.52	97.88	4.22
Random 1	73.33	0.75	98.45	6.63	99.01	9.5
Random 2	78.39	1	98.93	6.72	99.04	9.5
Random 3	69.84	0.75	97.52	5.04	98.31	6.75
Average	82.94	0.64	98.56	6.11	98.25	7.08

TABLE VII
AVERAGE STEADY STATE MPPT EFFICIENCY AND TIME TO TRACK MPP – TCT CONFIGURATION (HARDWARE)

MPPT →	P&O		CS		PSO	
PSC ↓	η/%	T/s	η/%	T/s	η/%	T/s
Left side triangle	75.38	0.75	99.5	6.78	99.1	7.25
Lower side triangle	94.84	0.33	99.3	7.25	94.07	6.78
Trapezium	98.35	0.5	98.62	6.67	96.89	4.33
Random 1	80.8	0.67	97.73	6.75	99.39	9.67
Random 2	78.54	1	98.81	6.5	99.18	9.5
Random 3	72.84	0.75	99.08	7.33	98.92	7.5
Average	83.45	0.67	98.84	6.88	97.92	7.51

The P&O method offers by far the quickest convergence, which is nearly 10 times faster than the metaheuristic MPPT techniques but fails to track MPP under 4 out of the 6 PSCs. This coupled with the continuous oscillation in the operating point even after convergence leads to a poor MPPT efficiency of around 83% compared to roughly above 98% that is offered by the CS and PSO algorithms. Between the CS and PSO algorithms, PSO has more oscillation and a tendency to get stuck at LMPP in cases where the GMPP is closely surrounded by multiple LMPP, such as lower side triangle shading. The results also prove that under very fast changing PSCs, where the PSC has changed even before the algorithm has converged for the previous PSC, the P&O method would track MPP more effectively than any of the metaheuristics-based algorithms. This remains a key disadvantage of all metaheuristic algorithms.

VII. CONCLUSION

The first focus area of the research is in the choice of suitable SPV array configuration for reduction of power loss due to PSCs in urban areas. In this, the A-QT-CT configuration offers a maximum power extraction of around 2% lesser on average than the best performing TCT configuration while having 15% lesser cross-links. The TCT configuration thus remains the best choice for rooftop applications, but A-QT-CT configuration comes very close and can be a valid contender. The choice of configuration between these two thus comes down to cost analysis of conductor material depending on size of the array and PSCs likely to be encountered. Amongst the MPPT strategies, the P&O method is by far the fastest, converging within 34 ms in the dynamic shading change simulation tests compared to the 295 ms and 420 ms taken by CS and PSO respectively. This is at the expense of MPPT efficiency as the P&O offers 98% unlike the CS and PSO which both offer 99.6%. In hardware experiments, the configurations, when used with the CS MPPT technique, offer superior performance than with the P&O and PSO MPPT techniques, as the CS method can track the GMPP most accurately. The CS algorithm offers 15.5% and 0.7% greater MPPT efficiency than the P&O and PSO algorithms respectively here while also being 0.8 faster than the PSO to converge. The P&O method is again much faster to converge here taking just under a second. The P&O and PSO algorithms suffer from oscillations in the operating point during steady state which is not the case with CS. The combination of CS MPPT method with TCT or A-QT-CT SPV array configuration are thus very suitable for application in rooftop SPV systems for the type of PSCs encountered in urban areas.

REFERENCES

[1] V. C. Chavan and S. Mikkili, "A typical review on static reconfiguration strategies in photovoltaic array under non-uniform shading conditions," in *CSEE Journal of Power and Energy Systems*, Jan. 2020.

[2] M. Jalal, I. U. Khalil, A. U. Haq, A. Flah, and S. a. M. A. Wahab, "Advancements in PV array reconfiguration techniques: Review article," in *IEEE Access*, p. 1, Jan. 2024.

[3] M. N. R. Nazer, A. Noorwali, M. F. N. Tajuddin, M. Z. Khan, M. A. I. A. Tazally, J. Ahmed, T. S. Babu, N. H. Ghazali, C. Chakraborty, and N. M. Kumar, "Scenario-based investigation on the effect of partial shading condition patterns for different static solar photovoltaic array configurations," in *IEEE Access*, vol. 9, pp. 116050–116072, Jan. 2021.

[4] R. K. Pachauri, O. P. Mahela, A. Sharma, J. Bai, Y. K. Chauhan, B. Khan, and H. H. Alhelou "Impact of partial shading on various PV array configurations and different modeling approaches: A comprehensive review," in *IEEE Access*, vol. 8, pp. 181375–181403, Jan. 2020.

[5] C. Saiprakash, A. Mohapatra, B. Nayak, T. S. Babu, and H. H. Alhelou, "A novel benzene structured array configuration for harnessing maximum power from PV array under partial shading condition with reduced number of cross ties," in *IEEE Access*, vol. 10, pp. 129712–129726, Jan. 2022.

[6] P. K. Bonthagorla and S. Mikkili, "A novel fixed PV array configuration for harvesting maximum power from shaded modules by reducing the number of cross-ties," in *IEEE Journal of Emerging and Selected Topics in Power Electronics*, vol. 9, no. 2, pp. 2109–2121, Mar. 2020.

[7] T. Ramesh, K. Rajani, and A. K. Panda, "A novel triple-tied-cross-linked PV array configuration with reduced number of cross-ties to extract maximum power under partial shading conditions," in *CSEE Journal of Power and Energy Systems*, Jan. 2020.

[8] S. R. Pendem, S. Mikkili, S. S. Rangarajan, S. Avv, R. E. Collins, and T. Senjyu, "Optimal hybrid PV array topologies to maximize the power output by reducing the effect of non-uniform operating conditions," in *Electronics*, vol. 10, no. 23, p. 3014, Dec. 2021.

[9] P. R. Satpathy, T. S. Babu, S. K. Shanmugam, L. N. Popavath, and H. H. Alhelou, "Impact of uneven shading by neighboring buildings and clouds on the conventional and hybrid configurations of roof-top PV arrays," in *IEEE Access*, vol. 9, pp. 139059–139073, Jan. 2021.

[10] H. Oufettoul, N. Lamdihine, S. Motahhir, N. Lamrini, I. A. Abdelmoula, and G. Aniba, "Comparative performance analysis of PV module positions in a solar PV array under partial shading conditions," in *IEEE Access*, vol. 11, pp. 12176–12194, Jan. 2023.

[11] M. A. Hendy, Mohamed. A. Nayel, J. Rodriguez, and M. Abdelrahem, "Enhanced maximum power point tracking using modified PSO hybrid

with MPC under partial shading conditions," in *IEEE Access*, p. 1, Jan. 2024.
[12] T. V. Anh, T. N. Trieu, P. V. H. Nghi, and B. Van Hien, "Fast and accurate GMPPT based on modified P&O algorithm," in *IEEE Access*, vol. 12, pp. 129588–129600, Jan. 2024.
[13] J. S. Koh, R. H. G. Tan, W. H. Lim, and N. M. L. Tan, "A modified particle swarm optimization for efficient maximum power point tracking under partial shading condition," in *IEEE Transactions on Sustainable Energy*, vol. 14, no. 3, pp. 1822–1834, Mar. 2023.
[14] R. Sangrody, S. Taheri, A. -M. Cretu, and E. Pouresmaeil, "An improved PSO-based MPPT technique using stability and steady state analyses under partial shading conditions," in *IEEE Transactions on Sustainable Energy*, vol. 15, no. 1, pp. 136–145, Jan. 2024.
[15] C. Yuan, J. Xia, F. Huang, P. Zhao, and L. Kong, "A novel hermite interpolation-based MPPT technique for photovoltaic systems under partial shading conditions," in *IEEE Photonics Journal*, vol. 16, no. 2, pp. 1–10, Feb. 2024.
[16] K. Xia, Y. Li, and B. Zhu, "Improved photovoltaic MPPT algorithm based on ant colony optimization and fuzzy logic under conditions of partial shading," in *IEEE Access*, vol. 12, pp. 44817–44825, Jan. 2024.
[17] M. N. I. Jamaludin, M. F. N. Tajuddin, J. Ahmed, A. Azmi, S. A. Azmi, and N. H. Ghazali, "An effective SALP swarm based MPPT for photovoltaic systems under dynamic and partial shading conditions," in *IEEE Access*, vol. 9, pp. 34570–34589, Jan. 2021.
[18] M. Etezadinejad, B. Asaei, S. Farhangi, and A. Anvari-Moghaddam, "An improved and fast MPPT algorithm for PV systems under partially shaded conditions," in *IEEE Transactions on Sustainable Energy*, vol. 13, no. 2, pp. 732–742, Nov. 2021.
[19] J. S. Koh, R. H. G. Tan, W. H. Lim, and N. M. L. Tan, "A real-time deterministic peak hopping maximum power point tracking algorithm for complex partial shading condition," in *IEEE Access*, vol. 12, pp. 43632–43644, Jan. 2024.
[20] K. K. Mohammed, S. Buyamin, I. Shams, and S. Mekhilef, "Hybrid global maximum power tracking method with partial shading detection technique for PV systems," in *IEEE Journal of Emerging and Selected Topics in Power Electronics*, vol. 10, no. 4, pp. 4821–4831, Nov. 2021.
[21] A. Ibrahim, R. Aboelsaud, and S. Obukhov, "Maximum power point tracking of partially shading PV system using cuckoo search algorithm," in *Proceedings of International Journal of Power Electronics and Drive Systems (IJPEDS)*, vol. 10, no. 2, p. 1081, Apr. 2019.
[22] M. I. Mosaad, M. O. A. El-Raouf, M. A. Al-Ahmar, and F. A. Banakher, "Maximum power point tracking of PV system based Cuckoo search algorithm; review and comparison," in *Energy Procedia*, vol. 162, pp. 117–126, Apr. 2019.
[23] S. Mohammadnejad, A. Khalafi, and S. M. Ahmadi, "Mathematical analysis of total-cross-tied photovoltaic array under partial shading condition and its comparison with other configurations," in *Solar Energy*, vol. 133, pp. 501–511, May 2016.
[24] Yang X.-S. and Deb S., "Cuckoo search via Lévy flights," in *Proceedings of Nature & Biologically Inspired Computing*, 2009, p. 210–214.
[25] A. M. Reynolds and M. A. Frye, "Free-flight odor tracking in drosophila is consistent with an optimal intermittent scale-free search," in *PloS One,* vol. 2, no. 4, p. e354, Apr. 2007.
[26] A. M. Eltamaly, "An improved Cuckoo search algorithm for maximum power point tracking of photovoltaic systems under partial shading conditions," in *Energies*, vol. 14, no. 4, p. 953, Feb. 2021.
[27] J. Kennedy and R. Eberhart, "Particle swarm optimization," in *Proceedings of ICNN'95 - International Conference on Neural Networks*, Perth, WA, Australia, 1995, pp. 1942–1948, vol. 4.
[28] Y. Shi and R. Eberhart, "A modified particle swarm optimizer," in *Proceedings of 1998 IEEE International Conference on Evolutionary Computation Proceedings. IEEE World Congress on Computational Intelligence*, Anchorage, AK, USA, 1998, pp. 69–73.

Abhinav Bhattacharjee received the B.E. degree in Electrical & Electronics Engineering from Goa College of Engineering, Farmagudi, Goa, India in 2014, and the M.Tech degree in power electronics and drives from Vellore Institute of Technology, Vellore, India in 2017. He joined as a Lecturer in Electrical Engineering at Government Polytechnic Bicholim, Goa, India, in 2017, and is currently pursuing his Ph.D. degree in electrical and electronics engineering at National Institute of Technology Goa, Cuncolim, India. His research interests include solar photovoltaic systems, DC-DC converters and applications of metaheuristic algorithms and soft computing techniques.

Suresh Mikkili obtained his M.Tech and Ph.D. degrees in Electrical Engineering from the National Institute of Technology, Rourkela in the years 2008 and 2013, respectively. He holds the position of Associate Professor in the Department of Electrical and Electronics Engineering (EEE) at the National Institute of Technology Goa (NIT Goa), India, starting from January 2013.

His research interests include smart electric grid, electric vehicles, grid connected/stand-alone PV systems, wireless power transfer, power quality issues and applications of soft computing techniques. He authored two books published by CRC Press, Taylor & Francis Group, in August 2015 and 2021, respectively. He has also authored the AICTE approved textbook titled "Power Systems-I" for B.Tech III year students. He has published over 135 papers in prestigious international journals (SCI/SCI-E) and international conferences. The government of India awarded him an Early Career Researcher Award.

Low- and High-Speed Control Strategy for PMSM Drive System Based on MMC

Jianfei ZHAO, Sucheng HUANG, and Yuanyuan XING

***Abstract*—This paper proposes a modular multilevel converter (MMC)-based control strategy for high-power permanent magnet synchronous motors (PMSM), covering both low- and high-speed ranges in electric vehicle applications. Specifically, an improved hybrid injection method based on phase voltage harmonics is introduced. The injection waveform is optimized considering the common-mode voltage, high-frequency circulating current, and phase voltage to minimize capacitor voltage fluctuations. In addition, a novel quasi-proportional-resonant (quasi-PR) controller based on an enhanced filter is developed to mitigate circulating current issues. Experimental results demonstrate that the proposed hybrid injection method effectively suppresses capacitor voltage fluctuations, reduces bridge-arm current amplitude, and improves system stability. Furthermore, the proposed quasi-PR controller achieves lower circulating current and further enhances system robustness and disturbance rejection capability.**

***Index Terms*—Circulating current suppression, modular multilevel converter, permanent magnet synchronous motor, suppression of capacitor voltage fluctuations.**

I. Introduction

In light of the accelerated growth of the new energy sector, there has been a notable increase in research activity within the field of motor drive systems. The utilization of medium-voltage and high-voltage converters for the speed control of high-power permanent magnet synchronous motor (PMSM) has the potential to significantly reduce energy consumption, enhance the speed control performance and extend the operational lifespan of the motor [1]. The modular multilevel converter (MMC) exhibits advantageous characteristics, including high reliability, high-power quality and high-voltage level [2]. These attributes position the MMC as a promising candidate for advancement in the domain of high-power motor drive systems [3].

MMC application to PMSM control is associated with significant capacitor voltage fluctuations during motor startup and low-speed operation. This fluctuation results from low load current, which causes current imbalance across submodules and inefficient capacitor charging. The high switching frequency of the MMC converter can further exacerbate the issue by introducing ripple currents, increasing voltage variations. Minimizing these fluctuations is crucial for stable PMSM operation, especially at low speeds. Excessive capacitor voltage fluctuations can cause submodule overvoltage, waveform distortion, and system instability [4]. In 2010, ABB proposed a method [5] and enabled the startup of the induction motor [6], which involved injecting high-frequency common-mode voltage at the AC output side and high-frequency current into the three-phase circulating current. [7] proposed an adaptive switching frequency control method for carrier phase-shift modulation, which improves the system's efficiency by dynamically adjusting the switching frequency. This method enhances the modulation strategy in the MMC, contributing to more stable operation and reduced voltage fluctuation. The high-frequency injection method generates common-mode voltage by injecting high-frequency current through the ground capacitor, causing interference between the ground and signal lines. This increases bearing wear but effectively reduces capacitor voltage fluctuations at low-speed PMSM operation by balancing the current across MMC submodules and improving energy distribution [8]. [9] proposed a flying-capacitor MMC (FCMMC) to attain power balance between the upper and lower bridge-arms without the injection of a common-mode voltage. The concept of the star and delta channel MMC was first proposed in [10] and [11] respectively. In essence, the full bridge sub-modules were connected to the midpoint of the three-phase bridge-arms using star/delta connections, injecting high-frequency circulating current by generating a regulation voltage. In addition to introducing common-mode interference, the high-frequency circulating current injected by the high-frequency injection also resulted in elevated bridge-arm currents [12]. The injected common-mode voltage waveform was modified from a sine wave to a square-wave, thereby reducing the requisite injected current amplitude [13]. [14] employed a delay treatment at the square-wave mutation and replaced the square-wave with trapezoidal waveform.

Consequently, the low frequency suppression scheme based on the high-frequency injection method is more widely applicable. However, for constant torque loads, further reducing the amplitude of high-frequency circulating currents

Manuscript received May 8, 2025; revised July 14, 2025; accepted August 15, 2025. Date of publication December 30, 2025; date of current version September 9, 2025. No funding was received to assist with the preparation of this manuscript. *(Corresponding author: Jianfei Zhao.)*

All authors are with School of Mechatronic Engineering and Automation, Shanghai University, Shanghai 200444, China (e-mail: jfzhao@shu.edu.cn; Mr_huang@shu.edu.cn; xingyuanyuan@shu.edu.cn).

Digital Object Identifier 10.24295/CPSSTPEA.2025.00030

while suppressing capacitor voltage fluctuations remains an area for further study.

As the motor speed increases, the capacitor voltage fluctuation decreases. However, it leads to an increase in circulating current, which becomes a more significant issue. Harmonic components in circulating currents cause distortion of bridge-arm currents, increasing current demand and switching losses [15]. A novel proportional integral and resonance control was devised to achieve the static free tracking of the fundamental frequency components and the control of the high-frequency harmonic components [16]. [17] integrated fuzzy control with traditional PI control, proposing a method based on fuzzy adaptive PI control. Furthermore, circulation suppression could be achieved by improving the network topology, adjusting the modulation strategy, and modelling the network state. [18] replaced the half bridge submodule with full bridge submodule, allowing the MMC to operate at full power without overmodulation. [19] suggested a method based on the use of dead band control mechanism.

A number of other scholars have concentrated their efforts on providing theoretical guidance for the design and optimization of MMC circulation suppression methods. [20] presented a method to calculate the circulating current in a synchronous rotating coordinate system. [21] proposed an MMC small signal modelling method based on harmonic state space equations. In [22], a novel DC impedance model was put forth to address the deficiencies of the extant MMC DC impedance model, which failed to incorporate the internal dynamic performance of the MMC. [23] put forth an optimal second harmonic component injection strategy while ignoring the potential loss imbalance between the submodule power devices. However, most of the aforementioned methods neglected the existence of higher-frequency components in the circulating current such as the quadruple frequency circulating component [24]. Therefore, there has been significant essential to investigate strategies for suppressing circulating currents to develop more effective suppression methods.

This paper can be summarized as follows: Section II analyses MMC working principle and proposes the improved hybrid injection method based on phase voltage harmonic. Section III presents a novel quasi-PR control circulating current suppression strategy based on enhanced adaptive filter. Section IV evaluates the simulation results. Section V builds an experimental platform to verify the effectiveness of the proposed control strategy. Finally, the conclusion and references are presented.

II. Improved Hybrid Injection Low Frequency Suppression Method Based on Phase Voltage Harmonic

A. MMC Working Principle

Fig. 1 shows the MMC PMSM circuit topology.

The MMC circuit consists of three-phase units, each comprising N submodules and a bridge-arm inductance L_{arm}. where U_{dc} is the DC side voltage; I_{dc} is the DC side current;

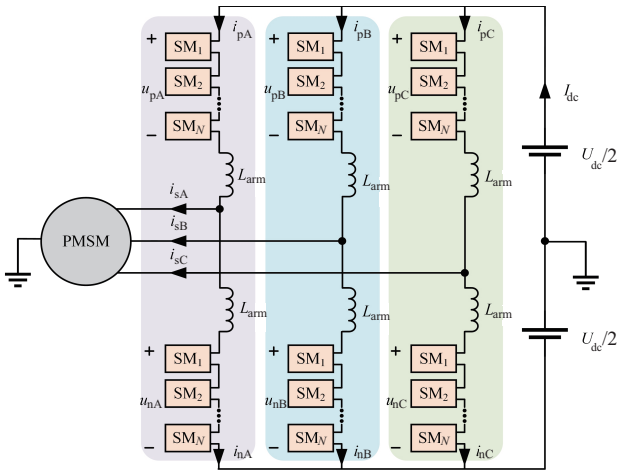

Fig. 1. MMC and PMSM circuit topology structure

u_{pj} and u_{nj} are the upper and lower bridge-arm voltages; i_{pj} and i_{nj} are the upper and lower bridge-arm currents; i_{sj} is the three-phase current.

Suppose the phase voltage can be expressed as:

$$u_{sj} = U_{sm}\sin(\omega t) = m\frac{U_{dc}}{2}\sin(\omega t) \tag{1}$$

where U_{sm} is the amplitude of the phase voltage; ω is the angular frequency; m is the voltage modulation ratio; and the specific expression is:

$$m = \frac{U_{sm}}{U_{dc}/2} \tag{2}$$

Assume that the phase current can be expressed as:

$$i_{sj} = I_{sm}\sin(\omega t + \varphi) \tag{3}$$

where I_{sm} is the amplitude of the phase current and φ is the power factor angle of the AC side.

There is current flowing directly through the upper and lower bridge-arms during the operation of the MMC. The non-fundamental frequency component of this current is generally referred to as the circulating current i_{cirj}. According to Kirchhoff's current law, the j-phase upper and lower bridge-arm currents can be expressed as:

$$i_{pj} = i_{cirj} + \frac{i_{sj}}{2} \tag{4}$$

$$i_{nj} = i_{cirj} - \frac{i_{sj}}{2} \tag{5}$$

where i_{pj} is upper bridge-arm current; i_{nj} is the lower bridge-arm current.

B. Dual-Sinusoidal Injection Method

In the double-sine injection method, the injected high-

frequency common-mode voltage u_{cm} and high-frequency circulating current i_{cm} are written as:

$$u_{cm} = U_{cm}\sin(\omega_h t) \tag{6}$$

$$i_{cm} = I_{cm}\sin(\omega_h t) \tag{7}$$

where U_{cm} and I_{cm} are the amplitude of high-frequency common-mode voltage and circulating current separately; ω_h is common-mode voltage angular frequency $\omega_h = 2\pi f_h$; f_h is common-mode voltage frequency.

The fundamental frequency component in bridge-arm power p_{low} can be expressed as:

$$p_{low} = \frac{U_{dc} i_{sj}}{4}[1 - m^2\sin^2(\omega t + \eta_{sj})] \tag{8}$$

The amplitude of high-frequency circulating current needed to be injected is:

$$I_{cm} = \frac{U_{dc} i_{sj}}{2U_{cm}}[1 - m^2\sin^2(\omega t)] \tag{9}$$

From (9), U_{cm} is in inverse proportion to I_{cm}. Since U_{cm} is limited by the duty cycle and U_{dc}, U_{cm} must meet the following requirements to prevent overmodulation:

$$U_{cm} \leqslant \frac{(1-m)}{K}\frac{U_{dc}}{2} \tag{10}$$

The range of K in (10) is 1−1.2. According to (9), when U_{cm} takes the maximum value, I_{cm} can be given by:

$$I_{cm} = \frac{K i_{sj}}{1-m}[1 - m^2\sin^2(\omega t + \eta_{sj})] \tag{11}$$

C. Design of Improved Hybrid Injection Method Based on Phase Voltage Harmonics

High-frequency square-wave common-mode voltage and circulating current injection can improve waveform utilization. However, the presence of abundant harmonics necessitates tracking both the fundamental frequency ω_h and its third harmonic $3\omega_h$, thereby imposing stricter requirements on the control bandwidth compared to the dual-sinusoidal injection method. Moreover, when the square-wave circulating current passes through the bridge-arm inductance, it may cause a steep voltage spike at the current's zero-crossing point.

To address these issues, square-wave injection is replaced by a combined sinusoidal and third harmonic waveform. To address these issues, square-wave injection is replaced by a combined sinusoidal and third harmonic waveform. This composite waveform not only approximates the square wave to retain its high fundamental voltage utilization but also smooths the current waveform, thereby reducing voltage spikes across the bridge-arm inductance. The third harmonic component adjusts the waveform shape to suppress abrupt transitions near zero crossings, improving modulation stability and lowering the amplitude of the required circulating current. This reduces switching stress and enhances converter efficiency under low-speed conditions.

TABLE I
INTERVAL SELECTION

u_{sA}	u_{sB}	u_{sC}	Interval
+	+	−	1
−	+	−	2
−	+	+	3
−	−	+	4
+	−	+	5
+	−	−	6

The injected common-mode voltage u_{cm} and circulating current i_{cm} are given by:

$$u_{cm} = \begin{cases} -U_{cm} & (0 < t \leqslant \dfrac{1}{2f_h}) \\ U_{cm} & (\dfrac{1}{2f_h} < t < \dfrac{1}{f_h}) \end{cases} \tag{12}$$

$$i_{cm} = I_{cm}[\sin(\omega_h t) + \frac{1}{6}\sin(3\omega_h t)] \tag{13}$$

In order to increase the speed of command input and to reduce the calculation session time, the look-up table method is used for phase voltage harmonic injection. The process is: Firstly, three-phase sinusoidal voltage u_{sA}, u_{sB}, and u_{sC} were obtained by vector control. Then, select the corresponding intervals according to positive and negative three-phase voltage values and Table I. Finally, compare the magnitude of the same positive and negative sign voltages to get the injected voltage u_z. Table I is the interval selection table.

Interval 1:
If $|u_{sA}| \geqslant |u_{sB}|$, $u_z = u_{sB}/2$; If $|u_{sA}| < |u_{sB}|$, $u_z = u_{sA}/2$.
Interval 2:
If $|u_{sA}| \geqslant |u_{sC}|$, $u_z = u_{sC}/2$; If $|u_{sA}| < |u_{sC}|$, $u_z = u_{sA}/2$.
Interval 3:
If $|u_{sB}| \geqslant |u_{sC}|$, $u_z = u_{sC}/2$; If $|u_{sB}| < |u_{sC}|$, $u_z = u_{sB}/2$.
Interval 4:
If $|u_{sB}| \geqslant |u_{sA}|$, $u_z = u_{sA}/2$; If $|u_{sB}| < |u_{sA}|$, $u_z = u_{sB}/2$.
Interval 5:
If $|u_{sC}| \geqslant |u_{sA}|$, $u_z = u_{sA}/2$; If $|u_{sC}| < |u_{sA}|$, $u_z = u_{sC}/2$.
Interval 6:
If $|u_{sC}| \geqslant |u_{sB}|$, $u_z = u_{sB}/2$; If $|u_{sC}| < |u_{sB}|$, $u_z = u_{sC}/2$.

The three-phase voltage after harmonic injection u'_{sj} can be written as:

$$u'_{sj} = u_{sj} + u_z \tag{14}$$

After harmonic injection, the amplitude of the phase voltage

is 0.87 times the amplitude of its fundamental component. The fundamental utilization is higher than that of sine wave of the same amplitude. Thus, the range of values for U_{cm} is further increased:

$$U_{cm} \leqslant \frac{(1-0.87m)}{K}\frac{U_{dc}}{2} \tag{15}$$

After third harmonic injection, the low frequency component of the bridge-arm power p'_{low} can be expressed as:

$$p'_{low} = \frac{U_{dc} i_{sj}}{4}[1 - m^2 \sin^2(\omega t + \eta_{sj}) - \frac{m^2}{24}\sin^2(\omega t + \eta_{sj})] \tag{16}$$

In addition, the amplitude of the injected high-frequency circulating current I_{cm} is written as:

$$I_{cm} = \frac{36\pi}{304}\frac{U_{dc} i_{sj}}{U_{cm}}[1 - m^2 \sin^2(\omega t + \eta_{sj}) - \frac{m^2}{24}\sin^2(\omega t + \eta_{sj})] \tag{17}$$

Take the maximum of U_{cm} in (15) and substitute it into (17). Then, the required injection circulating current amplitude in the phase voltage harmonic improvement hybrid injection method can be expressed as:

$$I_{cm} = \frac{72\pi}{304}\frac{K i_{sj}}{1-0.87m}[1 - m^2 \sin^2(\omega t + \eta_{sj}) - \frac{m^2}{24}\sin^2(\omega t + \eta_{sj})] \tag{18}$$

Capacitor voltage fluctuation decreases as motor speed increases. Thus, the fluctuation will be acceptable for normal operation after the motor speed reaches a certain value. The injection control strategy proposed in this chapter is only applicable to the low speed condition of the motor. And different system parameters have different speed cut-off points. In this paper, the MMC is selected to start up with 0.5 N·m light load. The calculation shows that when the rotational speed is 200 rpm, the fluctuation range has been reduced to 20% of the rated capacitor voltage. Therefore, in this paper, the speed is divided into a low speed band of 0−200 rpm and a medium-high speed band of 200−900 rpm.

In summary, the control diagram of the low frequency suppression strategy proposed in this paper is shown in Fig. 2.

The system control structure consists of: 1) A classic speed-current double closed-loop control. 2) Given high-frequency circulating current tracking, i_{cm} is obtained according to (18) and u_{cj} is obtained through the P controller. 3) High-frequency common-mode voltage injection. u_{cm} is accessed by (12). 4) Phase voltage harmonics injection. u'_{sj} is acquired by (14).

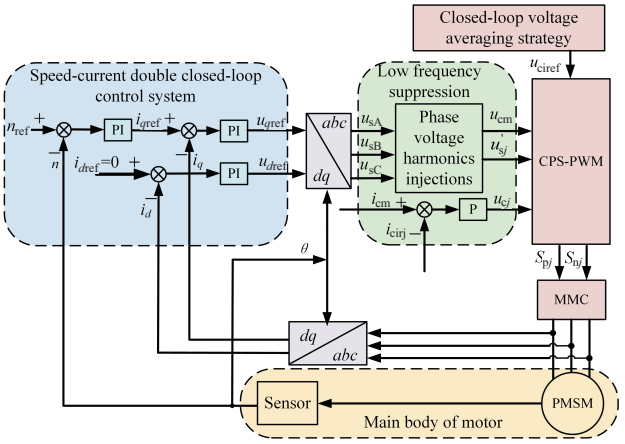

Fig. 2. The control diagram of the low-frequency suppression strategy proposed in this paper.

5) Closed loop voltage averaging strategy. The u_{ciref} of each submodule is obtained through the P controller. 6) Carrier phase shifted pulse width modulation (CPS-PWM). The switching function for the MMC part is obtained.

III. A Novel Quasi-PR Control Circulating Current Suppression Strategy Based on Enhanced Adaptive Filters

A. MMC Circulating Current Analysis

The expression for circulating current is:

$$\begin{cases} i_{cira} = \dfrac{I_{dc}}{3} + \sum_{n=2}^{\infty} n I_{nm} \cos(n\omega_n t + \theta_{nm}) \\ i_{cirb} = \dfrac{I_{dc}}{3} + \sum_{n=2}^{\infty} n I_{nm} \cos\left[n(\omega_n t - \dfrac{2\pi}{3}) + \theta_{nm} \right] \\ i_{cirb} = \dfrac{I_{dc}}{3} + \sum_{n=2}^{\infty} n I_{nm} \cos\left[n(\omega_n t + \dfrac{2\pi}{3}) + \theta_{nm} \right] \end{cases} \tag{19}$$

where I_{nm} and θ_{nm} are separately the peak and the initial phase of circulating current harmonics after n times; and i_{cira}, i_{cirb}, i_{circ} are circulating current in three-phase circuits.

From (19), the circulating current actually consists of a DC component $I_{dc}/3$ and even harmonics such as second, fourth, and sixth component. The amplitude is inversely proportional to the frequency. The circulating current is specified as a voltage drop across the bridge-arm inductance. Therefore, the circulating current can be suppressed by superimposing a suppression component of the same phase sequence on the voltage modulating waveform of the upper and lower bridge-arms, thereby generating a reverse inductive voltage drop u_{csj}.

Since the circulating current harmonics are dominated by the second frequency component, based on the principle of vector control, the negative sequence second frequency rotating coordinate system can be used to transform the second frequency circulating current into a direct current and then suppress it by using a PI controller. Fig. 3 shows the MMC

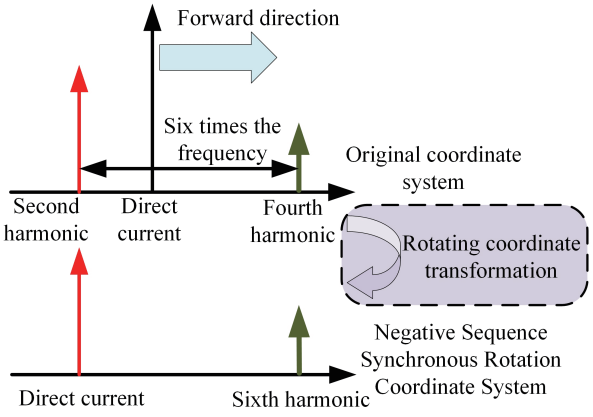

Fig. 3. MMC circulation spectrum diagram.

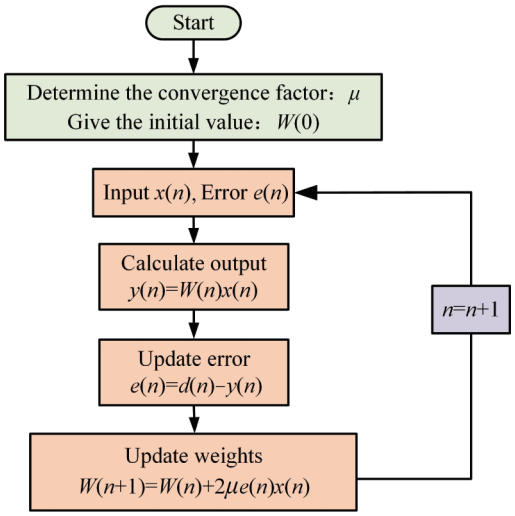

Fig. 4. LMS adaptive algorithm flowchart.

circulating current spectrum, where the horizontal coordinate is the direction and the vertical coordinate is the amplitude.

However, due to the presence of other harmonics in the circulating current, the component obtained after the coordinate transformation is not a complete direct current.

As shown in Fig. 3, the left side of the horizontal axis represents the second harmonic component and the right is the fourth harmonic, and the distance between them is the sixth harmonic. The fourth circulating current harmonic becomes the sixth harmonic in the negative sequence synchronous rotating coordinate system, and the presence of the sixth harmonic leads to poor tracking and suppression of the circulating current by the PI controller.

B. Design of Improved Adaptive Filter

The least mean squares (LMS) algorithm is an important method in adaptive filter design, which has the advantages of simple principle, few parameters, easy to implement and small computation, etc. The algorithm flowchart is shown in Fig. 4.

The adaptive filter should converge faster and exhibit smaller steady-state error under external disturbances. A fixed convergence coefficient involves a trade-off between speed and stability, whereas a time-varying coefficient can dynamically balance both through iterative adaptation. The new weight coefficient update formula is:

$$W(n+1)=W(n)+2\mu(n)e(n)x(n) \tag{20}$$

The criterion for the variable step-size LMS algorithm is as follows: a larger step size is used in the early stage of iteration to achieve fast convergence, while a smaller step size is used in the later stage to improve steady state performance when the system reaches steady state. To overcome the convergence-stability trade-off in conventional LMS filters, we introduce a variable-step strategy using a sigmoid function. The function dynamically increases the convergence rate during large-error conditions and decreases it as the error reduces, improving both response speed and steady-state accuracy. This approach is novel in the context of harmonic suppression for MMC-driven PMSM systems.

The function is transformed based on the sigmoid function to better match the function curve to the convergence coefficient adjustment criterion. In addition, a compensation factor is introduced to improve the characteristics at the lower end of the function by dynamically adjusting the convergence coefficient of the algorithm. The resulting updating formula is:

$$\mu(n)=a\left[1-\frac{1+b}{1+b(\exp(c\left|e(n)e(n-1)\right|)+k\left|e(n-1)\right|)}\right] \tag{21}$$

where k is the compensation coefficient, which is assumed to be 0.01; a, b, and c are the adjustment coefficients:

1) The parameter a can set an upper bound for the convergence coefficient so the value of μ ranges from (0, a].

2) The parameter b primarily affects the lower end characteristics of the convergence coefficient variation curve.

3) The parameter c primarily influences the variation amplitude of the convergence coefficient as $e(n)$ approaches 0.

C. Design of Circulating Current Suppressor Based on Quasi-PR Control

The harmonics of the MMC circulating current are mainly composed of the direct flow and the second component, so the expression of the circulating current is given by:

$$i_{\text{cir}j}=\frac{I_{\text{dc}}}{3}+w_{2f\_1}\cos(2\theta)+w_{2f\_2}\sin(2\theta) \tag{22}$$

Adaptive filters use error feedback from an adaptive algorithm to adjust the convergence and weighting coefficients to better track harmonic currents. The adaptive filter output is the circulating current harmonics:

$$y(n)=w_1\cos(2\theta)+w_2\sin(2\theta)=w_1x_1(n)+w_2x_2(n) \tag{23}$$

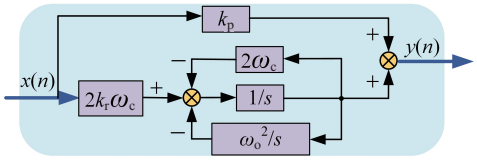

Fig. 5. Structure of quasi-PR controller.

The error is calculated as:

$$e(n) = i_{cirj} - y(n) \tag{24}$$

The LMS algorithm update formula is:

$$\begin{cases} w_1(n+1) = w_1(n) + 2\mu(n)e(n)x_1(n) \\ w_2(n+1) = w_2(n) + 2\mu(n)e(n)x_2(n) \end{cases} \tag{25}$$

The quasi-PR controller introduces a resonant peak at a target frequency in the stationary $\alpha\beta$ frame. It eliminates the need for coordinate transformation while providing strong harmonic suppression for fixed-frequency circulating current components. This approach simplifies implementation, avoids frequency mismatch, and is novel in MMC-PMSM systems when used in conjunction with hybrid injection. The specific structure is shown in Fig. 5. Its transfer function is:

$$G_{QPR}(s) = k_p + \frac{2k_r\omega_c s}{s^2 + 2\omega_c s + \omega_o^2} \tag{26}$$

where k_p and k_r are the proportional gain and resonant gain; ω_o is the resonant frequency and ω_c is the cut-off frequency.

The PR controller uses predistorted bilinear transformation:

$$s = \frac{\omega_o}{\tan(0.5\omega_o T_s)} \frac{1 - z^{-1}}{1 + z^{-1}} \tag{27}$$

Combining the z inverse transformation:

$$\begin{aligned} y(k) = k_r[&\frac{b_1}{2\omega_o a_1}e(k) + \frac{b_2}{2\omega_o a_1}e(k-2)] - \\ &\frac{a_2}{a_1}y(k-1) - \frac{a_3}{a_2}y(k-2) \end{aligned} \tag{28}$$

where the parameters are:

$$\begin{cases} a_1 = 1 + \dfrac{\omega_c}{\omega_o}\sin(\omega_o T_s) \\ a_2 = -2\cos(\omega_o T_s) \\ a_3 = 1 - \dfrac{\omega_c}{\omega_o}\sin(\omega_o T_s) \\ b_1 = -b_2 = \omega_c \sin(\omega_o T_s) \end{cases} \tag{29}$$

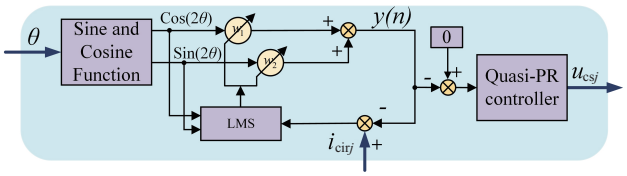

Fig. 6. Novel type of circulating current suppressor.

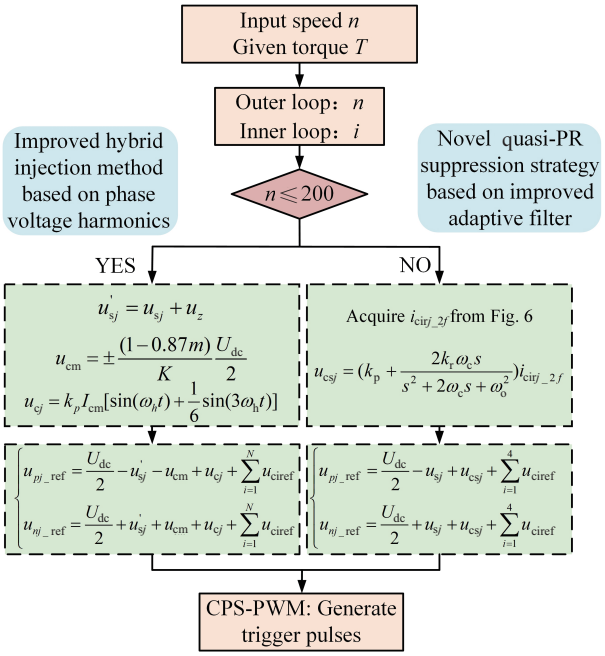

Fig. 7. Overall block diagram of high and low speed control.

The control block diagram of the novel circulating current suppressor based on the improved adaptive filter algorithm and the quasi-PR control is finally obtained as shown in Fig. 6.

The process of control action can be divided into the following three main parts:

1) First, the filter input signal is obtained using the sine-cosine function with i_{cirj} and θ as input parameters;

2) Then, the online adjustment of the circulating current harmonic amplitude weight coefficients is achieved by the variable convergence coefficient LMS algorithm;

3) Finally, with the target of turning the circulating current decreasing to 0, the u_{csj} is obtained by the quasi-PR controller and superimposed on the voltage modulated waveform of the upper and lower bridge-arms.

The overall block diagram of the MMC PMSM low- and high-speed control proposed in this paper is shown in Fig. 7.

IV. Simulation Results

Analysis of Improved hybrid injection method based on phase voltage harmonics

The three-phase five-level MMC PMSM simulation model is built according to the parameters as shown in Table II.

Under a 0.5 N·m load, the motor accelerates from 0 to 150 rpm with a frequency of 10 Hz during steady-state operation,

TABLE II
MMC PMSM SIMULATION PARAMETERS

Parameters	Value
DC bus voltage(V)	200
Number of submodules per	4
Number of motor pole pairs	4
Submodule capacitor(mF)	2.2
Bridge-arm inductor(mH)	7
System control frequency(Hz)	10000
Carrier frequency(Hz)	2000
Stator resistor(mΩ)	8
d-axis inductor(μH)	50
q-axis inductor(μH)	86

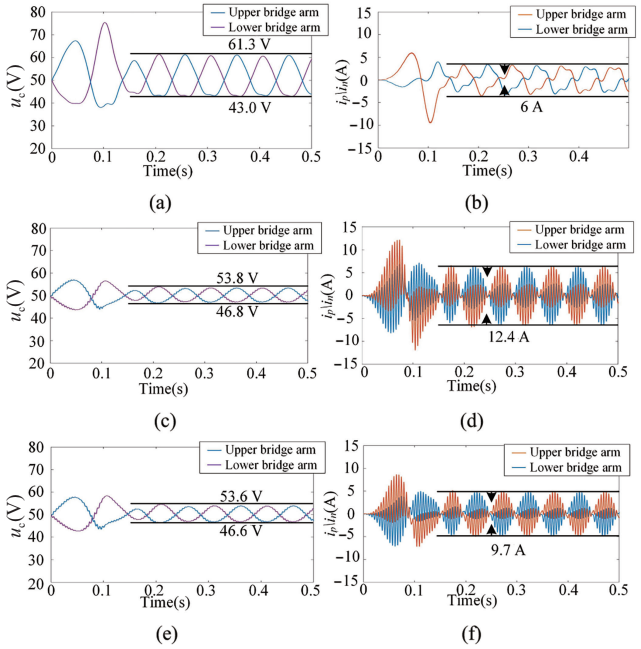

Fig. 8. (a) Capacitor voltage waveform with no high-frequency injection, (b) Bridge-arm current waveform with no high-frequency injection, (c) Capacitor voltage waveform with dual-sinusoial injection, (d) Bridge-arm current waveform with dual-sinusoial injection, (e) Capacitor voltage waveform with improved hybrid injection, (f) Bridge-arm current waveform with improved hybrid injection.

and the capacitor voltage waveform for this condition are shown in Fig. 8 shows the capacitor voltage waveform and bridge-arm current waveform under different methods.

As shown in Figs. 8(a), (c), and (e), without low-frequency suppression, the capacitor voltage fluctuates between 43 V and 61.3 V. After applying the dual-sinusoidal injection method, the fluctuation range is reduced to 46.8–53.8 V, indicating a peak-to-peak reduction of 11.3 V. The improved hybrid injection method, which incorporates phase voltage harmonic injection, achieves a similar level of fluctuation control, with a voltage range of 46.6–53.6 V.

As shown in Figs. 8(b), (d), and (f), applying the dual-sinusoidal injection method increases the peak-to-peak value of the steady-state bridge-arm current from 6 A to 12.4 A compared to the case without low-frequency suppression—an increase of 106.67%. In contrast, the proposed hybrid injection method incorporating phase voltage harmonic injection reduces the current amplitude to 9.7 A, representing a 21.17% reduction. The specific comparison results are summarized in Table III.

TABLE III
SPECIFIC DETAILS OF DIFFERENT STRATEGY

Strategy	Capacitor Voltage Fluctuation (V)	Bridge-Arm Current Peak(A)
No high-frequency injection	18.3	6
Dual-sinusoidal injection	7.0	12.4
Improved hybrid injection	7.0	9.7

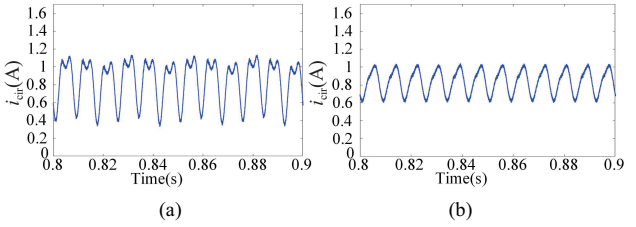

Fig. 9. Circulating current waveform. (a) CCSC, (b) Novel circulating current suppression method proposed in this paper.

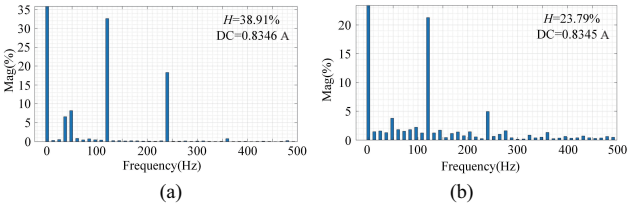

Fig. 10. FFT analysis of circulation. (a) CCSC, (b) Novel circulating current suppression method proposed in this paper.

B. Analysis of A Novel Circulating Current Suppression Method Based on Quasi-PR Control and Adaptive Filters

The harmonic inclusion rate H of the circulating current is defined to further analyse the harmonic situation:

$$H = \sqrt{I_1^2 + I_2^2 + I_3^2 \cdots + I_{\max}^2} \,/\, I \times 100\% \tag{30}$$

where I_x is the RMS value of the harmonic component of the circulating current with frequency x Hz, and I is the magnitude of the DC component of the circulating current.

The circulating current waveform of the negative sequence coordinate transform based circulating current suppression control algorithm (CCSC) and suppression algorithm proposed in this paper are shown in Fig. 9. The circulating current FFT results under the two algorithms are shown in Fig. 10.

Fig. 9 illustrates that, compared with CCSC, the proposed circulating current suppression algorithm achieves an 11.3% reduction in the second harmonic component of the circulating current. Fig. 10 demonstrates that the harmonic content of the circulating current decreases from 38.91% to 23.79%, corresponding to a 15.12% reduction.

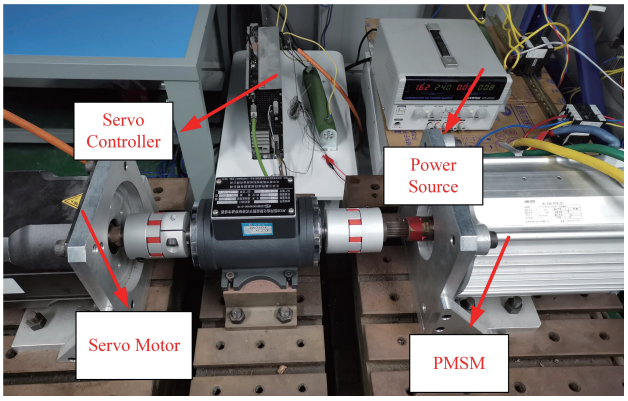

Fig. 11. Physical image of the towing motor platform.

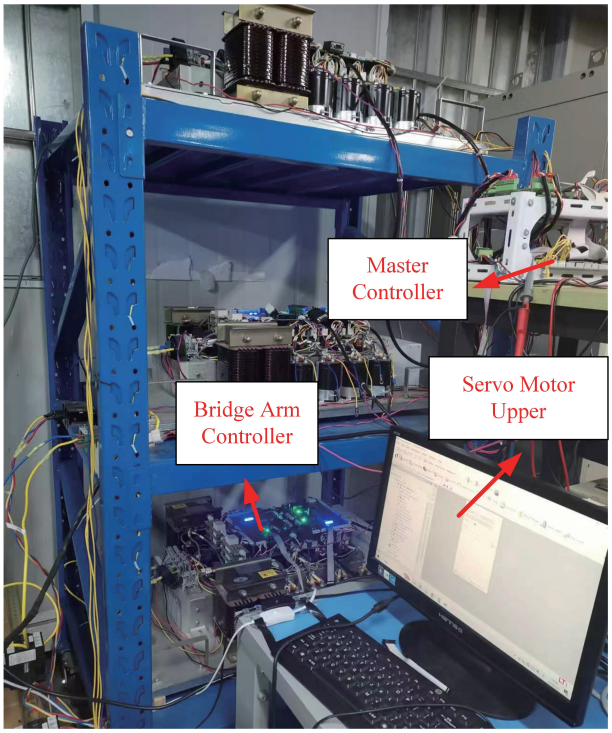

Fig. 12. MMC physical image.

V. Experimental Validation

In order to further verify the effectiveness of the proposed low-frequency suppression strategy, an experimental study was carried out on the constructed MMC PMSM experimental prototype, using the motor-to-drag platform physically shown in Fig. 11. The PMSM is connected to the MMC as the drive motor, and receives torque and speed commands from the host computer through the serial port. The servo motor and the drive motor are connected in coaxial for simulating the load.

The physical structure of the MMC prototype is shown in Fig. 12. The DC bus voltage is supplied by an external DC power source. The main circuit consists primarily of submodules installed on the six bridge arms of the three-phase system, along with the bridge-arm inductance. Each submodule adopts a half-bridge topology, and the specific device parameters are listed in Table II.

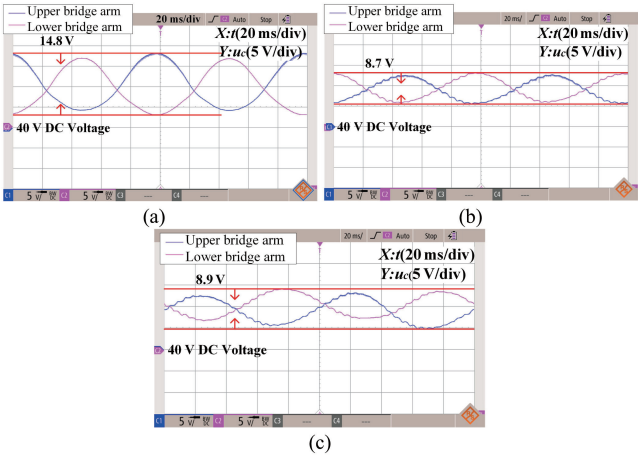

Fig. 13. Capacitor voltage waveform. (a) No high-frequency injection, (b) Dual-sinusoidal injection, (c) Improved hybrid injection based on phase voltage harmonic.

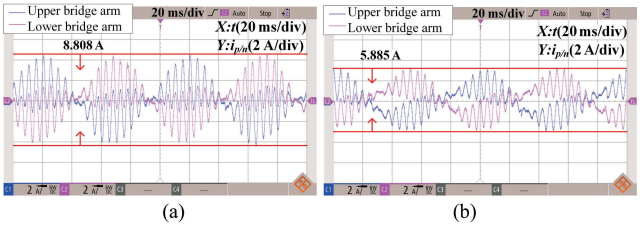

Fig. 14. Circulating current waveform. (a) Dual-sinusoidal injection, (b) Improved hybrid injection based on phase voltage harmonic.

A. Improved Hybrid Injection Method Based on Phase Voltage Harmonics

Fig. 13 shows the upper and lower bridge-arm capacitor voltage waveform under the motor speed of 150 rpm and current amplitude of 3 A.

Without low-frequency suppression, the peak capacitor voltage fluctuation reaches 14.8 V, accounting for 29.6% of the rated capacitor voltage. With the dual-sinusoidal injection method, the peak fluctuation is reduced to 8.7 V (17.4% of rated voltage), corresponding to a 12.2% suppression compared to the unsuppressed case. The proposed hybrid injection method incorporating phase voltage harmonics achieves a similar suppression effect, with a peak fluctuation of 8.9 V. The corresponding bridge-arm current waveforms under both injection methods are shown in Fig. 14.

When dual-sinusoidal injection is performed, the peak value of bridge-arm current reaches 8.808 A. When the improved hybrid injection based on phase voltage harmonic is performed, the peak value of bridge-arm current is reduced to 5.885 A, which is 33.18% lower compared to dual-sinusoidal injection method. The results indicate that the proposed hybrid injection method significantly reduces the amplitude of the injected circulating current.

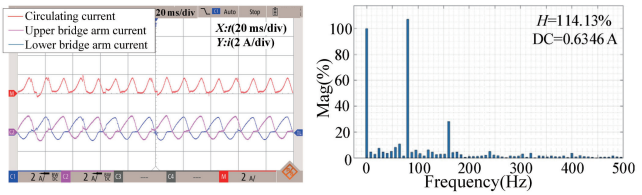

Fig. 15. No circulating current suppression. (a) B phase circulating current, (b) Circulating current FFT analysis.

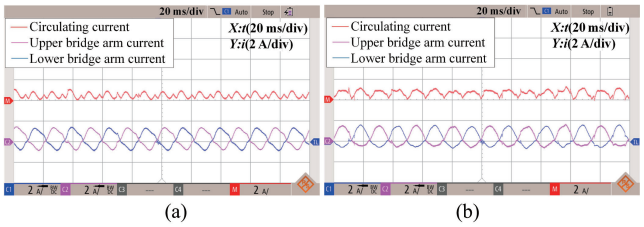

Fig. 16. B phase circulating current waveform. (a) CCSC, (b) Novel circulating current suppression.

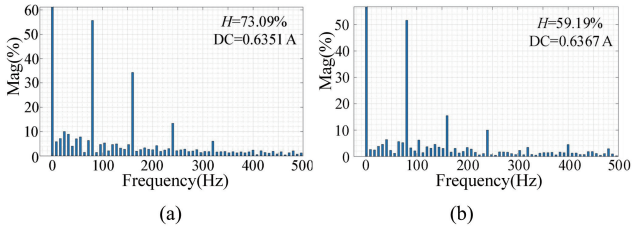

Fig. 17. Circulating current FFT analysis. (a) CCSC, (b) Novel circulating current suppression.

B. Novel Circulating Current Suppression Method Based on Quasi-PR Control and Adaptive Filter

In order to verify the effectiveness of the novel circulating current suppression method based on quasi-PR control and adaptive filter, an experimental study was carried out on the experimental prototype.

In the case of no circulating current suppression control, the motor speed is set to 600 rpm and the current amplitude is 2 A. The waveform of the B-phase upper and lower bridge-arm currents and circulating current are shown in Fig. 15(a), which corresponds to the circulating fundamental frequency of 40 Hz. The results of the circulating current FFT analysis are shown in Fig. 15(b), which shows that circulating current harmonics are mainly composed of even components such as second harmonic and fourth harmonic.

Subsequently, the CCSC and the novel circulating current suppression method based on quasi-PR control and adaptive filter were applied to the above systems. Fig. 16 illustrates the B phase circulating current waveform. Fig. 17 demonstrates the corresponding FFT analysis of this phase circulating current.

As shown in Figs. 16 and 17, the CCSC strategy reduces the harmonic containment rate H from 114.13% to 73.09%, representing a 41.04% decrease compared to the case without circulating current suppression. Additionally, the proportion of the second harmonic component relative to the DC component of the circulating current is reduced by 51.47%. Furthermore, compared to the CCSC strategy, the proposed suppression method reduces the harmonic containment rate from 73.09% to 59.19%, corresponding to a 13.90% reduction. Similarly, the proportion of the second harmonic component in the circulating current is further decreased by 4.05%. These results show that the proposed method reduces total harmonic distortion without increasing low-frequency or fourth harmonic components. This contributes to more effective circulating current suppression and enhanced efficiency of the drive system. The specific comparison results are summarized in Table IV.

TABLE IV
SPECIFIC DETAILS OF DIFFERENT STRATEGY

Strategy	Harmonic containment rate H
No circulating current suppression	114.13%
Traditional circulating current suppression (CCSC)	73.09%
Novel circulating current suppression	59.19%

VI. CONCLUSION

This paper investigates the application of MMC as a converter in electric vehicles and proposes a low-speed and high-speed control strategy for the PMSM drive system. To address the increased bridge-arm current caused by high-frequency current injection under low-speed conditions, which leads to elevated current stress on the switching devices, an improved hybrid injection strategy based on phase voltage harmonics is proposed. Furthermore, to overcome the limitations of coordinate transformation in accurately extracting the second harmonic component of the circulating current, a novel quasi-PR suppression strategy incorporating an adaptive filter is developed. Simulation and experimental results indicate that, while achieving a comparable level of capacitor voltage fluctuation suppression, the proposed method reduces the bridge-arm current by 33.19% compared with the dual-sinusoidal injection method, thereby effectively alleviating current stress on the switching devices. Compared to the conventional CCSC strategy, the proposed suppression method reduces the proportion of the second harmonic component in the circulating current by 4.05% and lowers the total circulating current harmonic content H by 13.9%, resulting in improved circulating current suppression.

Overall, the proposed strategies enhance the operational performance and robustness of electric vehicle drive systems.

REFERENCES

[1] A. Viatkin, M. Ricco, R. Mandrioli, T. Kerekes, R. Teodorescu, and G. Grandi, "A novel modular multilevel converter based on interleaved half-bridge submodules," in *IEEE Transactions on Industrial Electronics*, vol. 70, no. 1, pp. 125–136, Jan. 2023.

[2] Y. Zhang, S. Li, X. Zhang, C. Liu, Z. Liu, and B. Luo, "A hybrid low

capacitance modular multilevel converter for medium voltage PMSM drive and its control method," in *IEEE Access*, vol. 11, pp. 92796–92806, 2023.

[3] A. Marzoughi, R. Burgos, D. Boroyevich, and Y. Xue, "Design and comparison of cascaded H-bridge, modular multilevel converter, and 5-L active neutral point clamped topologies for motor drive applications," in *IEEE Transactions on Industry Applications*, vol. 54, no. 2, pp. 1404–1413, Mar.-Apr. 2018.

[4] Y. Zhang, Z. Guo, H. Li, and F. Peng, "A low-cost active reflected wave canceller for MMC motor drive using SiC devices," in *2022 International Power Electronics Conference (IPEC-Himeji 2022- ECCE Asia)*, Himeji, Japan, 2022, pp. 1090–1094.

[5] A. J. Korn, M. Winkelnkemper, and P. Steimer, "Low output frequency operation of the modular multi-level converter," in *2010 IEEE Energy Conversion Congress and Exposition*, Atlanta, GA, USA, 2010, pp. 3993–3997.

[6] J. Yu and C. Xia, "Capacitor voltage fluctuation suppression method based on improved MMC topology for variable-frequency drive application," in *CPSS Transactions on Power Electronics and Applications*, vol. 7, no. 2, pp. 150–159, Jun. 2022.

[7] Y. Zhang, Y. Zhang, and Z. Wang, "Reliability-oriented adaptive switching frequency scheme for modular multilevel converters," in *CPSS Transactions on Power Electronics and Applications*, vol. 9, no. 1, pp. 1–9, Mar. 2024.

[8] S. Jiang and Z. Bai, "Low frequency operation control method for modular multilevel converter based on improved arm current prediction," in *2023 IEEE 6th International Electrical and Energy Conference (CIEEC)*, Hefei, China, 2023, pp. 1346–1351.

[9] S. Du, B. Wu, N. R. Zargari, and Z. Cheng, "A flying-capacitor modular multilevel converter for medium-voltage motor drive," in *IEEE Transactions on Power Electronics*, vol. 32, no. 3, pp. 2081–2089, Mar. 2017.

[10] S. Du, B. Wu, and N. Zargari, "A control strategy for star-channel modular multilevel converter in variable-speed motor drive application," in *IEEE Transactions on Industrial Electronics*, vol. 66, no. 7, pp. 5094–5101, Jul. 2019.

[11] S. Du, B. Wu, and N. R. Zargari, "A delta-channel modular multilevel converter for zero/low-fundamental-frequency operation," in *IEEE Transactions on Industrial Electronics*, vol. 66, no. 3, pp. 2227–2235, Mar. 2019.

[12] R. Aguilar, L. Tarisciotti, and J. Pereda, "Circulating current suppression in DAB assisted low-voltage variable frequency MMC," in *IEEE Transactions on Industry Applications*, vol. 58, no. 5, pp. 6322–6331, Sept.-Oct. 2022.

[13] Zhang, T. Song, Y. Qi, H. Li, S. Hua, and J. Cai, "Research on improved low frequency control strategy of MMC driven permanent magnet synchronous motor," in *2022 China International Conference on Electricity Distribution (CICED)*, Changsha, China, 2022, pp. 971–975.

[14] N. Aarzoo and G. Poddar, "Input current source-based modular multilevel converter for wound field synchronous machine drive with improved low-speed operation," in *IEEE Journal of Emerging and Selected Topics in Industrial Electronics*, vol. 4, no. 1, pp. 419–429, Jan. 2023.

[15] Z. Li, Q. Song, B. Zhao, Z. Yu, R. Zeng, and B. Cui, "Analysis of ride-through capability of unidirectional-current MMC with arm current unidirectionality disrupted," in *IEEE Transactions on Power Electronics*, vol. 39, no. 8, pp. 9257–9267, Aug. 2024.

[16] J. Han and C. Liu, "Quasi proportional resonant controller based MMC grid side harmonic suppression research," in *2022 IEEE International Conference on Power Systems and Electrical Technology (PSET)*, Aalborg, Denmark, 2022, pp. 240–245.

[17] W. Chao, J. Huang, C. Deng, and L. Dai, "Fuzzy adaptive PI circulating current suppressing control for MMC-HVDC," in *2023 IEEE 6th Information Technology,Networking,Electronic and Automation Control Conference (ITNEC)*, Chongqing, China, 2023, pp. 1163–1167.

[18] H. Wang, P. Huang, Y. Chen, Z. Lin, and R. Huang, "Impedance coupling suppression mechanism of high-voltage direct-current transmission system with large-scale renewable energy," in *2023 10th International Forum on Electrical Engineering and Automation (IFEEA)*, Nanjing, China, 2023, pp. 738–743.

[19] S. Jakkula, N. P. Rao, and A. Shukla, "A novel circulating current suppression control utilizing negative insertion in MMC," in *2024 IEEE Applied Power Electronics Conference and Exposition (APEC)*, Long Beach, CA, USA, 2024, pp. 238–243.

[20] Q. Wang, H. Ye, and G. Zhang, "Analysis of the circulating current characteristics of MMC in DQ frame," in *2017 IEEE Conference on Energy Internet and Energy System Integration (EI2)*, Beijing, China, 2017, pp. 1–6.

[21] Y. Wang, C. Zhao, and R. Iravani, "Small signal stability investigation of the MMC-HVDC grid," in *IEEE Transactions on Power Delivery*, vol. 37, no. 5, pp. 4448–4459, Oct. 2022.

[22] R. Mishra and V. Agarwal, "Modified series chain link MMC for offshore wind farms with boosted AC voltage: Frequency-domain modeling and submodule capacitor voltage ripple optimization," in *IEEE Transactions on Industrial Electronics*, vol. 70, no. 9, pp. 8676–8687, Sept. 2023.

[23] J. Xu, J. Wang, Y. Yang, J. Wang, and G. Li, "Optimal suppression strategy for capacitor voltage ripples of hybrid MMCs under unbalanced grid voltages," in *IEEE Transactions on Power Delivery*, vol. 38, no. 1, pp. 244–254, Feb. 2023.

[24] X. Chen and J. Zhang, "MMC circulation suppression optimization strategy based on quasi-PIλR controller," in *2023 IEEE International Conference on Advanced Power System Automation and Protection (APAP)*, Xuchang, China, 2023, pp. 167–172.

Jianfei Zhao received the B.S. and M.S. degrees in Mechatronic Engineering from the Xi'an Jiaotong University, Xi'an, China, in 2000 and 2003, respectively. He received the Ph.D. degree in Electrical Engineering from Shanghai Jiao Tong University, Shanghai, China, in 2012. From 2003 to 2006, he worked as a R&D Engineer and Project Manager in R&D Center of Myway-labs Co.,Ltd in Japan. Now, he is working as an Associate Professor with the Mechatronic Engineering and Automation School, Shanghai University. He is the author of more than 50 academic papers. His research interests include power electronics and electronic vehicles. Dr. Zhao was a recipient of the Science and Technology Progress Award of the Ministry of Education of China in 2009 and 2012, the Science and Technology Progress Award of Shanghai City in 2019, the Science and Technology Progress Award of China Electrotechnical Society in 2009 and 2010.

Sucheng Huang received the B.S. degree in Electrical Engineering and Automation from Shanghai University, Shanghai, China, in 2024 and now he is pursuing the M.S. degree in Electrical Engineering at the same university. His research interest mainly involves in the drive control of new energy electric vehicles.

Yuanyuan Xing received the B.S. degree in Electrical Engineering and Automation from Shanghai University, Shanghai, China, in 2023, where she is currently pursuing the M.S. degree in electrical engineering. Her research interests include electric vehicle drive control and new energy generation.

Adaptive Gain Changer for Precise Passivity Theory Controlled IM-DC Motor System for FEV Application

Arathy Rajeev V. K. and P. VALSALAL

***Abstract*—A passivity based control (PBC) technique is implemented for boost converter and inverter fed to induction motor coupled with DC motor. The boost converter has the advantage of giving high output voltage with less switching losses due to low operating voltage of MOSFET and low operating duty cycle. For gain optimization a feedback loop have been designed and implemented in this paper. It is found that feedback loop efficiency contributes to dynamic error detection and thereby reducing transient settling time of controller. The inverter provide reference speed to induction motor having motor torque and, load torque is applied through DC motor. The exact tracking error dynamics passive output feedback control is selected among PBC techniques as it satisfies exponential stability criteria. The system tracks the variation in speed and torque for few seconds and is verified by MATLAB/Simulink as well as field programmable gate arrays (FPGA) controller in hardware platforms.**

***Index Terms*—Boost converter, energy shaping damping injection (ESDI), exact tracking error dynamics passive output feedback (ETEDPOF), field programmable gate arrays (FPGA), full electric vehicle (FEV), induction motor (IM), passivity based control (PBC).**

Nomenclature

V_s, i_s, Ψ_s	Stator voltage, current and flux linkage vectors.
i_r, Ψ_r	Rotor current and flux linkage vectors.
R_s, R_r, L_s, L_r	Stator and rotor resistance and inductance.
M	Mutual inductance between stator and rotor.
τ, τ_m	Normalised time and overall mechanical time constant.
ω_k, ω, ω_{sR}	Angular velocity of reference frame, rotor and rated stator frequency.
Θ, N	Rotor angle and positive constant related to mass of the load and coefficient of gravity.
T_E	Generated electromagnetic torque.
J	Energy storage matrix.
R	Energy dissipation matrix.
j	Imaginary axis in s-plane.
B	Friction coefficient.
L	Inductance of converter.
C	Capacitance of converter.
u	average control input.
i	current input.
E	converter input voltage.
v	converter output voltage.
i_{am}	current input to inverter or motor current.
U	output voltage of boost converter.
D	duty cycle of boost converter.

Manuscript received June 6, 2025; revised August 22, 2025; accepted September 21, 2025. Date of publication December 30, 2025; date of current version December 2, 2025. No funding was received to assist with the preparation of this manuscript. (*Corresponding author: Arathy Rajeev V. K.*)

Both authors are with Department of EEE, CEG, Anna University, Chennai 600025, India (e-mail: arathy@student.annauniv.edu; valsalal@annauniv.edu).

Digital Object Identifier 10.24295/CPSSTPEA.2025.00035

I. Introduction

THE environmental issues caused by greenhouse gases have resulted in focusing more on energy conservation and emission reduction. Conventional fuel vehicles used for transportation is one of the major causes of emission as fuel vehicles which contribute to greenhouse gas emissions. Hence electric vehicles (EVs) are used after the development of batteries for promoting eco-friendly vehicles. The EV and hybrid electric vehicle (HEV) are more common in the market and people have started using them. The major concerns of EV are high instant power, high-power density and fast torque response [1].

The ability to operate at constant power for a wide range of speed, high efficiency and good overload performance are the major requirements of EV. These depend on battery capacity utilization, size and weight of motor as well as drive. Generally, induction motor, BLDC motor and SRM motors are widely used for EV application. Because of ruggedness, three phase induction motor is chosen for this study [2].

Generally, induction motor is less complicated, durable equipment and it runs at almost constant speed when it is controlled directly from main supply voltage. The dynamics of an induction motor is nonlinear. Even though induction motor has got many advantages, controlling of this motor, is challenging one, because rotor fluxes and currents deviate more. A passivity bend composite adaptive position control technique for induction motors is explained [3]. First, it is demonstrated that an induction motor dynamics are completely passive and a composite adaptation method is suggested to regulate position of induction motor. The passivity theory then officially establishes the global stability of induction motor position control system. Both voltage and frequency need to be changed in order to produce adjustments in speed and torque. The following insight is that voltage to frequency ratio ought to be relatively constant. Furthermore, lower efficiency and higher losses of induction motor when operating at varied speeds are main disadvantages. The demand for efficient drive systems is met by sophisticated controllers, which are not only altered losses and efficiency

but also looked for best stator current values to reduce source power consumption. The main problem is decreasing power resources which requires development of optimal controller design for electrical machines. Z. G. Wu deals with the problem of asynchronous passive control for Markov jump systems [4]. A hidden Markov model describes the asynchronization phenomena, which occurs between controller modes and system modes. The investigation demonstrates that there is a chance to reduce power consumption and increase induction motor efficiency. Drive system optimization is the term used to describe the control system, which meets all these requirements. Moreover, some optimal controllers have been developed to achieve good speed control principles while others have been created to increase accuracy and efficiency [5]. However, today's focus is on energy conservation. The energy efficiency is discussed in passivity based control (PBC), which deals with total energy of system. To offer precise monitoring of time-varying speed and flux trajectories in high magnetic saturation regions, a passivity-based controller considers saturation of magnetic material in the primary flux channel of induction motor [6]–[8].

In order to create the first wireless AC motor, a wireless shaded-pole induction motor (SPIM) skill-fully combines wireless power transmission into a single-phase SPIM [9]. The objective is to suggest a receiver self-driving circuit and drives SPIM with variable voltage and frequency. As a result, the suggested wireless SPIM gains the undeniable advantages of being completely sealable and electrocution-free. The construction of this type of induction motor is updated by Mei et al. [10]. The six-pole double-stator, double-rotor, distributed-winding axial flux induction motor with decreased back iron for electric cars is built. The design element reveals that both sets of magnetic fluxes from stator windings pass through rotor of motor without affecting them. This construction eliminates axial attractive force, and hence reducing the mechanical bearing loss. The motor is also smaller and lighter, saving more materials overall.

The total energy of the system is algebraic sum of energy stored in system and energy dissipated from the system. The desired trajectory is tracked based on Euler Lagrange equation using Hamiltonian operator [11]. The dissipation energy of the system is adjusted using a constant damping factor. A PBC method namely, exact tracking error dynamics passive output feedback (ETEDPOF) is selected to control induction motor as it tracks dynamic error which reduces the effect of transients in the system. ETEDPOF method is a simple linear time-invariant controller. The system error dynamics is plotted using Hamiltonian operator. This is stabilized by finding equilibrium points by equating the dynamics to zero. Therefore, structural dissipation matching condition is satisfied and hence asymptotically stable equilibrium points is achieved in close loop system. ETEDPOF method is preferred controller over energy shaping damping injection (ESDI) method since the controller state computation is absent. The existing control techniques are presented in Section II. The hardware controller is discussed in Section III. Problem is stated in Section IV. Proposed system is described in Section V. Proposed control method design procedure is elaborated in Section VI. Induction motor is modelled using ETEDPOF control, in Section VII. Modelling of boost converter is given in Section VIII. Software results are produced in Section IX. Comparison of proposed system with sliding mode controller (SMC) is given in Section X. Hardware results are in Section XI. Application and conclusion of research work are shown in Sections XII and XIII respectively.

II. Few Existing Control Strategies

Fault tolerant control is proposed to drive induction motor by limiting the current and voltage to a specified value [12]. A stator turn-to-turn defect detection method for induction motors operated by direct torque control for electric car powertrains is created [13]. The devised approach is based on stator currents and applying discrete wavelet transformation technique. This is a time-frequency domain-based technique which handles non-stationary signals. Zero voltage switching to turn on and zero current switching to turn off a single stage single phase isolated AC-DC converter is discussed in [14]. This converter is used for EV onboard charging with power decoupling. The design and functionality of 1-DOF (degree of freedom) and 2-DOF configurations with two controllers and associated prefilters are printed and hence the main circuit performs better than a 1-DOF structure. J. Su, R. Rao et al. [15] describe model predictive control algorithm for same EV application using induction motor. Here, the weight coefficient in cost function is adjusted for speed variations. A genetic algorithm for two stators with one rotor axial flux induction motor is discussed [16]. The machine is applied for EV and speed optimization time is better by using this genetic algorithm technique.

Due to presence of flux, current limit in an induction motor drive is not as straightforward as one in a permanent magnet motor drive. The performance of existing fault-tolerant three-phase induction motor drives has been re-examined by M. Tousizadeh [17], has taken into account, the effects of both inverter, and machine voltage limits as well as current limits. The effects of machine characteristics, operating point on voltage limit and speed limit are separated by obtaining postfault machine voltage equations. Only machine model is utilised in traditional predictive torque control (PTC) for estimating stator flux, current, and electromagnetic torque [18]. The given control technique, in contrast to conventional PTC, provides a nonlinear switching feedback element in prediction equation to deal with model errors, disturbances, and fluctuation in motor characteristics. Based on Lyapunov stability criteria, gains of feedback terms are chosen. For the purpose of estimating speed and rotor flux, an adaptive full order observer is employed. A high efficiency traction motor is designed and controlled using space vector modulation technique for achieving long driving range of EV [19]. Each open-ended phase winding in an induction motor is powered using a single H-bridge inverter. The common mode voltage and zero sequence voltage are analysed. Flux weakening is the major drawback for EV application. Recently, a study is made regarding improvement of flux, which can be extended to induction motor [20]. SMC for EV is discussed in [21]. The torque distribution coefficients are varied for dual motor EV stability. Maximum torque per ampere is

TABLE I
FEW EXISTING CONTROL STRATEGIES FOR EV USING INDUCTION MOTOR

Control methodology	Peak overshoot speed/rps	Settling time/s
Fault tolerant control	65 (Reference 50 rad/s)	0.61
Model predictive control	2500 (Reference speed 2500 rpm)	0.90
Sliding model predictive torque control	No overshoot smooth transition (Reference speed 150 rad/s)	0.45
Predictive-PI control	No overshoot smooth transition (Reference 12000 rpm)	0.61

realised in [22]. PBC is used for DC motor speed control in [23]. The motor is driven using boost converter and load torque estimation is done to eliminate speed sensors. The voltage source converter (VSC) is a linear time invariant system. PBC is used in [24] to derive control law for dual loop control method. The control algorithm is proposed for permanent magnet traction electric motor. Torque producing current and flux producing currents govern this control method. Comparison of strategies of EV are shown in Table I.

III. FIELD PROGRAMMABLE GATE ARRAYS (FPGA)

Application specific integrated circuit (ASIC) and FPGA share many of the same structural building blocks. The primary distinction between them is that FPGA has pre-set design, whereas ASIC has fixed architectures of fundamental components for different purposes [25]. Users of FPGAs can create their own digital circuits or architecture by designing and synthesising their own fields of programmable fundamental elements. In this programmable area, digital circuits are divided and operated in parallel [26]. The main advantage of FPGA is parallelism, which enables tens or even hundreds of processes to run simultaneously. The number of fundamental components is the only restriction on number of parallel circuits. The clock speed, which is ten times slower than the clock of an ASIC, is one of the numerous shortcomings. The difference is due to the fact that ASICs is tailored for speed and power consumption whereas FPGAs have general-purpose parts. The FPGA have utilised maximum clock frequency of 50 MHz and high-speed data processing, where diverse processing methods can be parallelized, and hence may be thanked for hardware description languages (HDL).

Because of their affordable volume cost and shorter time to market than other options, FPGAs are a strong solution for digital system implementation. Typically, FPGAs consist of the following features that make them more reliable and market friendly:

1) Programmable logic blocks carry out logic operations.

2) The programmable routing, that links these bit logic operations.

3) I/O blocks form off-chip connections and are coupled to logic blocks via routing interconnect.

IV. PROBLEM STATEMENT

The control of induction motor for EV application requires precise speed control for a wide range. The efficiency and performance of machine are required to be good at high speeds. The proposed controller uses less number of gain parameters, two gain values to achieve desired trajectory. Other control technique (SMC), require five gain parameter adjustment for the proposed system. Non-linear control techniques and various pulse width modulation (PWM) strategies are used to achieve speed control but control complexity is increased. Hence, nonlinearities are linearised in operating range and control law is generated using ETEDPOF method. PBC is a linear control technique which can overcome all complexities with online gain monitoring method. One of the PBC control namely ETEDPOF is proposed and voltage input is given from a boost converter to increase the efficiency. The induction motor is coupled with a DC motor as load. The controller is verified using MATLAB/Simulink model and is further implemented using FPGA hardware controller. The load torque is varied with respect to varying reference speed for thorough analysis.

V. PROPOSED SYSTEM

The block diagram of proposed system is given in Fig.1. The input is from a battery supply. If the system is connected for charging, rectifier and filter in Fig.1, will be connected to system. There is cascaded multiple supply input based on EV's mode of operation. The induction motor is triggered using an inverter. The input of inverter is controlled using boost converter which acts like a programmable DC supply. The LC filter is used to reduce the harmonics of rectified AC supply. A diode bridge rectifier is used for rectification. The gate pulses to boost converter and inverter are given from FPGA controller. The ETEDPOF control technique is used to drive induction motor, which tracks the dynamic error of state variables. For gain optimization, a feedback loop have been designed and implemented in this paper. It is found that feedback loop efficiency contributes to dynamic error detection and thereby reducing transient settling time of controller. The DC link capacitor stabilises the voltage to inverter or provides a ripple free voltage to inverter.

FPGA is selected, as one can implement parallel tasks for controlling action. In addition to control algorithm, FPGA must do other functions such as two channel high sample rate data acquisition, high-rate digital filtering on both channels, PWM modulation, command execution, and serial communication with computer to send voltage and current measurements. In Fig. 1, every activity is running in parallel with high priority. With exception of order being higher, digital filters are likewise created as transfer functions and implemented in the same manner as the controller. Digital filters' transfer functions are 4th order, regardless of order of transfer function, and the calculation speed is constant. Noises produced by high frequency switching are filtered out by filters.

Data conversion, which turns the relative value of digital data from A to D (analog to digital) converter into physical value,

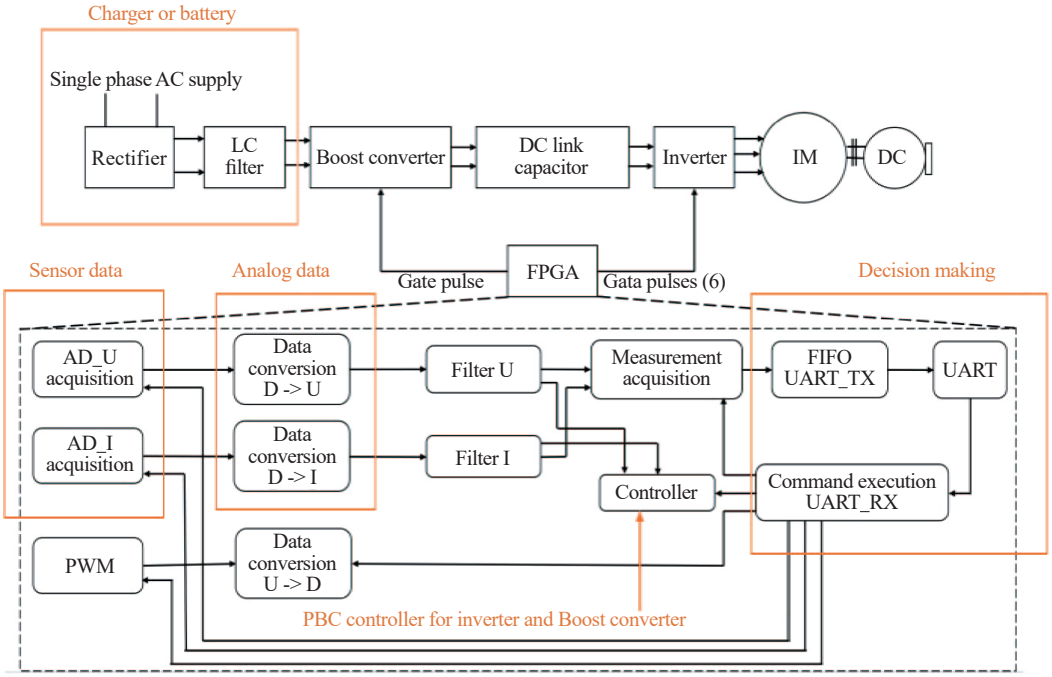

Fig. 1. Block diagram of proposed system.

is a crucial data processing step throughout the processing chain, from collection to control. Additionally, serial computer connectivity and measurement gathering are two crucial jobs. Using measurement acquisition, output voltage and inductor current of boost converter may be recorded. Samples of these measurements are then uploaded to the computer and plotted on a graph.

The proposed system is controlled using PBC based ETEDPOF controller as explained in Fig. 2. The system comprises of two power electronic converters, boost converter and inverter. The capacitor voltage and inductor current of boost converter are adjusted in such a way that whole system operates in continues conduction mode. The inverter always receives a minimum input voltage from boost converter. The induction motor is also proposed to run in a minimum of 0.5 duty cycle to reduce losses and improve steady state error. The variation in speed, start and stop of vehicle are verified using DC motor load for PBC algorithm.

The grid along with boost converter based on PBC, act as a programmable DC supply. The analysis is done using MATLAB/Simulink model and is implemented using FPGA controller in hardware. In prototype model, DC motor is connected to wheel of EV and controller gives pulse to induction motor. The power circuit and control circuit are available in controller part of the proposed system. The proposed system circuit diagram is given in Fig. 3.

Rectifier: DC supply is generated from single phase AC supply using a rectifier.

LC filter: DC harmonics present in rectified supply is eliminated with help of LC filter. The ripples in voltage are reduced below 3%.

Boost converter: The input is boosted to minimum voltage or reference voltage proportional to speed of the machine.

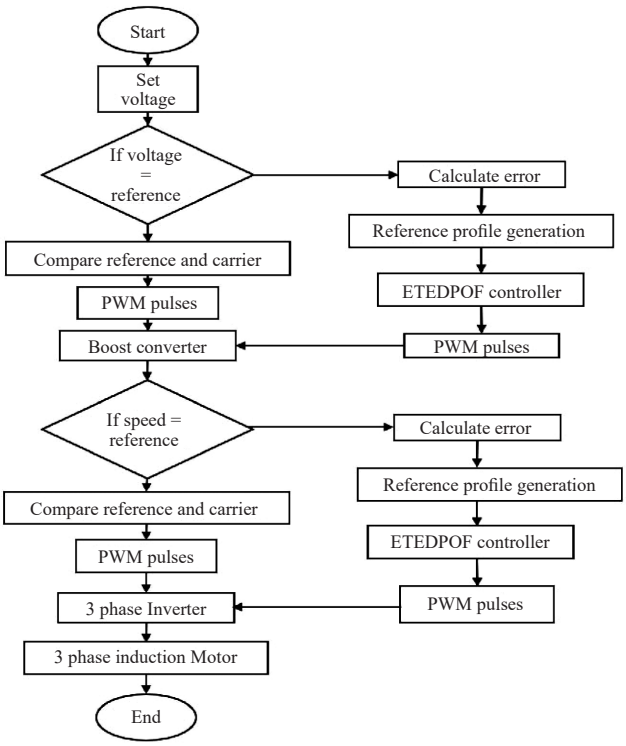

Fig. 2. Flowchart of proposed system.

Boost converter is used by considering, there is no zero-speed condition but only break condition. The system will run at minimum speed of 500 rpm always.

DC-link capacitor: The voltage is balanced and ripples are reduced using an interlink DC capacitor between two converters.

Inverter: The DC voltage is converted to AC by an inverter.

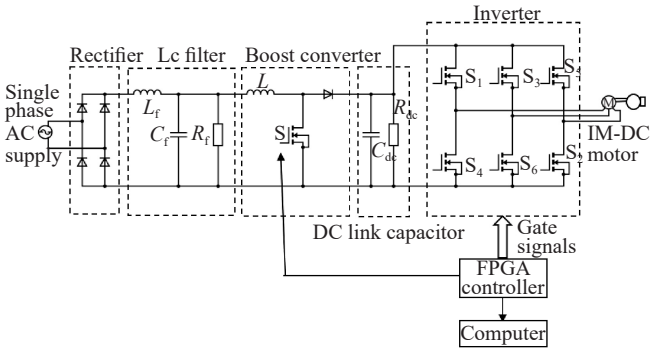

Fig. 3. Proposed system circuit diagram.

This AC supplies induction motor. The input is a varying DC according to reference speed. The gate pulses are fed from the speed observer.

IM coupled with DC motor: The wheel operation in an EV is represented by mechanical coupling of induction motor with DC motor and is used for driving a full EV (FEV).

VI. Exact Tracking Error Dynamics Passive Output Feedback Design Procedure

ETEDPOF method is used to derive control law for inverter fed induction motor. In this method, average system model characterizes exact dynamic model of stabilization error. The energy management structure of error dynamics is expressed in a generalized Hamiltonian form. So, the passive output is related to error dynamics. By identifying this error dynamics, a time invariant feedback controller is designed. According to Hebertt Sira-Ramirez et al. [2], if a dissipation matching condition is satisfied then equilibrium point will be semi-globally asymptotically stable equilibrium for a closed loop system. For control law generation, tracking of reference state trajectory with analogous reference control input trajectory is attained by

$$u - u^* = -\gamma\, \tilde{b}^{\mathrm{T}} \left[\frac{\partial H(e)}{\partial e} \right]^{\mathrm{T}} = -\gamma\, \tilde{b}^{\mathrm{T}} M e \tag{1}$$

where

$$\tilde{b} = b + \frac{\partial J(u)}{\partial u} \left[\frac{\partial H(e)}{\partial e} \right]^{\mathrm{T}} \tag{2}$$

The variations in control variable of state system are tracked by Jacobian matrix and the computed error is minimized using a Hamiltonian operator which represents energy stored in the system.

VII. Modelling of Induction Motor for EV Using ETEDPOF Method

The machine model of induction motor is given in [7].

$$V_{\mathrm{s}} = R_{\mathrm{s}} i_{\mathrm{s}} + j\omega_{\mathrm{k}} \Psi_{\mathrm{s}} + \frac{\mathrm{d}\Psi_s}{\mathrm{d}_\tau} \tag{3}$$

$$0 = R_{\mathrm{r}} i_{\mathrm{r}} + j(\omega_{\mathrm{k}} - \omega)\Psi_{\mathrm{r}} + \frac{\mathrm{d}\Psi_r}{\mathrm{d}_\tau} \tag{4}$$

where, $\Psi_{\mathrm{s}} = L_{\mathrm{s}} i_{\mathrm{s}} + M i_{\mathrm{r}}$, $\Psi_{\mathrm{r}} = L_{\mathrm{r}} i_{\mathrm{r}} + M i_{\mathrm{s}}$.

$$T_{\mathrm{e}} = |\Psi_{\mathrm{s}} \times i_{\mathrm{s}}|_{\mathrm{z}} = \tau_{\mathrm{m}} \frac{\mathrm{d}\omega}{\mathrm{d}t} + B\omega + N\sin\theta \tag{5}$$

$$\tau = \omega_{\mathrm{sR}} \times t \tag{6}$$

The above-mentioned equations are basic machine model equations of induction motor. From these equations the cartesian representation model is derived for control law generation for the proposed system.

A. Control Law Generation

The state variables are stator currents in cartesian representation i_d and i_q, which can be expressed as

$$\frac{\mathrm{d}i_d}{\mathrm{d}t} = \frac{1}{N}(V_d - e_d) \tag{7}$$

$$\frac{\mathrm{d}i_q}{\mathrm{d}t} = \frac{1}{N}(V_q - e_q) \tag{8}$$

The electromotive forces in (7) and (8) can be expressed as

$$e_d = R_{\mathrm{s}} i_d + \frac{L_{\mathrm{m}}}{T_{\mathrm{r}}}(i_d - i_{\mathrm{r}}) - (n_{\mathrm{p}}\omega + \frac{1}{T_{\mathrm{r}}}\frac{i_q}{i_{\mathrm{r}}}) N i_q \tag{9}$$

$$e_q = R_{\mathrm{s}} i_{\mathrm{q}} + (n_{\mathrm{p}}\omega + \frac{1}{T_{\mathrm{r}}}\frac{i_q}{i_{\mathrm{r}}})(N i_d + L_{\mathrm{m}} i_{\mathrm{r}}) \tag{10}$$

Equations have to be divided into Hamiltonian model representation to determine energy parameters, i.e., we have to separate energy dissipation and storage elements to form a state variable depending parameter which can be controlled externally. The state space model of induction motor is decomposed into J, R and M matrices as given below.

$$u = Jx + Rx + M\dot{x} \tag{11}$$

where, $\boldsymbol{J} = \begin{bmatrix} 0 & \frac{\omega_{\mathrm{e}} T_{\mathrm{r}}}{L_{\mathrm{m}}} & 0 \\ \frac{-\omega_{\mathrm{e}} T_{\mathrm{r}}}{L_{\mathrm{m}}} & 0 & 0 \\ 0 & 0 & 0 \end{bmatrix}$, $\boldsymbol{R} = \begin{bmatrix} R_\sigma & 0 & 0 \\ 0 & \frac{1}{L_{\mathrm{m}}} & 0 \\ 0 & 0 & B \end{bmatrix}$,

$\boldsymbol{M} = \begin{bmatrix} \sigma L_{\mathrm{S}} & 0 & 0 \\ 0 & \frac{T_{\mathrm{r}}}{L_{\mathrm{m}}} & 0 \\ 0 & 0 & J \end{bmatrix}$, $x = [i_{\mathrm{s}}\ \ \Psi_{\mathrm{r}}\ \ \omega_{\mathrm{m}}]$. $u = [V_{\mathrm{s}} - V_{\mathrm{b}}\ \ i_{\mathrm{s}}\ T_{\mathrm{l}}]$.

After decomposing these matrices, the stability criterion is verified. It is found that J is skew symmetric in nature and R is a symmetric matrix. Now the control law is generated from (3). The solution may be given as

$$V_{\mathrm{s}} = \gamma\,[R_\sigma i_{\mathrm{s}}^* + V_{\mathrm{b}} + R_{\mathrm{i}}(i_{\mathrm{s}}^* - i_{\mathrm{s}})] \tag{12}$$

The above control law has no integral or derivative terms. Therefore, the system control law is linear in nature. The desired trajectory of stator current converges to actual values. The damping factor is tuned nearer to system equilibrium point to

achieve desired trajectory during transient condition.

B. Reference Profile Generation

The control law in (12) is found to depend only on stator currents of induction motor. In induction motor it is represented as ratio of corresponding stator voltage and stator resistance. It can be represented as.

$$i_s^* = \frac{V_S}{R_S} \tag{13}$$

Stator current in each phase depends on torque angle based on (5). The flux in each phase is required to predict the position of rotor phase and pulses should be send to inverter switches based on rotor position.

C. Gain Optimization

The coefficients g_1 and g_2, which are obtained, may be tuned manually by trial-and-error method. Since the traditional method is time consuming, it is better to go for error profile generation of system and find system error dynamics trajectory, which is done in this paper. For any system to be stable, the dynamics is forced to nullify. This is used to find time varying gain coefficients of linear controller.

$$\dot{e} = \dot{x} - \dot{x}^* \tag{14}$$

By substituting the state space equation for actual and desired system, we obtain dynamic error trajectory of the system which is as follows:

$$\dot{e}(t) = (J - R)\left[\frac{\partial H(e)}{\partial e}\right]^{\mathrm{T}} + J\left[\frac{\partial H(x^*)}{\partial x^*}\right]^{\mathrm{T}} e_{\mathrm{u}} + \varepsilon - \varepsilon^* \tag{15}$$

where

$$e_{\mathrm{u}} = -\gamma\left[\frac{\partial H(x^*)}{\partial x^*}\right] J^{\mathrm{T}}\left[\frac{\partial H(e)}{\partial e}\right]^{\mathrm{T}} \tag{16}$$

The J matrix is independent of switching function 'u'. Therefore, e_{u} can be neglected and (15) becomes

$$\dot{e}(t) = (J - \tilde{R})\left[\frac{\partial H(e)}{\partial e}\right]^{\mathrm{T}} \tag{17}$$

where

$$\tilde{R} = \begin{bmatrix} g_1 & 0 \\ 0 & g_2 \end{bmatrix} \tag{18}$$

Substituting gain values in (18) and equating to zero, we get

$$g_1 = R_\sigma = \omega_{\mathrm{r}} L_d e_d \tag{19}$$

$$g_2 = R_{\mathrm{s}} = -\omega_{\mathrm{r}} L_q e_q \tag{20}$$

Gain parameters are found to depend on speed, self-inductance and electromotive forces generated inside an electric motor. The speed value is fed from speed sensor and will be varying instantaneously. Online adaptive gain is obtained by making current dynamics of the state equation zero. This is also similar and opposite in nature, so the supply voltage can increase or decrease with this equation. Both running and braking of EV can be controlled using this developed controller. The motor specifications are given in Table II.

TABLE II
SPECIFICATIONS OF INDUCTION MOTOR

Parameters	Values
No. of poles	4
Rated power	1000 W
Rated voltage	460 V
Rated speed	4000 rpm
Torque constant	1.2 Nm/A
Phase resistance	1.115 Ω
Phase inductance	5.974 mH
Moment of inertia	0.2×10^{-3} Nm/s^2

VIII. MODELLING OF BOOST CONVERTER SYSTEM USING ETEDPOF METHOD

The machine always runs at open loop speed and never reaches zero speed unless it is halted. Boost converter, which always has a minimum voltage, is chosen for this study based on these two criteria. Since target trajectory is a linearized model of converter system, ETEDPOF technique monitors the error more quickly. The controller now functions as a linear controller. The state space average model for boost converter is shown below.

$$L\frac{\mathrm{d}i}{\mathrm{d}t} = -(1-u)v + E \tag{21}$$

$$C\frac{\mathrm{d}v}{\mathrm{d}t} = (1-u)i - i_{\mathrm{a}} \tag{22}$$

The control law is generated for boost converter using ETEDPOF method is given as

$$U = U^* - \gamma\,(iv^* - vi^*) \tag{23}$$

The output voltage and reference values in control law are derived by equating system dynamics to zero. Therefore, reference values are derived as

$$U^* = \frac{V^*}{(1-D)} \tag{24}$$

$$v^* = k_v \omega^* \tag{25}$$

$$i^* = \frac{i_{\mathrm{a}}}{(1-D)} \tag{26}$$

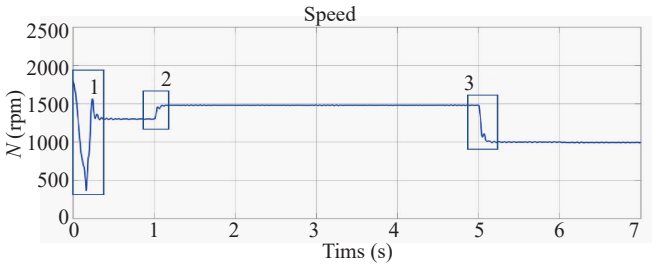

Fig. 4. Speed tracking response.

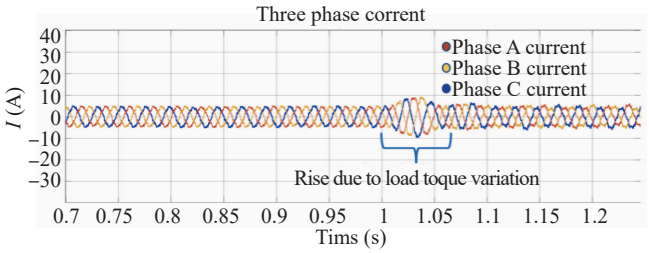

Fig. 5. Inverter input current.

The voltage reference value coming from inverter's controller output, v^* in U^*, calculates the voltage needed for anticipated speed as shown in (25). Current and voltage sensors, which are placed across passive circuit components give real values. These are two controllers used to activate converter and inverter. The simulation of system is performed based on flow chart given in Fig. 2.

IX. Results and Discussion

The grid voltage is rectified by boost converter through a LC filter to reduce harmonics injection. The converter boosts voltage to the required level according to speed trajectory of induction motor coupled with DC motor. The inverter switches as per ETEDPOF control strategy which requires state variable information from the machine. The FPGA controller updates sensor values faster compared with all other controllers so that the instantaneous error in the system is reduced.

The system is simulated in MATLAB for a step change variation of speed and load toque. The desired speed trajectory is tracked by controller in 0.2 s. Fig. 4 shows the speed trajectory in which, box 1 indicates initial inrush current suppression in 0.5 s. Box 2 represents variation in tracking desired speed given as reference in 0.2 s. Box 3 represents dip in speed, which is tracked by the controller in same time of 0.2 s. The variation in stator current of the machine due to variation in load torque is 2 A and is shown in Fig. 5. Effective electromagnetic torque generated in the machine is shown in Fig. 6, which is observed to be proportional with speed. The input voltage pulse to the inverter is given in Fig. 7 and is recorded as 600 V. The specifications of main system are given in Table III.

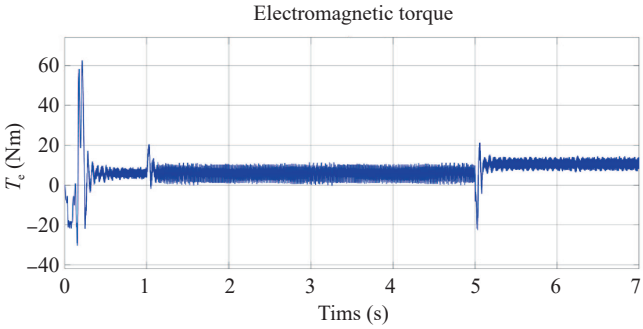

Fig. 6. Torque tracking response.

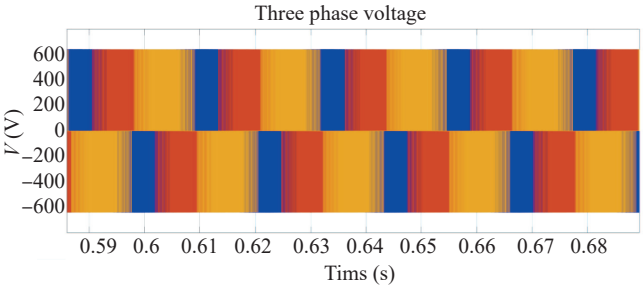

Fig. 7. Inverter input voltage.

TABLE III
Specifications of Proposed System

Circuit	Electric component	Values
LC filter	L_f	31 mH
	C_f	65 μF
	R_f	100 Ω
Boost converter	L	96 mH
DC link capacitor	C_{dc}	100 μF
	ESR	0.1 Ω
	EPR	1 Ω
	R_{dc}	100 Ω

X. Comparison of Proposed System With Sliding Mode Controller

ETEDPOF control strategy tracks a reference trajectory based on the speed change and provides proportional voltage for system to run the vehicle. The load torque variation determines change in total weight applied to motor during running of vehicle and the time it takes to track reference speed at this condition. Both systems are simultaneously run at varying speed and varying load torque condition. Speed is found to settle at 3000 rpm reference in 0.2 s without initial rise. When the gear is shifted from one to another, the speed should track a lower reference speed which is also examined. The low speed tracking of both controllers is given in Fig. 8.

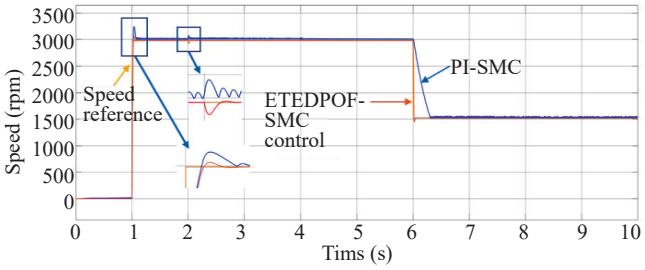

Fig. 8. Speed response for varying load torque.

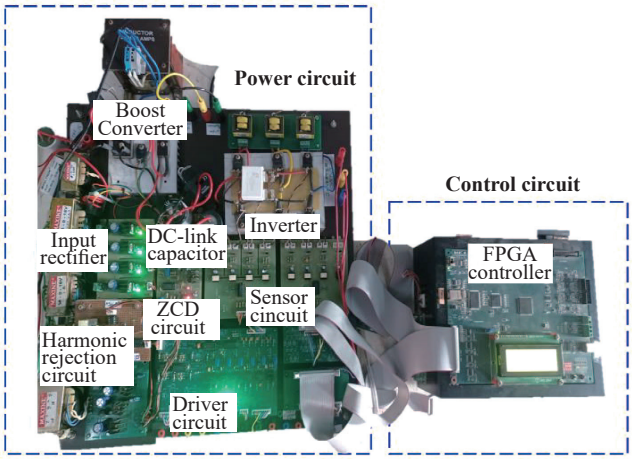

Fig. 9. Main circuit of hardware platform of the prototype for proposed system.

XI. Hardware Implementation of Proposed System

After software analysis and comparison with SMC, the system is built with FPGA controller to verify its hardware performance. The prototype hardware model is designed (Fig. 9) and simulated results are verified. The main circuit of system is understood from Fig. 9. Hardware consists of harmonic rejection circuit with inductor and capacitor circuit. Input rectifier is connected from coupling transformer to cut reverse flow of current. Main circuit consists of zero crossing detector for position estimation of rotor of induction motor.

A. FPGA Spartan 6 Driver

The controller gives signals to driver circuit of boost converter and inverter. The grid current and voltage are rectified and harmonics are reduced. The sensor voltage and current readings are recorded in DSO-X-2014A by Keysight technologies. Hardware of proposed system is built and analysed using FPGA controller using Xilinx software. The boost converter input is filtered using LC filter. The inverter input voltage is aligned by DC-link capacitor. The experimental laboratory setup is given in Fig. 10.

B. Cruise Speed Control Performance

After ripple rejection, grid current is 1.9 A as shown in Fig. 11(a). Speed reference fed to the system is shown in Fig. 11(b). It

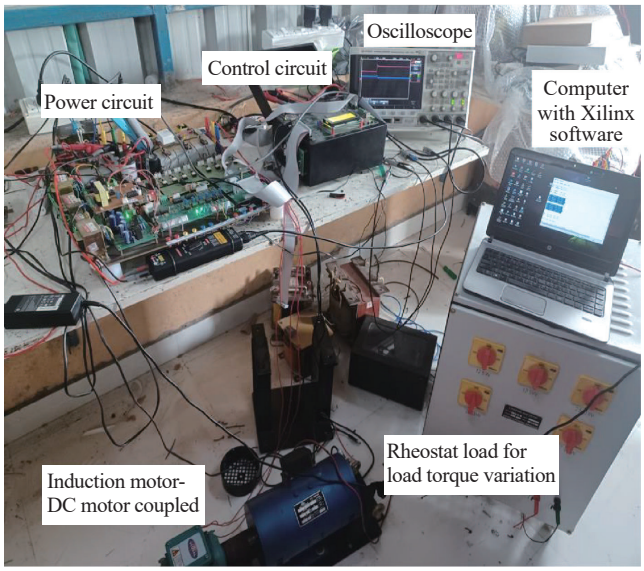

Fig. 10. Laboratory setup of proposed system.

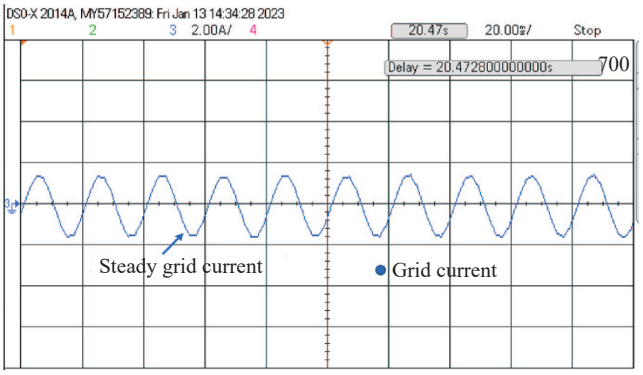

(a)

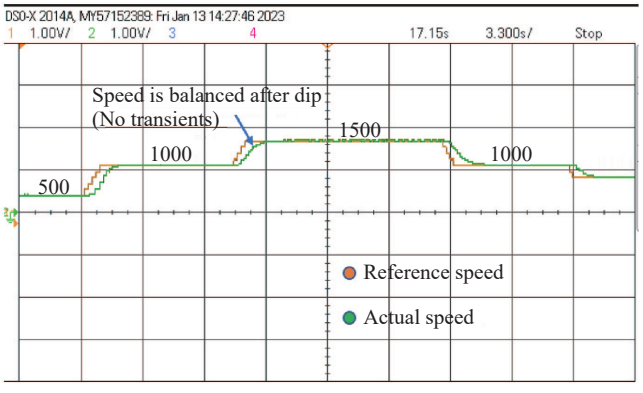

(b)

Fig. 11. (a) Grid current, (b) Reference speed tracking of ETEDPOF controller.

is variable in nature considering difficult roads other than highways for testing vehicle control efficiency. The desired speed is varied two times (2 × 500 rpm) and three times (3 × 500 rpm) as shown in Fig. 11(b) for verifying the settling time of controller which is found to be 1.2 s.

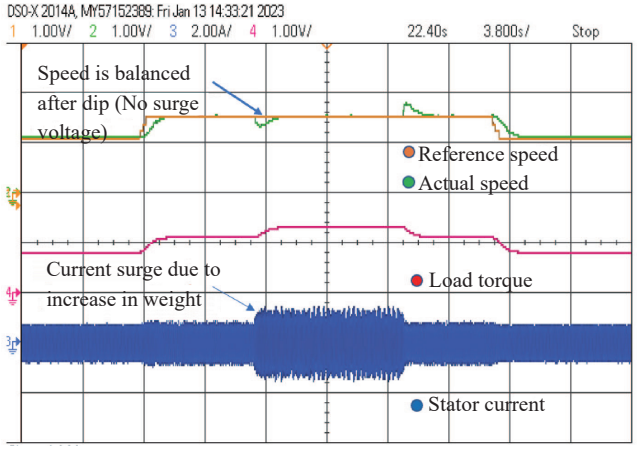

Fig. 12. Machine parameter analysis.

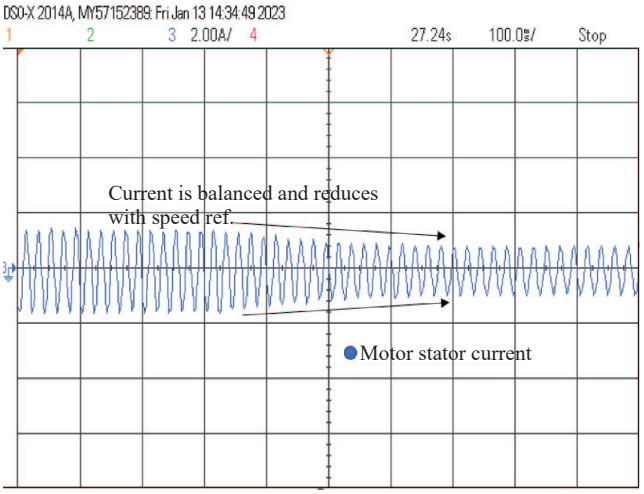

Fig. 13. Motor stator current variation with respect to load torque.

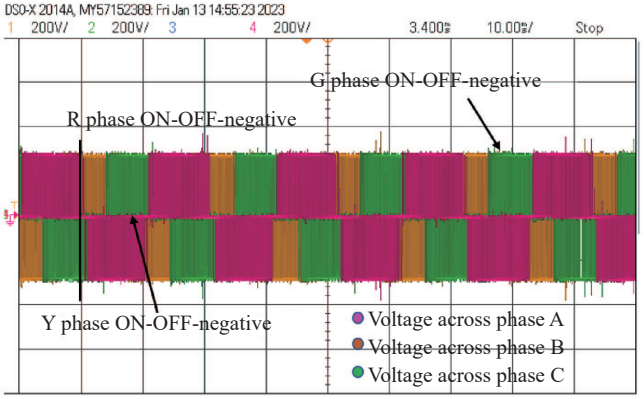

Fig. 14. Inverter output voltage.

C. Varying Load Torque Performance

In Fig. 12, speed desired value is varied from 1000 to 1500 rpm again in single step and torque is varied from 0.8,1.2 and 1.5 Nm. A ripple is found at 4.3 s where the torque is increased to 1.5 Nm and then reduced as observed in Fig. 13. The stator current of induction motor is maximum of 2.5 A and then reduced when the load torque is released. The variation of stator current when load torque is released from 1.2 Nm to 0.8 Nm is shown in Fig. 13. The respective voltage waveform is shown in Fig. 14. The three-phase current with phase shift is observed in Fig. 15. The amplitude is found to be 230 V. The line-to-line voltage of 450 V is taken across each phase and plotted using oscilloscope. This is shown separately to view the phase shift (60°) of each voltage appear across windings and is represented in Fig. 15. The voltage is a square pulse almost equal to sine wave.

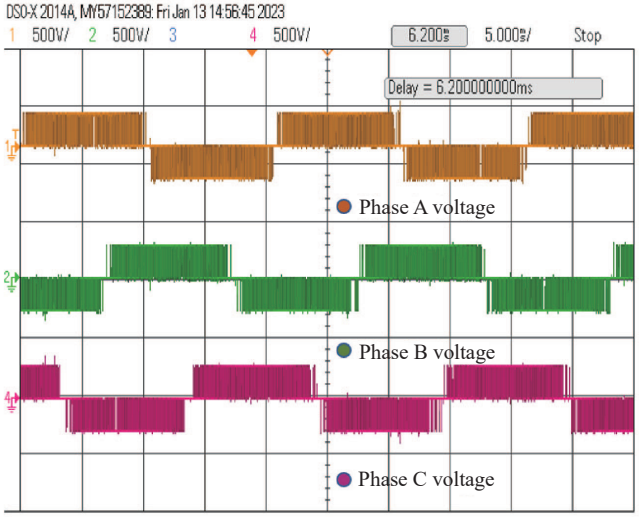

Fig. 15. Three phase induction motor input voltage.

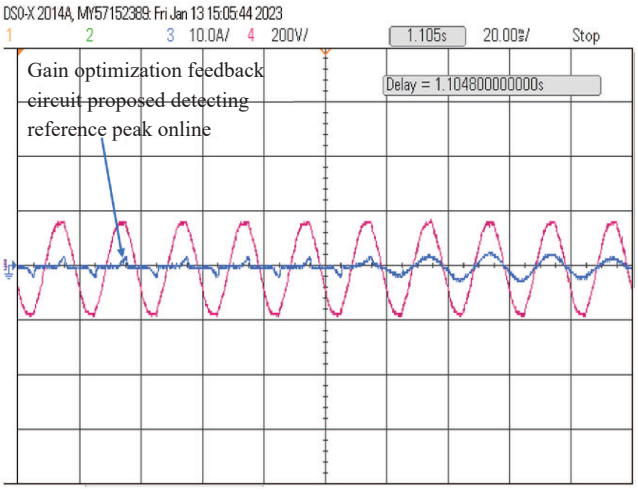

Fig. 16. Gain optimization circuit functioning waveform.

D. Proposed Online Gain Detector

The optimized gain according to (19) and (20) is implemented in hardware as feedback loops and is desired to find transient and optimum speed voltage. Fig.16 shows the controller desired peak detection according to proposed gain optimization circuit. It is also found from waveform that in online condition, the gain is optimized within 0.05 s. This will increase stability of the system.

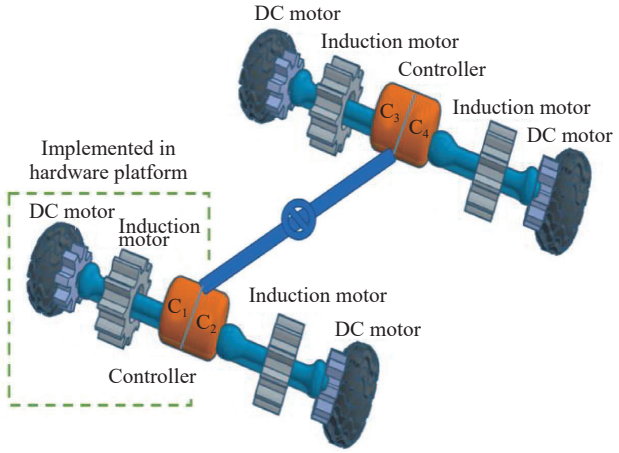

Fig. 17. Electric vehicle assembly.

XII. Application of Proposed System for EV

The settling time of speed and overshoot in voltage are less in the proposed control strategy. So, for smooth running of machine at 1500 rpm with overshoot of 1650 rpm sustained for 0.2 s and without vibration, this system is one of the best approaches for EV. The proposed controller is meant for only one wheel of EV which can be used for other three wheels for a car model as shown in Fig.17. C_1, C_2, C_3 and C_4 are controllers proposed in this work and are used for all wheels of electric car. Fig.17 represents a 3D car model, analyzed in TRICAD software to represent the proposed controller for induction motor coupled with DC motor model for electric car. ETEDPOF controller (C_1) for induction motor coupled with DC motor is connected through shaft. The same controller can be used for other three wheels for a car model.

XIII. Conclusion

Passivity based control (PBC) is an energy-based estimation technique. One of the PBC technique, ETEDPOF estimation method is used in this work. The controller tracks the speed within 0.2 s minimum and 1.2 s maximum at 1500 rpm of induction motor. A car model is presented with proposed controller for induction motor, which is coupled with DC motor. When the speed is varied from 500 rpm to 1000 rpm as well as 1500 rpm the delay in settling to reference trajectory is 0.2 s. The current transfer is smooth with very less ripple of 0.2 A and overshoot in voltage due to variation in load torque is only 10 V which is sustained for 0.2 s. In online condition, gain is optimized within 0.05 s in hardware platform. Decision making time for controller is less than 0.1 s and the initial overshoot is 0 V in hardware. This is due to soft starting strategy. The peak detection of gain circuit decides the instant of trigger. The sensor voltage and current readings are recorded in DSO-X-2014A for settling time observation. The initial reference of 500 rpm is tracked within no delay in time. The controller reduces torque ripple and therefore increases stability of the system. Using Hamiltonian operator, system state space is achieved as exponential stability. The decomposition of matrices makes system to arrive at desired trajectory settling time of 0.2 s. Hence it is desired to implement PBC for electric vehicles using induction motor. Presence of speed sensor is the limitation of this work and can be eliminated. In future, this work may be extended by using the same ETEDPOF controller technique for new converter topology. The same system can be modified to sensorless using speed observers.

Appendix I

List of Abbreviations

ASIC	Application specific integrated circuit.
BLDC	Brushless direct current motor.
DOF	Degree of freedom.
ESDI	Energy shaping damping injection.
ETEDPOF	Exact tracking error dynamics passive output feedback.
EV	Electric vehicle.
FPGA	Field programmable gate arrays.
FEV	Full electric vehicle.
HDL	Hardware description languages.
HEV	Hybrid electric vehicle.
IM	Induction motor.
PBC	Passivity based control.
PTC	Predictive torque control.
PWM	Pulse width modulation.
SMC	Sliding mode controller.
SPIM	Shaded pole induction motor.
SRM	Switched reluctance motor.
VSC	Voltage source converter.

Appendix II

Stability Analysis of PBC Method for Proposed System

A generalized Hamiltonian form is used to explain the energy management structure of error dynamics. Thus, error dynamics are connected to the passive output. The design of a time-invariant feedback controller is accomplished by recognizing these error dynamics. PBC states that the equilibrium point for a closed loop system will be a semi-globally asymptotically stable equilibrium if a dissipation matching condition is met. Equation provides the state reference trajectory of a three-phase BLDC motor supplied by an inverter:

$$\dot{x}^*(t) = (J - R)\left[\frac{\partial H(x^*)}{\partial x^*}\right]^{\mathrm{T}} + bu^* + \varepsilon \tag{27}$$

It is possible to determine the inaccuracy in system dynamics by comparing the desired and actual state spaces. For the error in system, the Hamiltonian is given as

$$H(e) = \frac{1}{2} e^{\mathrm{T}} Me \tag{28}$$

$$\frac{\partial H(e)}{\partial e} = Me = M(x - x^*) \tag{29}$$

Applying the above equation to proposed system and simplifying

$$\frac{\partial H(e)}{\partial e} = [(L_d)(i_d - i_d^*)(L_q)(i_q - i_q^*)(J)(\omega_{\mathrm{m}} - \omega_{\mathrm{m}}^*)] \tag{30}$$

For finding nature of stability of origin in error space, dynamics of the error system in (15) is given as

$$\dot{H}(e) = -\left[\frac{\partial H(e)}{\partial e}\right]\tilde{R}\left[\frac{\partial H(e)}{\partial e}\right]^{\mathrm{T}} \tag{31}$$

In the above equation, $\tilde{R}$ is dissipation matrix and is represented as

$$\tilde{R} = R + \left[b + \frac{\partial J(u)}{\partial u}\left[\frac{\partial H(e)}{\partial e}\right]^{\mathrm{T}}\right] \cdot \gamma\left[b + \frac{\partial J(u)}{\partial u}\left[\frac{\partial H(e)}{\partial e}\right]^{\mathrm{T}}\right]^{\mathrm{T}} \tag{32}$$

Since J matrix is independent on control variable 'u', the above equation reduces and value of $\tilde{R}$ is obtained as, $\tilde{R} \geqslant 0$.

Here, γ is positive damping factor and hence $\tilde{R}$ is a positive definite matrix. Now the Hamiltonian error matrix can be expressed as

$$\dot{H}(e) = -\{(R+\gamma)[(i_d - i_d^*)^2 + (i_q - i_q^*)^2] + J(\omega_{\mathrm{m}} - \omega_{\mathrm{m}}^*)\} \tag{33}$$

The equilibrium point near the origin of the error space is asymptotically stable because $\dot{H}$(e) is negative semi-definite. The outcome is not global as the control input is limited to values between 0 and 1.

References

[1] W. Wang and J.-Y. Chen, "Passivity-based sliding mode position control for induction motor drives," in *IEEE Transactions on Energy Conversion*, vol. 20, no. 2, pp. 316–321, Jun. 2005.

[2] L. U. Gokdere and M. A. Simaan, "A passivity-based method for induction motor control," in *IEEE Transactions on Industrial Electronics*, vol. 44, no. 5, pp. 688–695, Oct. 1997.

[3] W.-J. Wang and J.-Y. Chen, "Compositive adaptive position control of induction motors based on passivity theory," in *IEEE Transactions on Energy Conversion*, vol. 16, no. 2, pp. 180–185, Jun. 2001.

[4] Z. -G. Wu, P. Shi, Z. Shu, H. Su, and R. Lu, "Passivity-based asynchronous control for Markov jump systems," in *IEEE Transactions on Automatic Control*, vol. 62, no. 4, pp. 2020–2025, Apr. 2017.

[5] P. J. Nicklasson, R. Ortega, G. Espinosa-Perez, and C. G. J. Jacobi, "Passivity-based control of a class of Blondel-Park transformable electric machines," in *IEEE Transactions on Automatic Control*, vol. 42, no. 5, pp. 629-647, May 1997.

[6] F. Wang, G. Lin, and Y. He, "Passivity-based model predictive control of three-level inverter-fed induction motor," in *IEEE Transactions on Power Electronics*, vol. 36, no. 2, pp. 1984–1993, Feb. 2021.

[7] C. Cecati, "Position control of the induction motor using a passivity based controller," in *IEEE Transactions on Industry Applications*, vol. 36, no. 5, pp. 1277–1284, Sept.-Oct. 2000.

[8] C. Cecati and N. Rotondale, "Torque and speed regulation of induction motors using the passivity theory approach," in *IEEE Transactions on Industrial Electronics*, vol. 46, no. 1, pp. 119–127, Feb. 1999.

[9] H. Wang, K. T. Chau, C. H. T. Lee, L. Cao, and W. H. Lam, "Design, analysis, and implementation of wireless shaded-pole induction motors," in *IEEE Transactions on Industrial Electronics*, vol. 68, no. 8, pp. 6493–6503, Aug. 2021.

[10] J. Mei, C. H. T. Lee, and J. L. Kirtley, "Design of axial flux induction motor with reduced back iron for electric vehicles," in *IEEE Transactions on Vehicular Technology*, vol. 69, no. 1, pp. 293–301, Jan. 2020.

[11] J. Linares-Flores, J. Reger, and H. Sira-Ramírez, "Load torque estimation and passivity-based control of a boost-converter/DC motor combination," in *IEEE Transactions on Control Systems Technology*, vol. 18, no. 6, pp. 1398–1405, Nov. 2010.

[12] M. Tousizadeh, H. S. Che, J. Selvaraj, N. A. Rahim, and B. -T. Ooi, "Performance comparison of fault-tolerant three-phase induction motor drives considering current and voltage limits," in *IEEE Transactions on Industrial Electronics*, vol. 66, no. 4, pp. 2639–2648, Apr. 2019.

[13] H. H. Eldeeb, H. Zhao, and O. A. Mohammed, "Detection of TTF in induction motor vector drives for EV applications via Ostu's-based DDWE," in *IEEE Transactions on Transportation Electrification*, vol. 7, no. 1, pp. 114–132, Mar. 2021.

[14] A. Tausif, H. Jung, and S. Choi, "Single-stage isolated electrolytic capacitor-less EV onboard charger with power decoupling," in *CPSS Transactions on Power Electronics and Applications*, vol. 4, no. 1, pp. 30–39, Mar. 2019.

[15] J. Su, R. Gao, and I. Husain, "Model predictive control based field weakening strategy for traction EV used induction motor," in *IEEE Trans actions on Industry Applications*, vol. 54, no. 3, pp. 2295–2305, May-Jun. 2018.

[16] J. Mei, Y. Zuo, C. H. T. Lee, and J. L. Kirtley, "Modeling and optimizing method for axial flux induction motor of electric vehicles," in *IEEE Transactions on Vehicular Technology*, vol. 69, no. 11, pp. 12822–12831, Nov. 2020.

[17] K. V, R. Rai, and B. Singh, "Sliding model-based predictive torque control of induction motor for electric vehicle," in *IEEE Transactions on Industry Applications*, vol. 58, no. 1, pp. 742–752, Jan.-Feb. 2022.

[18] M. J. Akhtar and R. K. Behera, "Space vector modulation for distributed inverter-fed induction motor drive for electric vehicle application," in *IEEE Journal of Emerging and Selected Topics in Power Electronics*, vol. 9, no. 1, pp. 379–389, Feb. 2021.

[19] A. Credo, M. Villani, G. Fabri, and M. Popescu, "Adoption of the synchronous reluctance motor in electric vehicles: A focus on the flux weakening capability," in *IEEE Transactions on Transportation Electrification*, vol. 9, no. 1, pp. 805–818, Mar. 2023.

[20] D. Diallo, M. E. H. Benbouzid, and A. Makouf, "A fault-tolerant control architecture for induction motor drives in automotive applications," in *IEEE Transactions on Vehicular Technology*, vol. 53, no. 6, pp. 1847–1855, Nov. 2004.

[21] N. T. Dung, B. -H. Nguyen, L. H. Tran, C. D. Manh, and T. Vo-Duy, "Sliding-mode-based driving torque distribution for dynamic control of dual-motor electric vehicles," in *Proceedings of 2025 IEEE International Conference on Mechatronics (ICM)*, Wollongong, Australia, 2025, pp. 1–6.

[22] A. G. Garganeev, A. Ibrahim, and D. I. Ulyanov, "Modified algorithm for controlling the traction electric motor of a electric vehicle," in *Proceedings of 2025 IEEE 26th International Conference of Young Professionals in Electron Devices and Materials (EDM)*, Altai, Russian Federation, 2025, pp. 1260–1263.

[23] Jesús Linares-Flores, Johann Reger, and Hebertt Sira-Ramírez, "Load torque estimation and passivity-based control of a boost converter/DC-motor combination," in *IEEE Transactions on Control Systems Technology*, vol. 18, no. 6, pp. 1398–1405, Nov. 2010.

[24] Y. Liao, X. Wang, and F. Blaabjerg, "Passivity-based analysis and design of linear voltage controllers for voltage-source converters," in *IEEE Open Journal of the Industrial Electronics Society*, vol. 1, pp. 114–126, 2020.

[25] D. G. Dorrell, A. M. Knight, L. Evans, and M. Popescu, "Analysis and design techniques applied to hybrid vehicle drive machines—Assessment of alternative IPM and induction motor topologies," in *IEEE Transactions on Industrial Electronics*, vol. 59, no. 10, pp. 3690–3699, Oct. 2012.

[26] Z. Wang, T. W. Ching, S. Huang, H. Wang, and T. Xu, "Challenges faced by electric vehicle motors and their solutions," in *IEEE Access*, vol. 9, pp. 5228–5249, 2021.

Arathy Rajeev V. K. was born on July 27, 1991. She has received B.Tech. degree in Electrical and Electronics Engineering from Mahatma Gandhi University, Kerala, India in 2013, M.E degree in power electronics and drives from Anna University, Chennai, India in 2015 and currently pursuing Ph.D. at Anna University, Chennai, India. Her areas of interest include energy storage, analysis and control of electrical drives, EV.

P. Valsalal has received BE, ME and Ph.D. degrees in the year 1990,1993 and 2006 respectively. Currently she is working as Professor at College of Engineering, Guindy, Anna University. Her research area is in the field of electrical engineering. She has got around 50 research publications at her credit.

A No-Reconstruction Fault-Tolerant Control Method for Open-Switch Faults in Standard IM Drives

Lei WANG, Yingying SHE, Yujin SONG, Weikang WANG, and Zhixi WU

***Abstract*—The power switch faults in standard two-level three-phase inverter-fed motor drives cause severe speed oscillation, and decline the system stability. The fault-tolerant methods which require topology reconstruction have the disadvantages of additional cost and unreliability. It is of great significance to study the no-reconstruction fault-tolerant (NFT) method, which only changes the control algorithm. In this paper, a novel NFT method is proposed for induction motor (IM) drive, which consists of the two-mode control algorithm and the algorithm transition strategy. In the healthy mode, conventional model predictive flux control (MPFC) is adopted; in the tolerant mode, a novel MPFC algorithm is proposed to eliminate the effect of the fault power switch by setting the reference fault phase current as zero. The two modes alternate in each current cycle. An algorithm transition strategy is proposed for the smooth transition of two modes, which has the ability to revert to healthy operation even if misdiagnoses occur. The proposed NFT method can significantly reduce the speed oscillation after the fault occurs, and experiment results verify its effectiveness.**

***Index Terms*—Algorithm transition strategy, no-reconstruction fault-tolerant method, standard induction motor drive, two-mode model predictive flux control algorithm.**

I. Introduction

TWO-LEVEL three-phase inverter-fed motor drives are most widely used in many industrial occasions due to their simple structure and low cost. However, the reliability of the two-level three-phase inverter is not enough because of the topology limitation. The inverter faults, which can be divided into short-switch and open-switch faults, account for a large percentage of motor drive faults [1]. The short-switch faults are usually converted to open-switch faults by hardware protection [2]. The open-switch faults cause the loss of inverter voltage vector, leading to severe speed oscillation or even the motor drive shutdown.

With the increasing demand for high reliability, the research on inverter fault tolerance is of great significance. Researchers have proposed some more complex topologies to improve the inverter fault-tolerant ability, such as four-leg inverter [3], [4], dual inverter [5], [6], and multilevel inverter [7], [8]. This scheme aims to increase the number of voltage vectors so that the motor drive can still operate after missing part of the voltage vector, called the passive fault tolerance (PFT). However, the cost of these topologies is greatly higher than standard motor drives. In recent years, the fault-tolerant methods of the standard motor drive have attracted more and more attention, whose idea is to adjust inverter topology and control algorithm after the fault diagnosis, called the active fault tolerance (AFT). Fault diagnosis can detect and locate the fault switch, whose scheme generally includes data processing, feature extraction, and fault classification [9], [10]. It is the precondition of AFT.

The most simple AFT method is to add redundant legs or inverters. After fault diagnosis, the fault leg or inverter is replaced by a redundant one. Further, switch-reduced fault-tolerant methods have been proposed to avoid the cost of redundant legs or inverters, such as four-switch inverter [11]–[13], four-switch four leg inverter [14], mono-inverter dual motor drive [15]–[17], four-leg inverter dual motor drive [18], [19], and five-leg inverter dual motor drive [20], [21]. After fault diagnosis, the fault leg is isolated, and the inverter topology turns to the suitable tolerant topologies by certain switches. Generally, the motor phase terminal or the neutral point is reconnected to the capacitor mid-point or healthy leg. Although the AFT can save high costs compared to PFT, it still has many disadvantages: it needs lots of redundant switches to realize the topology reconstruction; the other healthy power switch in the isolated leg is wasted; designing suitable fault-tolerant topologies and control methods for different fault situations is also a big challenge.

Hence, realizing the fault tolerance of standard motor drives without topology reconstruction is of great meaning, called the no-reconstruction fault tolerance (NFT). The NFT method only changes the control algorithm after fault diagnosis at no extra cost. Researchers have realized NFT for open-phase faults of PMSM drive based on finite control set model predictive control [22], [23]. A fault-tolerant current control method has been proposed for open-switch faults of permanent-magnet generator system [24]. However, these methods ignore the healthy power switch in the fault leg, causing big torque loss. To fully utilize the remaining healthy power switches in standard PMSM drive, research in [25] has proposed a current optimization-based NFT method for open-switch and open-phase faults, and research in [26] has proposed a field-oriented

Manuscript received June 13, 2025; revised September 1, 2025; accepted October 10, 2025. Date of publication December 30, 2025; date of current version December 2, 2025. No funding was received to assist with the preparation of this manuscript.(*Corresponding author: Yujin Song.*)

All authors are with the Wuhan Second Ship Design and Research Institute, Wuhan 430200, China (e-mail: 15809705@qq.com; 1072608260@qq.com; wy_syj960110@163.com; hhwangweikang@foxmail.com; 15827276876@163.com).

Digital Object Identifier 10.24295/CPSSTPEA.2025.00036

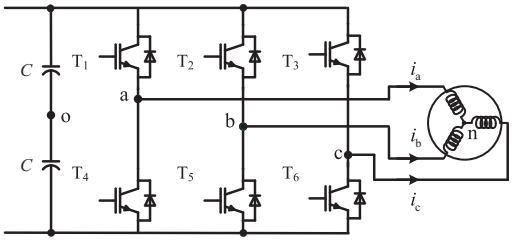

Fig. 1. The circuit diagram of standard IM drive.

control-based NFT method to improve the current tracking and algorithm transition for open-switch faults. In these methods, the five healthy power switches are all used in fault tolerance. Thus, the system can work in the healthy state for half of each current cycle and in the tolerant state for the other half, obtaining a better control performance. However, both researches directly control the currents in the two-phase rotating coordinate system. It means that electrical angle estimation is unavoidable, whose accuracy can affect the reference tracking and the control algorithm transition. Besides, the fault type is considered known, meaning additional fault diagnosis is required in practice.

In this paper, a model predictive flux control (MPFC)-based NFT method for standard induction motor (IM) drive is proposed, where the five healthy power switches are all used in fault tolerance. The contributions can be listed as follows:

1. The proposed two-mode control algorithm directly controls the stator flux vector in the static coordinate system, avoiding the requirement of static-to-rotating coordinate transformation and electrical angle estimation. It is general for any switch faults.

2. The proposed algorithm transition strategy can realize not only the fast fault diagnosis but also the smooth control algorithm transition. Especially, it has the ability to revert to healthy operation even if misdiagnoses occur.

This paper is organized as follows. The proposed two-mode control algorithm is presented in Section II, and the algorithm transition strategy is discussed in Section III. Then, Section IV shows the experiment results, and Section V gives the conclusion.

II. Proposed Two-Mode Control Algorithm

The topology of the standard IM drive is shown in Fig. 1. C is the DC bus capacitor. a, b, c are three inverter legs. o is the capacitor mid-point. n is the motor neutral point. i_a, i_b, i_c are phase currents. T_x (x = 1 – 6) are six power switches. Each inverter leg has two switching states S_x (x = a, b, c), where '1' means upper switch on, and '0' means lower switch on.

A. IM Model

The model of IM in the static coordinate system can be expressed as

$$\boldsymbol{\dot{x}} = \boldsymbol{A}\boldsymbol{x} + \boldsymbol{B}\boldsymbol{v}_s \tag{1}$$

where $\boldsymbol{A} = \begin{bmatrix} -\lambda(R_sL_r + R_rL_s) + j\omega_r & \lambda(R_r - jL_r\omega_r) \\ -R_s & 0 \end{bmatrix}$, $\lambda = 1/$

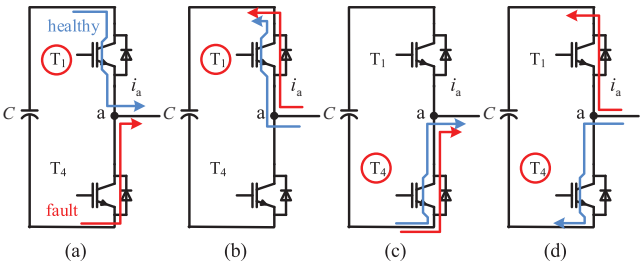

Fig. 2. The current circuits of inverter leg a. (a) $S_a = 1$, $i_a > 0$, (b) $S_a = 1$, $i_a < 0$, (c) $S_a = 0$, $i_a > 0$, (d) $S_a = 0$, $i_a < 0$.

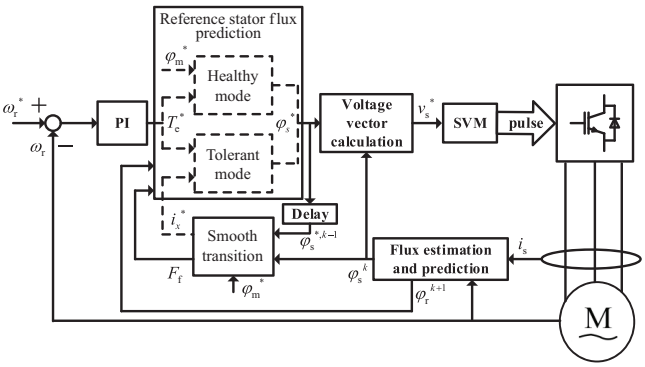

Fig. 3. The control diagram of proposed NFT method.

$(L_sL_r - L_m^2)$, $\boldsymbol{x} = [\boldsymbol{i}_s \quad \boldsymbol{\varphi}_s]^T$, $\boldsymbol{B} = [\lambda L_r \quad 1]^T$, $\boldsymbol{i}_s$, $\boldsymbol{\varphi}_s$, and $\boldsymbol{v}_s$ are stator current, stator flux, and voltage vectors, respectively. L_m, L_s, and L_r are mutual, stator, and rotor inductance, R_s and R_r are stator and rotor resistance, ω_r is electrical rotor speed.

The output torque T_e can be calculated as

$$T_e = 1.5n_p\lambda L_m(\boldsymbol{\varphi}_r \otimes \boldsymbol{\varphi}_s) \tag{2}$$

where n_p is the number of pole pairs, $\otimes$ means cross-product operation, $\boldsymbol{\varphi}_r$ is the rotor flux vector.

B. Control Basic

Inverter leg a as an example, the current circuits under different switching states are shown in Fig. 2. It shows that the T_1 fault doesn't affect the control of IM drive when i_a is negative, and the T_4 fault doesn't affect the control of IM drive when i_a is positive. Thus, after a power switch fault occurs, the current cycle of the fault leg can be divided into two parts: healthy and fault parts. In the fault part, the control algorithm must be adjusted for fault tolerance.

The control diagram of the proposed NFT method is shown in Fig. 3. First, the reference torque is obtained by Proportional-Integral (PI) regulator. Then, the inverter voltage vector is directly calculated by the proposed two-mode control algorithm, which consists of the control algorithms in healthy and tolerant modes. Here, the stator flux vector is used for the smooth algorithm transition. Last, the control signals of power switches are generated by space vector pulse width modulation (SVM).

C. Control Algorithm of Healthy Mode

The predictive model of (1) can be derived by Euler-forward method as

$$\boldsymbol{x}^{k+1} = (1 + \boldsymbol{A}T_s)\,\boldsymbol{x}^k + \boldsymbol{B}T_s\boldsymbol{v}_s^k \tag{3}$$

where T_s is sampling period. The superscript k means the value at the step k.

According to (2), the output torque at step k+1 can be predicted as

$$T_e^{k+1} = 1.5n_p\lambda L_m\,(\boldsymbol{\varphi}_r^{k+1} \otimes \boldsymbol{\varphi}_s^{k+1}) \tag{4}$$

Substituting T_e^{k+1} and $\boldsymbol{\varphi}_s^{k+1}$ by their reference values, the predictive model of (2) can be expressed by

$$T_e^* = 1.5n_p\lambda L_m\,(\boldsymbol{\varphi}_r^{k+1} \otimes \boldsymbol{\varphi}_s^*) \tag{5}$$

The rotor flux at step k+1 can be predicted by

$$\boldsymbol{\varphi}_r^{k+1} = \boldsymbol{\varphi}_r^k + T_s\left(\frac{R_r L_m}{L_r}\boldsymbol{i}_s^k - \left(\frac{R_r}{L_r} - \mathrm{j}\omega_r\right)\boldsymbol{\varphi}_r^k\right) \tag{6}$$

Taking $\boldsymbol{\varphi}_r^{k+1}$ as known, the reference stator flux can be calculated by (5)

$$\boldsymbol{\varphi}_s^* = \boldsymbol{\varphi}_m^* \cdot \exp(\mathrm{j}\angle\boldsymbol{\varphi}_s^*),\ \angle\boldsymbol{\varphi}_s^* = \angle\boldsymbol{\varphi}_r^{k+1} + \theta^{k+1}$$
$$\theta^{k+1} = \arcsin\left(\frac{T_e^*}{1.5n_p\lambda L_m|\boldsymbol{\varphi}_r^{k+1}|\boldsymbol{\varphi}_m^*}\right) \tag{7}$$

where $\boldsymbol{\varphi}_m^*$ is the reference value of stator flux amplitude, θ^{k+1} is the angle difference of $\boldsymbol{\varphi}_s^*$ and $\boldsymbol{\varphi}_r^{k+1}$.

According to (3), the stator flux at step k+1 can be predicted as

$$\boldsymbol{\varphi}_s^{k+1} = (\boldsymbol{v}_s - R_s\boldsymbol{i}_s^k)T_s + \boldsymbol{\varphi}_s^k \tag{8}$$

Substituting $\boldsymbol{\varphi}_s^{k+1}$ and $\boldsymbol{v}_s$ by their reference values, the reference voltage vector can be calculated as

$$\boldsymbol{v}_s^* = \frac{\boldsymbol{\varphi}_s^* - \boldsymbol{\varphi}_s^k}{T_s} + R_s\boldsymbol{i}_s^k \tag{9}$$

D. Control Algorithm of Tolerant Mode

When IM operates in the fault part, the current circuit is changed as Fig. 2 shows. It makes the actual and reference inverter vectors different. Since the fault leg current in the fault part can be approximated to zero, T_e and $|\boldsymbol{\varphi}_s|$ can't be constant simultaneously.

Hence, in the proposed algorithm, the $|\boldsymbol{\varphi}_s|$ is no longer controlled constantly. Instead, the reference fault leg current is set to zero under tolerant mode to eliminate the effect of fault switch.

According to (3), the relationship between $\boldsymbol{i}_s^{k+1}$ and $\boldsymbol{\varphi}_s^{k+1}$ can be rewrote as

$$\boldsymbol{i}_s^{k+1} = \left(1 + \frac{T_s}{\tau_\sigma}\right)\boldsymbol{i}_s^k + \frac{T_s}{(T_s + \tau_\sigma)R_\sigma} \cdot \left(\left(\frac{k_r}{(\tau_r)} - \mathrm{j}\omega_r k_r\right)\boldsymbol{\psi}_r^k + \frac{\boldsymbol{\varphi}_s^{k+1} - \boldsymbol{\varphi}_s^k}{T_s} + R_s\boldsymbol{i}_s^k\right) \tag{10}$$

where $k_r = L_m/L_r$, $R_\sigma = R_s + k_r^2 R_r$, $\tau_\sigma = 1/(\lambda L_r R_\sigma)$, $\tau_r = L_r/R_r$.

Substituting $\boldsymbol{i}_s^{k+1}$ and $\boldsymbol{\varphi}_s^{k+1}$ by their reference values in (10), the components of $\boldsymbol{\varphi}_s^*$ in the two-phase static coordinate system can be calculated as

$$\begin{bmatrix}\boldsymbol{\varphi}_{s\alpha}^* \\ \boldsymbol{\varphi}_{s\beta}^*\end{bmatrix} = (T_s + \tau_\sigma)R_\sigma\begin{bmatrix}\boldsymbol{i}_{s\alpha}^* \\ \boldsymbol{i}_{s\beta}^*\end{bmatrix} = \begin{bmatrix}M \\ N\end{bmatrix} \tag{11}$$

where $M = \boldsymbol{\varphi}_{s\alpha}^k R_\sigma(T_s + \tau_\sigma)^2/\tau_\sigma\boldsymbol{i}_\alpha^k - (k_r/\tau_r\boldsymbol{\varphi}_{r\alpha}^k + \omega_r k_r\boldsymbol{\varphi}_{r\beta}^k + R_s\boldsymbol{i}_\alpha^k)T_s$, $N = \boldsymbol{\varphi}_{s\beta}^k - R_\sigma(T_s + \tau_\sigma)^2/\tau_\sigma\boldsymbol{i}_\beta^k - (k_r/\tau_r\boldsymbol{\varphi}_{r\beta}^k - \omega_r k_r\boldsymbol{\varphi}_{r\alpha}^k + R_s\boldsymbol{i}_\beta^k)T_s$. The subscripts α, β mean the components of variables in the two-phase static coordinate system.

The components of $\boldsymbol{\varphi}^*$ in the three-phase static coordinate system can be represented as

$$\begin{bmatrix}\boldsymbol{\varphi}_{sa}^* \\ \boldsymbol{\varphi}_{sb}^* \\ \boldsymbol{\varphi}_{sc}^*\end{bmatrix} = (T_s + \tau_\sigma)R_\sigma\begin{bmatrix}\boldsymbol{i}_{sa}^* \\ \boldsymbol{i}_{sb}^* \\ \boldsymbol{i}_{sc}^*\end{bmatrix} + \begin{bmatrix}1 & 0 \\ -\frac{1}{2} & \frac{\sqrt{3}}{2} \\ -\frac{1}{2} & -\frac{\sqrt{3}}{2}\end{bmatrix}\begin{bmatrix}M \\ N\end{bmatrix} \tag{12}$$

where the subscripts a, b, c mean the components of variables in the three-phase static coordinate system.

Once the reference fault leg current is set to zero, the corresponding component of $\boldsymbol{\varphi}_s^*$ can be obtained. For example, if i_{sa}^* is set zero, $\boldsymbol{\varphi}_{sa}^*$ can be calculated by (12). Substituting $\boldsymbol{\varphi}_{sa}^*$ into (5), the other components of $\boldsymbol{\varphi}_s^*$ can be finally obtained. The cases of leg b and c are similar.

Then, the reference stator flux in the two-phase static coordinate system can be calculated as

$$\begin{bmatrix}\boldsymbol{\varphi}_{s\alpha}^* \\ \boldsymbol{\varphi}_{s\beta}^*\end{bmatrix} = \begin{cases}\begin{bmatrix}\boldsymbol{\varphi}_{s\alpha}^* \\ \dfrac{T_e^*/(1.5n_p\lambda L_m) + \boldsymbol{\varphi}_{s\alpha}^*\boldsymbol{\varphi}_{r\beta}^{k+1}}{\boldsymbol{\varphi}_{r\alpha}^{k+1}}\end{bmatrix}, & if\ \boldsymbol{i}_{sa}^* = 0 \\ \begin{bmatrix}\dfrac{\sqrt{3}\,T_e^*/(\boldsymbol{\varphi}_{r\alpha}^{k+1}1.5n_p\lambda L_m) - 2\boldsymbol{\varphi}_{sb}^*}{1 - \sqrt{3}\,\boldsymbol{\varphi}_{r\beta}^{k+1}/\boldsymbol{\varphi}_{r\alpha}^{k+1}} \\ (\boldsymbol{\varphi}_{s\alpha}^* + 2\boldsymbol{\varphi}_{sb}^*)\sqrt{3}\end{bmatrix}, & if\ \boldsymbol{i}_{sb}^* = 0 \\ \begin{bmatrix}\dfrac{\sqrt{3}\,T_e^*/(\boldsymbol{\varphi}_{r\alpha}^{k+1}1.5n_p\lambda L_m) + 2\boldsymbol{\varphi}_{sc}^*}{-\sqrt{3}\,\boldsymbol{\varphi}_{r\beta}^{k+1}/\boldsymbol{\varphi}_{r\alpha}^{k+1}} \\ -(\boldsymbol{\varphi}_{s\alpha}^* + 2\boldsymbol{\varphi}_{sb}^*)/\sqrt{3}\end{bmatrix}, & if\ \boldsymbol{i}_{sc}^* = 0\end{cases} \tag{13}$$

Substituting (13) into (9), the reference voltage vector under tolerant mode can be obtained.

E. Phase Current Protection

According to the above analysis, the control logic of the proposed algorithm is to maintain the phase current of the fault leg as zero by controlling the corresponding phase component of $\boldsymbol{\varphi}_s^*$ in the three-phase static coordinate system. And the reference torque is generated by the other healthy phases. However, when the denominator in (13) is near zero, the calculated healthy phase components of $\boldsymbol{\varphi}_s^*$ will be too large. As (10) shows, the healthy phase currents will also come to a high

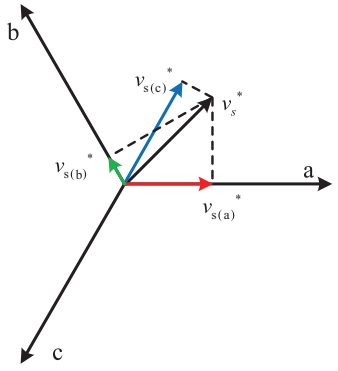

Fig. 4. The adjusted reference voltage vector for phase current protection.

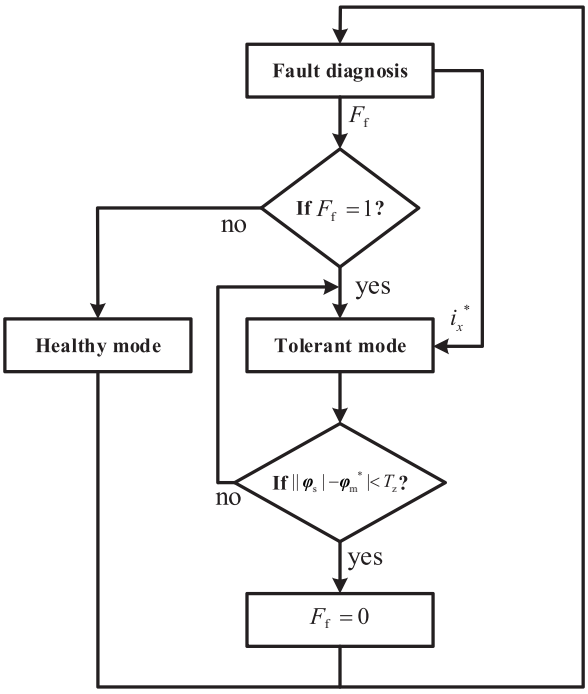

Fig. 5. The flow chart of control algorithm transition strategy.

value.

In actual application, the current protection must be considered. Meanwhile, the phase current of the fault leg should still be controlled to zero. Hence, when the phase current of the healthy leg is over the current limit, the fault phase component of v_s^* remains unchanged, and the healthy phase components of v_s^* are set to zero. The adjusted reference voltage vector is shown in Fig. 4. In Fig. 4, $\boldsymbol{v}_{s(a)}^*$, $\boldsymbol{v}_{s(b)}^*$, and $\boldsymbol{v}_{s(c)}^*$ represent the reference voltage vector. $\boldsymbol{v}_{s(a)}^*$, $\boldsymbol{v}_{s(b)}^*$, or $\boldsymbol{v}_{s(c)}^*$ is set to 0 under the fault conditions of inverter leg a, b, and c fault, respectively.

III. Control Algorithm Transition

Since the control algorithms under healthy and tolerant modes execute alternately in each current cycle, the smooth transition of control algorithms is one key point of the NFT.

In this paper, a control algorithm transition strategy is designed, which consists of the transition from healthy to tolerant mode and the transition from tolerant to healthy mode. Unlike

TABLE I
The Fault Diagnosis Lookup Table

F_a	F_b	F_c	F_f	i_x^*
$< -T_z$	$> T_z$	$> T_z$	1	$\boldsymbol{i}_a^* = 0$
$> T_z$	$< -T_z$	$< -T_z$	1	$\boldsymbol{i}_a^* = 0$
$> T_z$	$< -T_z$	$> T_z$	1	$\boldsymbol{i}_b^* = 0$
$< -T_z$	$> T_z$	$< -T_z$	1	$\boldsymbol{i}_b^* = 0$
$> T_z$	$> T_z$	$< -T_z$	1	$\boldsymbol{i}_c^* = 0$
$< -T_z$	$< -T_z$	$> T_z$	1	$\boldsymbol{i}_c^* = 0$

the existing NFT methods, the fault switch is no longer seen as known. A MPFC-based fault diagnosis algorithm in our previous work [27] is used to realize the algorithm transition from healthy to tolerant mode for any switch fault. The deviation of the estimated stator flux amplitude and its reference value is used for the algorithm transition from tolerant to healthy mode. The flow chart is shown in Fig. 5, where F_f means the fault flag ('0' is healthy and '1' is faulty), and $\boldsymbol{i}_x^*$ means the reference value of fault phase current.

The fault diagnosis signals can be obtained by [27] as

$$\begin{bmatrix} F_a \\ F_b \\ F_c \end{bmatrix} = \begin{bmatrix} \boldsymbol{\varphi}_{sa}^k - \boldsymbol{\varphi}_{sa}^{*,k-1} \\ \boldsymbol{\varphi}_{sb}^k - \boldsymbol{\varphi}_{sb}^{*,k-1} \\ \boldsymbol{\varphi}_{sc}^k - \boldsymbol{\varphi}_{sc}^{*,k-1} \end{bmatrix} \tag{14}$$

where F_a, F_b, and F_c are three phase fault diagnosis signals. Then, F_f and $\boldsymbol{i}_x^*$ can be obtained by the fault diagnosis lookup table shown in Table I, where T_z is the fault diagnosis threshold value.

Since the above fault diagnosis is based on the error between the calculated $\boldsymbol{\varphi}_s^*$ and the actual $\boldsymbol{\varphi}_s$, the fault diagnosis will be disabled when the control algorithm of tolerant mode executes. It is because the error is slight under this algorithm. Hence, if no additional transition is used, the control algorithm of tolerant mode will always execute in the current cycle, wasting the healthy power switch.

Considering that the stator flux amplitude is constant in the control algorithm of healthy mode and variational in the tolerant mode, the transition can be smooth when they reach the same value. The judge of transition from tolerant to healthy mode can be expressed as

$$F_f = 0, \text{ if } ||\boldsymbol{\varphi}_s^*| - \boldsymbol{\varphi}_m^*| < T_z \tag{15}$$

Based on the combination of two transitions, even if there is a mistake in one transition, it can be corrected by another. This transition strategy has the ability to revert to healthy operation even if misdiagnoses occur. For example, when F_f is generated as '1', the control algorithm of tolerant mode is executed. After half the current cycle, it will automatically turn into the healthy mode with F_f as '0'. This process is repeated during each current cycle, which can greatly increase the reliability of the control algorithm transition.

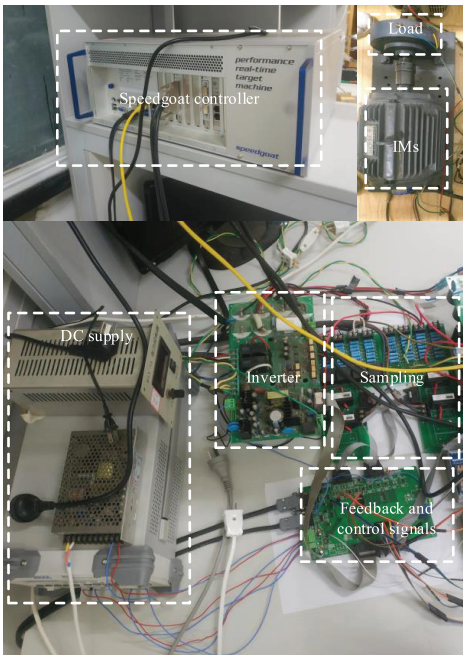

Fig. 6. The experimental platform.

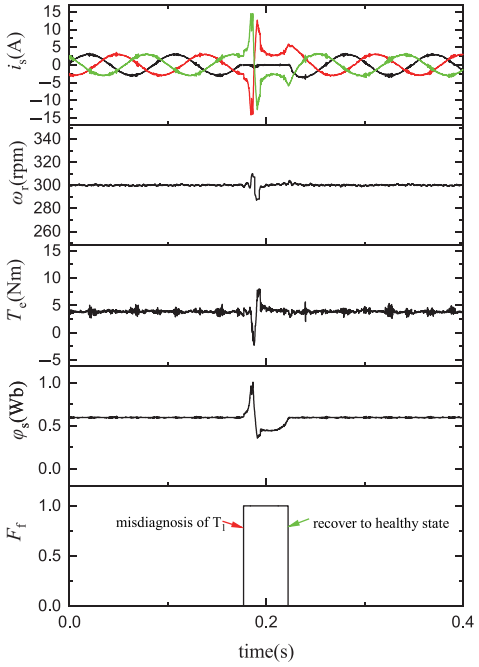

Fig. 7. The ability of anti-misdiagnosis of proposed NFT method.

TABLE II
PARAMETERS OF EXPERIMENTAL PLATFORM

Parameter	Value	Parameter	Value
DC-link voltage	400 V	Rotor inductance	330.03 mH
DC-link capacitor	2040 μF	Mutual inductance	319.7 mH
Sampling frequency	10 kHz	Rated power	2.2 kW
Dead time	2.5 μs	Rated speed	1430 r/min
Stator resistance	2.804 Ω	Rated current	4.9 A
Rotor resistance	2.178 Ω	Pole pairs	2
Stator inductance	330.03 mH	Rated Torque	10 Nm

IV. EXPERIMENTS

The experimental platform consists of a Speedgoat controller, one three-phase inverter (using IGBT PM25RSB120) with its power supply, sampling and control boards, and IM with magnetic powder brake, as Fig. 6 shows. The parameters of the experimental platform are presented in Table II.

Since the fault tolerance performances of six power switches are similar, T_1 fault is selected as the example to verify the effectiveness of the proposed method. The open-switch fault is simulated by putting the corresponding control signal as open. Fig. 7 presents the ability of anti-misdiagnosis of proposed NFT method. A misdiagnosis signal of T_1 is set at 0.19 s. It shows that even if misdiagnoses occur, the IM can automatically revert to the healthy operation state.

Fig. 8 presents the comparison of steady-state performance under the reference speed of 500 rpm and the load of 3 Nm. Here, the fault diagnosis threshold value T_z is set as a suitable value of 0.02. This value was determined through extensive experimental tests under various operating conditions (different speeds and loads) to ensure it was always greater than the maximum observed steady-state flux tracking error in healthy operation, thus preventing false alarms, while remaining small enough to enable rapid fault detection. The current limit value is set as 15 A to ensure safe operation. The reference value of stator flux amplitude is set as 0.6. The fault flag F_f shows the execution time of the control algorithms of healthy and tolerant modes. The speed oscillation is nearly 90 rpm (18% of reference speed) in Fig. 8(a). And the speed oscillation is nearly 40 rpm (8% of reference speed) in Fig. 8(b), which is nearly half of Fig. 8(a).

Fig. 9 presents the comparison of steady-state performance under the reference speed of 300 rpm and the load of 3 Nm. The speed oscillation is nearly 160 rpm (53.3% of reference speed) in Fig. 9(a). And the speed oscillation is reduced to nearly 25 rpm (8% of reference speed) in Fig. 9(b), which is much smoother than the former. It shows that when the reference speed is lower, the improvement of the proposed NFT method over fault operation is more significant.

Fig. 10 presents the comparison of steady-state performance under the reference speed of 500 rpm and the load of 7 Nm. The speed oscillation is nearly 220 rpm (44% of reference speed) in Fig. 10(a). And the speed oscillation is reduced to nearly 100 rpm (20% of reference speed) in Fig. 10(b). Compared to Fig. 8, the speed oscillations are increased because of the bigger load. The speed oscillation of proposed NFT method is still less than half of the case without tolerance.

Fig. 11 presents the speed-change performance under the reference speed of 300 to 500 rpm and the load of 3 Nm. Fig. 12 presents the load-change performance under the reference speed of 500 rpm and load of 3 to 7 Nm. It can be seen that the proposed NFT method is still effective during the dynamic process. Its response time is similar to the case without tolerance, and the dynamic response curve is much smoother.

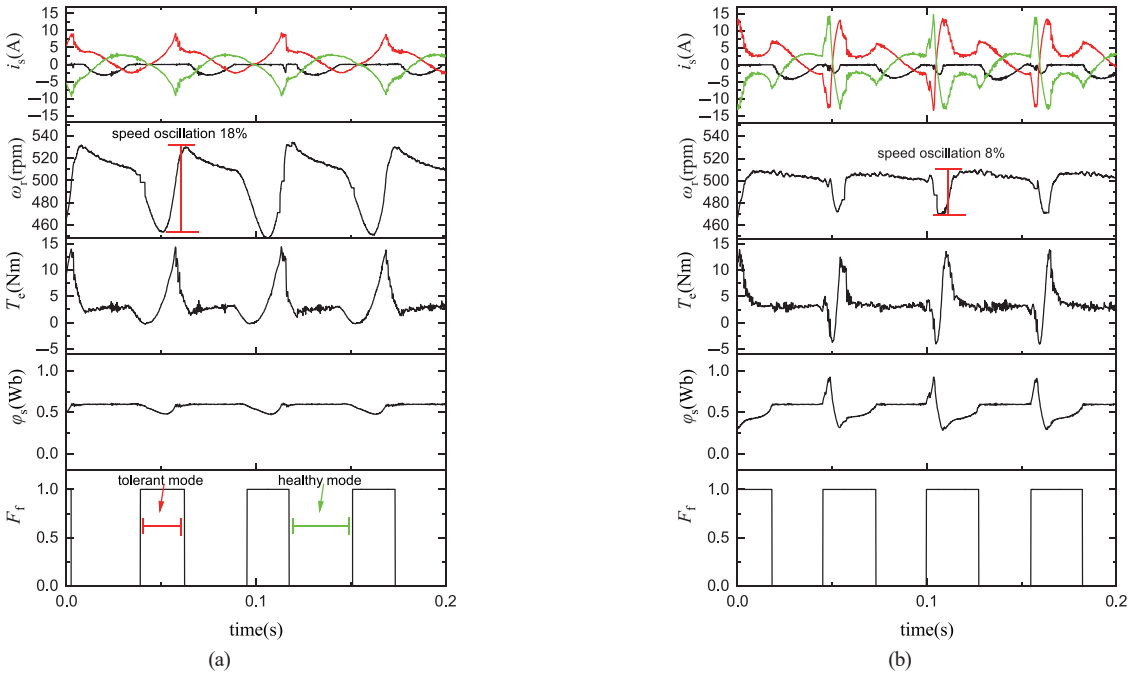

Fig. 8. The current, speed, torque, stator flux, and fault flag comparison of steady-state performance under the reference speed of 500 rpm and the load of 3 Nm: (a) without tolerance, (b) with proposed NFT method.

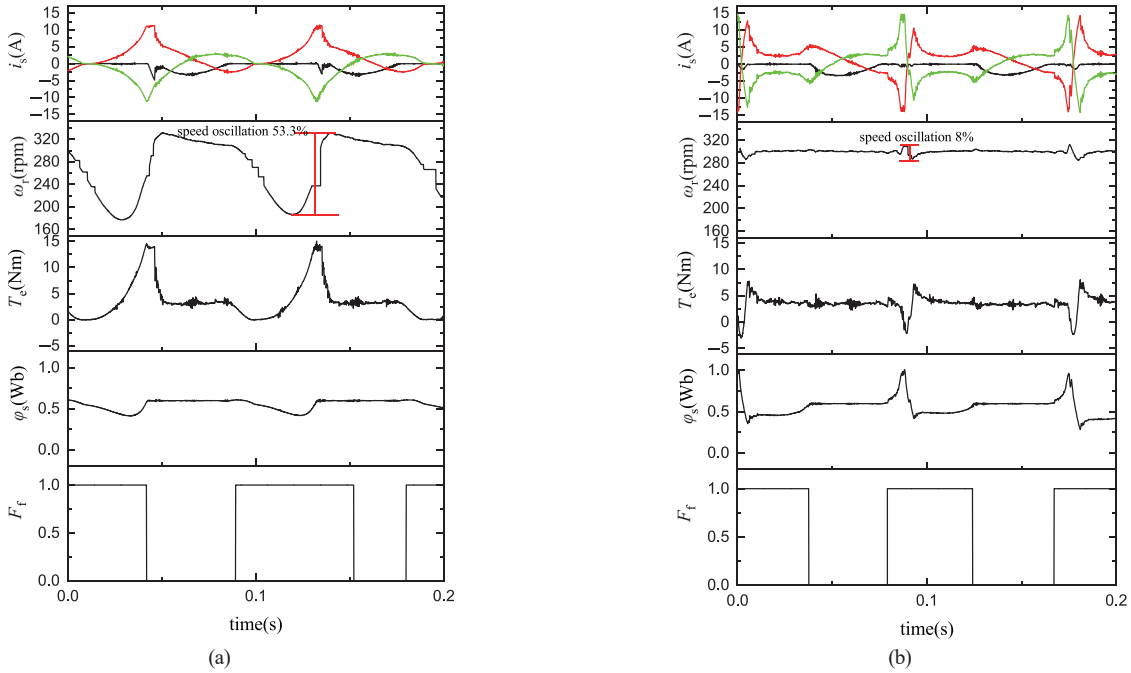

Fig. 9. The current, speed, torque, stator flux, and fault flag comparison of steady-state performance under the reference speed of 300 rpm and the load of 3 Nm: (a) without tolerance, (b) with proposed NFT method.

V. Compared with Other Methods

The proposed method is compared with other methods as shown in TABLE III. Traditional AFT methods often involve hardware reconfiguration (e.g., switching to a four-switch topology), which requires additional hardware (switches, relays) and complex control re-synthesis for each topology. In contrast, the proposed NFT method requires no hardware modification or reconfiguration, significantly reducing cost and complexity. The performance comparison is thus multifaceted: while some reconfiguration methods might achieve better post-fault performance theoretically, the proposed method offers a cost-to-performance ratio and simplicity of implementation, making it highly suitable for cost-sensitive applications where ultra-high post-fault performance is not the primary goal but continuous

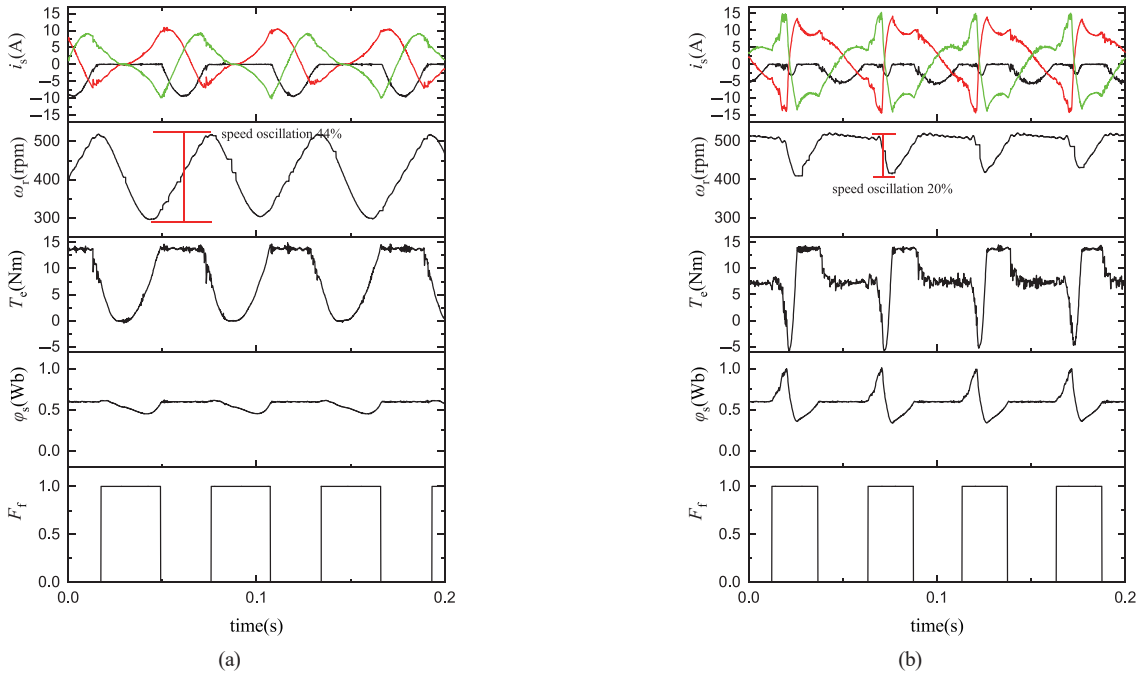

Fig. 10. The current, speed, torque, stator flux, and fault flag comparison of steady-state performance under the reference speed of 500 rpm and the load of 7 Nm: (a) without tolerance, (b) with proposed NFT method.

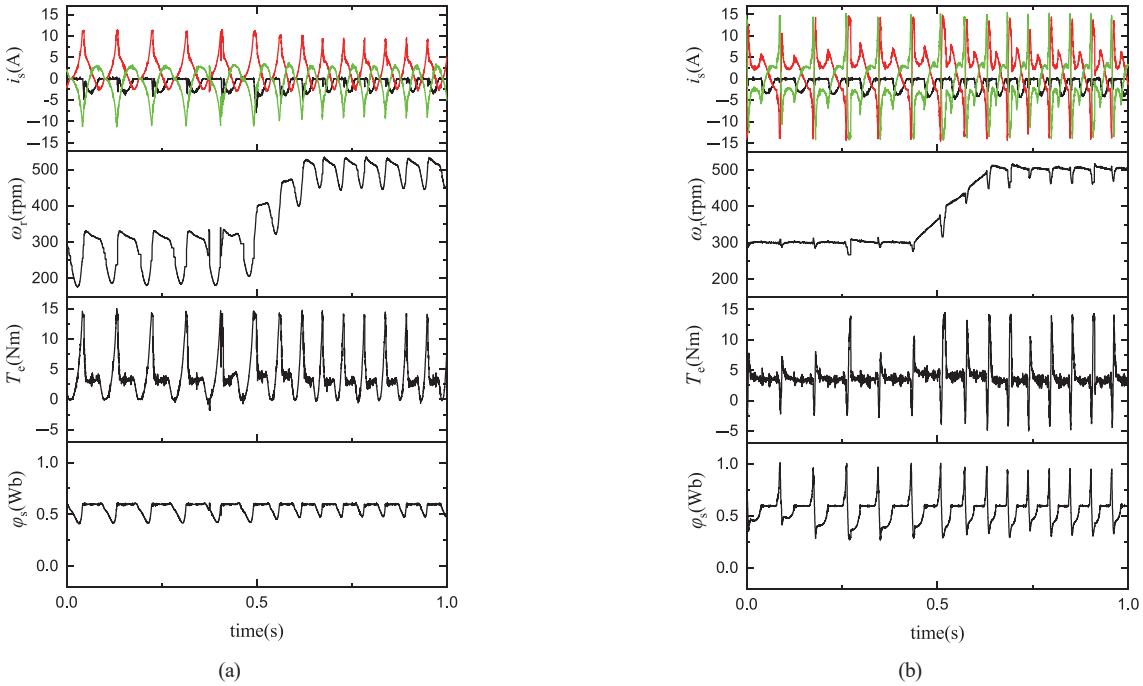

Fig. 11. The current, speed, torque, and stator flux comparison of speed-change performance under the reference speed of 300 to 500 rpm and the load of 3 Nm: (a) without tolerance, (b) with proposed NFT method.

operation is. The experimental results provided demonstrate the significant performance gain over the non-tolerant case, which is the key benchmark for a fault-tolerant scheme.

The proposed method has the following advantages. Firstly, it avoids the transformation from a static to a rotating coordinate system and the estimation of electrical angles. Secondly, the existing methods all directly perform fault tolerance after obtaining the location of the power switch failure, without considering the impact of incorrect diagnosis. Once the fault diagnosis is incorrect, it will inevitably enter the fault-tolerant mode, wasting the power switches that are still healthy. However, the proposed method has the ability to automatically switch back to the healthy mode even if incorrect diagnosis occurs.

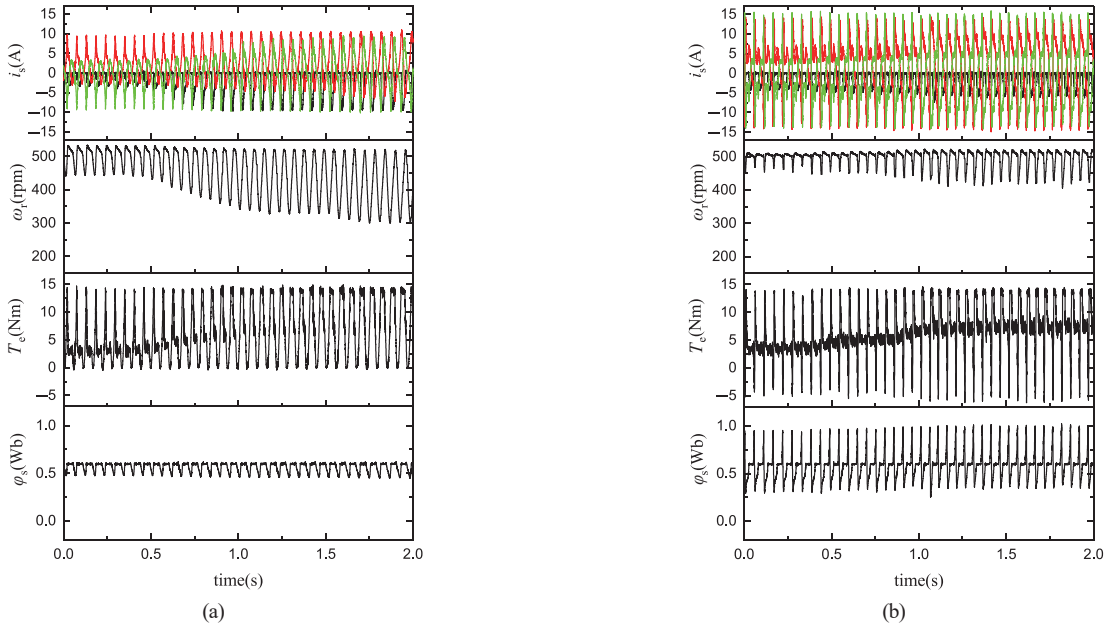

Fig. 12. The current, speed, torque, and stator flux comparison of load-change performance under the reference speed of 500 rpm and the load of 3 to 7 Nm: (a) without tolerance, (b) with proposed NFT method.

TABLE III
COMPARED WITH OTHER METHODS

Method	Topology	System signals needed	Transition stralegy	Fault location meeded	Hardwar /software cost	Remaining healthy switches utilixed
[3]	Four-leg inverter	Basic control signals	Recomstruction	Yes	High	No
[5]	Dual inverler	Basic control signals	Recomstruction	Yes	High	No
[7]	Multilevel inverter	Basic control signals	No-reconstruction	Yes	High	No
[11]	Four-switch inwerler	Basic control signals	Recomstruction	Yes	High	No
[14]	Four-switch four leg inverter	Basic control signals	Recomstruction	Yes	High	No
[24]	Basic tapology inwerler	Basic control signals Precise rodor angle estimation	No-reconstruction	Yes	Low	No
[26]	Basic tapology inwerler	Basic control signals Precise rodor angle estimation	No-reconstruction	Yes	Low	No
proposed	Basic tapology inwerler	Basic control signals	No-reconstruction srnouth trarsition	No	Low	Yes

VI. CONCLUSION

This paper proposes a novel no-reconstruction fault-tolerant method, which can realize the fault tolerance of standard IM drives without the requirement of topology reconstruction. Five healthy power switches are all used in fault tolerance. Thus, the system can work in the healthy state for half of each current cycle and in the tolerant state for the other half. Compared to existing NFT methods which also utilize five healthy power switches, the proposed method has the following contributions: first, the requirement of static-to-rotating coordinate transformation and electrical angle estimation is avoided based on the proposed two-mode control algorithm; second, a control algorithm transition strategy is designed, which can realize both the fast fault diagnosis and the smooth algorithm transition. Especially, it has the ability to revert to healthy operation even if misdiagnoses occur.

REFERENCES

[1] B. Lu and S. K. Sharma, "A literature review of IGBT fault diagnostic and protection methods for power inverters," in *IEEE Transactions on Industry Applications*, vol. 45, no. 5, pp. 1770–1777, Sept.-Oct. 2009.

[2] W. Zhang, D. Xu, P. N. Enjeti, H. Li, J. T. Hawke, and H. S. Krishnamoorthy, "Survey on fault-tolerant techniques for power electronic converters," in *IEEE Transactions on Power Electronics*, vol. 29, no. 12, pp. 6319–6331, Dec. 2014.

[3] R. R. Errabelli and P. Mutschler, "Fault-tolerant voltage source inverter for permanent magnet drives," in *IEEE Transactions on Power Electronics*, vol. 27, no. 2, pp. 500–508, Feb. 2012.

[4] P. Garg, S. Essakiappan, H. S. Krishnamoorthy, and P. N. Enjeti, "A fault-tolerant three-phase adjustable speed drive topology with active common-mode voltage suppression," in *IEEE Transactions on Power Electronics*, vol. 30, no. 5, pp. 2828–2839, May 2015.

[5] Z. Wang, J. Chen, M. Cheng, and Y. Zheng, "Fault-tolerant control of paralleled-voltage-source-inverter-fed PMSM drives," in *IEEE Transactions on Industrial Electronics*, vol. 62, no. 8, pp. 4749–4760, Aug. 2015.

[6] G. Chen and X. Cai, "Reconfigurable control for fault-tolerant of parallel converters in PMSG wind energy conversion system," in *IEEE Transactions on Sustainable Energy*, vol. 10, no. 2, pp. 604–614, Apr. 2019.
[7] X. Wang, Z. Wang, Z. Xu, J. He, and W. Zhao, "Diagnosis and tolerance of common electrical faults in T-type three-level inverters fed dual three-phase PMSM drives," in *IEEE Transactions on Power Electronics*, vol. 35, no. 2, pp. 1753–1769, Feb. 2020.
[8] X. Wang, Z. Wang, M. Gu, Z. Xu, Z. Zou, W. Wang, and M. Cheng, "Fault-tolerant control of common electrical faults in dual three-phase PMSM drives fed by T-type three-level inverters," in *IEEE Transactions on Industry Applications*, vol. 57, no. 1, pp. 481–491, Jan.-Feb. 2021.
[9] W. Huang, J. Du, W. Hua, W. Lu, K. Bi, Y. Zhu, and Q. Fan, "Current-based open-circuit fault diagnosis for PMSM drives with model predictive control," in *IEEE Transactions on Power Electronics*, vol. 36, no. 9, pp. 10695–10704, Sept. 2021.
[10] X. Zhou, J. Sun, P. Cui, Y. Lu, M. Lu, and Y. Yu, "A fast and robust open-switch fault diagnosis method for variable-speed PMSM system," in *IEEE Transactions on Power Electronics*, vol. 36, no. 3, pp. 2598–2610, Mar. 2021.
[11] M. Tousizadeh, H. S. Che, J. Selvaraj, N. A. Rahim, and B. -T. Ooi, "Fault-tolerant field-oriented control of three-phase induction motor based on unified feedforward method," in *IEEE Transactions on Power Electronics*, vol. 34, no. 8, pp. 7172–7183, Aug. 2019.
[12] D. Sun, J. Su, C. Sun, and H. Nian, "A simplified MPFC with capacitor voltage offset suppression for the four-switch three-phase inverter-fed PMSM drive," in *IEEE Transactions on Industrial Electronics*, vol. 66, no. 10, pp. 7633–7642, Oct. 2019.
[13] K. Hu, Z. Liu, I. A. Tasiu, and T. Chen, "Fault diagnosis and tolerance with low torque ripple for open-switch fault of IM drives," in *IEEE Transactions on Transportation Electrification*, vol. 7, no. 1, pp. 133–146, Mar. 2021.
[14] W. Li, S. Xuan, Q. Gao, and L. Luo, "Investigation of a four-switch four-leg inverter: Modulation, control, and application to an IPMSM drive," in *IEEE Transactions on Power Electronics*, vol. 34, no. 6, pp. 5655–5666, Jun. 2019.
[15] T. Liu and M. Fadel, "An efficiency-optimal control method for mono-inverter dual-PMSM systems," in *IEEE Transactions on Industry Applications*, vol. 54, no. 2, pp. 1737–1745, Mar.-Apr. 2018.
[16] T. Liu, M. Fadel, J. Li, and X. Ma, "A MTPA control strategy for mono-inverter multi-PMSM system," in *IEEE Transactions on Power Electronics*, vol. 36, no. 6, pp. 7165–7177, Jun. 2021.
[17] Š. Janouš, J. Talla, V. Šmídl, and Z. Peroutka, "Constrained LQR control of dual induction motor single inverter drive," in *IEEE Transactions on Industrial Electronics*, vol. 68, no. 7, pp. 5548–5558, Jul. 2021.
[18] S. Ito, T. Moroi, Y. Kubo, K. Matsuse, and K. Rajashekara, "Independent control of two permanent-magnet synchronous motors fed by a four-leg inverter," in *IEEE Transactions on Industry Applications*, vol. 51, no. 1, pp. 753–760, Jan.-Feb. 2015.
[19] Y. Song, J. Sun, Y. Zhou, Y. Liu, H. Luo, and J. Zhao, "Minimization of capacitor voltage difference for four-leg inverter dual-parallel IM system," in *IEEE Transactions on Power Electronics*, vol. 37, no. 4, pp. 3969–3979, Apr. 2022.
[20] W. Wang, J. Zhang, and M. Cheng, "A dual-level hysteresis current control for one five-leg VSI to control two PMSMs," in *IEEE Transactions on Power Electronics*, vol. 32, no. 1, pp. 804–814, Jan. 2017.
[21] Y. -S. Lim, J. -S. Lee, and K. -B. Lee, "Advanced speed control for a five-leg inverter driving a dual-induction motor system," in *IEEE Transactions on Industrial Electronics*, vol. 66, no. 1, pp. 707–716, Jan. 2019.
[22] A. Kontarček, P. Bajec, M. Nemec, V. Ambrožič, and D. Nedeljković, "Cost-effective three-phase PMSM drive tolerant to open-phase fault," in *IEEE Transactions on Industrial Electronics*, vol. 62, no. 11, pp. 6708–6718.
[23] M. Moujahed, M. Hajji, H. Benazza, M. Jemli, and M. Boussak, "Fault tolerant control of permanent magnet synchronous motor traction module," *2018 9th International Renewable Energy Congress (IREC)*, Hammamet, Tunisia, 2018, pp. 1–5.
[24] C. M. Hackl, U. Pecha, and K. Schechner, "Modeling and control of permanent-magnet synchronous generators under open-switch converter faults," in *IEEE Transactions on Power Electronics*, vol. 34, no. 3, pp. 2966–2979, Mar. 2019.
[25] X. Wang, Z. Wang, M. Gu, B. Wang, W. Wang, and M. Cheng, "Current optimization-based fault-tolerant control of standard three-phase PMSM drives," in *IEEE Transactions on Energy Conversion*, vol. 36, no. 2, pp. 1023–1035, Jun. 2021.
[26] Z. Zhang, Y. Hu, G. Luo, C. Gong, X. Liu, and S. Chen, "An embedded fault-tolerant control method for single open-switch faults in standard PMSM drives," in *IEEE Transactions on Power Electronics*, vol. 37, no. 7, pp. 8476–8487, Jul. 2022.
[27] Y. Song and J. Zhao, "Model predictive flux control-based open-circuit fault diagnosis method for two-level three-phase inverter induction motor drive," in *2022 41st Chinese Control Conference (CCC)*, Hefei, China, 2022, pp. 3912–3916.

Lei Wang was born in January 1982. He graduated from Huazhong University of Science and Technology with the master's degree. Currently, he is a senior engineer at Wuhan Second Ship Design and Research Institute. He has been engaged in the research of ship electrical systems and equipment for a long time, and has been responsible for the research and equipment development of multiple ship electrical devices.

Yingying She was born in November 1983. She obtained her doctoral degree from Huazhong University of Science and Technology. Currently, she is a researcher at Wuhan Second Ship Design and Research Institute. She has been engaged in the research and development of ship control systems for a long time and has undertaken the overall design of various ship electrical and control systems.

Yujin Song was born in Heilongjiang, China, in 1996. He received the B.S. degree and the Ph.D. degree in Control Science and Engineering, in 2017 and 2023, from the Department of Control Science and Engineering, School of Automation, Huazhong University of Science and Technology, Wuhan, China. Currently, he is working at Wuhan Second Ship Design and Research Institute. His research interests include fault tolerant control and advanced control strategies for power electronics and power converter.

Weikang Wang was born in Hubei Province, China, in 1996. He received the B.S. degree and the Ph.D. degree in 2017 and 2023 from the School of Automation, Huazhong University of Science and Technology, Wuhan, China. Currently, he is working at Wuhan Second Ship Design and Research Institute. His research interests include DC–DC converters and high frequency power conversion.

Zhixi Wu was born in Henan, China, in 1996. He received the B.S. degree in Automation from Hunan University, Changsha, China, in 2018, as well as the M.S. degree and the Ph.D. degree in control science and engineering from the Huazhong University of Science and Technology, Wuhan, China, in 2021 and 2025. Currently, he is working at Wuhan Second Ship Design and Research Institute. His research interests include multilevel converters and fault diagnosis for power converters.

A Novel Space Vector Modulation Scheme for Common-Mode Voltage Reduction in the Hybrid Active Neutral-Point-Clamped Three-Level Inverter with Balanced and Unbalanced DC-Links

Chuanjing HOU, Desheng JIA, Changwei QIN, Xiaoyan LI, and Jiandong LI

***Abstract*—The hybrid active neutral-point-clamped (HANPC) three-level inverter (TLI) requires much less SiC MOSFETs than a full-SiC ANPC TLI while providing comparable power density. Therefore, the HANPC TLI is an ideal solution for balancing performance and cost. However, excessive common-mode voltage (CMV) amplitudes are observed in conventional modulation methods, especially under unbalanced DC-links. This paper presents a CMV reduction method for the HANPC TLI with balanced and unbalanced DC-links. The scheme employs real-time sampling of photovoltaic array voltages on the DC side, followed by dynamic updates to the space vector diagram (SVD). Due to its inherent advantage of low CMV, zero vector and medium vectors are selected for reference vector synthesis. According to the position of the medium vectors in the updated SVD, the duty cycles are recalculated to ensure the output current quality. Furthermore, switching sequences are optimized through five-segment symmetrical patterning, ensuring minimal switching actions in power devices. Theoretical analysis demonstrates that this modulation method effectively reduces both the magnitude and root-mean-square (RMS) value of CMV while ensuring that SiC MOSFETs and Si IGBTs operate at high and low frequencies, respectively. The hardware-in-loop (HIL) tests validate the efficacy of the proposed modulation strategy.**

***Index Terms*—Common-mode voltage, hybrid active neutral-point-clamped (HANPC), silicon carbide (SiC), unbalanced DC-links.**

I. Introduction

THREE-LEVEL inverters (TLI) are recognized as fundamental components in modern power conversion systems, particularly in renewable energy applications, due to their superior performance over conventional two-level topologies [1], [2]. By generating three distinct voltage levels, these inverters significantly reduce voltage stress on switching devices, minimize output harmonic distortion, and lower electromagnetic interference (EMI) [3]–[5]. These characteristics enable enhanced system efficiency and improved power quality. Reliable operation is ensured for grid-connected photovoltaic (PV) systems.

The hybrid active neutral-point-clamped (HANPC) TLI topology is recognized as an advanced power electronic configuration. Compared with conventional neutral-point-clamped (NPC) inverters, diodes are replaced by active switching devices in HANPC implementations. Improved loss distribution uniformity is achieved through this structural modification. The reduced conduction voltage across switching devices is obtained. Consequently, operational efficiency and power density are elevated [6]–[8].

In the HANPC topology, each phase leg is typically constructed with six switching devices. Four low-frequency switches and two high-frequency switches are integrated in this configuration. Such a configuration makes the inverter more flexible in control and able to adapt to different loads and working conditions requirements. It enables it to have a wide range of application prospects and advantages in high-voltage high-power power electronics applications [9], [10].

In PV systems, however, the advantages of HANPC inverters are often challenged by inherent DC-links voltage imbalances. Such imbalances arise from partial shading, module degradation, or mismatched string configurations in solar arrays [11]–[13]. These conditions lead to unequal power generation across PV strings, causing asymmetric voltage distribution in the DC-links capacitors, the presence of unbalanced neutral-point voltage can degrade the overall performance of both the equipment and the grid [14].

Under severe imbalance, the neutral-point voltage oscillates excessively, amplifying common-mode voltage (CMV) and inducing leakage currents through the parasitic capacitance between PV panels and ground [15]–[17]. Elevated CMV not only degrades system efficiency but also poses safety risks, accelerates component aging, and violates grid codes for

Manuscript received June 16, 2025; revised August 3, 2025; accepted August 24, 2025. Date of publication December 30, 2025; date of current version September 9, 2025. This work was supported by the Taishan Scholar Project of Shandong Province under the grant tsqn202312223, the Natural Science Foundation of Shandong Province under the grant ZR2024MF039 and grant ZR2025MS1051, the National Natural Science Foundation of China under the grant 62573273, and the Development Plan for Youth Innovation Team of Higher Education Institutions in Shandong Province under the grant 2023KJ127. *(Corresponding authors: Changwei Qin and Xiaoyan Li.)*

All authors are with the School of Information and Electrical Engineering, Shandong Jianzhu University, Jinan 250101, China, and Shandong Key Laboratory of Smart Buildings and Energy Efficiency, Jinan 250101, China (e-mail: houchuanjing1211@sdjzu.edu.cn; 2022085101@stu.sdjzu.edu.cn; qinchangwei20@sdjzu.edu.cn; xylee2023@sdjzu.edu.cn; 2023080127@stu.sdjzu.edu.cn).

Digital Object Identifier 10.24295/CPSSTPEA.2025.00033

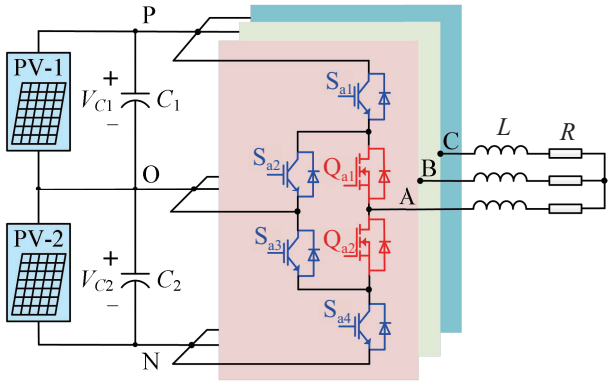

Fig. 1. Topology of the HANPC TLI with unbalanced DC-links.

electromagnetic compatibility (EMC) [18], [19]. Traditional CMV mitigation strategies, such as passive filters or complex modulation schemes, often introduce trade-offs between hardware complexity, efficiency, and current quality [20]. For instance, passive damping resistors reduce CMV at the expense of increased losses, while advanced modulation methods like virtual vector synthesis may compromise dynamic response or require excessive computational resources [21]–[23]. [24] presents a space vector modulation (SVM) strategy for suppressing the CMV in the reduced switch count (RSC) TLI with unbalanced neutral-point voltage, due to topological limitations, this method abandons the medium vector with a lower CMV amplitude. [25] proposes an optimized DPWM (O-DPWM) scheme to reduce the leakage current for three-level inverters under different neutral-point voltage conditions. The proposed method has demonstrated effective suppression of leakage current under unbalanced operating conditions, while exhibiting limited effectiveness in common-mode voltage suppression.

To this end, this paper presents a novel CMV suppression strategy for the HANPC TLI, which is applicable for both balanced and imbalanced DC-links capacitor voltage conditions. Real-time sampling of DC-links capacitor voltages enables continuous updates to the space vector diagram. A revised duty cycle calculation algorithm is introduced. The core innovation lies in the comprehensive utilization of medium vectors for reference voltage vector synthesis.

The remainder of this paper is organized as follows: Section II presents the topology and working principles of the HANPC TLI. Section III introduces the proposed modulation scheme. Section IV gives comprehensive experimental results to verify the correctness and effectiveness of the proposed method. Finally, Section V concludes this article.

II. Working Principle of HANPC TLI with Balanced and Unbalanced DC-Links

In this section, a detailed presentation of the HANPC TLI topology is given, which includes topology structure and operational principles. Fig. 1 shows the general circuit of HANPC TLI, each capacitor is connected to a PV array at both ends [26]. The capacitor voltage is denoted by V_{C1} and V_{C2}, respectively. The HANPC TLI comprises four Si IGBTs switches (S_{x1}, S_{x2}, S_{x3}, and S_{x4}) and two SiC MOSFETs switches (Q_{x1} and Q_{x2}) (x=a, b, c) in each phase.

TABLE I
Output States and Output Voltages Corresponding to Switching States of HANPC TLI

Output state	Output voltage	Switching states (x = a, b, c)					
		S_{x1}	S_{x2}	S_{x3}	S_{x4}	Q_{x1}	Q_{x2}
[P]	V_{C1}	1	0	1	0	1	0
[O+]	0	1	0	1	0	0	1
[O–]	0	0	1	0	1	1	0
[N]	$-V_{C2}$	0	1	0	1	0	1

TABLE II
Basic Voltage Vectors and CMVs for HANPC TLI with Unbalanced DC-Links

Vectors	State	CMV	State	CMV
Zero	[PPP]	V_{C1}	[OOO]	0
	[NNN]	$-V_{C2}$		
P-Type Small	[POO]	$V_{C1}/3$	[PPO]	$2V_{C1}/3$
	[OPO]	$V_{C1}/3$	[POP]	$2V_{C1}/3$
	[OOP]	$V_{C1}/3$	[OPP]	$2V_{C1}/3$
N-Type Small	[NOO]	$-V_{C2}/3$	[NNO]	$-2V_{C2}/3$
	[ONO]	$-V_{C2}/3$	[NON]	$-2V_{C2}/3$
	[OON]	$-V_{C2}/3$	[ONN]	$-2V_{C2}/3$
Medium	[PON]	$(V_{C1}-V_{C2})/3$	[OPN]	$(V_{C1}-V_{C2})/3$
	[NPO]	$(V_{C1}-V_{C2})/3$	[NOP]	$(V_{C1}-V_{C2})/3$
	[ONP]	$(V_{C1}-V_{C2})/3$	[PNO]	$(V_{C1}-V_{C2})/3$
Large	[NNP]	$(V_{C1}-2V_{C2})/3$	[PNP]	$(2V_{C1}-V_{C2})/3$
	[NPN]	$(V_{C1}-2V_{C2})/3$	[NPP]	$(2V_{C1}-V_{C2})/3$
	[PNN]	$(V_{C1}-2V_{C2})/3$	[PPN]	$(2V_{C1}-V_{C2})/3$

Table I summarizes the output states and voltage levels corresponding to all switching states of the HANPC TLI, where "1" and "0" represent the on and off states of semiconductors, respectively. It should be noted that the NPC TLI merely has three output states [P], [N], and [O], the HANPC topology contains four output states [P], [N], [O+], and [O–].

The CMV calculation formula is calculated as follows:

$$v_{CM} = \frac{v_{AO} + v_{BO} + v_{CO}}{3} \tag{1}$$

where v_{AO}, v_{BO}, and v_{CO} are three-phase output voltages. All the basic voltage vectors are summarized in Table II. Obviously, the basic vectors marked in red exhibit the highest CMV magnitudes and should therefore be excluded during reference vector synthesis. Conversely, the vectors highlighted in blue generating minimal CMV and are prioritized in the proposed space vector modulation scheme to achieve effective CMV suppression. Based on this analysis, a systematic CMV mitigation strategy for the HANPC TLI under both balanced and unbalanced DC-links capacitor voltage conditions will be

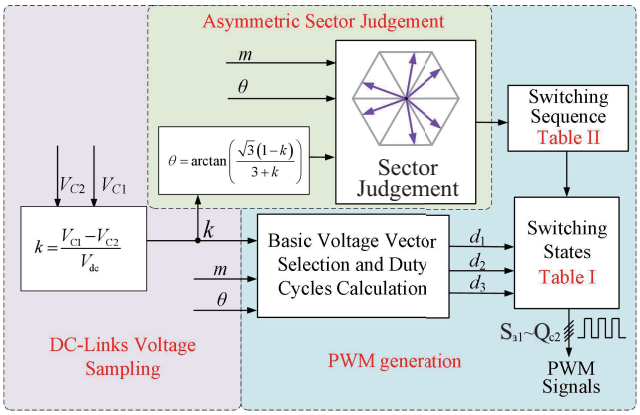

Fig. 2. Overall diagram of the proposed novel modulation method.

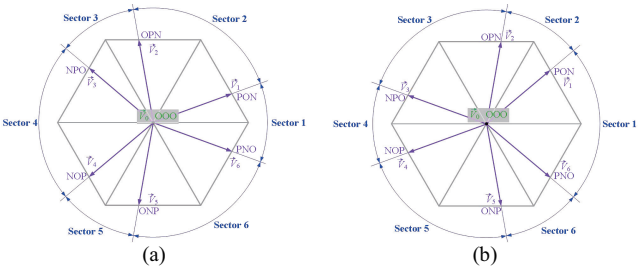

Fig. 3. SVDs for HANPC TLI with unbalanced DC-links. (a) $k > 0$, (b) $k < 0$.

elaborated in the following section.

III. Proposed Modulation Strategy

The proposed modulation strategy consists of three components. Initially, the two capacitor voltages on the DC-links are sampled, and the capacitor voltage unbalance factor k is calculated by the formula. Subsequently, the space vector diagram (SVD) is updated according to the capacitor voltage imbalance factor for sector judgment of the reference voltage vector (V_{ref}). Finally, the duty cycle is calculated based on the capacitor voltage unbalance factor, and the drive signal of the power switching tube is generated based on the corresponding switching sequence. The overall diagram of the proposed method is shown in Fig. 2.

A. DC-Links Voltage Sampling and Sector Judgement

Firstly, the voltages across capacitors C_1 and C_2 are sampled, and noted as V_{C1} and V_{C2}, respectively.

Next, the unbalanced factor k is defined as:

$$k = \left(V_{C1} - V_{C2}\right) / V_{dc} \tag{2}$$

Under unbalanced neutral point (NP) voltage conditions, the capacitor voltage fluctuates in response to variations in the voltages of the two PV arrays, resulting in a corresponding alteration of the SVD, as illustrated in Fig. 3. Consequently, the medium vector expression can be represented by the following equation:

$$\begin{cases} \vec{V}_1\ [\mathrm{PON}] = \dfrac{3+k}{6}\cdot V_{dc} + \mathrm{j}\cdot\dfrac{\sqrt{3}\cdot(1-k)}{6}\cdot V_{dc} \\ \vec{V}_2\ [\mathrm{OPN}] = -\dfrac{k}{3}\cdot V_{dc} + \mathrm{j}\cdot\dfrac{\sqrt{3}}{3}\cdot V_{dc} \\ \vec{V}_3\ [\mathrm{NPO}] = \dfrac{k-3}{6}\cdot V_{dc} + \mathrm{j}\cdot\dfrac{\sqrt{3}\cdot(1+k)}{6}\cdot V_{dc} \\ \vec{V}_4\ [\mathrm{NOP}] = \dfrac{k-3}{6}\cdot V_{dc} - \mathrm{j}\cdot\dfrac{\sqrt{3}\cdot(1+k)}{6}\cdot V_{dc} \\ \vec{V}_5\ [\mathrm{ONP}] = -\dfrac{k}{3}\cdot V_{dc} - \mathrm{j}\cdot\dfrac{\sqrt{3}}{3}\cdot V_{dc} \\ \vec{V}_6\ [\mathrm{PNO}] = \dfrac{3+k}{6}\cdot V_{dc} - \mathrm{j}\cdot\dfrac{\sqrt{3}\cdot(1-k)}{6}\cdot V_{dc} \end{cases} \tag{3}$$

Since the position of the medium vector in the SVD will change with the capacitor voltage offset on the DC-links, it is necessary to compute the position of the medium vector in real time when judging sectors, and the angle of the medium vector [PON] can be calculated by the following formula:

$$\theta = \arctan\left(\frac{\sqrt{3}(1-k)}{3+k}\right) \tag{4}$$

B. Duty Cycle Calculation and Drive Signals Generation

Taking Sector 1 as an example, two fundamental voltage vectors [PON] and [PNO] are used to synthesize the reference voltage vector. The voltage-second balance equation is written as follows:

$$\begin{cases} \vec{V}_{ref} = \vec{V}_1\cdot d_1 + \vec{V}_6\cdot d_6 + \vec{V}_0\cdot d_0 \\ d_1 + d_6 + d_0 = 1 \end{cases} \tag{5}$$

where d_1, d_6, and d_0 are the duty cycle of [PON], [PNO], and [OOO].

The corresponding duty cycle can be calculated as:

$$\begin{cases} d_1 = m\cdot\dfrac{\sqrt{3}}{3+k}\cdot\cos\theta + m\cdot\dfrac{1}{1-k}\cdot\sin\theta \\ d_6 = m\cdot\dfrac{\sqrt{3}}{3+k}\cdot\cos\theta - m\cdot\dfrac{1}{1-k}\cdot\sin\theta \\ d_0 = 1 - m\cdot\dfrac{2\sqrt{3}}{3+k}\cdot\cos\theta \end{cases} \tag{6}$$

Considering the symmetry of SVD, the duty cycle formulas in other sectors are similar to the above analysis and will not be repeated here.

In Sector 1, to satisfy the requirements of reduced switching numbers and harmonic distortions, the switching sequence is arranged as [O_+O_O_]-[PNO_]-[PO_N]-[PNO_]-[O_+O_O_], as shown in Fig. 4. Within each sampling period, the switching states of all Si IGBTs (S_{a1}–S_{c4}) are maintained unchanged, thereby avoiding additional switching losses. For the SiC

TABLE III
SWITCHING SEQUENCE OF THE PROPOSED METHOD

Sector	Switching sequence
1	[$O_+O_-O_-$]-[PNO_-]-[PO_-N]-[PNO_-]-[$O_+O_-O_-$]
2	[$O_+O_+O_-$]-[PO_+N]-[O_+PN]-[PO_+N]-[$O_+O_+O_-$]
3	[$O_-O_+O_-$]-[O_-PN]-[NPO_-]-[O_-PN]- [$O_-O_+O_-$]
4	[$O_-O_+O_+$]-[NO_+P]-[NPO_+]-[NO_+P]-[$O_-O_+O_+$]
5	[$O_-O_-O_+$]-[O_-NP]-[NO_-P]-[O_-NP]-[$O_-O_-O_+$]
6	[$O_+O_-O_+$]-[O_+NP]-[PNO_+]-[O_+NP]-[$O_+O_-O_+$]

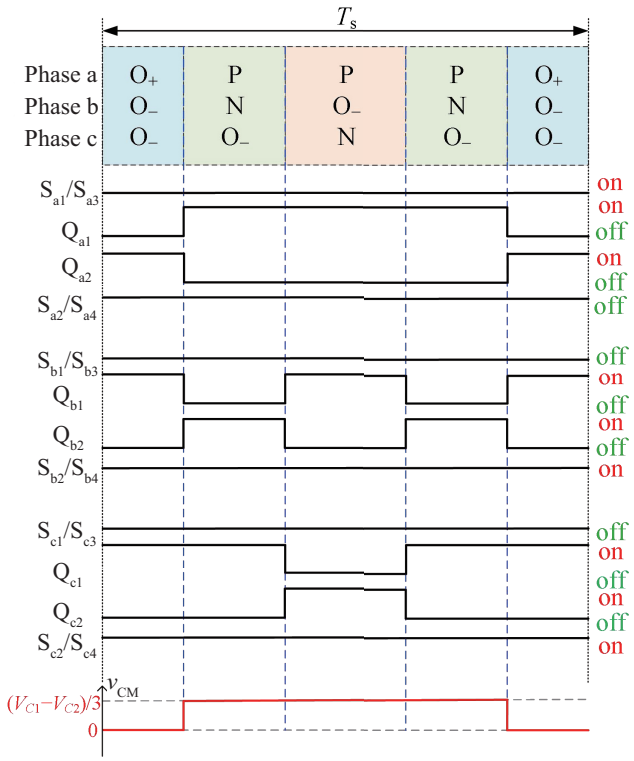

Fig. 4. Switching sequence, switching states, and CMV in Sector 1, k>0.

MOSFETs, the power devices of phase a and phase c undergo a single switching action per cycle, while the power devices of phase b exhibit two switching actions. Similar switching patterns are observed in other sectors. Furthermore, zero vector produces zero CMV, whereas the medium vectors generate a smaller CMV amplitude of only $(V_{C1}-V_{C2})/3$.

By designing a reasonable modulation strategy, the SiC MOSFETs can operate in high-frequency and the Si IGBTs can operate in fundamental frequency, which further reduces switching losses, and thus improves system efficiency. Table III summarizes the switching sequences in all sectors for the proposed modulation strategy.

IV. EXPERIMENTAL RESULTS

To validate the performance of the proposed modulation scheme, an experimental test system of the HANPC TLI is designed, as shown in Fig. 5. The main circuit is implemented

TABLE IV
PARAMETERS FOR EXPERIMENTAL TEST

Parameter	Value
DC Voltage (V_{dc})	540 V
AC output frequency (f)	50 Hz
Switching period (T_s)	100 μs
Sampling frequency (f_{SF})	10 kHz
DC-link capacitors (C_1 and C_2)	2350 μF
Voltage difference	−100 V, 0 V, 100 V
RL load	R_{load} = 10 Ω L_{load} = 7 mH

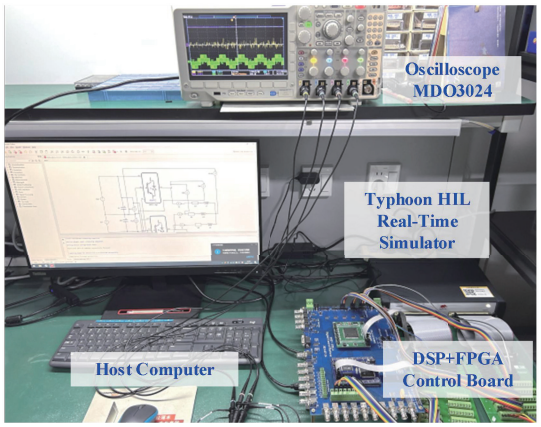

Fig. 5. Photograph of the hardware-based test rig.

based on hardware-in-the-loop (HIL) real-time simulator. The control board is designed to contain digital signal processor (DSP) 28335 from Texas Instruments and field-programmable gate array (FPGA) XC3S500E from Xilinx. The DSP is used to execute the system control strategy, while the FPGA is used to generate the PWM signals. The DSP sends data to the FPGA through an external interface (XINTF) module, which includes the sector number and the duty cycle.

The parameters for both simulation and experimental tests are given in Table IV. To demonstrate the significant advantages of the proposed modulation strategy, three modulation methods suitable for unbalanced conditions are used for comparisons. Method-1 is the hybrid SVM method in [27], method-2 is the CMV reduction method in [28], and method-3 is the proposed CMV reduction scheme.

The first verification is the operation of the three modulation methods in the balanced conditions, and the experimental results are shown in Fig. 6, in which the modulation index m is 0.4 and the voltage difference between two DC-links capacitors is set to be 270 V. The CMVs of method-1 and method-2 are relatively high, because the basic vectors with high CMV magnitudes are utilized by these two methods.

Since method-1 uses all the basic vectors to synthesize the V_{ref}, it achieves an output current total harmonic distortion (THD) of only 1.32%. However, this method exhibits signi-ficantly higher CMV amplitudes, with a peak-to-peak range of 360 V

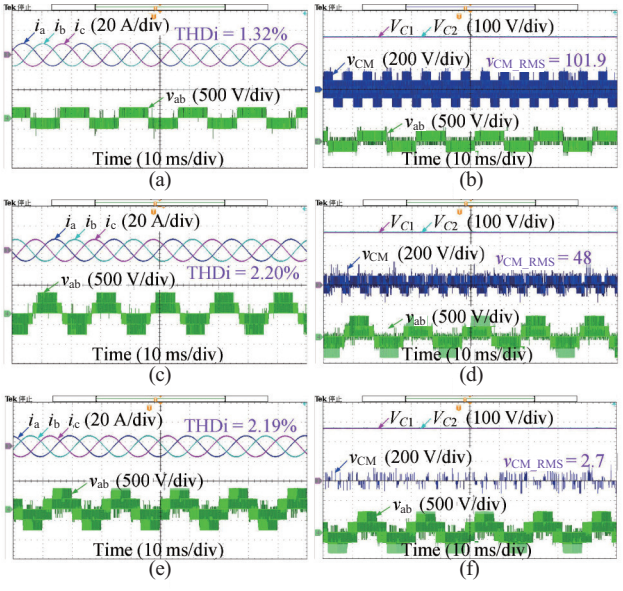

Fig. 6. Experimental results under balanced conditions (m = 0.4, k = 0). (a) Three-phase output currents and line voltage of Method-1, (b) DC power source voltage and common-mode voltage of Method-1, (c) Three-phase output currents and line voltage of Method-2, (d) DC power source voltage and common-mode voltage of Method-2, (e) Three-phase output currents and line voltage of Method-3, (f) DC power source voltage and common-mode voltage of Method-3.

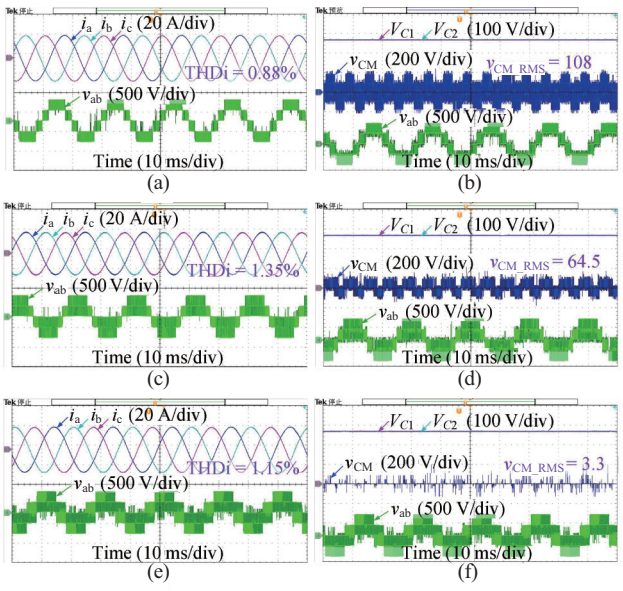

Fig. 7. Experimental results under balanced conditions (m = 0.8, k = 0). (a) Three-phase output currents and line voltage of Method-1, (b) DC power source voltage and common-mode voltage of Method-1, (c) Three-phase output currents and line voltage of Method-2, (d) DC power source voltage and common-mode voltage of Method-2, (e) Three-phase output currents and line voltage of Method-3, (f) DC power source voltage and common-mode voltage of Method-3.

(−178 V to 182 V) and an RMS value of 101.9 V. Method-2 optimizes vector selection by eliminating small vectors with high CMV amplitudes, reducing the CMV RMS value to 48 V while maintaining an output current THD of 2.20%.

The proposed method-3 adopts a medium-vector-dominated synthesis scheme, theoretically achieving zero CMV under balanced conditions. Experimental results confirm its CMV RMS value as low as 2.7 V, with an output current THD of 2.19%, demonstrating a synergistic optimization of CMV suppression and current quality. The proposed method can effectively suppress the CMV, whereas three-phase sinusoidal output currents can be guaranteed at the same time.

TABLE V
COMPARISONS OF DIFFERENT METHODS UNDER BALANCED CONDITIONS

Conditions		Range of CMV	RMS value of CMV	THDi
Method-1	m = 0.4	−178 V ~ 182 V	101.9 V	1.32 %
	m = 0.8	−179 V ~ 182 V	108 V	0.88 %
Method-2	m = 0.4	−85.2 V ~ 91.5 V	48 V	2.20 %
	m = 0.8	−85 V ~ 91 V	64.5 V	1.35 %
Method-3	m = 0.4	0 V	2.7 V	2.19 %
	m = 0.8	0 V	3.3 V	1.15 %

To further validate the adaptability of modulation strategies, experiments were repeated at a higher modulation index (m=0.8). As illustrated in Fig. 7, all three methods maintain stable operation under high modulation index conditions, with CMV suppression characteristics consistent with those observed at low modulation. Notably, method-3 restricts the CMV RMS value to 3.3 V and reduces the output current THD to 1.15%, confirming its applicability across a wide modulation index range. A systematic comparison of CMV suppression and THD performance under balanced DC-links conditions is summarized in Table V. Since method-3 avoids using the basic voltage vectors with high CMV magnitudes, the current THD value is slightly higher than that of method-1 and method-2. Fortunately, the current THD value of the proposed method remains at an acceptable level.

For DC-links voltage imbalance conditions, experiments were conducted with ±100 V deviations (k=±0.1852). As shown in Fig. 8, when the upper capacitor voltage is 100 V lower than the lower capacitor (k=−0.1852) at m=0.4, method-1 exhibits a CMV peak-to-peak range of 358.5 V (−211.5 V to 147 V) and an RMS value of 103.1 V, accompanied by a THD of 1.36%. Method-2 reduces the CMV RMS value to 59 V with a THD of 2.19%, while method-3 leverages the inherent low-CMV characteristics of medium vectors, achieving a CMV RMS value of 18.5 V and a THD of 2.7%.

At m=0.8 (Fig. 9), method-3 increases the CMV RMS value slightly to 25.8 V but further reduces the THD to 2.34%, demonstrating effective CMV suppression and high-quality current output under imbalanced conditions. Quantitative comparisons under these conditions are systematically presented in Table VI.

When the upper capacitor voltage exceeds the lower capacitor by 100 V (k = 0.1852), the experimental waveforms for the case of low and high modulation indices (m=0.4 and m=0.8) are shown in Fig. 10 and Fig. 11, respectively. The CMV suppression performance and output current quality remain consistent with those under negative imbalance conditions. Although the proposed method exhibits marginal THD degradation compared to method-1, it demonstrates a significant

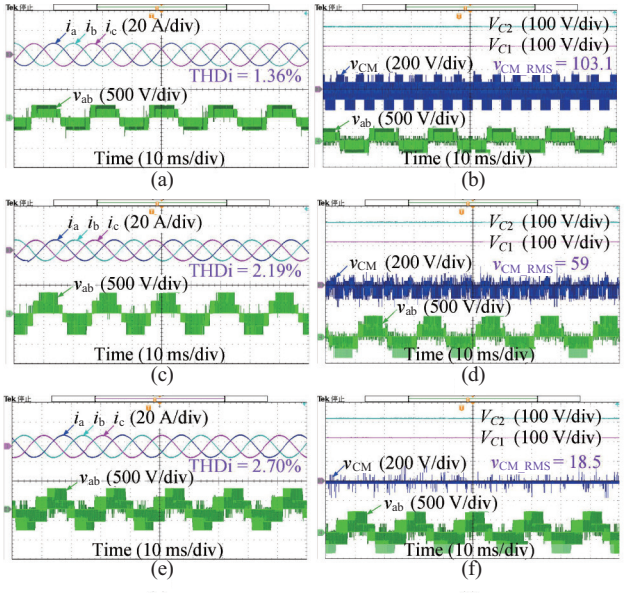

Fig. 8. Experimental results for negative unbalancing coefficient (m = 0.4, k = −0.1852). (a) Three-phase output currents and line voltage of Method-1, (b) DC power source voltage and common-mode voltage of Method-1, (c) Three-phase output currents and line voltage of Method-2, (d) DC power source voltage and common-mode voltage of Method-2, (e) Three-phase output currents and line voltage of Method-3, (f) DC power source voltage and common-mode voltage of Method-3.

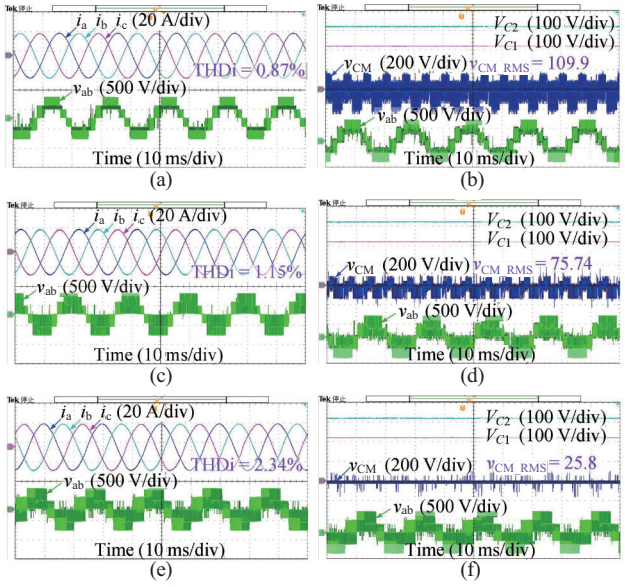

Fig. 9. Experimental results for negative unbalancing factor (m = 0.8, k = −0.1852). (a) Three-phase output currents and line voltage of Method-1, (b) DC power source voltage and common-mode voltage of Method-1, (c) Three-phase output currents and line voltage of Method-2, (d) DC power source voltage and common-mode voltage of Method-2, (e) Three-phase output currents and line voltage of Method-3, (f) DC power source voltage and common-mode voltage of Method-3.

advantage in CMV amplitude reduction. The quantitative performance for positive unbalancing factor is summarized in Table VII.

Overall, method-3 effectively reduces the CMV amplitude and RMS value under different modulation indexes and

TABLE VI
COMPARISONS OF DIFFERENT METHODS FOR NEGATIVE UNBALANCING FACTOR (K = −0.1852)

Conditions		Range of CMV	RMS value of CMV	THDi
Method-1	m = 0.4	−211.5 V ~ 147 V	103.1 V	1.36 %
	m = 0.8	−211.5 V ~ 147 V	109.9 V	0.87 %
Method-2	m = 0.4	−136 V ~ 73 V	59 V	2.19 %
	m = 0.8	−135.5 V ~ 73 V	75.74 V	1.15 %
Method-3	m = 0.4	−28 V ~ 0 V	18.5 V	2.70 %
	m = 0.8	−28 V ~ 0 V	25.8 V	2.34 %

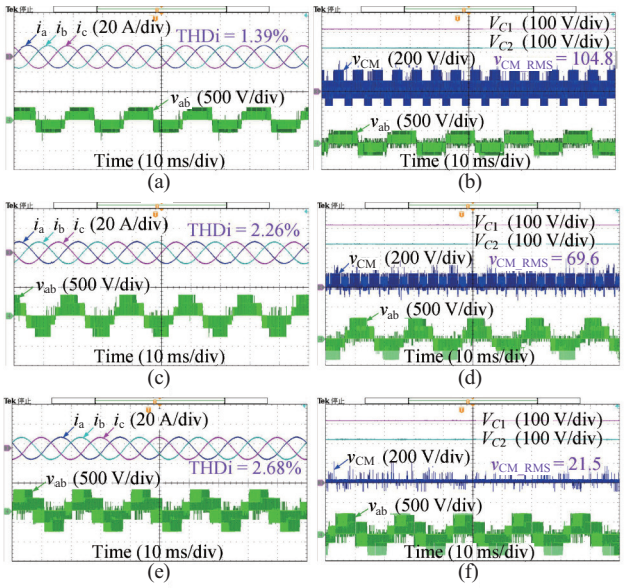

Fig. 10. Experimental results for positive unbalancing factor (m = 0.4, k = 0.1852). (a) Three-phase output currents and line voltage of Method-1, (b) DC power source voltage and common-mode voltage of Method-1, (c) Three-phase output currents and line voltage of Method-2, (d) DC power source voltage and common-mode voltage of Method-2, (e) Three-phase output currents and line voltage of Method-3, (f) DC power source voltage and common-mode voltage of Method-3.

different unbalance factors, thus ensuring the safe and stable operation of the inverter system.

Selected experimental waveforms of the power switch drive signals are depicted in Fig. 12. All three modulation methods achieved hybrid high-low frequency modulation. Method-1 and method-2 generate only one switching action per phase per cycle, whereas method-3 introduces optimized medium-vector timing to achieve precise CMV control, resulting in two switching actions for one phase while maintaining single switching actions for the other two phases, consistent with theoretical predictions. This design ensures minimal additional switching losses while prioritizing CMV suppression.

To verify the influence of unbalanced conditions on the DC side on the loss distribution, a co-simulation platform of Simulink and PLECS was built for the proposed common-mode voltage suppression method, and the corresponding losses were calculated and summarized in Fig. 13. It can be seen from the figure that under balanced conditions, due to its symmetrical

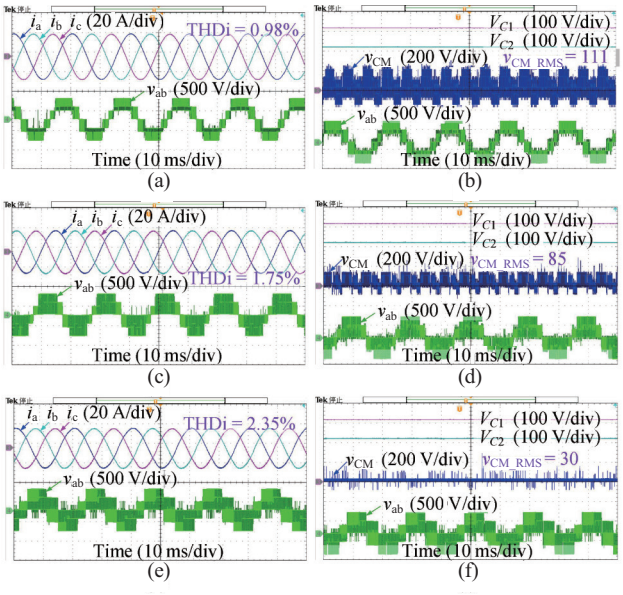

Fig. 11. Experimental results for positive unbalancing factor (m = 0.8, k = 0.1852). (a) Three-phase output currents and line voltage of Method-1, (b) DC power source voltage and common-mode voltage of Method-1, (c) Three-phase output currents and line voltage of Method-2, (d) DC power source voltage and common-mode voltage of Method-2, (e) Three-phase output currents and line voltage of Method-3, (f) DC power source voltage and common-mode voltage of Method-3.

TABLE VII
COMPARISONS OF DIFFERENT METHODS FOR NEGATIVE UNBALANCING FACTOR (K = 0.1852)

Conditions		Range of CMV	RMS value of CMV	THDi
Method-1	m = 0.4	−142.5 V ~ 217.5 V	104.8 V	1.39 %
	m = 0.8	−143 V ~ 217 V	111 V	0.98 %
Method-2	m = 0.4	−68 V ~ 140 V	69.6 V	2.26 %
	m = 0.8	−68 V ~ 141.5 V	85 V	1.75 %
Method-3	m = 0.4	0 V ~ 33 V	21.5 V	2.68 %
	m = 0.8	0 V ~ 32.5 V	30 V	2.35 %

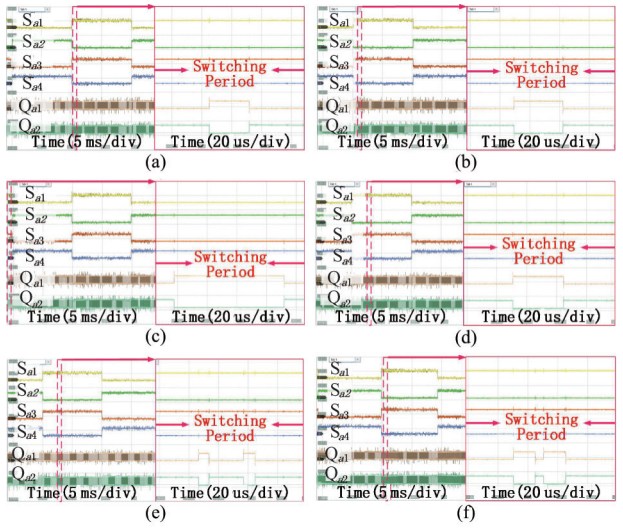

Fig. 12. Drive signals of power switches. (a) method-1, m = 0.8, k = 0, (b) method-1, m = 0.8, k = 0.1852, (c) method-2, m = 0.8, k = 0, (d) method-2, m = 0.8, k = 0.1852, (e) method-3, m = 0.8, k = 0, (f) method-3, m = 0.8, k = 0.1852.

characteristics, the conduction loss and switching loss of power devices can remain relatively balanced. Under the unbalanced condition on the DC-links, when k=−0.1852, the increase in the voltage of the lower capacitor C_2 will increase the switching loss of the power device Q_{a2}, but the overall loss can remain relatively balanced. The same conclusion can be extended to other conditions.

V. CONCLUSION

For the dual-input TLI system, this paper presents a novel CMV reduction method for HANPV TLI with balanced and unbalanced NP voltage conditions. This method eliminates vectors with higher CMV amplitudes. By sampling the DC-links capacitor voltages, an imbalance factor is calculated, which subsequently facilitates the reconfiguration of the SVD, thereby simplifying the computational complexity. Furthermore, a symmetrical five-segment switching sequence that starts and ends with zero vector is designed to reduce harmonics. Experiments verify the effectiveness of the proposed modulation strategy.

REFERENCES

[1] C. Zhang, *Advanced Control of Grid-Connected High-Power Converters*, Singapore: Springer Nature Singapore, 2023.

[2] C. Hou, D. Jia, C. Qin, and X. Li, "A novel topology and modulation strategy for the high-gain hybrid active neutral-point-clamped three-level inverter," in *CPSS Transactions on Power Electronics and Applications*, vol. 10, no. 1, pp. 44–54, Mar. 2025.

[3] G. Wang, X. Yuan, Y. Jiang, J. Wang, F. Wang, and Z. Liu, "An improved finite control set model predictive control based on a novel dual-port three-level inverter," in *CPSS Transactions on Power Electronics and Applications*, vol. 9, no. 4, pp. 430–442, Dec. 2024.

[4] C. Qin, X. Li, C. Hou, and C. Su, "A fast-processing implementation method of virtual space vector modulation for the impedance-source three-level inverter," in *IEEE Transactions on Circuits and Systems II: Express Briefs*, vol. 71, no. 7, pp. 3568–3572, Jul. 2024.

[5] C. Wang, Z. Li, X. Si, and H. Xin, "Control of neutral-point voltage in three-phase four-wire three-level NPC inverter based on the disassembly of zero level," in *CPSS Transactions on Power Electronics and Applications*, vol. 3, no. 3, pp. 213–222, Sept. 2018.

[6] L. M. Halabi, S. S. Hakami, and K. -B. Lee, "Integrated voltage vector–based SVPWM for reliability and performance enhancement of five-level HANPC inverters," in IEEE Transactions on Industrial Electronics, vol. 71, no. 2, pp. 1093–1103, Feb. 2024.

[7] Z. Cai, Y. Du, J. Su, X. Yang, Y. Shi, and J. Zhang, "Comprehensive optimization of ZVS variable frequency control for SiC/Si HANPC converter," in *IEEE Transactions on Industry Applications*, vol. 60, no. 1, pp. 1160–1171, Jan.-Feb. 2024.

[8] S. Belkhode, A. Shukla, and S. Doolla, "Enhanced hybrid active-neutral-point-clamped converter with optimized loss distribution-based modulation scheme," in *IEEE Transactions on Power Electronics*, vol. 36, no. 3, pp. 3600–3612, Mar. 2021.

[9] T. Sornsadaeng, P. Chanhom, D. Amorndechaphon, and S. Sirisukprasert, "A strategy for neutral voltage modulation ensuring fault tolerance in CHB multilevel inverters with reduced CMV and unbalanced DC sources," in *IEEE Access*, vol. 12, pp. 154138–154159, 2024.

[10] Q. Yan, H. Chen, T. Zhao, X. Yuan, L. Zhang, and R. Zhao, "A carrier-based discontinuous space-vector PWM for common-mode voltage reduction in dual-input three-level T-type inverters with unbalanced neutral-point voltages," in *IEEE Transactions on Power Electronics*, vol. 39, no. 9, pp. 11020–11033, Sept. 2024.

[11] C. Roncero-Clemente, E. Romero-Cadaval, M. Ruiz-Cortés, and O. Husev, "Carrier level-shifted based control method for the PWM 3L-T-type qZS inverter with capacitor imbalance compensation," in *IEEE Transactions on Industrial Electronics*, vol. 65, no. 10, pp. 8297–8306,

Oct. 2018.
[12] Y. Zou, L. Zhang, Y. Xing, H. Zhang, W. Mo, Y. Wu, and X. Shea, "Enhanced carrier-based discontinuous PWM for three-level inverters with unbalanced neutral-point voltage," in *IEEE Journal of Emerging and Selected Topics in Power Electronics*, vol. 12, no. 2, pp. 2176–2187, Apr. 2024.
[13] S. Bhowmick, D. Mukherjee, T. S. Basu, and C. Chakraborty, "A three-phase four-leg neutral-point-clamped photovoltaic inverter with decoupled active and reactive power control and DC-link voltage ripple minimization under unbalanced grid operation," in *IEEE Transactions on Power Electronics*, vol. 40, no. 6, pp. 7829–7843, Jun. 2025.
[14] J. Monteiro, V. Fernão Pires, A. Cordeiro, J. F. Silva, and S. Pinto, "Dual three-phase four-leg multilevel inverter with backstepping prediction for unbalanced low-voltage grids," in *IEEE Transactions on Industry Applications*, vol. 61, no. 4, pp. 6535–6546, Jul. -Aug. 2025.
[15] W. Li, X. Zhang, Z. Zhao, G. Zhang, G. Wang, and D. Xu, "Implementation of five-level DPWM on parallel three-level inverters to reduce common-mode voltage and AC current ripples," in *IEEE Transactions on Industry Applications*, vol. 56, no. 4, pp. 4017–4027, Jul. -Aug. 2020.
[16] X. Li, C. Qin, Z. Chu, and J. Fang, "A novel modulation scheme for simultaneous common-mode voltage reduction and neutral-point voltage balance in the reduced switch count quasi-Z-source three-level inverter," in *IEEE Transactions on Power Electronics*, vol. 38, no. 10, pp. 12035–12047, Oct. 2023.
[17] R. H. Cuzmar, A. Mora, J. Pereda, and R. P. Aguilera, "An improved reference generator based on MPC of circulating currents and common-mode voltage for modular multilevel matrix converters," in *IEEE Transactions on Industrial Electronics*, vol. 72, no. 2, pp. 1958–1968, Feb. 2025.
[18] J. Chen, D. Jiang, and Q. Li, "Attenuation of conducted EMI for three-level inverters through PWM," in *CPSS Transactions on Power Electronics and Applications*, vol. 3, no. 2, pp. 134–145, Jun. 2018.
[19] P. Tian, F. Chen, T. M. Jahns, and B. Sarlioglu, "The effect of gate drive resistance on the CM EMI performance of the balanced inverter with asymmetrical parasitic impedance distribution," in *IEEE Transactions on Industry Applications*, vol. 60, no. 6, pp. 9052–9065, Nov.-Dec. 2024.
[20] X. Xing, X. Li, F. Gao, C. Qin, and C. Zhang, "Improved space vector modulation technique for neutral-point voltage oscillation and common-mode voltage reduction in three-level inverter," in *IEEE Transactions on Power Electronics*, vol. 34, no. 9, pp. 8697–8714, Sept. 2019.
[21] X. Xing and H. Chen, "A fast-processing predictive control strategy for common-mode voltage reduction in parallel three-level inverters," in *IEEE Journal of Emerging and Selected Topics in Power Electronics*, vol. 9, no. 1, pp. 316–326, Feb. 2021.
[22] P. Liu, S. Duan, C. Yao, and C. Chen, "A double modulation wave CBPWM strategy providing neutral-point voltage oscillation elimination and CMV reduction for three-level NPC inverters," in *IEEE Transactions on Industrial Electronics*, vol. 65, no. 1, pp. 16–26, Jan. 2018.
[23] Z. Wang, J. Teng, M. Zhang, Z. Bu, X. Lin, L. Qi, W. Zhao, X. Li, and X. Sun, "Common-mode voltage suppression strategy for CHB-based motor drive based on topology and modulation optimization," in *IEEE Transactions on Power Electronics*, vol. 40, no. 1, pp. 1697–1716, Jan. 2025.
[24] Z. Chu, C. Qin, X. Li, J. Fang, L. Yang, and Y. Zhang, "Space vector modulation strategy for common-mode voltage suppression in the reduced switch count three-level inverter with unbalanced neutral-point voltages," in *CPSS Transactions on Power Electronics and Applications*, vol. 10, no. 2, pp. 130–140, Jun. 2025.
[25] Y. Zou, L. Zhang, Y. Xing, H. Zhuge, X. Shen, Y. Zhang, and Y. Lu, "An optimized DPWM with reduced leakage current for three-phase three-level inverters with unbalanced neutral-point voltage," in *IEEE Transactions on Power Electronics*, vol. 39, no. 12, pp. 16346–16360, Dec. 2024.
[26] Y. Jiang, X. Li, C. Qin, X. Xing, and B. Zhang, "A generalized modulation method for common-mode voltage reduction of dual-input three-level inverter," in *IEEE Access*, vol. 8, pp. 118762–118772, 2020.
[27] X. Wu, G. Tan, G. Yao, C. Sun, and G. Liu, "A hybrid PWM strategy for three-level inverter with unbalanced DC links," in *IEEE Journal of Emerging and Selected Topics in Power Electronics*, vol. 6, no. 1, pp. 1–15, Mar. 2018.
[28] C. Qin, X. Li, X. Xing, C. Zhang, and G. Zhang, "Common-mode voltage reduction method for three-level inverter with unbalanced neutral-point voltage conditions," in *IEEE Transactions on Industrial Informatics*, vol. 17, no. 10, pp. 6603–6613, Oct. 2021.

Chuanjing Hou received the Ph.D. degree in Control Science and Engineering from Shanghai Jiao Tong University, Shanghai, China, in 2018. He is currently an Associate Professor with the School of Information and Electrical Engineering, Shandong Jianzhu University. His research interests include high-gain multilevel inverter.

Desheng Jia received the B.S. degree in Electrical Engineering and Automation from Weifang University of Science and Technology University, Weifang, China, in 2022. He is currently pursuing the M.S. degree in Control Engineering with Shandong Jianzhu University, Jinan, China. His current research interests include SiC&Si hybrid ANPC three-level inverter.

Changwei Qin received the Ph.D. degree in Electrical Engineering from Shandong University, Jinan, China, in 2019. In 2020, he joined Shandong Jianzhu University, where he is currently an Associate Professor. His current research interests include control of multi-level converters and impedance source converters.

Xiaoyan Li received the Ph.D. degree in Electrical Engineering from Shandong University, Jinan, China, in 2020. From 2021 to 2023, she was a Postdoctoral Research Fellow with Shandong University, Jinan, China. In 2023, she joined Shandong Jianzhu University, where she is currently a Professor. Her current research interests include control of multi-level converters and power quality control.

Jiandong Li received the B.S. degree in Building Electrical and Intelligence from Shandong Jianzhu University, Jinan, China, in 2023. He is currently pursuing the M.S. degree in control engineering with Shandong Jianzhu University, Jinan, China. His research interests focus on multilevel inverters.

Duty Cycle Control Set Model Predictive DC-Link Voltage Control Method for PMSM Film-Capacitor-Driven System

Zhenrui ZHANG, Jing XU, Xinyu WANG, and Qingya ZHANG

***Abstract*—This paper proposes a robust duty cycle control set model predictive DC-link voltage control (DCS-MPDVC) to suppress the DC-link voltage oscillations in the permanent magnet synchronous motor (PMSM) film-capacitor drive system. This method applies an extended state observer (ESO) to suppress unmodeled disturbances and parameter variations and estimate the inductor current of the inverter. Subsequently, to ensure the constraint accuracy of the *dq*-axis current and DC-link voltage, a discrete duty cycle control set is constructed to reduce the prediction error within each control cycle. In addition, a sector judgment mechanism for voltage vector selection is introduced to reduce the computational complexity while maintaining the control performance. The proposed control strategy is experimentally verified on a film-capacitor hardware test platform using DSP, demonstrating the effectiveness of DCS-MPDVC in suppressing the DC-link voltage and optimizing the computational efficiency.**

***Index Terms*—Duty cycle control set system, extended state observer, oscillation suppression, permanent magnet synchronous motor.**

I. Introduction

THE film-capacitor driven system for permanent-magnet synchronous motors has recently been applied in industrial appliances like air-conditioners and aircraft propulsion systems due to its high-efficiency, high-power-density, and low-failure-rate advantages [1], [2]. However, reducing the capacitance value of the DC-link capacitor leads to DC-link voltage oscillations [3]. Active damping compensation based on vector control is an effective control method to tackle this issue. But, it can only passively maintain system stability by increasing damping [4]–[6]. Therefore, to address the adverse effects of DC-link voltage disturbances on the system, direct constraints are imposed on it to achieve better steady-state performance of the motor. For example, designing a DC-link voltage prediction equation and cost function using finite-control-set model predictive control (FCS-MPC) can achieve multi-objective optimization for the film-capacitor-driven system [7]. The constraint on the DC-link voltage can also be incorporated as an additional optimization objective in the cost function of FCS-MPC to achieve stability in the film-capacitor drive system [8]. The stability of FCS-MPC applied to the film-capacitor system has been demonstrated in [9]. A DC-link current observer has been developed in [10] to minimize sensor reliance. However, the accuracy of the predictive equation and control set limits the effectiveness of the constraint on the DC-link voltage. Some solutions have been proposed to address the control and prediction-accuracy issues of the electrolytic-capacitor system [11].

Motor parameter identification [12] and prediction error compensation [13] can solve the system problem of time-varying parameters. However, chip performance will affect their compensation effect, and these methods cannot solve the problem of inaccurate motor modeling. Compared with these schemes, it is simpler and more efficient to use disturbance observers (such as Luenberger observer [14], [15], extended Kalman filter [16], sliding mode observer [17], and adaptive observer [18]) to solve the problems of time-varying parameters and inaccurate modelling. Meanwhile, the disturbance observer not only observes the disturbance of the system but also simplifies the design of the predictive controller. Professor Han proposed anti-disturbance control technology and ESO [19], which can effectively reduce the impact of inaccurate mathematical modelling on the controller. The ESO can extend the unknown part of the motor modelling to an independent state variable and observe it to achieve the real-time acquisition of the motor state [20]. The ESO has more anti-disturbance and parameter-tuning advantages than the traditional disturbance observer. Based on the ESO, progress has also been made in reducing parameter disturbance. [21], [22] have utilized the ESO to develop an accurate prediction model. However, these methods are based on deadbeat model predictive control (MPC). Due to the absence of an explicit cost function, DC-link voltage constraints cannot be added, rendering these methods unsuitable for directly suppressing DC-link voltage oscillation.

When there is only a current prediction equation, solving the

Manuscript received July 29, 2025; accepted August 15, 2025. Date of publication December 30, 2025; date of current version September 9, 2025. This work was supported by the National Natural Science Foundation of China under the grant 51979021 and 51905229, Jiangsu University of Science and Technology Doctoral Research Start-up Funds under the grant 1172932302, and Basic science (Natural science) Research Project of Higher Education in Jiangsu Province under the grant 24KJD470004. (*Corresponding authors: Zhenrui Zhang.*)

All authors are with the Department of Marine Equipment and Technology Institute, Jiangsu University of Science and Technology, Zhenjiang 212003, China (e-mail: tabz00@qq.com, xujing@just.edu.cn, 202200000212@just.edu.cn, 202200000207@just.edu.cn).

Digital Object Identifier 10.24295/CPSSTPEA.2025.00029

deadbeat method can consider both steady-state performance and solution accuracy. However, the multi-objective optimization system has a coupling problem, and the control law cannot be solved directly. Therefore, it is necessary to solve the cost function online. Limited by the controller's performance, the finite control set method is mainly used for the solution. However, the control accuracy of the basic control set relying on the inverter switching state is challenging to meet the control requirements. In order to address this issue, a method proposed in [23] reduces the amplitude of six fundamental effective vectors to half of their original value. It combines two adjacent voltage vectors into a new vector. This approach expands the control set of voltage vectors, resulting in 20 voltage vectors and improved control accuracy. In [24], virtual vectors with different phase angles are generated by averaging the included angles of adjacent fundamental effective vectors, leading to an extended vector control set. This scheme effectively enhances the control accuracy of the vector phase angle. However, significant current ripple still exists at low speeds due to the large vector amplitude. [25] addresses this issue by selecting the optimal voltage vector through multiple iterations of voltage amplitude and angle. However, this approach requires considerable computational resources and is typically applied to high-performance chips such as FPGAs. Using the deadbeat method for duty cycle calculation can lead to performance degradation due to potential changes in motor parameters during operation [26], [27]. On the other hand, a discrete duty cycle is a control set design scheme that exhibits robustness [28], but it lacks an optimization strategy to improve algorithm efficiency. Therefore, further investigation and research are required to explore optimized control strategies for improving the constraint on the DC-link voltage.

This paper introduces the DCS-MPDVC for film capacitor PMSM drive systems to balance control accuracy and computational burden. This approach offers two key contributions:

1) Given the positive correlation between the predicted DC-link voltage and the predicted *dq*-axis currents, an anti-disturbance prediction model for DC-link voltage is developed based on the ESO to improve the prediction accuracy of the DC-link voltage and estimate the inductor current of the inverter. Meanwhile, an under-damped parameter allocation method is introduced and combined with a low-pass filter to enhance the observation accuracy, thus saving the hardware configuration of physical sensors.

2) A duty cycle control set is put forward to decrease the prediction errors associated with the DC-link voltage and *dq*-axis currents. Meanwhile, a sector judgment mechanism and a design method for the duty cycle control set are presented. In a single prediction process, the constraints on the DC-link voltage and *dq*-axis currents are strengthened by comprehensively applying optimal and sub-optimal basic voltage vectors.

This study validates the algorithm's effectiveness in reducing current ripple and suppressing voltage oscillation through a surface-mounted PMSM (SPMSM) film-capacitor drive setup. The paper is structured as follows: The basic design principle of the anti-disturbance prediction model and the method for configuring observer parameters are presented in Section II. Section III discusses the design principles of the duty cycle control set and sector judgment mechanism. Section IV focuses on conducting experimental verification, validating the advantages of the duty cycle control set, the observer, and the suppression of DC-link voltage oscillation.

II. Design and Analysis of Robust Model Predictive DC-Link Voltage Control

The current predictive controller of PMSM ignores the nonlinearity of the inverter and time-varying parameters. Therefore, this study uses the ESO methodology to design a predictive DC-link voltage model.

A. SPMSM's Current Mathematical Model

The accurate mathematical model of SPMSM in a rotating coordinate system can be expressed by

$$\begin{cases} \dfrac{\mathrm{d}i_d}{\mathrm{d}t} = -\dfrac{R_\mathrm{s}+\Delta R_\mathrm{s}}{L_\mathrm{s}+\Delta L_\mathrm{s}} i_d + \omega_\mathrm{e} i_q + \dfrac{1}{L_\mathrm{s}+\Delta L_\mathrm{s}} v_d + f_d \\ \dfrac{\mathrm{d}i_q}{\mathrm{d}t} = -\dfrac{R_\mathrm{s}+\Delta R_\mathrm{s}}{L_\mathrm{s}+\Delta L_\mathrm{s}} i_q - \omega_\mathrm{e}\left(i_d + \dfrac{\psi+\Delta\psi}{L_\mathrm{s}+\Delta L_\mathrm{s}} \right) + \dfrac{1}{L_\mathrm{s}+\Delta L_\mathrm{s}} v_q + f_q \end{cases} \tag{1}$$

where, i_d, i_q, v_d, and v_q are the motor's current and voltage in the rotating coordinate system(*dq*-axis). R_s is the motor's phase resistance. L_s are the SPMSM's inductance in the *dq*-axis. ω_e is the motor's electric angular velocity. ψ is the flux linkage of the permanent magnet. f_d and f_q represent the unknown disturbance in the *dq*-axis. The "Δ" represents the error between the motor's actual and controller parameters.

The PMSM current model in (1) is divided into two parts: the input and the lumped disturbance, as shown in

$$\begin{cases} \dot{\boldsymbol{i}}_\mathbf{s} = \boldsymbol{I}_\mathrm{f} + b\boldsymbol{v}_\mathrm{s} \\ \boldsymbol{Y} = \boldsymbol{i}_\mathbf{s} \\ \boldsymbol{I}_\mathrm{f} = \begin{bmatrix} i_{d\mathrm{f}} \\ i_{q\mathrm{f}} \end{bmatrix} = \begin{bmatrix} -\dfrac{R_\mathrm{s}+\Delta R_\mathrm{s}}{L_\mathrm{s}+\Delta L_\mathrm{s}} i_d + \omega_\mathrm{e} i_q + f_d \\ -\dfrac{R_\mathrm{s}+\Delta R_\mathrm{s}}{L_\mathrm{s}+\Delta L_\mathrm{s}} i_q - \omega_\mathrm{e} i_d - \omega_\mathrm{e}\dfrac{\psi+\Delta\psi}{L_\mathrm{s}+\Delta L_\mathrm{s}} + f_q \end{bmatrix} \end{cases} \tag{2}$$

where, $\boldsymbol{i}_\mathrm{s} = [i_d, i_q]^\mathrm{T}$, $\boldsymbol{v}_\mathrm{s} = [v_d, v_q]^\mathrm{T}$. b is regarded as the gain of the input value, and the current gain of the *d*-axis and *q*-axis of SPMSM is regarded as the same value. $\boldsymbol{I}_\mathrm{f}$ is a nonlinear current disturbance term.

B. Design of Disturbance Observer

The anti-disturbance predictive model adopts the ESO to estimate the motor's lumped disturbance. The disturbance value of the system model can be observed through the input and output of the system. Firstly, the observer model is established according to (2),

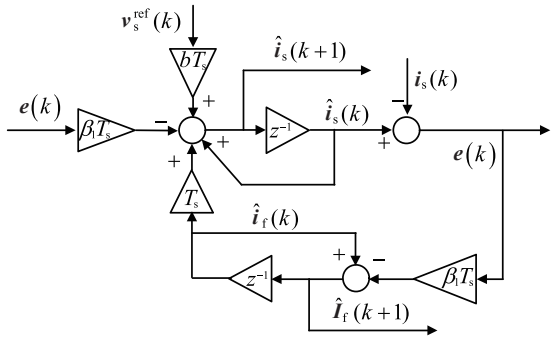

Fig. 1. The disturbance observer computation structure.

$$\begin{cases} \boldsymbol{e} = \hat{\boldsymbol{i}}_s - \boldsymbol{i}_s \\ \dot{\hat{\boldsymbol{i}}}_s = \hat{\boldsymbol{I}}_f + b\boldsymbol{v}_s - \beta_1 \boldsymbol{e} \\ \dot{\hat{\boldsymbol{I}}}_f = -\beta_2 \boldsymbol{e} \end{cases} \tag{3}$$

where, $\boldsymbol{e} = [e_d, e_q]^T$, $\hat{\boldsymbol{i}}_s = [\hat{i}_d, \hat{i}_q]^T$, $\hat{\boldsymbol{I}}_f = [\hat{i}_{df}, \hat{i}_{qf}]^T$.

After the Laplace transform, use (3) to calculate the transfer function of actual disturbance $\boldsymbol{I}_f$ and estimated disturbance $\hat{\boldsymbol{I}}_f$:

$$\hat{\boldsymbol{I}}_f = \beta_2 \frac{\boldsymbol{i}_s s - b\boldsymbol{v}_s}{s^2 + s\beta_1 + \beta_2} = \beta_2 \frac{\boldsymbol{I}_f}{s^2 + s\beta_1 + \beta_2} \tag{4}$$

(4) can be set through parameter configuration as a low-pass filter with a bandwidth ω_f. The transfer function of the second-order low-pass filter is

$$G(s) = \frac{\hat{\boldsymbol{I}}_f}{\boldsymbol{I}_f} = \frac{1}{\frac{s^2}{\omega_f^2} + 2\xi\frac{s}{\omega_f} + 1} \tag{5}$$

After comparing (5) with (4), $\beta_2 = \omega_f^2$, $\beta_1 = 2\omega_f\xi$, the damping coefficient ξ is set to 0.707 by using the design method of the Butterworth filter. The parameter configuration method based on the low-pass filter can be defined as:

$$\begin{cases} \beta_2 = \omega_f^2 \\ \beta_1 = 1.414\omega_f \end{cases} \tag{6}$$

Configure an observation bandwidth larger than the lumped disturbance to estimate the actual disturbance effectively.

C. DC-Link Voltage Anti-Disturbance Prediction Equation

The observer's discrete is obtained by the forward Euler expansion of (3). The control structure of the current disturbance observer is shown in Fig. 1.

$$\begin{cases} \boldsymbol{e}(k) = \hat{\boldsymbol{i}}_s(k) - \boldsymbol{i}_s(k) \\ \hat{\boldsymbol{i}}_s(k+1) = T_s[\hat{\boldsymbol{I}}_f(k) + b\boldsymbol{v}_s^{ref}(k) - \beta_1\boldsymbol{e}(k)] + \boldsymbol{i}_s(k) \\ \hat{\boldsymbol{I}}_f(k+1) = \hat{\boldsymbol{I}}_f(k) - T_s\beta_2\boldsymbol{e}(k) \end{cases} \tag{7}$$

The current disturbance $\boldsymbol{I}_f$ of the motor observed through (3) is brought into (2) to obtain an accurate motor current model. Then, according to the basic principle of FCS-MPC and the inverter basic voltage vectors $\boldsymbol{v}_s^{ref}$, the prediction equation is obtained by forward Euler expansion based on the sample time T_s.

$$\boldsymbol{i}_s(k+1) = T_s[\boldsymbol{I}_f(k) + b\boldsymbol{v}_s^{ref}] + \boldsymbol{i}_s(k) \tag{8}$$

Two-step prediction is adopted to obtain the predicted value of the $k+2$ control cycle because of the one-step control delay of the chip controller.

$$\boldsymbol{i}_s(k+2) = T_s[\hat{\boldsymbol{I}}_f(k+1) + b\boldsymbol{v}_s^{ref}] + \hat{\boldsymbol{i}}_s(k+1) \tag{9}$$

The current disturbance observer has very high observation accuracy and low observation error, namely $\boldsymbol{i}_s(k+1) \approx \hat{\boldsymbol{i}}_s(k+1)$, $\boldsymbol{I}_s(k+1) \approx \hat{\boldsymbol{I}}_s(k+1)$. Therefore, $\hat{\boldsymbol{I}}_f(k+1)$ and $\hat{\boldsymbol{i}}_s(k+1)$ can be obtained by the observer.

The current predictive equation is designed by (9). The predicted value of different basic voltage vectors is obtained through the prediction equation, and the predicted value is compared with the current reference value to obtain the cost function in (10). And constraints related to current limits can also be incorporated in

$$g = [i_d^{ref} - i_d(k+2)]^2 + [i_q^{ref} - i_q(k+2)]^2 \tag{10}$$

In (10), i_d^{ref} and i_q^{ref} are the dq-axis current reference values, which are usually calculated through the speed loop. g represents the prediction error. The voltage vector contained in the control set is brought in (10) individually to obtain the cost value (prediction error). The minimal prediction error g_{min} corresponds to the optimal voltage vector.

The topology structure is depicted in Fig. 2. The voltage equation of the DC-link is given by

$$C\frac{\mathrm{d}v_{dc}}{\mathrm{d}t} = i_L - i_{dc} \tag{11}$$

where, C is the capacitor value. i_L is the inductor current. i_{dc} is the DC-link current, and v_{dc} is the DC-link voltage.

The analysis can be carried out for (11), and the corresponding ESO shown in (12) can be established to observe the inductor current.

$$\begin{cases} e(k) = \hat{v}_{dc}(k) - v_{dc}(k) \\ \hat{v}_{dc}(k+1) = T_s\left[\frac{\hat{i}_L(k)}{C} - \frac{i_{dc}(k)}{C} - \beta_1 e(k)\right] + \hat{v}_{dc}(k) \\ \hat{i}_L(k+1) = -T_s\beta_2 e(k) + \hat{i}_L(k) \end{cases} \tag{12}$$

i_{dc} can be obtained from the equivalent formula of the inverter (using the control strategy of $i_d = 0$).

$$i_{dc}(k+2) = \frac{3v_q(k)\hat{i}_q(k+2)}{2v_{dc}(k)} \tag{13}$$

Based on the ESO for inductor current, the predicted current value, delay compensation, and the estimated applied voltage are combined to estimate the DC-link current of the following control cycle. (14) is used to predict the DC-link voltage.

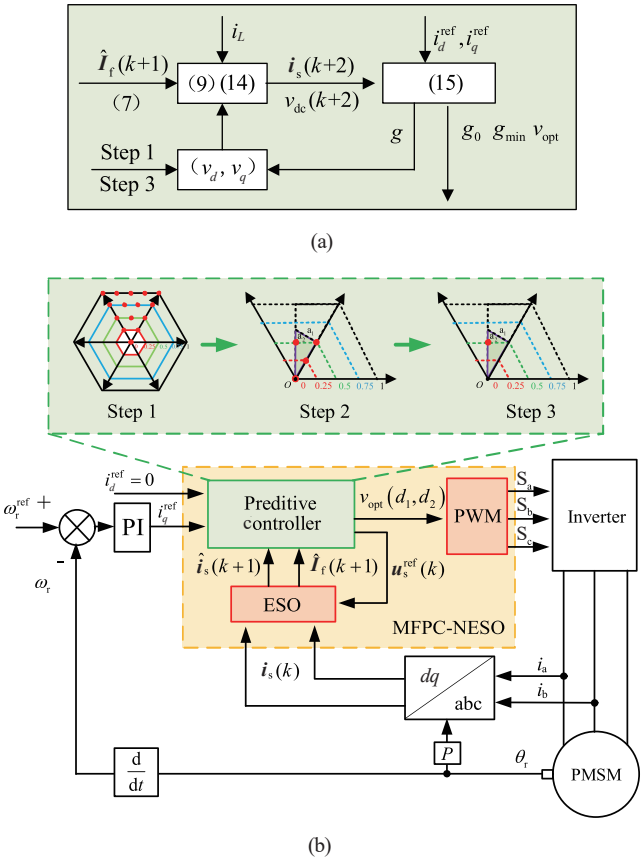

Fig. 2. DCS-MPDVC control structure diagram. (a) Predictive controller, (b) Overall control structure diagram.

$$\begin{cases} v_{\mathrm{dc}}(k+2) = v_{\mathrm{dc}}(k) + \dfrac{1}{C}\left[i_L(k) - i_{\mathrm{dc}}(k+2)\right] T_{\mathrm{s}} \\ i_{\mathrm{dc}}(k+2) = \dfrac{3\left[\hat{i}_d(k+2)v_d^{\mathrm{ref}}(k) + \hat{i}_q(k+2)v_q^{\mathrm{ref}}(k)\right]}{2v_{\mathrm{dc}}(k)} \end{cases} \tag{14}$$

As shown in (14), i_{dc} needs to be calculated using the motor current equation. Therefore, the accuracy of the current equation is essential for predicting the DC-link voltage.

The cost function of DC-link voltage control is [29]

$$\begin{cases} g_{\mathrm{dc}} = g + k_{\mathrm{v}}\left[v_{\mathrm{dc}}^{\mathrm{ref}} - v_{\mathrm{dc}}(k+2)\right]^2 \\ k_{\mathrm{v}} = \dfrac{I_{\mathrm{N}}^2}{V_{\mathrm{dc}}^2} \end{cases} \tag{15}$$

Furthermore, to ensure the system's stability, it is necessary to analyze its damping characteristics. The system damping is directly related to the control voltage. Given that the control strategy of $i_d = 0$ is adopted, the damping compensation related to the q-axis voltage is mainly considered. Therefore, the q-axis reference voltage value needs to be analyzed according to (15). Here, the cost function in the steady state is considered, and its partial derivative is taken to obtain the extreme value solution. First, when the voltage constraint is not added, the partial derivative of the cost function with respect to the q-axis voltage is:

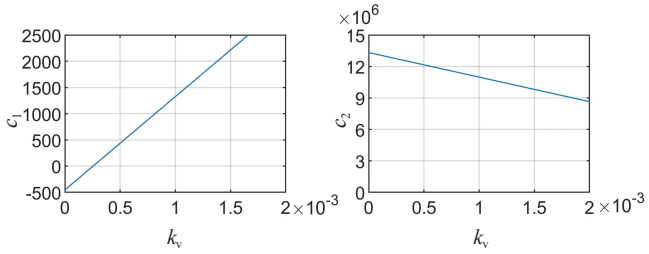

Fig. 3. The curve of system eigenvalues changing with k_{v}.

$$\frac{\partial g}{\partial v_q} = \frac{2T_{\mathrm{s}}^2 v_q}{L_q^2} - \frac{2T_{\mathrm{s}}\left(i_{q\mathrm{ref}} - i_q + \dfrac{R_{\mathrm{s}}T_{\mathrm{s}}i_q}{L_q} + \dfrac{\psi T_{\mathrm{s}}\omega_{\mathrm{e}}}{L_q}\right)}{L_q} \tag{16}$$

k_{v} is used to represent the weight coefficient of the voltage constraint term g_{v}, then the partial derivative of it concerning the q-axis voltage is:

$$\frac{\partial g_{\mathrm{v}}}{\partial v_q} = -\frac{3T_{\mathrm{s}}i_q k_{\mathrm{v}}\left(v_{\mathrm{dc}} - v_{d\mathrm{cref}} + \dfrac{T_{\mathrm{s}}i_L}{C} - \dfrac{3T_{\mathrm{s}}i_q v_q}{2Cv_{\mathrm{dc}}}\right)}{Cv_{\mathrm{dc}}} \tag{17}$$

Adding these two partial derivatives and setting the sum equal to zero allows us to obtain the analytical solution of the q-axis voltage corresponding to the extreme value of the cost function. At the same time, it is easy to prove that this solution is a minimum value by calculating the second-order partial derivative. Therefore, the q-axis voltage with voltage constraint can be expressed as

$$\begin{aligned} v_{q\_\mathrm{damp}} = {} & \frac{2T_{\mathrm{s}}}{L_q}\left(i_{q\mathrm{ref}} - i_q + \frac{R_{\mathrm{s}}T_{\mathrm{s}}i_q}{L_q} + \frac{\psi T_{\mathrm{s}}\omega_{\mathrm{e}}}{L_q}\right) \\ & + \frac{3T_{\mathrm{s}}i_q k_{\mathrm{v}}\left(v_{\mathrm{dc}} - v_{d\mathrm{cref}} + \dfrac{T_{\mathrm{s}}i_L}{C}\right)}{\dfrac{Cv_{\mathrm{dc}}}{L_q^2} + \dfrac{9T_{\mathrm{s}}^2 i_q^2 k_{\mathrm{dc}}}{2C^2 v_{\mathrm{dc}}^2}} \end{aligned} \tag{18}$$

After that, the inverter current value after applying the voltage constraint can be obtained by

$$\begin{aligned} i_{\mathrm{dc\_damp}} &\approx i_{\mathrm{dc}} + k_{\mathrm{v}}\frac{9L_q^2 I_q^2}{2CT_{\mathrm{s}}V_{\mathrm{dc}}^2}\tilde{v}_{\mathrm{dc}} + k_{\mathrm{v}}\frac{9L_q^2 I_q^2}{2C^2 V_{\mathrm{dc}}^2}i_L \\ &\triangleq i_{\mathrm{dc}} + a\tilde{v}_{\mathrm{dc}} + bi_L \end{aligned} \tag{19}$$

Subsequently, by using the eigenvalue analysis method [9] of traditional active-damping compensation, the characteristic equation of the system can be obtained:

$$s^2 + \underbrace{\left(\frac{a - P_L/V_{\mathrm{dc}}^2}{CV_{\mathrm{dc}}^2} + \frac{R_L}{L}\right)}_{c_1}s + \underbrace{\frac{\left[R_L\left(V_{\mathrm{dc}}^2 a - P_L\right) - V_{\mathrm{dc}}^2(b-1)\right]}{V_{\mathrm{dc}}^2 CL}}_{c_2} = 0 \tag{20}$$

Next, analyze the variation of two important stability coefficients c_1 and c_2, under rated conditions as k_{v} increases based on the motor parameters, as shown in Fig. 3. To a certain extent,

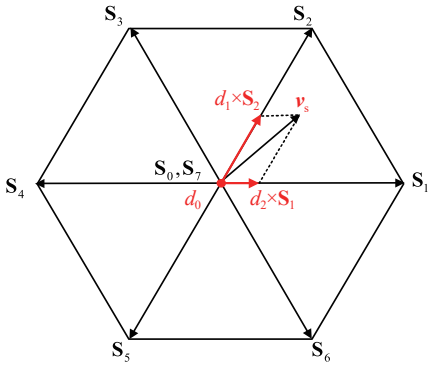

Fig. 4. The relationship between the optimal and suboptimal voltage vectors based on the duty cycle.

the value of c_2 is much greater than zero. So, the instability factor of the system is mainly reflected in the eigenvalue c_1. When $k_v = 0$, the characteristic coefficient of the system is negative, indicating that the system will oscillate. As k_v increases, when k_v is greater than the weight coefficient of the DC-link voltage constraint, the value of c_1 gradually shows a trend greater than zero. Therefore, the MPDVC plays the same role as the traditional active damping method in reshaping the damping and realizes the system's stable control from the active damping perspective.

Next, the key is to find out how to obtain the extreme value that makes the cost function zero. Since the optimization algorithm has a large amount of calculation, the burden on the motor controller is heavy. Therefore, the discrete control set is currently more mainstream. This paper proposes a high-efficiency optimization method based on the duty cycle discretization.

III. Design and Analysis of Duty Cycle Control Set

The voltage vector set used in FCS-MPC consists of fundamental voltage vectors determined by the inverter's output state, which directly corresponds to the motor's operational state. The utilization of inverter voltage plays a crucial role in minimizing prediction errors, particularly at low speeds, where the impact on current and DC-link voltage is more pronounced due to the significant difference in magnitude between the motor voltage vectors and the fundamental vectors. Therefore, optimizing the selection of voltage vectors in FCS-MPC is essential. This study proposes the inclusion of suboptimal voltage vectors alongside the optimal ones and introduces the duty cycle control set to synthesize virtual voltage vectors. This approach enables precise control with a negligible increase in computational load.

A. Duty Cycle Control Set Design

The basic voltage vector ($\mathbf{S}_i$, $i = 0 - 7$) of the two-level voltage source inverter is shown in Fig. 4. Assume the reference voltage vector at the control cycle is $\boldsymbol{v}_s$. One method uses the two adjacent basic vectors to synthesize this vector. Meanwhile, the duty cycle must be added to control the action time of these vectors. Then, in Fig. 4, the action time of $\mathbf{S}_2$ is d_2, and

TABLE I
Voltage Vector of Two-Level Voltage Source Inverter

S_i, i =	S_a	S_b	S_c	$v_{i,\alpha}$	$v_{i,\beta}$
0	0	0	0	0	0
1	1	0	0	$2v_{dc}\,d_i/3$	0
2	1	1	0	$v_{dc}\,d_i/3$	$\sqrt{3}v_{dc}\,d_i/3$
3	0	1	0	$-v_{dc}\,d_i/3$	$\sqrt{3}v_{dc}\,d_i/3$
4	0	1	1	$-2v_{dc}\,d_i/3$	0
5	0	0	1	$-v_{dc}\,d_i/3$	$-\sqrt{3}v_{dc}\,d_i/3$
6	1	0	1	$v_{dc}\,d_i/3$	$-\sqrt{3}v_{dc}\,d_i/3$
7	1	1	1	0	0

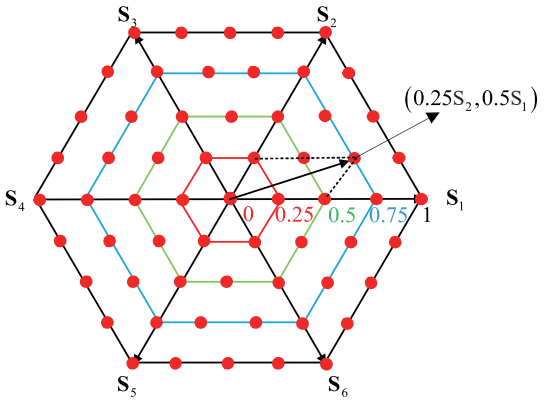

Fig. 5. Virtual voltage vector control set based on duty cycle control.

the action time of $\mathbf{S}_1$ is d_1. Therefore, the basic voltage vectors introduced in Table I are incorporated into the d_i control. Hence, the present study introduces a discrete duty cycle control scheme to streamline the calculation process.

The duty cycle of the motor voltage vector typically ranges from 0 to 1, allowing for active discretization based on this characteristic. For instance, Fig. 5 illustrates the time distribution of a vector divided into intervals of 0, 0.25, 0.5, 0.75, and 1. The figure also displays the distribution and quantity of vector control sets. Each point in Fig. 5 corresponds to different duty cycle control solutions for distinct vectors. Following the solution approach of FCS-MPC, the figure involves iterative calculations for 60 effective vectors (duty cycle control solutions) and zero vectors. Ultimately, the optimal virtual vector with the minimum cost function is chosen as the output for the inverter. However, computing 61 vectors puts a significant computational burden on the chip controller, thus necessitating further optimization of the control set. For example, in Fig. 4, assuming that $\boldsymbol{v}_s$ is the target voltage vector, the optimal voltage vector $\mathbf{S}_2$ and the suboptimal voltage vector $\mathbf{S}_1$ can be obtained during an iterative calculation of the basic effective voltage vector ($d_i \triangleq 1$) of the two-level inverter. So that the sector can be determined and the duty cycle can be optimized in this sector.

A similar design strategy for a discrete duty cycle has been proposed in a previous study [28]. Building upon this method, this paper introduces a novel optimization mechanism aimed

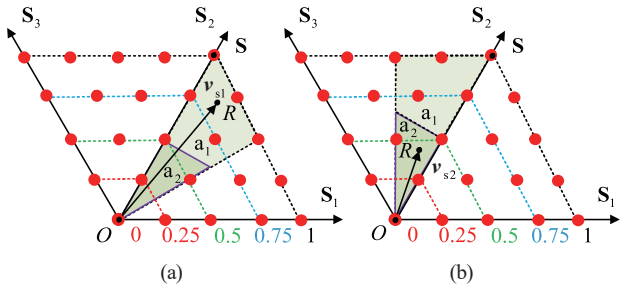

Fig. 6. The optimal vector solution in different target vector sectors. (a) Scenario1, (b) Scenario 2.

at improving the computational efficiency of optimal voltage vector.

B. Optimal Vector Sector Location Strategy

Further, as shown in Fig. 6, it is assumed that the target voltage vectors in two specific control cycles are $\boldsymbol{v}_{s1}$ and $\boldsymbol{v}_{s2}$. For scenario 1, $\mathbf{S}_2$ is the optimal basic voltage vector $\boldsymbol{v}_{opt}^{1st}$, and $\mathbf{S}_1$ is the suboptimal voltage vector $\boldsymbol{v}_{opt}^{2nd}$. For scenario 2, $\mathbf{S}_2$ is the optimal voltage vector $\boldsymbol{v}_{opt}^{1st}$, and $\mathbf{S}_3$ is the suboptimal voltage vector $\boldsymbol{v}_{opt}^{2nd}$. S is the vertex of the optimal basic voltage vector, R is the vertex of the reference voltage vector, and O is the vertex (origin) of the zero vector.

The sector of the target vector can be determined according to the optimal and the suboptimal basic vectors. This sector can be divided into two parts with equal areas, as shown in Fig. 6. Furthermore, the part in the green shadow area close to the optimal basic voltage vector can be used as the search area of the optimal virtual voltage vector. Then, the green shaded area can be further divided into a_1 and a_2 according to the vertical bisector of $\overrightarrow{OS}$. Finally, the search area of the optimal virtual vector can be determined by comparing the distance between $\overrightarrow{OR}$ and $\overrightarrow{SR}$. Here, the amplitude of $\overrightarrow{OR}$ and $\overrightarrow{SR}$ is expressed by the cost value (g_0 and g_{min}) of the zero and optimal basic voltage vectors, respectively. The control region of the optimal vector can be determined in (14).

$$\begin{cases} a_1(d^{1st}, d^{2nd}) = \left\{ \begin{matrix} (0.75,0),\ (1,0),\ (0.5,0.25), \\ (0.75,0.25),\ (0.5,0.5) \end{matrix} \right\} \\ a_2(d^{1st}, d^{2nd}) = \left\{ \begin{matrix} (0,0),\ (0.25,0), \\ (0.5,0),(0.25,0.25) \end{matrix} \right\} \end{cases} \tag{21}$$

Through the above analysis, if the target voltage vector is in the region of a_2 ($g_0 \leqslant g_{min}$), the duty cycle control solution of the optimal basic voltage vector $\boldsymbol{v}_{opt}^{1st}$ and the suboptimal basic voltage vector $\boldsymbol{v}_{opt}^{2nd}$ is {(0,0), (0.25,0), (0.5,0), (0.25,0)}. If the target voltage vector is in the region of a_1 ($g_0 > g_{min}$), the duty cycle control solution of the optimal basic voltage vector $\boldsymbol{v}_{opt}^{1st}$ and the suboptimal basic voltage vector $\boldsymbol{v}_{opt}^{2nd}$ is {(0.75,0), (1,0), (0.5,0.25), (0.75,0.25), (0.5,0.5)}. The control solution of these duty cycles is fixed regardless of the optimal basic vector. So, the vector control set can be expanded to each sector due to the symmetry of the active discrete duty cycle. Since the optimal and suboptimal vectors are known, amplitude computing can significantly reduce the computing time of the chip.

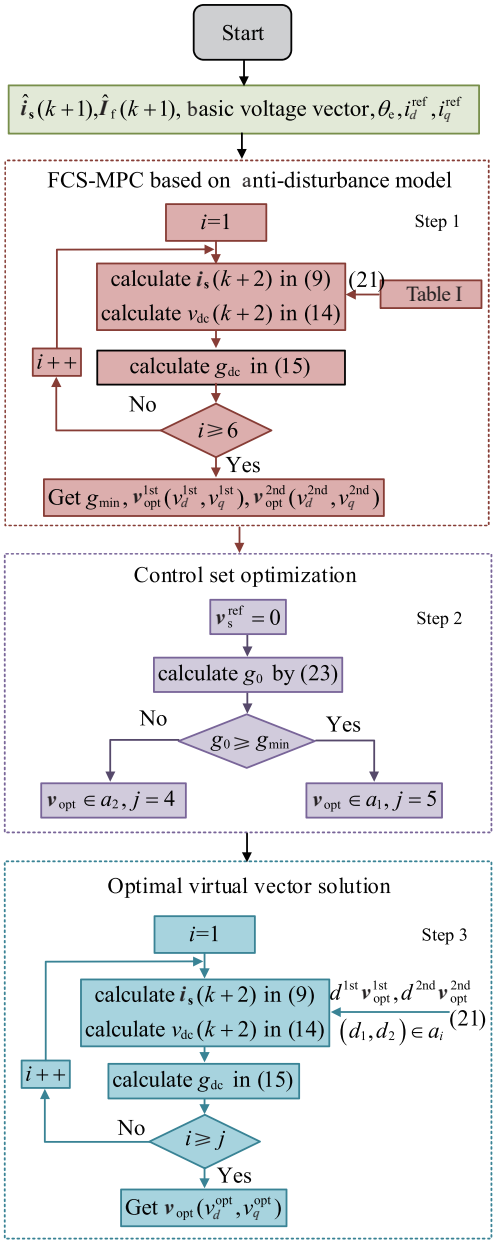

Fig. 7. Control step of DCS-MPDVC.

C. The Calculation Step of the Optimal Virtual Voltage Vector of DCS-MPDVC

The overall algorithm control flow chart is shown in Fig. 7. Step 1 is the same as FCS-MPC, and the calculation amount of the whole control program is mainly affected by this step. In this process, it is necessary to record the optimal and sub-optimal voltage vectors.

Step 1 :

The basic voltage vector must coordinate transformation (22) with the motor rotor position to obtain eight voltage vectors $\boldsymbol{v}_s^{ref}$

$(v_{i,d}, v_{i,q})_{i=1\text{–}6}$ in the dq-axis to facilitate the analysis.

$$T_{2s/2r}(\theta_e)=\begin{bmatrix}\cos\theta_e & \sin\theta_e\\ -\sin\theta_e & \cos\theta_e\end{bmatrix} \tag{22}$$

After coordinate transformation, six dq-axis voltage control solutions are brought into prediction (9), (14) and the cost function (15) to obtain the optimal $\boldsymbol{v}_{opt}^{1st}(v_d^{1st}, v_q^{1st})$ and the suboptimal $\boldsymbol{v}_{opt}^{2nd}(v_d^{2nd}, v_q^{2nd})$ voltage vectors. This step is similar to the FCS-MPC [30].

Step 2 :

The optimization area needs to be further reduced to save computation. First, calculate the cost value of the zero vector according to

$$\begin{aligned} g_0 =& \left[i_d^{ref} - T_s\hat{i}_{df}(k+1) + \hat{i}_d(k+1)\right]^2 \\ &+ \left[i_q^{ref} - T_s\hat{i}_{qf}(k+1) + \hat{i}_q(k+1)\right]^2 \end{aligned} \tag{23}$$

By comparing the size of g_0 and g_{min}, the duty cycle control set is obtained from

$$\begin{cases} \text{if } g_0 \leqslant g_{min} : \boldsymbol{v}_{opt} \in a_2(d^{1st}, d^{2nd}) \\ \text{if } g_0 > g_{min} : \boldsymbol{v}_{opt} \in a_1(d^{1st}, d^{2nd}) \end{cases} \tag{24}$$

Step 3 :

After the duty cycle control set is obtained in step 2, the virtual vector in the dq-axis based on the duty cycle solution (d^{1st}, d^{2nd}) can be obtained through

$$\boldsymbol{v}_s^{ref} = \begin{bmatrix} v_d \\ v_q \end{bmatrix} = \begin{bmatrix} d^{1st}v_d^{1st} + d^{2nd}v_d^{2nd} \\ d^{1st}v_q^{1st} + d^{2nd}v_q^{2nd} \end{bmatrix} \tag{25}$$

$\boldsymbol{v}_s^{ref}$ is calculated by the duty cycle in (18). All voltage vectors $\boldsymbol{v}_s^{ref}$ are evaluated successively via (9), (14) and (15) to obtain the optimal duty cycle (d_{opt}^{1st}, d_{opt}^{2nd}) and corresponding optimal virtual vector $\boldsymbol{v}_{opt}(v_d^{opt}, v_q^{opt})$ that minimizes (15).

D. DCS-MPDVC Overall Control Structure

The DCS-MPDVC's control structure is shown in Fig. 2. $i_d^{ref} = 0$ is used for realizing the SPMSM's current control. Because the time scales of the speed loop and the current loop are inconsistent, the proposed control structure retains the speed loop. Therefore, the reference value of the q-axis current comes from the speed loop controller. The electrical angle θ_e in (22) is obtained by the rotor position θ_r and motor pole pairs P. The inner loop current controller mainly uses the predictive equation, the lumped disturbance observer, the control set (Table I and (21)), the optimization mechanism (Fig. 6), and the cost function (14). After the measured value and estimated value are obtained for (9) and (14), the optimal voltage vector is calculated through the control flow in Fig. 7. The optimal voltage vector can be synthesized by the space vector modulation technology proposed in [31] to act on the motor (the control vector can also be synthesized by the rotor position and SVPWM, which requires more calculation).

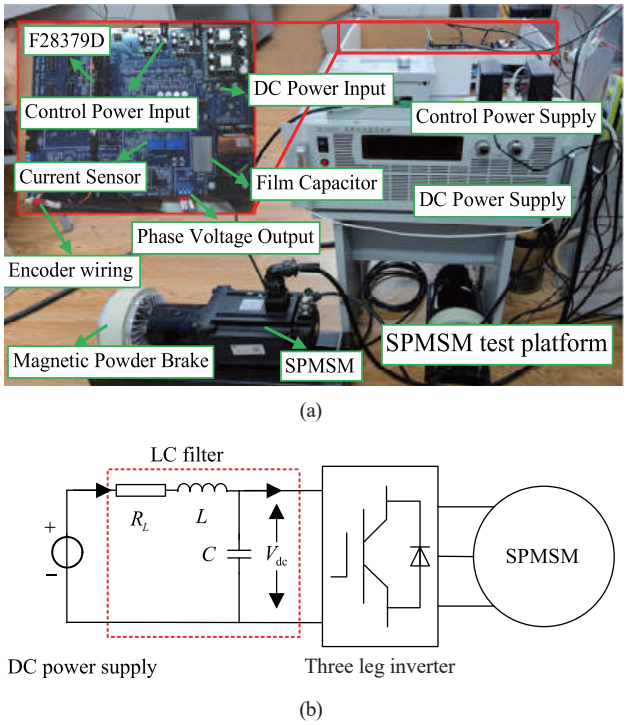

Fig. 8. Experimental hardware platform. (a) Experimental platform, (b) Topology of the experimental platform.

The DCS-MPDVC achieves optimal duty cycle control by implementing a simple judgment mechanism that requires only 4 or 5 additional subset calculation loops. The advantage of this approach is that the subsets are no longer required to undergo coordinate transformation, significantly enhancing both computational efficiency and control accuracy.

IV. Experimental Verification

To verify the proposed control strategy, a hardware experimental platform utilizing a film-capacitor SPMSM drive is employed in this study, as depicted in Fig. 8(a). The experimental setup consists of an SPMSM as the torque output and a magnetic particle brake as the load. The chip utilized is the TMS320F28379D, manufactured by Texas Instruments. The inverter topology entails a two-level voltage source inverter, with its structure depicted in Fig. 8(b). The inverter equipment is also from Texas Instruments (Model: TMDXIDDK379D) and incorporates an IPM module (Model: PS21765). The rectifier is substituted with a DC power supply. The film capacitor is utilized with the parameters referencing the hardware specifications mentioned in [32]. The nameplate parameters of the testing platform are provided in Table II. During the experiment, the controller data is transmitted in real time to the host computer via serial communication, and the host computer plots the experimental results. The switching frequency used in the experiment is 10 kHz (T_s = 0.0001), and the dead time is 5 μs. The experiment's observer bandwidth ω_f is 3000 rad/s, and b is $1/L_{s0}$. The PI controller parameters of the speed loop are K_p = 0.3, K_i = 5, which is designed according to [33]. In addition, unless otherwise specified the motor parameters involved in

TABLE II
EXPERIMENTAL PLATFORM PARAMETERS

Quantity	Symbol	Value
Inverter rated voltage	-	300 V
Inverter rated current	-	8 A
DC-link voltage	V_{dc}	292 V
LC resistance	R_L	0.5 Ω
LC filter inductance	L	3 mH
LC filter capacitance	C	25 μF
Phase resistance	R_{s0}	1.616 Ω
Phase inductance	L_{s0}	11.47 mH
Flux	φ_0	0.175 Wb
Rated current	i_N	4 A
Rated speed	ω_N	1000 rpm
Pole pairs	P	5
Inertia	J	0.0024 kg·m²

TABLE III
CALCULATION TIME OF DIFFERENT CONTROL METHODS

The control method	Time/μs
FCS-MPC	32
MPD2C in [28]	37.5
DCS-MPDVC	32

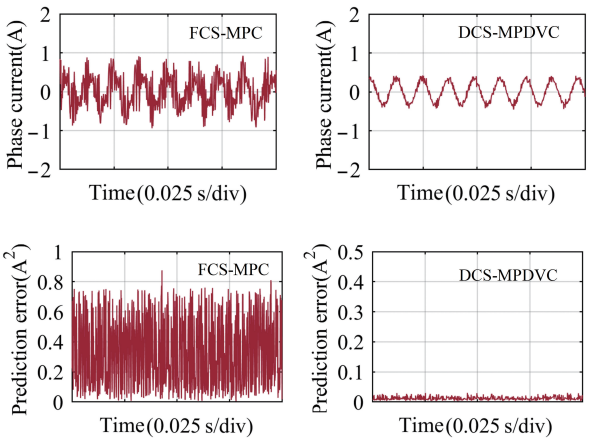

Fig. 9. Experimental results of phase current and predicted error at rated speed.

the controller are the nameplate parameters in Table II.

In this section, the steady-state characteristics of DCS-MPDVC are initially verified. Subsequently, the influence of the anti-interference prediction model on the optimization goal of the current is demonstrated following the enhanced control accuracy achieved by ESO. Finally, the effectiveness of DCS-MPDVC in suppressing DC-link voltage oscillation is evaluated through testing.

A. DCS's Experimental Results of Steady-State Characteristics

The test results of the calculation amount are presented in Table III. In DCS-MPDVC, optimizing the duty cycle does not require coordinate transformation but utilizes scalar calculation, only adding 6 μs to the calculation cycles compared to FCS-MPC. The duty cycle density and programming method proposed in this study align with the MPD2C method introduced in [28]. Moreover, constraints for predicting the DC-link voltage have been implemented. Optimizing the number of duty cycles has significantly enhanced computational efficiency.

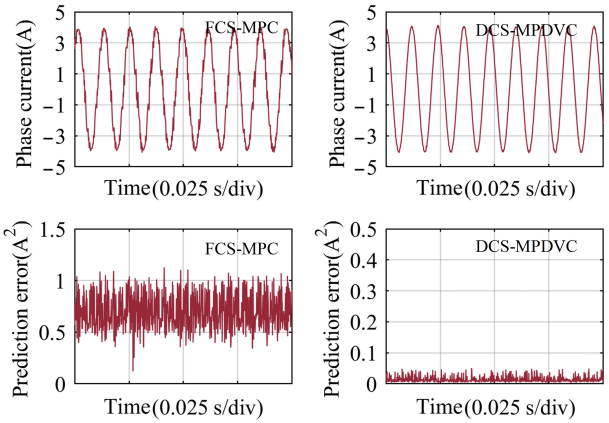

Fig. 10. Experimental results of phase current and predicted error at rated speed.

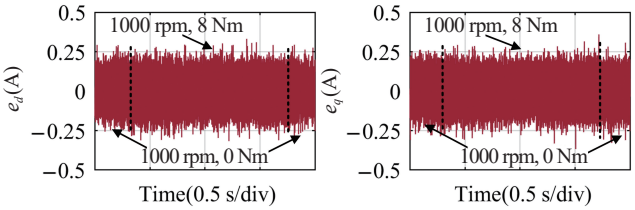

Fig. 11. Experimental results of ESO observation error.

Figs. 9 and 10 are the motor phase current test results and prediction errors under the control of FCS-MPC and DCS-MPDVC. At the rated speed (1000 rpm), the basic voltage vector amplitude is close to the optimal vector amplitude of the motor. However, the FCS-MPC's current distortion is still high because of the significant phase angle error. Because the duty cycle control set in DCS-MPDVC is widely distributed in the whole control area, the zero vector of different control cycles is unnecessary when synthesizing a control vector. Furthermore, the prediction error is slight, so the sinusoidal degree of the phase current is excellent for achieving the control requirements of low current ripple. It can be seen from Figs. 9 and 10 that the prediction error of the DCS-MPDVC is low, which means that the control set accuracy will significantly impact the controller.

B. Experimental Results of the DCS-MPDVC's Robustness

Fig. 11 presents the current observation error of ESO. The *dq*-axis current observation error during the dynamic process is almost negligible. Fig. 12 illustrates the observed disturbance values during the dynamic process, further confirming the excellent dynamic performance of the observer.

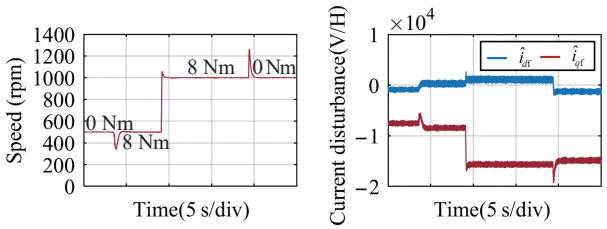

Fig. 12. Experimental results of *dq*-axis observation disturbance under different operating conditions.

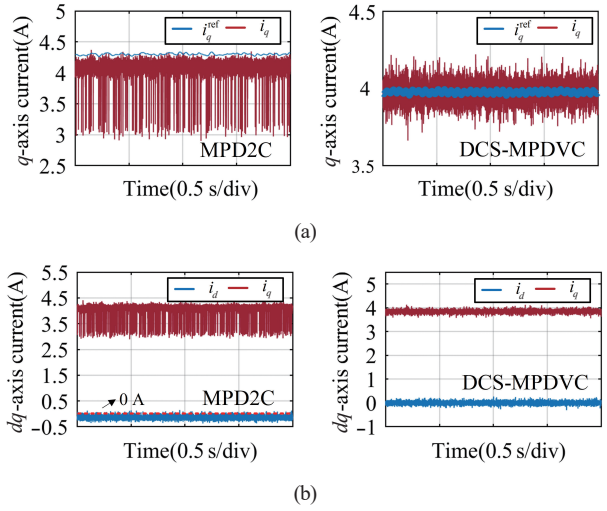

Fig. 13. MPD2C and RDCSMPC's experimental results of the motor *dq*-axis current with artificial parameter error. (a) Motor *q*-axis current and its reference value with artificial parameter error, (b) The motor *dq*-axis is current with an artificial parameter error.

Fig. 13 depicts two sets of comparative tests, and the experiment deliberately introduces an artificial error in the model parameters ($R_s = 2R_{s0}L_s = 2L_{s0}$, $\varphi = 0.5\varphi_0$). In Fig. 13(a), the absence of an anti-disturbance prediction model leads to a steady-state error along with a noticeable current ripple. Conversely, when the anti-interference prediction model is introduced, the steady-state error is eliminated, and the current ripple is significantly reduced. Fig.13(b) depicts the experimental results for the *dq*-axis current. An inaccurate prediction equation leads to non-zero deviation in the *d*-axis current, causing a control error. However, implementing the anti-disturbance prediction model ensures minimal ripples in the *d*-axis and *q*-axis current. This model closely tracks the reference value without any steady-state error.

The experimental results of observation for the inductor current are shown in Fig. 14. An oscilloscope observes the actual value of the inductor current. Through comparison, it can be seen that the steady-state values of the observed value and the actual value are the same, ensuring the system's normal operation.

C. MPDVC's Experimental Results of DC-Link Voltage Oscillation Suppression

Voltage oscillation suppression in a film-capacitor PMSM drive system typically relies on the controller's robustness and control accuracy. The experiment utilizes voltage prediction

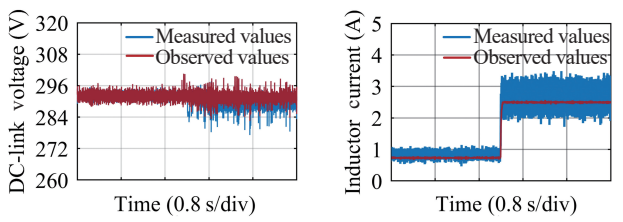

Fig. 14. The DC-link voltage and inductor current observed by the ESO.

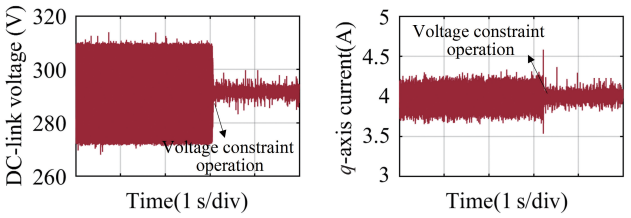

Fig. 15. Experimental results of DC-link voltage and *q*-axis current constraints when the motor operates under the rated working condition.

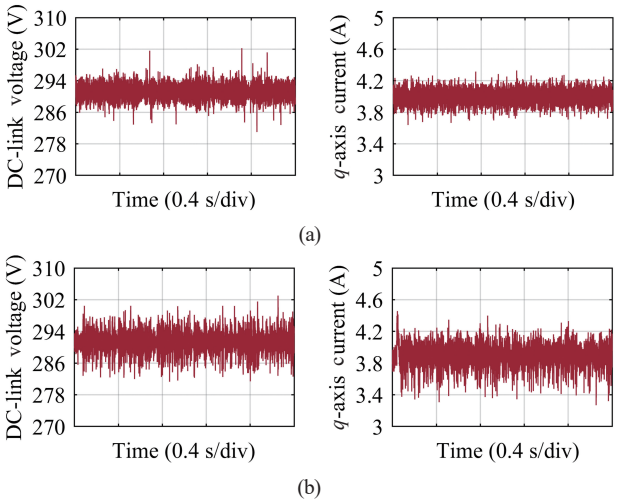

Fig. 16. The comparison experimental results of the stability between the traditional active damping method based on vector control and the proposed DC-link voltage prediction control method: (a) DCS-MPDVC, (b) Active damping compensation.

(14) and a cost function (15). Fig. 15 demonstrates the stabilization effect of DCS-MPDVC on the DC-link voltage during motor operation under rated working conditions. Adding voltage constraints to the cost function enables stable DC-link voltage control.

Fig. 16 shows the experimental results between the active damping method based on the vector control structure and the DC-link voltage constraint method of the control set proposed in [34]. The parameter configuration of the active damping refers to the design method in the paper. It can be seen that, compared with the voltage oscillation suppression achieved indirectly by the active damping, the method proposed in this paper for suppressing the DC-link voltage oscillation is more effective and can also lower the current ripple. These advantages are all due to the direct prediction-constraint structure of the

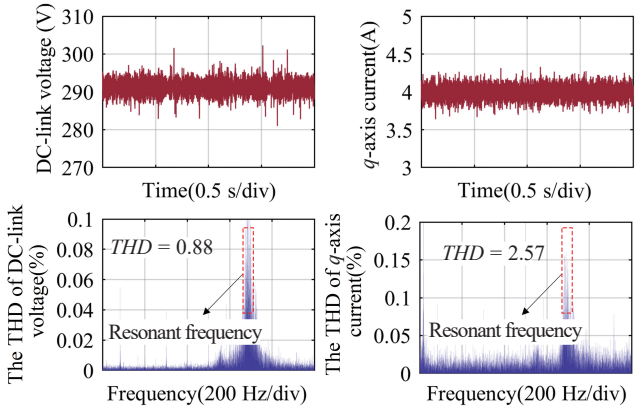

Fig. 17. Experimental results of DC-link voltage and q-axis current based on DCS-MPDVC (the control set is (21)).

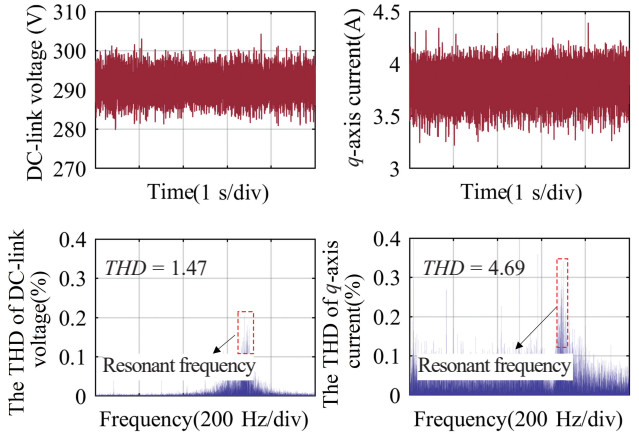

Fig. 18. Experimental results of DC-link voltage and q-axis current based on DCS-MPDVC (control set is (26)).

DC-link voltage.

Figs. 17–19 display the waveforms of the DC-link voltage, q-axis current, and their harmonic analysis under various control conditions. Fig. 16 presents the experimental results of the DCS-MPDVC. Fig. 17 represents the experimental results of the control set (26), while Fig. 18 depicts the experimental results of the prediction model (8).

$$\begin{cases} \text{if } g_0 \leqslant g_{\text{opt}} : v_{\text{opt}} \in a_2, a_2 = \{(0,0)\,(0.5,0)\} \\ \text{if } g_0 > g_{\text{opt}} : v_{\text{opt}} \in a_1, a_1 = \{(1,0)\,(0.5,0.5)\} \end{cases} \tag{26}$$

Compared to Fig. 17, Fig. 18 shows a significant rise in the harmonic content of the DC-link voltage at the oscillation frequency(700 Hz). This observation suggests that decreasing the density of the control set reduces the MPC's constraint ability to constrain the DC-link voltage and dq-axis current. Consequently, this results in a pronounced increase in current ripple and affects the constraint control of the DC-link voltage. Similarly, Fig. 19 exhibits an evident increase in the harmonics of the d-axis current and DC-link voltage compared to Fig. 17. This increase can be attributed to the DCS-MPDVC's inaccurate prediction.

In conclusion, the predictive controller's robustness and the

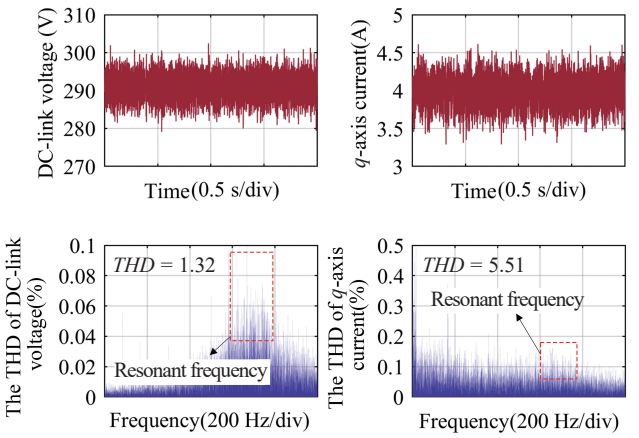

Fig. 19. Experimental results of DC-link voltage stability based on DCS-MPC.

control set's accuracy are essential for multi-objective optimization. The DCS-MPDVC possesses both characteristics, contributing to its superior performance in suppressing current ripple and DC-link voltage oscillation in a film-capacitor PMSM drive system.

V. Conclusion

This paper proposes that DCS-MPDVC solves the problems of significant prediction errors and low constraint accuracy in the film-capacitor permanent-magnet synchronous motor drive system. This method integrates an anti-disturbance prediction model and a duty cycle control set. A parameter configuration method of the ESO based on a low-pass filter is proposed to estimate the lumped disturbance and inductor current. This method effectively solves the estimation problems of unmodeled disturbances and inductor current, improves the prediction accuracy of the DC-link voltage, and reduces physical costs. In addition, a design scheme of the duty cycle control set is introduced, expanding the number of effective virtual voltage vectors from 6 to 60. This scheme includes a simple sector identification principle, which can improve control accuracy within a single control cycle while reducing prediction errors and computational complexity. Experimental results show that the proposed method has better constraint capabilities in the dq-axis and DC-link, making it suitable for the film-capacitor drive system.

References

[1] X. Liu and A. J. Forsyth, "Active stabilisation of a PMSM drive system for aerospace applications," in *Proceedings of 2008 IEEE Power Electronics Specialists Conference*, Rhodes, Greece, Jun. 2008, pp. 283–289.

[2] N. Zhao, G. Wang, B. Li, R. Zhang, and D. Xu, "Beat phenomenon suppression for reduced DC-link capacitance IPMSM drives with fluctuated load torque," in *IEEE Transactions on Industrial Electronics*, vol. 66, no. 11, pp. 8334–8344, Nov. 2019.

[3] Y. Liu, Z. Zhang, H. Guo, Q. Zhang, P. Yang, P. Zhu, and X. Zhuang, "An active DC-link stabilization strategy for permanent magnet synchronous motor drive system based on inverter voltage compensation," in *IEEE/ASME Transactions on Mechatronics*, vol. 27, no. 5, pp. 2786–2795, Oct. 2022.

[4] Z. Ren, D. Ding, G. Wang, B. Li, Q. Wang, G. Zhang, and D. Xu, "Adaptive virtual admittance reshaping-based resonance suppression strategy for PMSM drives with small DC-link capacitor," in *IEEE Transactions on Power Electronics*, vol. 39, no. 3, pp. 3109–3121, Mar. 2024.

[5] J. Huo, N. Zhao, G. Wang, G. Zhang, L. Zhu, and D. Xu, "An active damping control method for reduced DC-link capacitance PMSM drives with low line inductance," in *IEEE Transactions on Power Electronics*, vol. 37, no. 12, pp. 14328–14342, Dec. 2022.

[6] D. Ding, R. Gao, Q. Wang, B. Li, G. Zhang, G. Wang, L. Wu, and D. Xu, "Beatless control strategy based on impedance reshaping for PMSM drives with small DC-link capacitors," in *IEEE Transactions on Industrial Electronics*, vol. 71, no. 7, pp. 6829–6840, Jul. 2024.

[7] I. Won, Y. Cho, and K.-B. Lee, "Predictive control algorithm for capacitor-less inverters with fast dynamic response," in *Proceedings of 2016 IEEE International Conference on Power and Energy (PECon)*, Melaka, Malaysia, Nov. 2016, pp. 479–483.

[8] V. Smidl, S. Janous, and Z. Peroutka, "Improved stability of DC catenary fed traction drives using two-stage predictive control," in *IEEE Transactions on Industrial Electronics*, vol. 62, no. 5, pp. 3192–3201, May 2015.

[9] Z. Zhang, H. Guo, and Y. Liu, "DC-link voltage constraint strategy for DC power supply film-capacitor drive system based on improved model predictive control," in *IEEE Transactions on Industrial Electronics*, vol. 69, no. 10, pp. 9849–9859, 2022.

[10] C. Zheng, T. Dragicevic, and F. Blaabjerg, "Current-sensorless finite-set model predictive control for LC-filtered voltage source inverters," in *IEEE Transactions on Power Electronics*, vol. 35, no. 1, pp. 1086–1095, Jan. 2020.

[11] C. Xue, D. Zhou, and Y. Li, "Finite-control-set model predictive control for three-level NPC inverter-fed PMSM drives with LC filter," in *IEEE Transactions on Industrial Electronics*, vol. 68, no. 12, pp. 11980–11991, Dec. 2021.

[12] D. Q. Dang, M. S. Rafaq, H. H. Choi, and J.-W. Jung, "Online parameter estimation technique for adaptive control applications of interior PM synchronous motor drives," in *IEEE Transactions on Industrial Electronics*, vol. 63, no. 3, pp. 1438–1449, Mar. 2016.

[13] M. Siami, D. A. Khaburi, A. Abbaszadeh, and J. Rodriguez, "Robustness improvement of predictive current control using prediction error correction for permanent-magnet synchronous machines," in *IEEE Transactions on Industrial Electronics*, vol. 63, no. 6, pp. 3458–3466, Jun. 2016.

[14] C. Xia, M. Wang, Z. Song, and T. Liu, "Robust model predictive current control of three-phase voltage source PWM rectifier with online disturbance observation," in *IEEE Transactions on Industrial Informatics*, vol. 8, no. 3, pp. 459–471, Aug. 2012.

[15] A. Andersson and T. Thiringer, "Motion sensorless IPMSM control using linear moving horizon estimation with luenberger observer state feedback," in *IEEE Transactions on Transportation Electrification*, vol. 4, no. 2, pp. 464–473, Jun. 2018.

[16] F. Mwasilu, H. T. Nguyen, H. H. Choi, and J.-W. Jung, "Finite set model predictive control of interior PM synchronous motor drives with an external disturbance rejection technique," in *IEEE/ASME Transactions on Mechatronics*, vol. 22, no. 2, pp. 762–773, Apr. 2017.

[17] Y. Wu and G. Li, "Adaptive disturbance compensation finite control set optimal control for PMSM systems based on sliding mode extended state observer," in *Mechanical Systems and Signal Processing*, vol. 98, pp. 402–414, Jan. 2018.

[18] Y. A.-R. I. Mohamed, "Design and implementation of a robust current-control scheme for a PMSM vector drive with a simple adaptive disturbance observer," in *IEEE Transactions on Industrial Electronics*, vol. 54, no. 4, pp. 1981–1988, Aug. 2007.

[19] R. Madonski, G. Herbst, and M. Stankovic, "ADRC in output and error form: connection, equivalence, performance," in *Control Theory and Technology*, vol. 21, no. 1, pp. 56–71, Feb. 2023.

[20] Z. Zhang, X. Wang, and J. Xu, "Robust amplitude control set model predictive control with low-cost error for SPMSM based on nonlinear extended state observer," in *IEEE Transactions on Power Electronics*, vol. 39, no. 6, pp. 7016–7028, Jun. 2024.

[21] X. Wu, J. Kang, M. Yang, T. Wu, and S. Huang, "Model-free deadbeat predictive current control for SPMSM based on adaptive gain extended state observer," in *IEEE Transactions on Transportation Electrification*, pp. 1–1, 2024.

[22] J. Chen, Y. Fan, M. Cheng, Q. Zhang, and Q. Chen, "Parameter-free ultralocal model-based deadbeat predictive current control for PMVMs using finite-time gradient method," in *IEEE Transactions on Industrial Electronics*, vol. 70, no. 6, pp. 5549–5559, Jun. 2023.

[23] Y. Liu, S. Cheng, Y. Zhao, J. Liu, and Y. Li, "Optimal two-vector combination-based model predictive current control with compensation for PMSM drives," in *International Journal of Electronics*, vol. 106, no. 6, pp. 880–894, Jun. 2019.

[24] Z. Zhou, C. Xia, Y. Yan, Z. Wang, and T. Shi, "Torque ripple minimization of predictive torque control for PMSM with extended control set," in *IEEE Transactions on Industrial Electronics*, vol. 64, no. 9, pp. 6930–6939, Sept. 2017.

[25] Z. Ma, S. Saeidi, and R. Kennel, "FPGA implementation of model predictive control with constant switching frequency for PMSM drives," in *IEEE Transactions on Industrial Informatics*, vol. 10, no. 4, pp. 2055–2063, Nov. 2014.

[26] Y. Zhang, H. Jiang, and H. Yang, "Model predictive control of PMSM drives based on general discrete space vector modulation," in *IEEE Transactions on Energy Conversion*, vol. 36, no. 2, pp. 1300–1307, Jun. 2021.

[27] Y. Wang, X. Wang, W. Xie, F. Wang, M. Dou, R. M. Kennel, R. D. Lorenz, and D. Gerling, "Deadbeat model-predictive torque control with discrete space-vector modulation for PMSM drives," in *IEEE Transactions on Industrial Electronics*, vol. 64, no. 5, pp. 3537–3547, May 2017.

[28] Z. Zhou, C. Xia, T. Shi, and Q. Geng, "Model predictive direct duty-cycle control for PMSM drive systems with variable control set," in *IEEE Transactions on Industrial Electronics*, vol. 68, no. 4, pp. 2976–2987, Apr. 2021.

[29] T. Dragicevic, "Dynamic stabilization of DC microgrids with predictive control of point-of-load converters," in *IEEE Transactions on Power Electronics*, vol. 33, no. 12, pp. 10872–10884, Dec. 2018.

[30] M. Aguirre, S. Kouro, C. A. Rojas, J. Rodriguez, and J. I. Leon, "Switching frequency regulation for FCS-MPC based on a period control approach," in *IEEE Transactions on Industrial Electronics*, vol. 65, no. 7, pp. 5764–5773, Jul. 2018.

[31] I. Osman, D. Xiao, K. S. Alam, S. Shakib, M. P. Akter, and M. F. Rahman, "Discrete space vector modulation-based model predictive torque control with no suboptimization," in *IEEE Transactions on Industrial Electronics*, vol. 67, no. 10, pp. 8164–8174, 2020.

[32] N. Zhao, G. Wang, D. Ding, G. Zhang, and D. Xu, "Impedance based stabilization control method for reduced DC-link capacitance IPMSM drives," in *IEEE Transactions on Power Electronics*, vol. 34, no. 10, pp. 9879–9890, Oct. 2019.

[33] L. Harnefors, K. Pietilainen, and L. Gertmar, "Torque-maximizing field-weakening control: design, analysis, and parameter selection," in *IEEE Transactions on Industrial Electronics*, vol. 48, no. 1, pp. 161–168, Feb. 2001.

[34] D. Wang, K. Lu, P. O. Rasmussen, L. Mathe, Y. Feng, and F. Blaabjerg, "Voltage modulation using virtual positive impedance concept for active damping of small DC-link drive system," in *IEEE Transactions on Power Electronics*, vol. 33, no. 12, pp. 10611–10621, Dec. 2018.

Zhenrui Zhang was born in 1994 in Qingdao, Shandong Province, China. He received the B.S. degree in Engineering from Yantai University, in 2017. From 2017 to 2023, he pursued a consecutive master's and doctoral program at Dalian Maritime University in Dalian, China, and obtained the Ph.D. degree in engineering in 2023. He works as a full-time researcher at the Marine Equipment and Technology Institute of Jiangsu University of Science and Technology.

His research interests include permanent magnet synchronous motor drive control, model predictive control, thin film capacitor drive systems, and shipborne electric propulsion systems.

Jing Xu is an associate professor of mechatronic engineering at the Marine Equipment and Technology Institute, Jiangsu University of Science and Technology, Zhenjiang, China. He received his Ph.D. degree from the China University of Mining and Technology, Xuzhou, China 2018.

His research interests include signal processing, pattern recognition, and intelligent systems.

Xingyu Wang was born in 1989 in Jinzhou, Liaoning Province, China. He received the B.S. degree in Electrical Engineering and Automation and the M.S. degree in Electrical Engineering from Liaoning University of Engineering and Technology in 2014 and 2017, respectively. He received his Ph.D. degree in power electronics and electric drive from Northeastern University, Liaoning, China, in 2022. He is with the Marine Equipment and Technology Institute, Jiangsu University of Science and Technology, China.

His research interests include robotic manipulator motion control, server drive systems, intelligent manufacturing, sliding electrical contact, and basic theory of electrical equipment.

Qingya Zhang, born in 1990 in Lianyungang, Jiangsu Province, China. He received the B.S. degree in Engineering from Nanjing Institute of Technology, in 2014, and the M.S. degree in engineering from Jiangsu University of Science and Technology, in 2017. From 2017 to 2022, he studied at Huazhong University of Science and Technology as a Ph.D. student and obtained the Ph.D. degree in engineering in 2022. He works as a full-time researcher at the Marine Equipment and Technology Institute of Jiangsu University of Science and Technology.

His research interests include intelligent servo drive system and mechanical engineering.

CHINA POWER SUPPLY SOCIETY

China Power Supply Society (CPSS) founded in 1983 is a nonprofit, non-governmental academic and professional organization of scientists and engineers in the power supply & power electronics fields. CPSS is dedicated to achieving scientific and technological progress of power supply and the advancement of the power supply industry. CPSS website is www.cpss.org.cn.

ADMINISTRATIVE OFFICE

Add: 10th Floor, Datong Building, No.467 Huanghe Road, Nankai District, Tianjin, 300110, China

Tel: +86-22-27680796 Fax: +86-22-27687886

E-mail: cpss@cpss.org.cn Website: www.cpss.org.cn

CPSS TRANSACTIONS ON POWER ELECTRONICS AND APPLICATIONS

(Quarterly, Started in 2016)

Vol. 10 No. 4 Dec. 30, 2025

Sponsored by: China Power Supply Society (CPSS)

Technically Co-Sponsored by: IEEE Power Electronics Society (IEEE PELS)

Supported by: Sungrow Power Supply Co., Ltd.
Xiamen Kehua Hengsheng Co., Ltd.
Shenzhen Inovance Technology Co., Ltd.
StarPower Semiconductor Ltd.

Editor-in-Chief: Jinjun Liu

Published by: Editorial Office of CPSS TPEA

Address: 10th Floor, Datong Building, No. 467 Huanghe Road,
Nankai Dist., Tianjin, 300110, China

Tel: +86-22-27680796-18#

Fax: +86-22-27687886

E-mail: tpea@cpss.org.cn

Website: tpea.cpss.org.cn